JAEA

BEM-DDM Modelling of Rock Damage and Its Implications on Rock Laboratory Strength and In-situ Stresses

Flavio Lanaro and Hiroya MATSUI

Crystalline Environment Engineering Group
Geological Isolation Research and Development Directorate

JAEA-Research

BEM-DDM Modelling of Rock Damage
and Its Implications on
Rock Laboratory Strength and In-situ Stresses

Flavio Lanaro[※1] and Hiroya MATSUI[※2]

Tono Geoscientific Research Unit
Geological Isolation Research and Development Directorate
Japan Atomic Energy Agency
Akeyo-cho, Mizunami-shi, Gifu-ken

Within the framework of JAEA's Research & Development on deep geological environments for assessing the safety and reliability of the disposal technology for nuclear waste, this study was conducted to determine the effects of sample damage on the strength obtained from laboratory results (uniaxial compression and Brazilian test). Results of testing on samples of Toki granite taken at Shobasama and at the construction site for the Mizunami Underground Research Laboratory (MIU) at Mizunami, Gifu Pref., Japan, were analysed. Some spatial variation of the results along the boreholes suggested the presence of a correlation between the laboratory strength and the in-situ stresses measured by means of the hydro-fracturing method. To confirm this, numerical analyses of the drilling process in brittle rock by means of a BEM-DDM program (FRACOD^{2D}) were carried out to study the induced fracture patterns. These fracture patterns were compared with similar results reported by other published studies and were found to be realistic. The correlation between strength and in-situ stresses could then be exploited to estimate the stresses and the location of core discing observed in boreholes where stress measurements were not available. A correction of the laboratory strength results was also proposed to take into account sample damage during drilling. Modelling of Brazilian tests shows that the calculated fracture patterns determine the strength of the models. This is different from the common assumption that failure occurs when the uniform tensile stress in the sample reaches the tensile strength of the rock material. Based on the modelling results, new Brazilian tests were carried out on samples from borehole MIZ-1 that confirmed the failure mechanism numerically observed. A numerical study of the fracture patterns induced by removal of the overburden on a large scale produces fracture patterns and stress distributions corresponding to observations in crystalline hard rock in Canada, Japan and Sweden. In particular, despite the uncertainties affecting the choice of the applied loads and displacement boundary conditions, the depth at which fracturing due to removal of the overburden stops could be predicted and, for some parameter combinations, corresponds well with the limit between the Upper Highly Fractured Domain (UHFD) and the Lower Sparsely Fractured Domain (LSFD) observed at Shobasama and the MIU Construction Site. The fact that the stresses predicted close to the bedrock surface were very close to failure could also explain the reason why the strength of the intact rock increases almost linearly with depth in the UHFD. The numerical studies at different scale indicate the need for a robust technique for choosing the correct length of the newly initiated cracks in the BEM-DDM. To solve this problem, the concept of "weakest crack" was proposed in this study based on fractal geometry.

Keywords: Brazilian Test, Boundary Element Method, Correction, Displacement Discontinuity Method, Fractal Geometry, In-situ Stress, MIU, Sheeting Joints, Uniaxial Compressive Strength, Weakest Crack

---

※1 Research Fellow
※2 Editor

岩石の力学物性および初期応力状態に関する
BEM-DDM 解析とその評価

地層処分研究開発部門
東濃地科学研究ユニット

フラビオ・ラナオ[※1]、松井　裕哉[※2]

　本研究は、日本原子力研究開発機構が岐阜県瑞浪市で実施している超深地層研究所計画の一環として、室内試験で得られる強度（一軸圧縮強度や引張強度など）に対するボーリング時の応力解放などで発生する供試体の損傷の影響を把握することを主眼として実施したものである。

　まず、正馬様用地や超深地層研究所用地で掘削したボーリングコアを用いた土岐花崗岩の室内試験結果などを分析したところ、ボーリング孔軸方向の岩石強度などの空間的変化は、水圧破砕法で測定した初期応力状態と関連性があることが推定された。これを確認するため、BEM (Boundary Element Method)-DDM (Discrete Discontinuity Method)解析コード(FRACO2D)を用い、脆性岩盤中のボーリング掘削過程における割れ目発生のシミュレーションを行った。本解析で得られた新たな割れ目の発生パターンは、既往の研究で示されている結果と類似しており現実に近い状態が再現可能と判断した。また、この結果は、解析手法の有効性とともに、強度と初期応力の相関性が、応力測定が実施されていないコアディスキングが生じる場所とその地点の応力の推定に適用できる可能性があることも示している。さらに、岩石強度との相関はボーリング時のコアの損傷を考慮するためにも適用できる。

　これらを踏まえ、圧裂引張試験のモデル化・解析を実施したところ、解析で得られた新たな割れ目の発生パターンが圧裂引張強度に支配的な影響を及ぼすことが示された。これは、岩石材料供試体内で一様な引張が生じ、それが引張強度に達した段階で破壊するという一般的な仮定と異なっている。さらに、本解析結果に基づき、MIZ-1 のコアを用い既往の圧裂引張試験を若干改良した形の試験を、数値解析的に得られた破壊メカニズムを確認するため実施した。一方、サイトスケールでの地表面の削剥などによる土被り圧の解放に伴う割れ目の発生パターンに関する数値実験では、カナダ、瑞浪およびスウェーデンの結晶質岩盤で見られる割れ目分布などの観察結果に一致する割れ目の発生パターンと応力分布を得た。特に、設定した境界条件の不確実性にも関わらず、土被りの削剥に伴い発生する新たな割れ目の発生深度は概ね予測可能であり、幾つかの解析ケースでは、超深地層研究所用地で見られる上部高密度割れ目帯と下部低密度割れ目帯の境界深度に良く一致した。また、予測される基盤となる岩盤の地表面付近の応力状態が破壊状態に近いという事は、インタクトな岩石強度が上部高密度割れ目帯内で概ね線形的に増加している理由と考えられる。さらに、BEM-DDM 解析による異なるスケールの割れ目の発生・伸展に関する数値実験結果は、新たに発生した割れ目の大きさを選択するための技術の必要性を示している。この問題を解決するために、フラクタル幾何学に基づく”Weakest crack”の概念を提案した。

東濃地科学センター（駐在）：〒509-6132　岐阜県瑞浪市明世町山野内 1-64
[※1] 国際特別研究員
[※2] 編集者

Contents

目次

-1-

1. Introduction

This is a blank page.

Introduction

Flavio Lanaro

Japan Atomic Energy Agency

Abstract: This chapter illustrates the role of JAEA in conducting Research & Development on deep geological disposal of nuclear waste, on the reliability of the disposal technology and on safety assessment methods. Within this frame, the present study seeks a better understanding of the influence of the in-situ conditions on the sampling process through the analysis of sample damage. The correlation between sample damage and in-situ stress conditions provides a tool for correction of the laboratory test results and for predicting stresses and in-situ mechanical properties of the Toki granite at the MIU Construction Site (Mizunami, Gifu Pref., Japan). This study of the literature, sample conditions, available laboratory results and numerical models will lead to the proposal of a statistical method based on fractal geometry for quantifying cracking and fracturing in brittle rocks and describing its dependence on the level of stress.

1 Japanese nuclear power industry and the role of JAEA

The rising awareness on the environmental effects of carbon dioxide production has given new focus to the use of nuclear energy, even calling for a "Nuclear (Power) Renaissance". However, the public still seems to have reservations about the multiplication of new power plants. These reservations are mainly of safety character: operational safety, waste isolation and nuclear weapon non-proliferation. For ensuring sustainability of the nuclear fission power generation, efforts must be spent on:

- Develop an "International Safety Culture"

- Solve the issue of long-term isolation of nuclear waste

- Broaden the Public's knowledge on nuclear energy production, its environmental benefits and risks.

The concept of "Safety Culture" presents: i) national differences of interpretation; ii) degradation due to self-complacency of the achieved results and; iii) need of developing interdisciplinary and concise "Safety Cases" [1]. It can be concluded that the development of an international Safety Culture is necessary due to the global consequences of an accident and due to globalization of the market for nuclear plant components.

The issue of long-term isolation of the nuclear waste is a corner-stone for the future development of nuclear power industry. The solution of this problem, although not completely achieved and accepted, should be taken step by step as a chain of preliminary decisions to be refined with time based on the new scientific and technological achievements. Focus should be also given to the final decommission of the nuclear power plants at the end of their operative life and the relative generation of contaminated waste. The concepts illustrated here were presented and interdisciplinary discussed at the 15th International Conference on Nuclear Engineering (ICONE-15) held in Nagoya on April 22 to 26, 2007.

Spent fuel from nuclear power generation in Japan is reprocessed for recovering of uranium and plutonium with resulting high-level radioactive liquid waste. Liquid waste is mixed with raw materials and vitrified. After encapsulation in stainless steel canisters, the waste is temporarily stored for 30 to 50 years to cool down. It will be later disposed underground at a depth of at least 300 m [2]. The concept of geological disposal involves multiple barriers, engineered and natural, to isolate the waste from the human environment in the long term. The Nuclear Waste Management Organization of Japan (NUMO) was established in 2000 for implementing the Disposal Program. During this phase, still ongoing, research and development concerning the scientific aspects of disposal are carried out by the Japan Atomic Energy Agency (JAEA). JAEA was also crated in 2005 by merging two Institutes, the Japan Atomic Energy Research Institute and the Japan Nuclear Cycle Development Institute. This was the result of reforms undertaken by the Japanese Government, but also allowed to merge "basic research" with "applied research" with positive effects of stimulating interdisciplinary interaction and improving management [3]. The main research fields of JAEA [4] are:

- Research on the deep geological environment;

- Improvement of the reliability of disposal technology;

- Development of the advanced safety assessment methods.

JAEA has international cooperation with Belgium, France, Finland, Switzerland, South Korea, Sweden, USA and the international Organisation for Economic Co-operation and Development (OECD)'s Nuclear Energy Agency (NEA).

JAEA is currently carrying out the construction of two non-site specific laboratories, one for the study of sedimentary rock formations at Horonobe (Hokkaido) and one for the study of crystalline rocks at the Mizunami Underground (MIU) Laboratory (Gifu Pref.)[4]. This report will study the mechanical properties of the Toki granite at the MIU Construction Site and at the adjacent investigated site of Shobasama, some kilometres west of MIU. The investigations at different scales comprehend 19 deep boreholes (DH-series where DH-2 is close to MIU) drilled for the Regional Hydrogeological Study (RHS), eight boreholes drilled for the Akeyo Natural Analogue study (of which only AN-1 was deep), four deep boreholes at the Shobasama site (MIU-1 to 4) and one at the MIU Construction Site (MIZ-1)[5]. A 500 m deep borehole was also drilled in the Spring 2007 adjacent to the MIU Construction Site by the Tono Research Institute of Earthquake Science (TRIES).

Rock mechanics laboratory results are available for samples from borehole DH-2, AN-1, MIU-1 to 4 and MIZ-1. These rock mechanics data will be analysed and treated in this report.

2   Outline of this study

The research work presented in this report has to be ascribed to the field of "Research on the deep geological environment". The strength of the Toki granite from the Shobasama and MIU Construction Site is investigated with respect to in-situ sampling conditions and laboratory testing results (Figure 1).

2.1   Aim

A deeper understanding of the mechanical processes that affect the strength of the rock samples when tested in laboratory is sought. In particular, the occurrence of sample damage in the form of microcracking and core discing should be investigated in detail. These forms of damage are induced by the complicated stress-path the rock undergoes during sampling by drilling. For discerning between heterogeneities of the strength of the rock from those due to the in-situ stress field that causes drilling damage, the correlation between laboratory strength and in-situ stresses should be analysed for several rock cores. Since the in-situ stress field and rock damage can also be due to unloading of the rock mass due to removal of the overburden, the study of "sheeting

joints" and associated rock cracking is also needed. In this report, these aspects are studied by comparing analogous cases from the literature, by analysing site specific data from the Toki granite and by numerical modelling of the rock mass at different scales.

2.2 Approach

The correlation between the laboratory results and the in-situ conditions is investigated for: i) assessing and improving reliability of the available rock mechanics data; ii) making prediction of strength and in-situ stresses and; iii) reducing uncertainties on the data. According to Figure 1 this can be achieved by:

- Analyzing the laboratory results from uniaxial compressive and Brazilian testing;

- Analyzing the in-situ conditions in terms of granite facies, alteration, stresses and presence of fault zones;

- Investigating the influence of the in-situ conditions on the strength of the samples for laboratory testing by modelling by means of the boundary element (BEM) and discrete displacement method (DDM). The program FRACOD^{2D} [6] is used and completed with a function for "gravity acceleration";

- Correlating evidences from laboratory, in-situ stresses and numerical results about sample damage;

- Developing a statistical model that quantitatively describes the density and scale dependency of cracking in brittle rocks to be applied to analyse observed microcracks and fracture patterns and to build realistic pre-existing crack patterns for numerical modelling;

- Introducing corrections of the laboratory strength results that would return the in-situ properties of the rock;

- Validating the program FRACOD^{2D} against the results of a well constrained laboratory tests (i.e. Brazilian test) and making prediction of in-situ stresses based on the inferred level of damage of the core samples;

- Reducing uncertainties of the in-situ rock strength and processing of the laboratory results of Brazilian testing.

2.3 Plan of the activities

The following activities were carried out according to the approach described in Sec. 2.2:

1) Study the general geological and structural conditions of the Tono Area;

2) Study the crystalline structure of the Toki granite by thin-sections and x-ray spectroscopy;

3) Study the available results of laboratory testing on samples of Toki granite (mainly uniaxial compressive tests, Brazilian tests, fracture stiffness and fracture toughness);

4) Study the sampling process by coring;

5) Correlate the results of the laboratory tests with the in-situ conditions where the samples were taken: geology, depth, in-situ stresses, fault zones;

6) Make predictions of laboratory test results for those depths where samples are not available;

7) Make predictions of the in-situ stresses in boreholes where direct stress measurements are not available;

8) Make predictions of crack/fracture patterns at different scales (i.e. core, borehole and site scale);

9) Make prediction of stress distributions at different scales (i.e. borehole and site scale);

10) Promote software development by implementing the "gravity function" into the linear elastic fracture mechanics program FRACOD^{2D};

11) Validate the obtained results against other published results about the Shobasama and MIU Construction Site and/or about similar laboratory tests, material and sites overseas;

12) Develop a conceptual model for approaching modelling of brittle material by means of fracture mechanics at different scales.
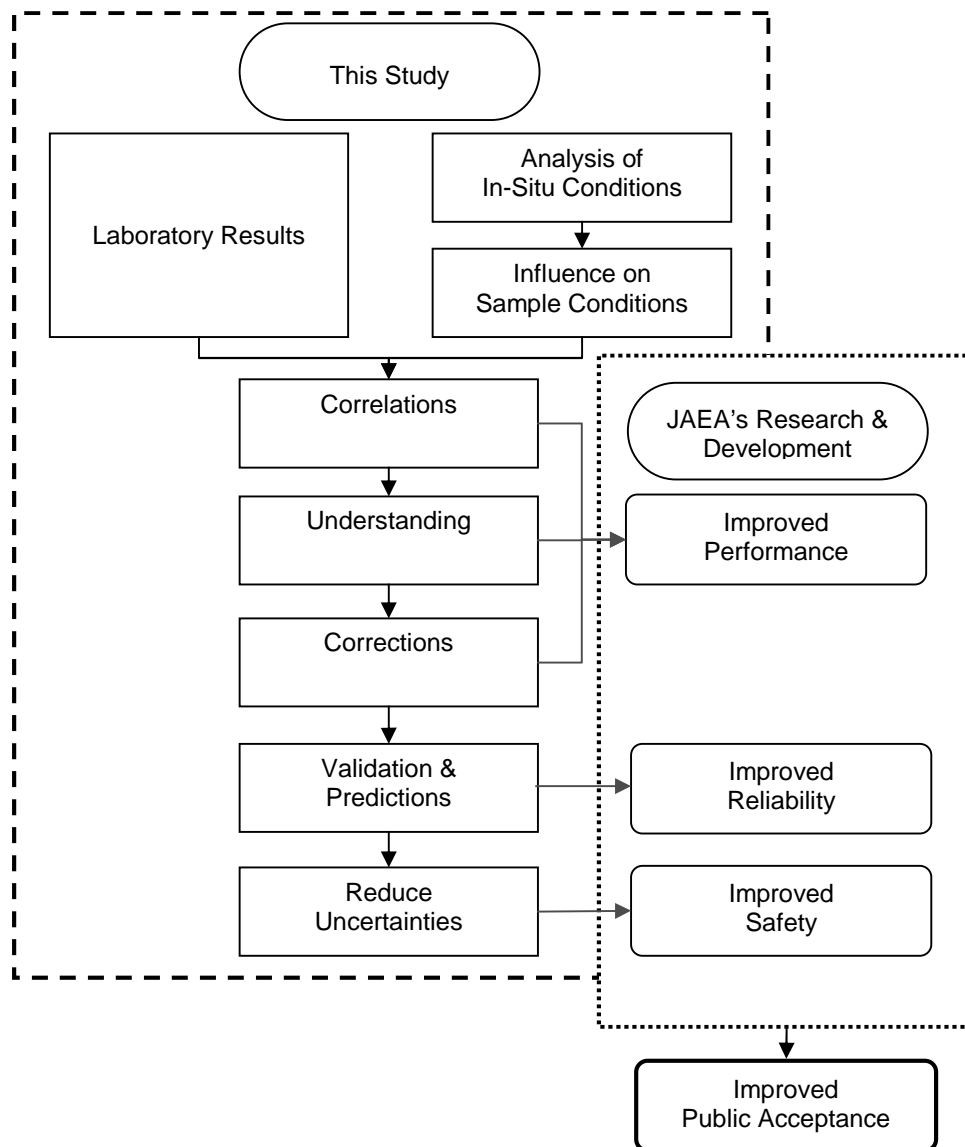

Figure 1. Flow-chart of the structure of this study and its implications for JAEA's Research & Development on deep geological environment.

3 Structure of the report

This report is structured as a collection of "papers". Each "paper" or "chapter" is designed to constitute an independent body of text that can be read separately without need to access all the previous chapters (except for the "DISCUSSION" chapter). The chapters/papers contained in this report are listed in Table 1. The titles of each chapter follow the logic that the later is built on the achievements of the former, so that the Reader should not encounter problem in understanding the research path that led from the introduction to the discussions and conclusion.

Table 1. Chapters and papers contained in this report.

Chapters/ Papers	Title	Authors
GEOLOGY	Geology of the Tono Area with focus on the Toki granite	Flavio Lanaro
PAPER1	Spatial variability of the compressive strength of the Toki granite at the Shobasama and Mizunami Construction Site, Japan *(to be submitted to Rock Mechanics and Rock Engineering)*	Flavio Lanaro, Toshinori Sato, Shigeo Nakama
PAPER2	Spatial variability of the Brazilian tensile strength of the intact Toki granite at Shobasama and Mizunami Construction Site, Japan	Flavio Lanaro
PAPER3	Modelling Brazilian tests with FRACOD^{2D} (FRActure propagation CODe) *(submitted to the International Journal of Rock Mechanics & Mining Science)*	Flavio Lanaro, Toshinori Sato, Mikael Rinne, Ove Stephansson
PAPER4	Drilling induced damage of core samples: evidences from laboratory testing and numerical modelling	Flavio Lanaro
PAPER5	Estimation of in-situ stress field based on core sample damage *(published in the Proceeding of the Autumn Meeting of the Mining and Materials Processing Institute of Japan, ISSN 019-7915, 2007)*	Flavio Lanaro, Shigeo Nakama, Toshinori Sato
PAPER6	Sample damage investigation by laboratory testing and DDM modelling by FRACOD^{2D} of Brazilian tests on Toki granite	Flavio Lanaro, Toshinori Sato, Akio Funato
PAPER7	Modelling the formation of sheeting joints with FRACOD^{2D} (FRActure propagation CODe)	Flavio Lanaro, Kiyoshi Amemiya, Atsuo Yamada
PAPER8	Thin-sections and x-ray spectroscopy of Toki granite samples from borehole MIZ-1	Flavio Lanaro, Kenji Amano, Kiminori Nakamata
DISCUSSION	Discussions and conclusions	Flavio Lanaro

4   Implications of this study

The results of this study will possibly have implications for JAEA's Research & Development but also more general implications in the field of Rock Mechanics.

4.1   Contribution to JAEA's Research & Development

This study is believed to give contribution to JAEA's Research & Development on the deep geological environment in the form of:

1) Improved understanding of the laboratory mechanical properties of the Toki granite (uniaxial compressive and Brazilian strength) (PAPER1 and PAPER2);

2) Improved understanding of the in-situ mechanical properties of the Toki granite (PAPER1 and PAPER2);

3) Improved understanding of the process of sample disturbance during drilling (PAPER1, PAPER2, PAPER4, PAPER6, PAPER7 and PAPER8);

4) Improvement in understanding of the process of formation of cracks in brittle rock in laboratory (PAPER3 and PAPER6);

5) Improvement in understanding the process of formation of fractures in brittle rock due to removal of the overburden (PAPER7);

6) Improvement of the prediction of the mechanical properties of the rock in-situ (PAPER1, PAPER2, PAPER3 and PAPER6);

7) Improvement in predicting the in-situ stresses (PAPER5);

8) Improvement in understanding of the distribution of in-situ stresses in the rock mass affected by fracturing and faulting at Shobasama and MIU Construction Site (PAPER7);

9) Improvement of the strategy for designing numerical models for linear elastic fracture mechanics by FRACOD^{2D} (DISCUSSION).

4.2   General applications

The results of this study might also have the following general applications:

- Empirical rock mass classification systems: The uniaxial compressive strength is often included among the input parameters. If there are differences between the in-situ and laboratory strength of the intact rock (PAPER1 and PAPER2), these will affect the results of the classification systems. Reliability of the classification results will be improved by corrections of the laboratory results;

- Estimation of the in-situ stresses: By analysing the correlation between intact rock strength and in-situ stresses in a certain homogeneous geological area, it would be possible to predict stresses at locations where measurements are not available (PAPER5);

- Quantification of crack and fracture patterns: Numerical modelling offers a unique possibility of following the crack propagation inside laboratory samples (PAPER3 and PAPER6), at the borehole (PAPER4) or site scale (PAPER7);

- A new way of interpreting the results of Brazilian testing: Numerical models show that the laboratory peak strength obtained in laboratory is probably not only marginally correlated with the tensile strength of the rock constituting the samples but depends on the fracture propagation properties under confinement stresses (PAPER3 and PAPER6);

- Model for describing density and size distribution of cracks and fractures: Within the framework of fractal geometry, a model for describing the density (number of cracks in a certain rock volume) and size distribution (proportion of cracks with different length in a certain rock volume) is proposed. The parameters of this model depend on the level of stress through the fractal dimension of the crack pattern and other proportionality constants (DISCUSSION). This has repercussion on the analysis of natural and numerical crack and fracture patterns and can be used to quantify sample damage in laboratory

5   References

1) IAEA: Geological disposal of radioactive waste, IAEA Safety standards for protecting people and the environment, International Atomic Energy Agency, Safety Requirements No. WS-R-4 ,2006.

2) Final Act: Specified Radioactive Waste Final Disposal Act, Japanese Law, July 7, 2000.

3) JAEA: Japan Atomic Energy Agency (JAEA), JAEA's company brochure, Public Relations Division, p. 27, 2005.

4) JAEA: Research and development on geological disposal technologies, JAEA's company brochure, Geological Isolation Research and Development Directorate, JAEA, p.10. , 2007

5) Hanamuro T., Saito H., Asamori K., Iyatomi Y., Tsuruta T., Yabuuchi S., Mizuno T., Sato T., Nakatsuka N., Shigeta N., Hasegawa K., Takeda S. eds.:ICGM'04, 2004. International Conference on JNC Underground Research Laboratory Projects in Mizunami and Horonobe, Japan – Part1: International Conference on Geoscientific Study in Mizunami '04 (ICGM'04) – Record–, Japan Nuclear Cycle Development Institute (JNC), Report JNC TN7400 2004-010., p. 157, 2004.

6) Shen B., Rinne M., Stephansson O. : FRACOD2D - Two dimensional fracture propagation code (Version 2.3.1), FRACOM Ltd, Finland (www.fracom.fi) , 2007.

This is a blank page.

-11-

2.　Geology

This is a blank page.

Geology of the Tono Area
with focus on the Toki granite

Flavio Lanaro

Japan Atomic Energy Agency

Abstract: This chapter offers an overview of the petrography, fracturing and large-scale structures occurring in Toki granite at the Tono area (Gifu Pref., Japan). Geological descriptions of the investigated Shobasama and MIU Underground Laboratory Construction Site are also given together with the layout of the facility. The overview provides the starting point for the analyses related to the strength of the Toki granite treated in the rest of this report.

1   Introduction

The role of the Japan Atomic Energy Agency (JAEA) is to support the nuclear waste management plan of Japan with the knowledge provided by research and development results. This knowledge will allow:

(1) Improved reliability of the geological disposal technology;

(2) Tested technical choices and solutions;

(3) Guidelines for regulatory requirements.

The concept of the Japanese geological repository for high radioactive waste is illustrated in Figure 1 (JNC, 2005). The isolation comprehends engineered and natural barriers. The engineered barriers consist of immobilisation of the waste in glass form, stainless steel canister, steel overpack, bentonite and sand buffer. The natural barrier is offered by the geological environment which should guarantee long-term stability and good isolation during the decay time of the radionuclides.

Non site-specific research and testing is to be performed at two Sites under the supervision of JAEA. These sites were chosen to be:

➢ The Mizunami Underground Research Laboratory in crystalline rocks located in the Gifu Prefecture, Central Japan;

➢ The Horonobe Underground Research Laboratory in sedimentary rocks located in the northern Hokkaido Island.

Extensive investigations were also carried out at the Tono Mine and the Shobasama Site located in the Toki and Mizunami Municipalities that are pertinent to the Mizunami URL Site. This report will focus on the geology and rock mechanics of the Mizunami URL. The Mizunami URL is a full scale laboratory for site-non-specific testing of the investigation and construction techniques which are expected to be the technical basis for the design and safety assessment of a nuclear waste repository. After the sub-surface investigations have been completed at Mizunami (Phase I), the construction of a main shaft and a ventilation shaft is presently being carried out (Phase II). The two shafts have today reached a depth of about 200 m heading to a final depth of 1000 m. The purposes of the Phase II are:

➢ The refinement of the investigation techniques, from borehole information to shaft information;

➢ The improvement of engineering techniques for deep underground excavations.

Pilot boreholes will be drilled from the actual bottom of the shafts and will provide the opportunity and information for the development of the investigation and construction techniques.

The operational Phase III will consist of investigations at the Middle and Main Stages.

In this report, particular attention will be paid to geological settings such as formation, faulting, erosion and upheaval that have affected the Toki granite rock basement in geological time. Furthermore, the effects of these geological processes (e.g. grain size, alteration, weathering and fracturing) will be correlated to the mechanical properties of the Toki granite obtained from laboratory testing on core samples.
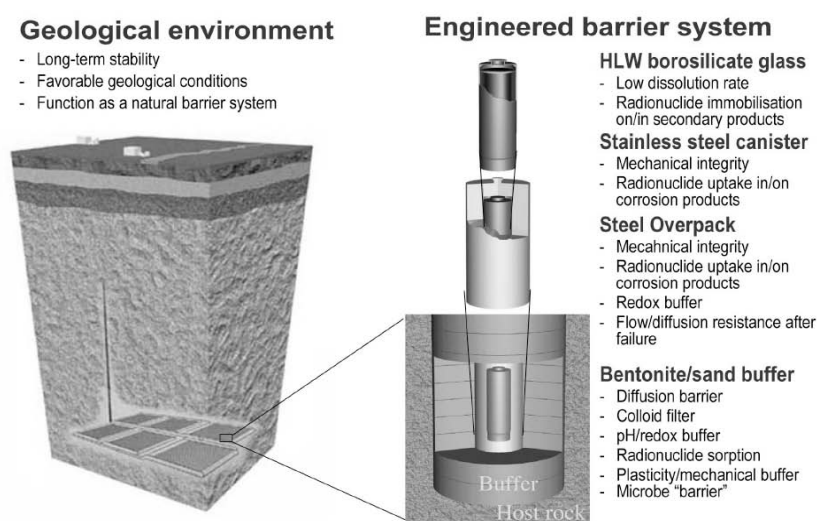

Figure 1. Concept of the nuclear waste isolation and disposal by means of natural and engineered barriers in Japan [1].

2 Geology of the Tono Area (Gifu Pref., Japan)

2.1 Evolutionary aspects

Before 20 Ma ago, the Japanese Islands were attached to the Asian continent. At this time, several granitic intrusions originated in the upper crust of Paleozoic rocks (sandstone and shale), among them the Toki granite formation at Mizunami. The age of the Toki granite was determined based on chemical U-Th Total PB Isochron Method (CHIME) and resulted to be about 68 Ma (60-100 Ma) [2]. This age correspond to a drop of the magma temperature below 700°. The cooling process from this temperature to the actual temperature of about 25° has occurred since then and could be reconstructed by means of K-Ar Methods for dating the biotite minerals. The FT Method indicates that the closure of the apatite crystals, which occurs at about 125°, took place between 45 and 38 Ma (Figure 2). Considering a hypothetical temperature gradient of about 25-30°C/km, which is also the present temperature gradient in the crust of Japan, the apatite would have crystallized at a depth between 3.3 and 4 km [3].
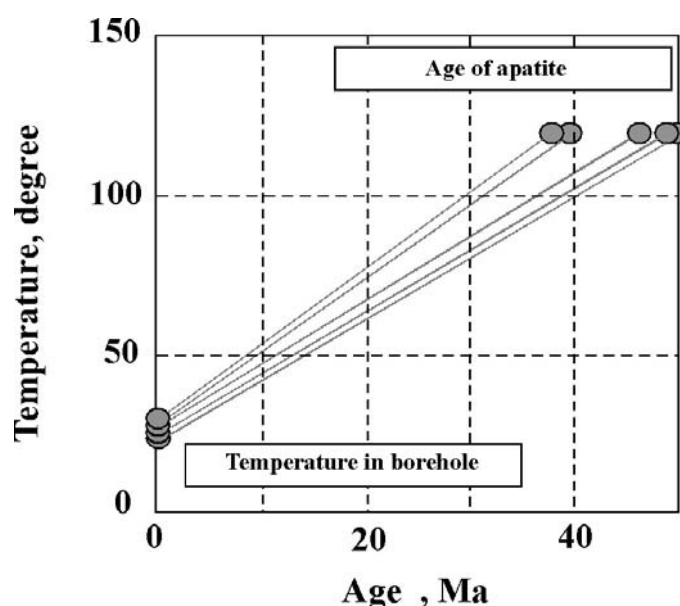

Figure 2. Estimation of the cooling rate from the closure of the Apatite crystals of the Toki granite at Mizunami [3].

Between the age of 45-38 Ma and the age of formation of the present sedimentary cover, processes of continental erosion might have occurred. This period was characterized a by a rather static tectonic history characterized by the push of the Pacific plate towards the Mariana Trench, when either uplift or subsidence seem to have occurred. However, starting from around 20 Ma, the Japan See opened up in a rather short time producing the formation of the Japanese Archipelago and its rotation of about 50° clockwise.

This very active tectonic period with formation of fault-bounded graben structures seems to have last until 15 Ma. Graben were probably originated by a NNW－SSE normal faulting produced by horizontal paleo stress [4]. Most of the sedimentary formations at Mizunami originated during this time between 20 and 15 Ma ago by filling the graben basins. It is not possible to say at present in what extent the erosion processes took place before or during such a tectonic active period. However, these processes produced a landscape of the Toki granite bedrock characterized by paleo-channels that would later be filled with see and lacustrine sediments (see Figure 4)[5].

The channels on the peneplained subsurface of the basement granite are often filled with coarse sediments. Rainwater permeating to the unconformity between the sediments and the granitic basement migrates mainly via the channel structure. Detrital and carbonaceous materials, pyrite

and zeolites can then fixate minerals dissolved and transported by the groundwater (e.g. Uranium mineralisations) [6],[7]. Mineralizations are often weak or non-existent where the groundwater migration is rapid while they are much stronger where groundwater is stagnant.

After the opening of the Japan See, the tectonics of Southwest Japan was characterised by deformations induced by the collision of the Izu-Bonin Arc from south probably dating from the Middle Miocene (Figure 3). This tectonic event changed the paleostresses into a compressional regime that produced the inversion of the initially normal faults. The Itoigawa-Shizuoka Tectonic Line (ISTL) represents the eastern end of the zonally arranged continuous sedimentary terraces. However, as approaching the ISTL, also other regional features such as the Akaishi Tectonic Line (ATL) appear to have originated due to the collision of the Izu-Bonin Arc. The amount of lateral separation along the ATL was estimated to be larger than 50 km and produced a northward migration of southwest Japan while the block east of ATL would rotate counterclockwise [8]. This stress regime might have originated coaxial folding in the sedimentary formations at Mizunami that successively underwent some hinge rotation and plunging (Figure 5) [9]. An estimated uplift of about 340 m would have affected the Mizunami and Tono area since the formation of the Seto Group 1.5 Ma ago [10].

There seems to be proofs that the faults around Mizunami Site (e.g. Tsukiyoshi Fault) would have experienced their maximum displacement about 15 Ma ago. In fact, the fault movements dislocate the sediments of the oldest formations (Mizunami Group) of about 30 m [2] but not the Pliocene rocks of the Seto Group. Despite this, there could be the possibility that the faults already existed before the sedimentary formations. Indications of this might be observed at the Shobasama Site, where a larger width of the deformed and core zone of the Tsukiyoshi Fault was observed in the Toki granite than in the Mizunami Sedimentary Group. This might, however, be related to differences in stiffness and healing processes between the granitic and the sedimentary formations.

Figure 3. The present tectonic regime in Southwest Japan due to the Izu-Bonin Arc collision. Other tectonic features are also represented: the Akaishi Tectonic Line (ATL); the Itoigawa-Shizuoka Tectonic Line (ISTL); Median Tectonic Line (MTL) [8].
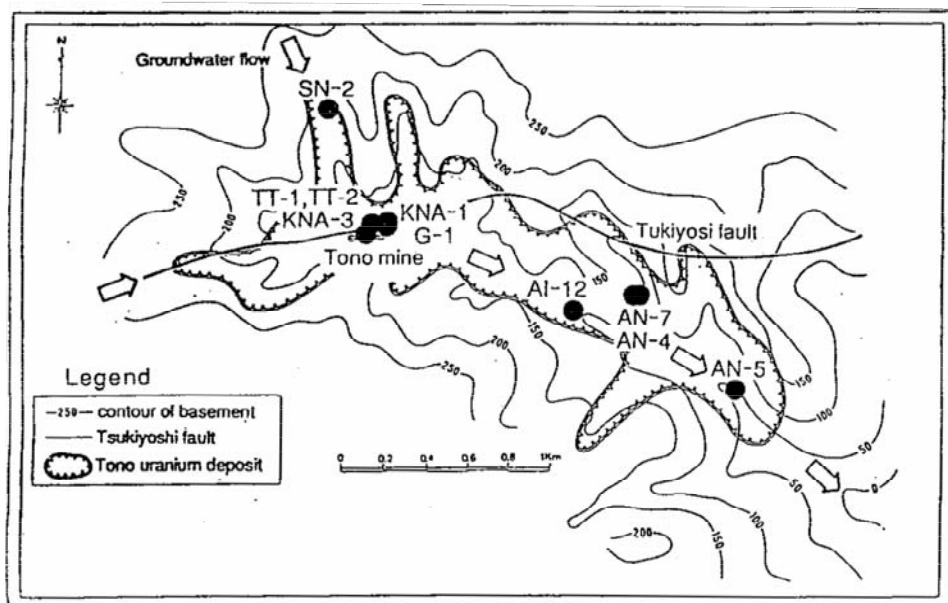
Figure 4. Paleo-channels on the peneplained granitic basement observed at the Tono Mine [11].
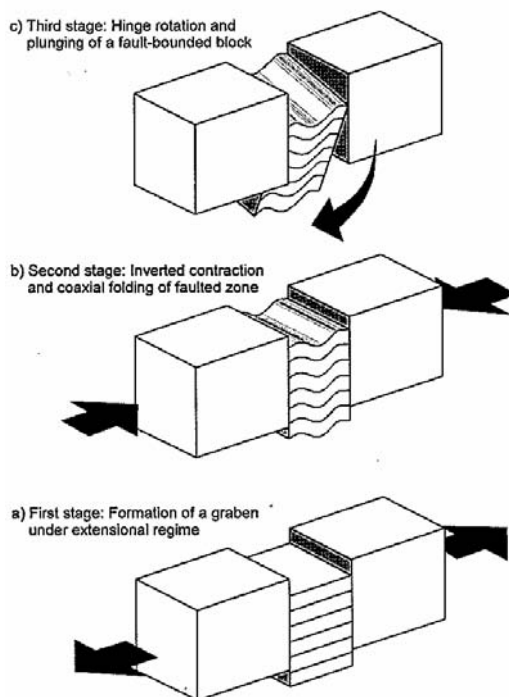
Figure 5. Reconstruction of the tectonic history of the Miocene sedimentary basins in Southwest Japan and Mizunami [9].

Large scale tectonic features were recognized at the scale of 50×50 km (Figure 6). Most of the faults strike NW-SE or NE-SW and intercept each other at an angle between 60° and 70°. These faults are namely the Shirakawa, Adera, Hanadate, Kasahara, Kasahara, Sanageyama Kita, Enasan, Byoubusan, Akou and Adera Faults. Most of the NE-SW striking faults are persistent and continue beyond the boundary of the area of interest. On the other hand, most of the NW-SE striking faults terminate against the above mentioned faults.

Figure 6. Large scale tectonic features in the area of the Toki and Mizunami Municipalities. The boundaries of the research area for the Regional Hydrogeological Study (RHS) are also shown (after ref. 2)).

2.2 Regional settings

The Mizunami Basin belongs to the "Setouchi Miocene Series" which is one of the typical geological environments in Central and Western Ja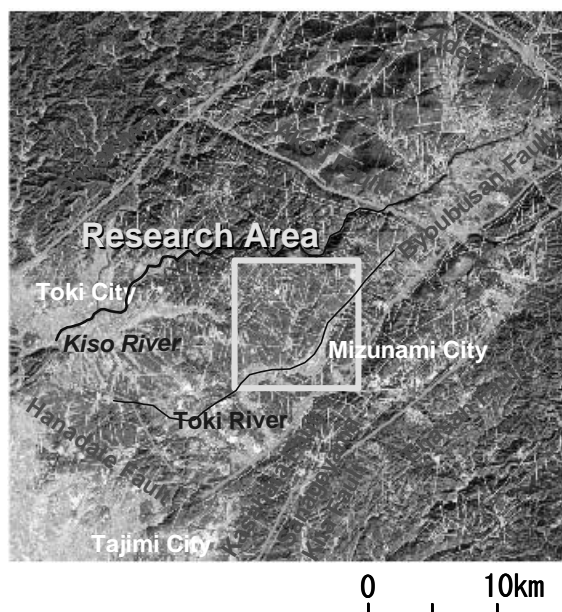pan [11]. A Regional Hydrogeological Study (RHS) was conducted on an area of about 12×12 km centred on the Sites of the Tono Mine, Shobasama and the MIU URL Construction Site. From this study, it can be concluded that the Sites all present rather similar geology in terms of genesis, rock types and faulting.

In **Table** 1, the main geological groups and formations appearing at the Mizunami URL Site are listed. They consist of a sedimentary cover onto a granite basement. The sedimentary cover is composed by the Seto Group and the Mizunami Group [12]. The Mizunami Group is composed by the following formations:

> - Oidawara Formation
> - Akeyo Formation
> - Hongo Formation
> - Toki lignite-bearing Formation

in descending order. The distribution of the sedimentary cover over the granitic bedrock is shown in Figure 7. A NW-SE cross section of the site is also shown in Figure 8. The section shows the presence of the paleo-channels in the granite basement and of the reverse activation of some faults such as the Tsukiyoshi and Yamada Fault.
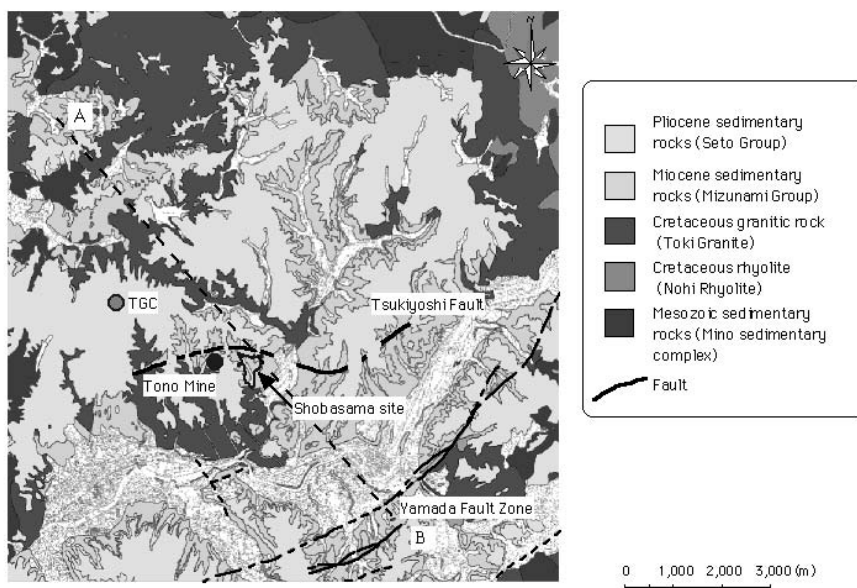
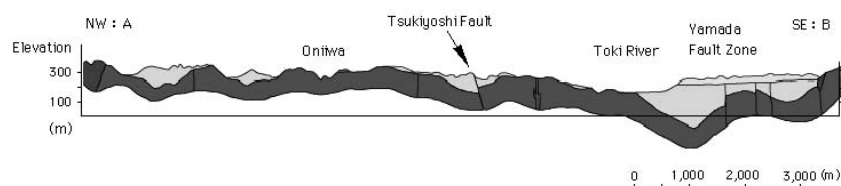**Figure 7. Map of the geology at the scale of the Regional Hydrogeological Study (RHS) (after ref. 14)).**

Figure 8. Geological NW-SE cross section the Toki-Mizunami area (section A-B in Figure 7) (after ref. 14)).

The granitic bedrock, called Toki granite, presents three facies depending on the biotite-muscovite content and the grain size. The surface of the Toki granite formation, at the Regional Hydrogeological Study (RHS) scale, presents two paleo-channels that make the thickness of the sedimentary formations to vary from place to place [2]. These paleo-channels trend preferentially N-NW and seem to convey. Alteration of the granite at the contact with the lignite-bearing formation seems to decrease at the slopes of the granite bedrock surface.

The Toki granite is rich in Uranium, which explain the possibility that this element would concentrate at the location of the Tono Uranium Mine [11]. The Uranium deposits are often imbedded in sandstone and are limited to the paleochannels at the surface of the Toki granite bedrock. The age of the mineralization was estimated by fission-track method to be about 10 Ma [13].

Some other geological formations have being recognised at the Regional Model scale and are as follows:

> Mino Sedimentary Complex (Mesozoic sedimentary rocks)

> Nohi Rhyolites (Cretaceous granitic rocks)

Unconformities are encountered at each change of rock type:

> Between the Seto Group and the Mizunami group

> Between the Oidawara and the Akeyo formation [11]

➢ Between the Hongo formation and the Toki lignite-bearing formation

➢ Between the Toki lignite-bearing formation and the Toki granite (no basal conglomerate layer at Mizunami).
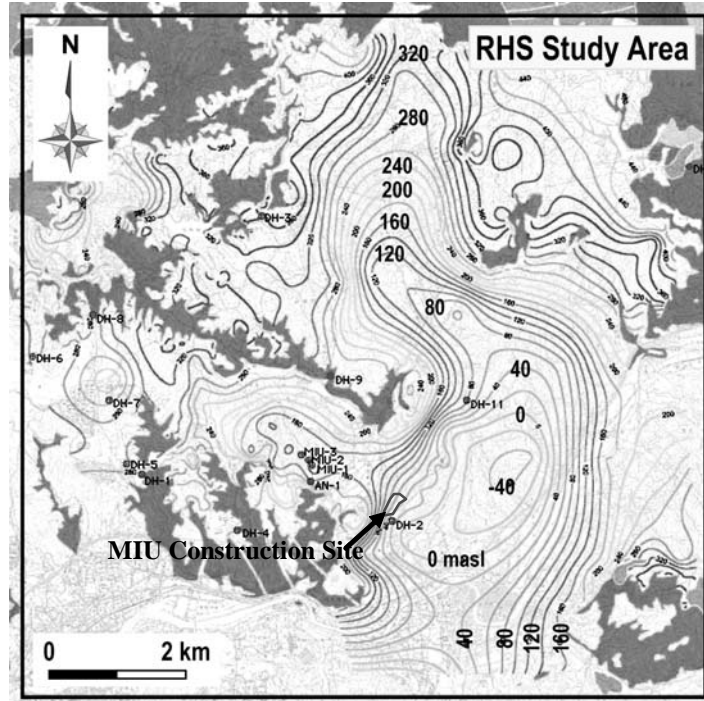

Figure 9. Magneto-telluric survey and its correlation to the Toki granite outcrops (pink colour). Two paleo-channels striking NW-SE can be observed in the central part of the RHS Study Area at Mizunami.

Table 1. Common rock types according to the Regional Hydrogeological Study (RHS) (after ref. 14),15),11)).

Name	Group	Formations	Members/Facies	Rock Types
Seto Group	Pliocene Group (pre-tertiary rock)	(lacustrine and fluviatile)		Clay, conglomerate, gravels (unconsolidated)
Mizunami Group/ Kanj Group	Miocene Group	Oidawara Formation (shallow marine)		Diatomaceous mudstone and fine-grained tuffaceous sandstones with basal conglomerates
		Akeyo formation (brackish to shallow marine)	Hazama Member	Pumiceous tuff and pumiceous sandstone
			Yamanouchi Member	Siltstone to fine-granined sandstone
			Togari Member	Medium-granined tuffaceous sandstone
			Tsukiyoshi Member	Tuffaceous sandstone
		Hongo formation		As same as Akeyo formation but two layers of pebbles: lower with granitic unsorted irregular shape; upper: sub-angular and sub-rounded quartz porphyry boulders
		Toki Lignite-bearing formation (lacustrine)		Arcosic and muddy sandstone and conglomerate, lignite layers. Upper and Lower formation. Uranium deposits often located in the Lower formation.
Toki granite	Cretaceous granitic rock	(Igneous)	Muscovite-bearing biotite granite	Medium to coarse grained biotite granite
			Hornblende-bearing biotite granite	Coarse grained biotite granite
			Leucocratic granite	Medium grained biotite granite

In general, the geological structures of the Miocene series should directly reflect the structural features of the granitic basement. Faulting affects the regional area at Tono, Shobasama and MIU Construction Site. In the 12×12 km model, two major faults are recognized:

(1) The Yamada Fault Zone of rather wavy shape and located at the SE corner of the model;

(2) The Tsukiyoshi Fault also of quite wavy shape and located slightly north of the three Sites. The Tsukioshi Fault follows the homonymous peneplain channel on the granite basement.

The fault strikes ENE-WSW dipping 60°-70° towards south. A central cataclastic zone of thickness between 10 to 20 m is present. Associated to the fault, a fracture zone of about 100 m extends on each side of the fault. This fault offsets the Mizunami Group and the Toki granite but not the Seto Group sedimentary layers on top of it. Cumulative displacements resulted in a reverse slip of about 30 m [16].

These two faults divide the Mizunami-Toki area into three divisions [16]:

(1) The North Division is characterised by Miocene strata dipping about 10° to the south or southwest and toward the Tsukiyoshi Fault;

(2) The Middle Division, between the Tsukiyoshi and Yamada Fault, also present gently dipping strata toward S and SE associated with undulating and irregular structures. The granitic basements comes to the surface here and divides the sedimentary rocks into two distinct basins: the Mizunami (NE) and the deeper Tokishiki basin (W-SW). In the vicinity of the Yamada Fault, remarkable asymmetric synclinal structures parallel to the faults are observed;

(3) The South Division is the most complicated and characterised by the fact that the basement rises to shallow depth and forms steps and terraces towards the Middle Division. In this division, the Yamada Fault displays different structural features such as enchelon arrangements, terraces and upheaved platforms.

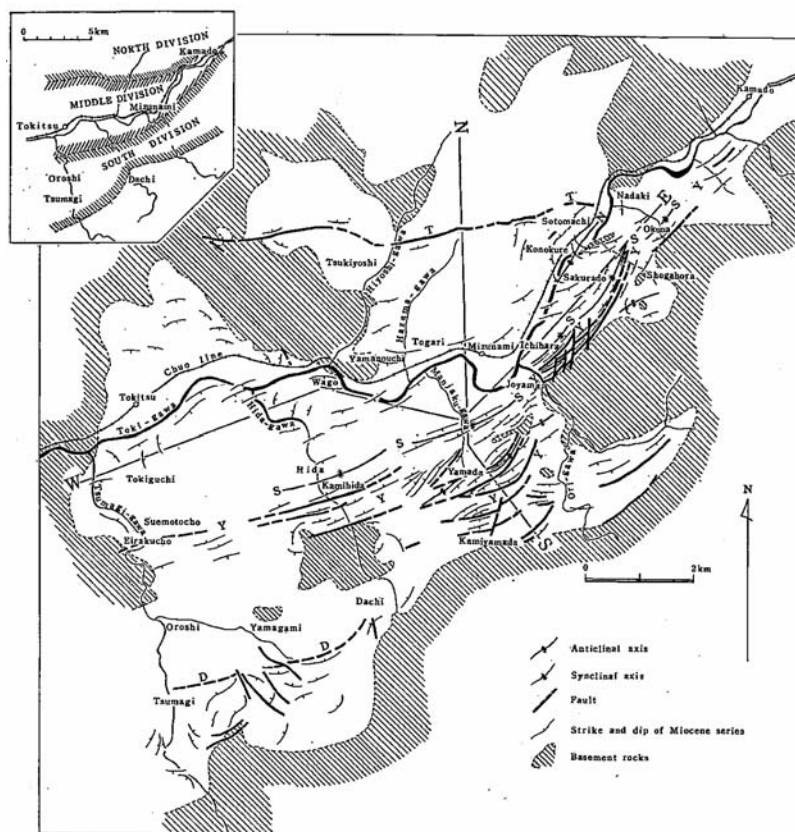**Figure 10. Tectonic map of the Mizunami and Tokishiki area. On the map, T indicates the Tsukiyoshi Fault, Y the Yamada Fault, S the Shogahora-Kamihida synclinal, D the Dachi-Tsumagi tectonic zone and N the Nadaki pitching anticline** [16]**.**

The analysis of the groundwater at the Tono Mine shows that the composition of the water in the unconsolidated sediments is completely different than the groundwater contained in the

sedimentary rocks and in the granitic basement [17]. In the unconsolidated sediments, present rain water was observed. On the other hand, in the sedimentary rocks and the granitic basement, the chemical composition of the groundwater plots in the Na-montmorillonite (albite) stability field and Ca-montmorillonite stability field. Plagioclase and montmorillonite identified in the sedimentary and granitic rock are interpreted as products of weathering and alteration [11]. Weathering of the plagioclase by CO_2 and calcite dissolution has occurred.

Carbon isotopes measurements (13C and 14C) allowed determining the age of the groundwater in the sedimentary rocks that was established to be of the late Wurm glacial stage (13000-15000 years BP). The water in the granitic basement shows a neutral pH.

2.3 *The Shobasama Site*

The Shobasama Site lies very close to the MIU Construction Site, and was originally chosen as location for the Underground Research Laboratory. As it will be shown in the following Sections, the geology of the Shobasama and the MIU Construction Site are very similar. The MIU-boreholes were drilled for the characterisation of this Site were pre-existent boreholes of the AN-series were present (Figure 11).

The sedimentary formations, the presence of an Upper Highly Fractured and a Lower Sparsely Fractured Domain in the Toki granite, which will be observed for the MIU Construction Site at Mizunami, occur even here (Figure 12). In borehole MIU-2, it was observed that the UHFD presents on average 4.7 fractures/m, while the fracture frequency in the sedimentary formations and in the LSFD is lower and approaches 2 fractures/m (Figure 13).
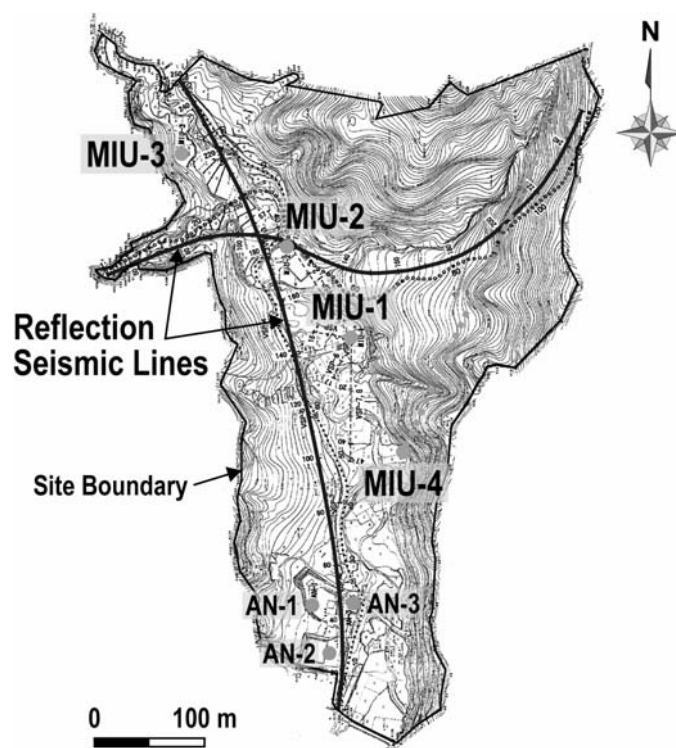
Figure 11. Layout of the Shobasama Site [18]**.**
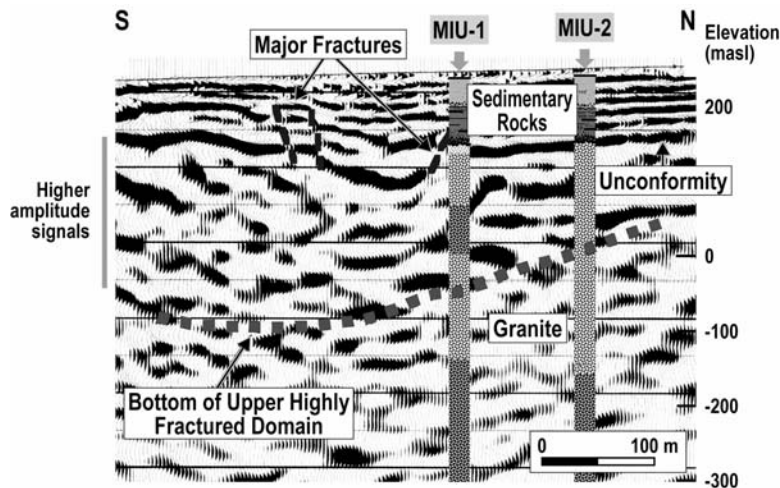
Figure 12. Seismic N-S profile at the Shobasama Site with indication of the fracture domains, faults, and sedimentary formations [18]**.**
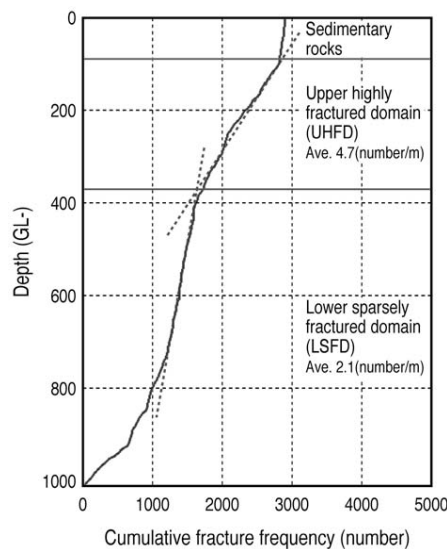
Figure 13. Cumulative fracture frequency along borehole MIU-2 at the Shobasama Site [18]**.**

2.4 *The MIU Construction Site at Mizunami*

The MIU Mizunami Construction Site is designed to be a purpose-built generic Laboratory rather than a site-specific facility to be constructed at a potential waste disposal Site [19].

2.4.1 Layout of the facility

The layout of the Mizunami Underground Research Laboratory is shown in Figure 14 [18]. The facility consists of two vertical circular shafts excavated from the ground surface down to a depth of about 1000 m. The shafts, which diameters are 6.5 and 4.5 m respectively, are separated by a distance of 40 m. Two experiment levels are planned at the Middle Stage at 500 m and at the Main Stage at 1000 m depth, together with nine sub-stages at depth interval of 100 m and connecting the two shafts.
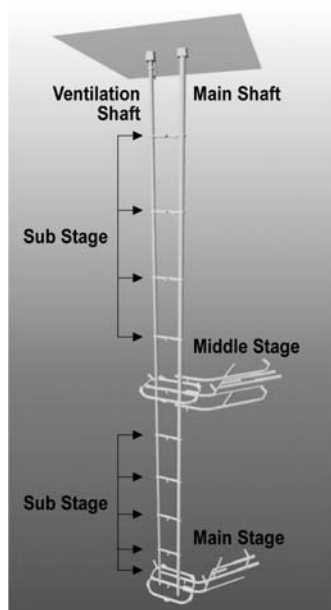
Figure 14. Layout of the Mizunami Underground Research Laboratory [19)

2.4.2 Site description

Several boreholes were drilled at the construction site of the Mizunami Underground Research Laboratory during different phases of the investigation conducted for the Tono, Shobasama and MIU Construction Site:

- AN-boreholes were drilled for the regional investigations at Tono Mine (Regional Model scale, Figure 4)

- DH-boreholes were drilled for the investigations at the Regional Hydrogeologic Study Project (Local Model scale, Figure 15)

- MSB-boreholes are shallow boreholes drilled for the investigation of the MIU Construction Site (Figure 16)

- MIZ-1 is the investigation deep borehole drilled down to 1300 m at the MIU Construction Site (Figure 16)

- 05ME-boreholes

- 06MI-boreholes are drilled from the Main and Ventilation Shaft.

The geological information collected by means of these boreholes has been interpreted to provide site descriptive models. Figure 17 shows two seismic profiles produced at the MIU Construction Site. Both profiles show that the Site is centred on one of the Toki granite paleo-channels. The unconformities between the Akeyo and the Toki lignite-bearing formation, and between the latter and the Toki granite can be observed. A boundary within the Toki granite confirms the presence of two fracture domains: the Upper Highly Fractured Domain (about 1.4 fractures/m) and Lower Sparsely Fractures Domain (less than 1 fracture/m). In the UHFD, an average conductivity of 2.7×10^{-8} m/sec was measured, while in the LSFD the conductivity was 1.1×10^{-9} m/sec, respectively.

Some faults were also recognised which seem to have experienced strike-slip motion (F1 and F2 in Figure 17b). These faults were identified in nine superficial locations by field surveys (Itoh et

al., 2006). The same picture is also shown by the earlier seismic cross section in Figure 17a. This appears to be more intricate, probably due to the convergence of several faults at the MIU Construction Site or due to the alignment of the seismic profile with some of the faults. This is shown by the integrated model of faults and lineaments in Figure 18 [2]. Based on surface and borehole information and seismic profiles, a model for the faults at the MIU Constraction Site was built as in Figure 18 and Figure 19.
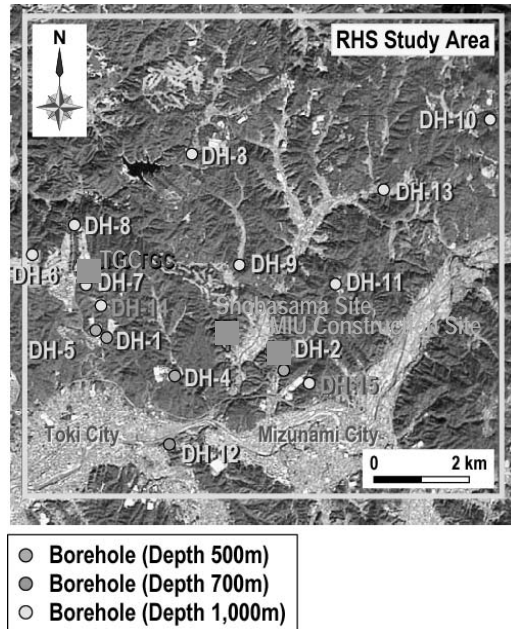
Figure 15. Position of the boreholes drilled for the Regional Hydrogeological Study.
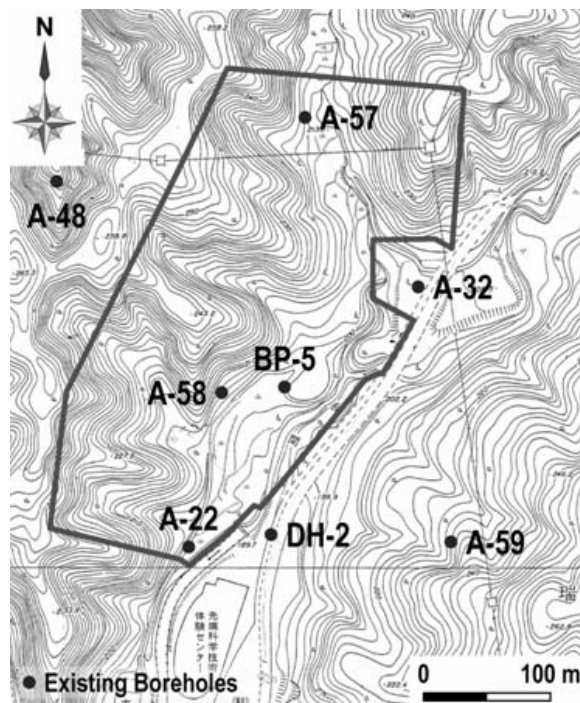
Figure 16. Position of the boreholes drilled at the MIU Construction Site [2].

a)

Fracture frequency of low-angle fractures in the DH-2 borehole

Reflection seismic data around the DH-2 borehole
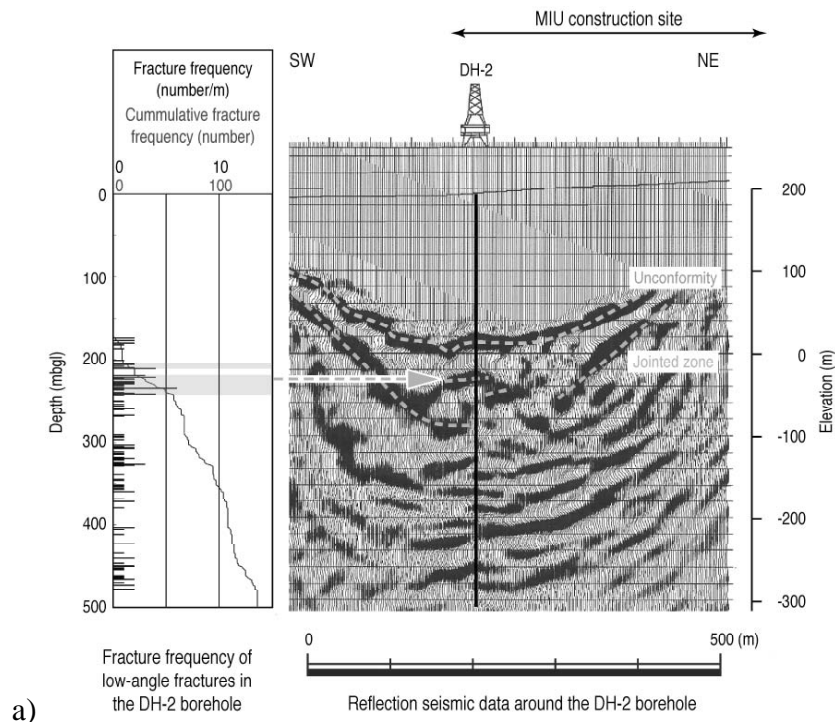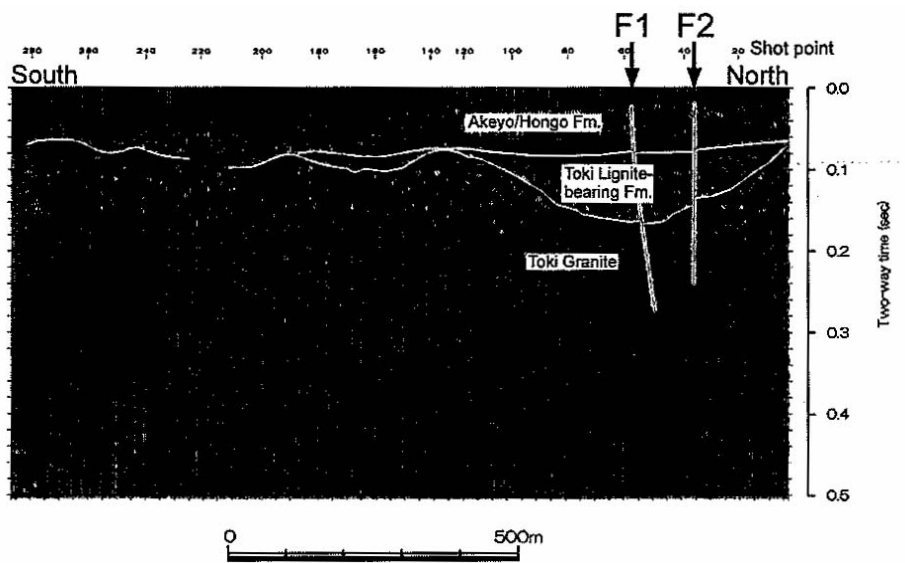
b)

Figure 17. Seismic profiles taken at the MIU Construction Site: a) SW-NE seismic profile centred on borehole DH-2 [2]; b) N-S seismic profile running along the SW side of the construction area [9] (Probably the same seismic profile).
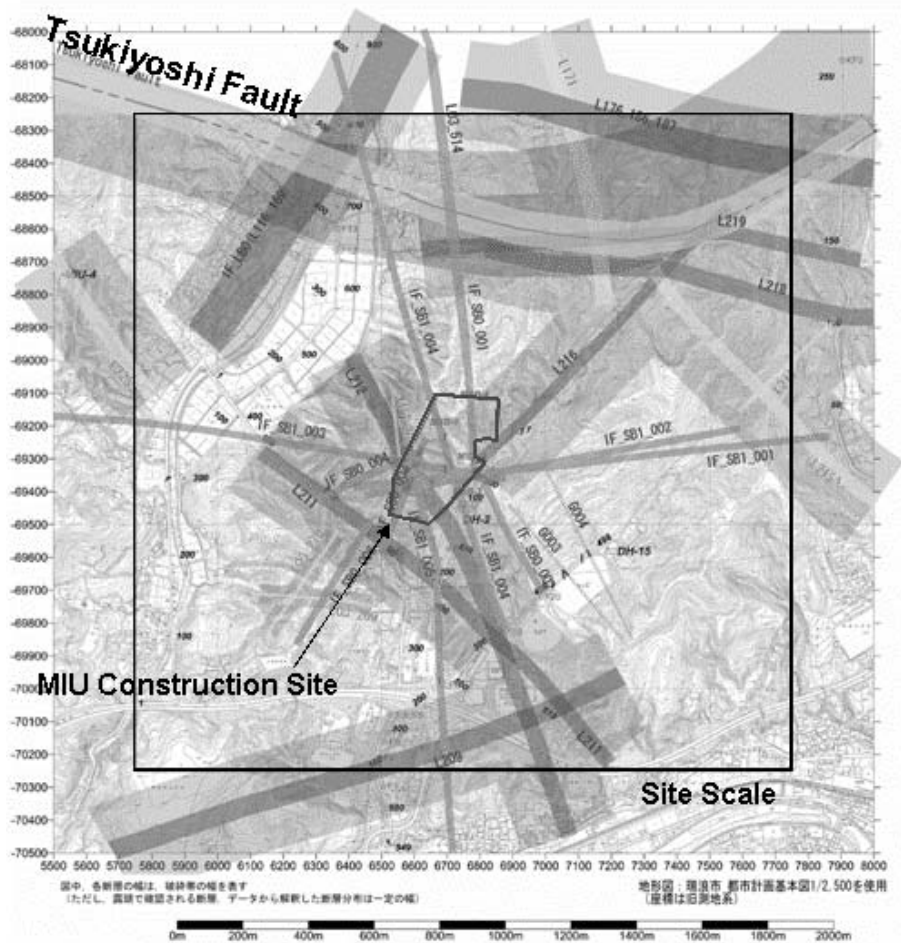
Figure 18. Model of the inferred faults, lineaments and fracture zones at the MIU Construction Site [2].
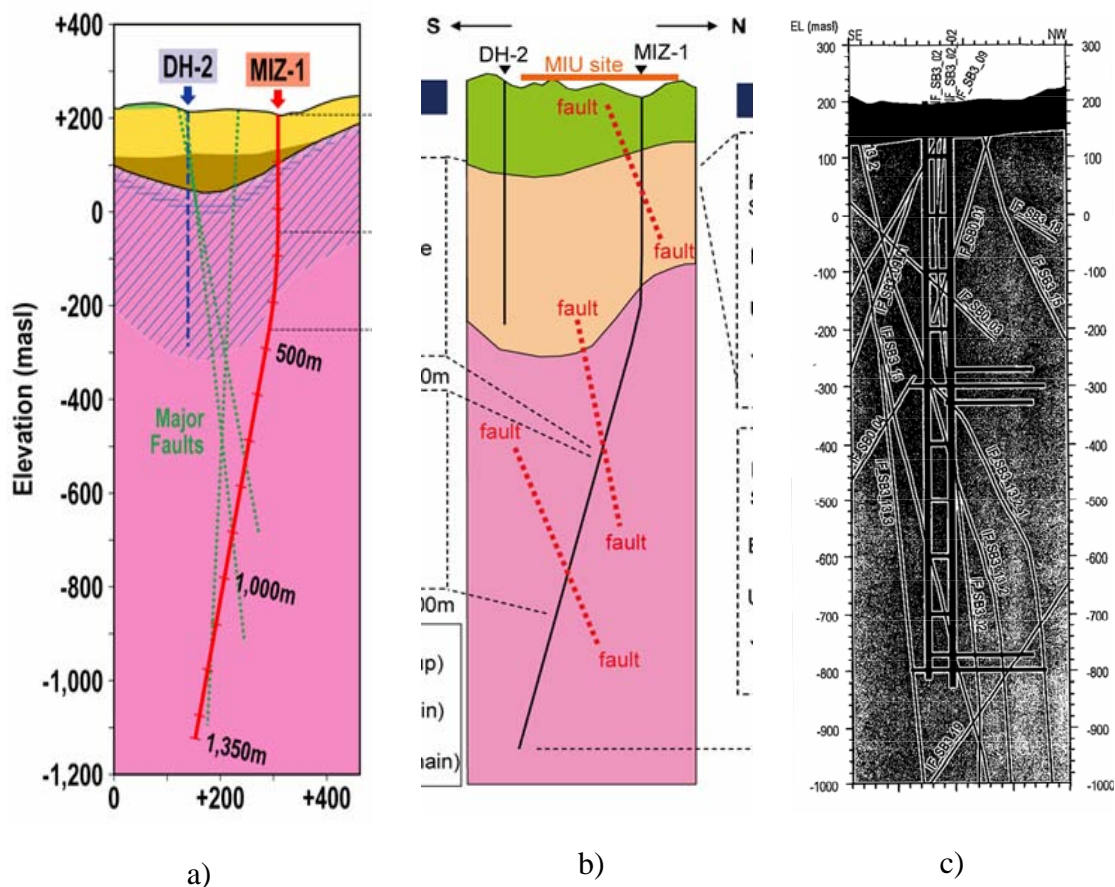
Figure 19. Vertical cross sections of the geological model at MIU Construction Site: a) reported in ref. 2); b) included in the Rock Mechanics Model of the site [20) and; c) used for the groundwater flow simulations performed in 2006 (Step 4).

3 Conclusions

From this literature study about the Tono area and Toki granite, the following issues can be identified that will be investigated in this report:

➢ Implications of the overburden on the rock stresses during crystallization of the Toki granite;

➢ Implications of the overburden pressure on the fracturing of the superficial fracturing of the granite (surface-parallel fractures/sheet joints);

➢ Influence of the topography on the orientation of the sub-horizontal fractures?

➢ Is there a plausible explanation of the presence of two fracture domains in the Toki granite? For example exfoliation, erosion or hydrofracturing processes.

4 References

1) JNC: H17: Development and management of the technical knowledge base for the geological disposal of HLW, JNC TN1400 2005-022, p.68, 2005.

2) Tsuruta T., Ota K., Amano K., Matsuoka T., Sesaki K.: Geological investigations during the Surface-Based investigation phase of the Mizunami Underground Research Laboratory (MIU) Project. ICGM'04, JNC TN7400 2004-010, pp.83-95 , 2004.

3) Amano K.:. Personal communication, Japan Atomic Energy Agency, Japan ,2006.

4) Tsunakawa H.: Stress field during the rotation of Southwest Japan. Journal of Geomagnetisn and Geoelectricity, Vol. 38, pp.537-543, 1986.

5) Doi K., Hirono S., Sakamiki Y. : Uranium mineralisationby groundwater in sedimentary rocks, Japan. Econ. Geol.Vol. 70, pp.628-646 , 1975.

6) Sakamaki, Y. : Geological environments of Nigyo-Toge and Tono Uranium deposit, Japan. Geological Environments of sandstone-type Uranium deposits, IAEA-TECDOC 328, pp.135-154, 1985.

7) Doi K., Hirono S.: Behaviour of Uranium migration in epigenetic Uranium ore deposits with reference to radioactive waste isolation in geological media, Waste Management, Vol. 10, pp. 275-284, 1990.

8) Kano K.: Re-arrangement of the shallow-level structure of Southwest Japan Arc due to the collision of the Izu-Bonin Arc. Bulletin of the Earthquake Research Institute – University of Tokyo, Vol. 77, pp.231-248, 2002.

9) Itoh Y., Amano K., Kumazaki N : Integrated description of deformation modes in asedimentary basin: A case study around a shallow drilling site in the Mizunami Area, Eastern part of southwest Japan. Island Arc, Vol. 15, pp.165-177, 2006.

10) Sasao, E., Amano, K., Ota, K.: Natural analogue study in the Tono Uranium deposit – Quantitative estimation of uplift and subsidence, and vertical displacement rate, Atomic Energy Research, Vol. 11, No. 2, pp.167-179, 2005.

11) Yusa Y.,Ishimaru K., Ota K., Umeda K.: Geological and geochemical indicators of paleohydrogology in Tono Uranium deposits, Japan, Paleohydrogeological methods and their applications, Proc. NEA Workshop, Paris (France), 9-10 November 1992, pp.117-146, 1993.

12) Itoigawa, J. : Geology and paleontology of Mizunami City. Bulletin Mizunami Fossil Museum, No. 1, pp. 3-42 (in Japanese), 1974

13) Ochiai Y., Tekeda S., Yanagizawa K., Nakatsuka N.: Natural analogue study on Uranium deposit in Japan. Proc. 3rd CEC Natural Analogue Working Group Meeting, CEC Report No. EUR11725EN, pp.126-138, 1989.

14) Itoigawa, J. : Geology of the Mizunami District, Central Japan. Monograph of the Mizunami Fossil Museum, No. 1, pp.1-50 (in Japanese with English abstract), 1980.

15) TODO Organisation research Group : Fault bounded inland basin of multiple blocks: an example from the sedimentary basin of the Tokai Group around Tajimi City in Gifu Prefecture, Central Japan, Earth Sciences, Vol. 53, pp.291-306 (in Japanese), 1999.

16) Matsuzawa I., Uemura T.: Geotectonic studies of the Toki Miocene sedimentary basin, Central Japan. Journal of Earth Science, Nagoya University, Vol. 15, pp.35-79, 1967.

17) Ota K., Seo T., Mizutani Y. : Geochemical characterization of groundwater at Tono area, Gifu Prefecture – (III) – origin and age of groundwater. Abst. 1992 Annual Meeting at Energy Soc. Japan, 113 (in Japanese with English abstract). Annual Congr. "Underground Space Use: Analysis of the Past and Lessons for the future (eds. Erdem Y. and Solak T.), Taylor & Francis Group, London, pp.335-341, 1992.

18) Takeda, S. : Current status of R&D activities at Tono Geoscience Center – Mizunami Underground Research Laboratory Project and Regional Hydrogeological Study Project. ICGM'04, JNC TN7400 2004-010, pp.83-95, 2004.

19) Sato T., Imazu M., Mikake S., Tamai T., Yamamoto M., Sakamaki M. : Status of Japanese Underground Research Laboratory – Design and construction of 1000 m-deep shafts and research tunnels. Proc. ITA, 2005

20) Nakama S. : . Presentation at JAEA on October 5, 2006.

This is a blank page.

-33-

3. Spatial variability of the compressive strength of the Toki granite at the Shobasama and Mizunami Construction Site, Japan (Paper 1)

This is a blank page.

Spatial variability of the compressive strength of the Toki granite at the Shobasama and Mizunami Construction Site, Japan

Flavio Lanaro, Toshinori Sato, Shigeo Nakama

Japan Atomic Energy Agency

Abstract: This paper studies the spatial variability of the laboratory results of uniaxial compressive tests on the Toki granite at the Shobasama and Mizunami Construction Site, Japan. Some of the spatial variability observed in the laboratory results can be indirectly attributed to the high fracture frequency of the upper highly fractured rock domain where some of the samples were taken. For samples taken from the lower sparsely fractured rock domain, however, the uniaxial compressive strength of the granite seems to be very strongly correlated to level of in-situ rock stress (i.e. maximum shear stress) determined by measurement results obtained from the hydro-fracturing method. The correlation between the laboratory results and the level of in-situ stress is explained by the damage due to the release of the stresses the cores undergo during drilling. An attempt to correct the laboratory results for estimating the in-situ intact rock strength based on its correlation with the in-situ stresses was carried out.

1   Introduction

The Japan Atomic Energy Agency (JAEA) is currently performing extensive investigations on crystalline rocks at depth at the Mizunami Construction Site (Gifu, Central Japan). The studies were preceded by similar investigations at the Shobasama Site in the same municipality. The goal of the site investigations is to improve the knowledge on deep geological environments and enhance reliability and confidence in the safety and design of a final repository for high level radioactive waste in crystalline rocks.

For the design and operation of a repository facility, the strength of the intact rock, especially in sparsely fractured bedrocks such as the Toki granite in Mizunami, is one of the key parameters. The knowledge of the rock mass heterogeneity and the result of the sampling process on the intact rock strength measured in laboratory are important for predicting brittle failure and optimizing rock support.

Eberhardt et al. [1] have shown that the uniaxial compressive strength of samples of the Lac du Bonnet granite (URL, Canada) decreases from about 240 to about 180 MPa and even 140 MPa for samples taken at 130, 240 and 420 m below the surface, respectively. At these depths, the difference between the major and minor principal stresses increases from about 5-10 MPa at 130 m, 13 MPa at 240 m, to about 41 MPa at 420 m depth. Although the major principal stress at URL is in general higher than the stresses measured in Mizunami, the difference between the maximum and minimum in-situ stresses for the two sites are comparable. Thus, potential damage of the cores of Toki granite is also expected resulting in reduced uniaxial compressive strength of the core samples (compared to the undisturbed in-situ strength).

Core damage during drilling is mainly induced by tensional stresses appearing parallel to the core axis (e.g. ref. 2),3)). Such tensile stresses are partially induced by the geometry of the core stub and partially enhanced by the maximum in-situ shear stress. The results reported by Lavrov et al. [4] also confirm this fact: samples subjected to tensile stresses about 50 to 80% of the Brazilian tensile strength exhibited a reduced compressive strength when tested in uniaxial compression.

In this paper, a short description of two geographically close sites investigated by JAEA for the location of an underground laboratory in crystalline rock is given. The results from laboratory testing on the Toki granite are presented and related to different geological features such as fracture frequency, weathering, facies and in-situ rock stresses. Furthermore, a conceptual model for describing the in-situ variation of the uniaxial compressive strength with depth of the Toki granite is proposed based on a correction of the results obtained in laboratory. The difference between the strength in laboratory and in-situ is then explained with the damage that the cores might have suffered during drilling in highly stresses bedrock at depth.

2 Geology of the Sites

The Shobasama and the Mizunami Construction Sites are located in the Gifu Prefecture in Central Japan. The Sites are just a few kilometers apart from each other and are characterized by very similar geological conditions. A Cretaceous granite basement about 68 Ma old (Toki granite) is covered by Miocene sedimentary rocks dating from 20 to 1 Ma ago [5], [6], [7]. The Toki granite basement presents a surface characterized by paleo-channels. Weathering is found at the bottom of the paleo-channels but tend to significantly decrease along the slopes of the basement. Below the weathered layer, the Toki granite seems to be affected by rather heavy fracturing to a depth varying between 100 and 500 m. This bedrock volume is addressed as the Upper Highly Fractured Domain (UHFD; fracture frequency of between 1 and 5 fractures/m). Below this domain, the fracture frequency drops in what is called the Lower Sparsely Fractured Domain (LSFD; fracture frequency less than 1 fracture/m). All the geological features described here are in common for the two Sites.

2.1 Shobasama Site

The Shobasama Site lies along a creak basin in the territory of Mizunami City (Figure 1, left). Several boreholes were drilled at this Site. However, only borehole MIU-1 to 4 and AN-1 were sampled for rock mechanics testing. On the northern edge, the Site is intersected by a large fault zone (Tsukiyoshi Fault) that trends E-W and dips about 60° to 70° towards S (Figure 1, right). The Site, originally chosen as location for the Mizunami Underground Laboratory, was abandoned on advantage of the nearby Mizunami Construction Site.
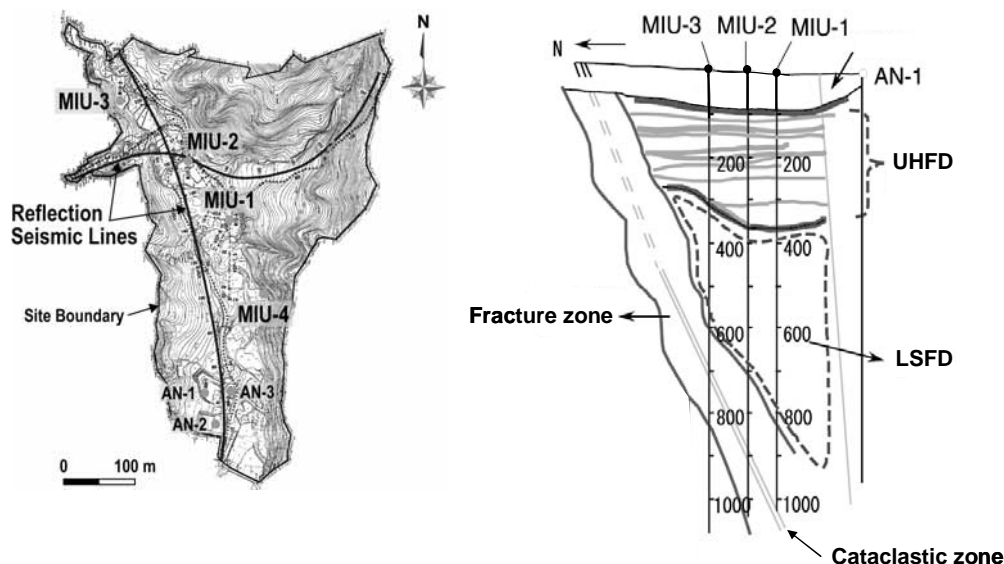
Figure 1. Map of the Shobasama Site (left) and vertical cross section of the geological conceptual model of the site along a NNW-SSE line (right) [8].

2.2 *Mizunami Construction Site*

The Mizunami Construction Site is located on the flank of a hill and limited on the
SE edge by a river (Figure 2). The geological model of the Site comprehends the UHFD and
LSFD domains as defined above. Furthermore, the Tsukiyoshi Fault contours the Northern edge of
the Site. The excavation of the Main and Ventilation Shaft has being carried out down to a depth
of approximately 200 m from the surface by April 2007.
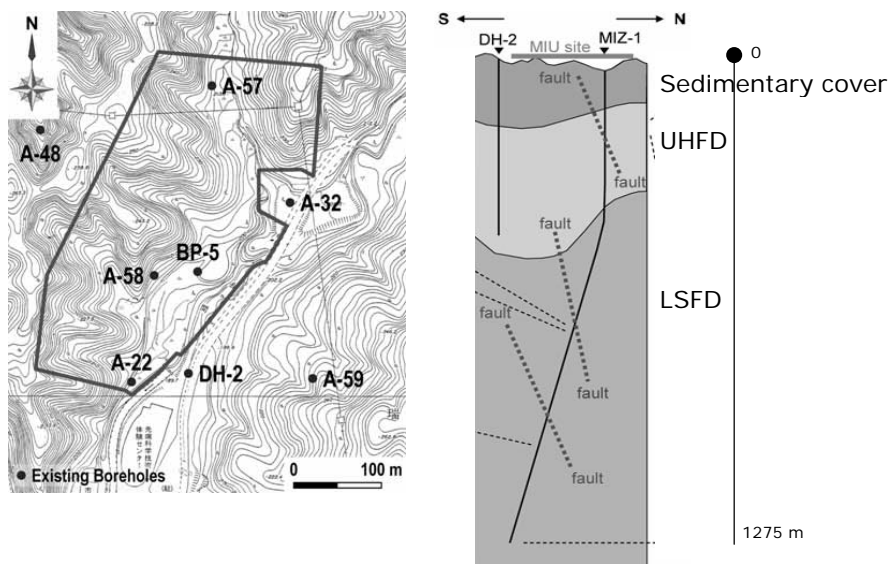
**Figure 2. Map of the Mizunami Site (left) and vertical cross section of the geological
conceptual model of the site along a NNE-SSW line (right) [8].**

3   Laboratory test results

Laboratory tests were carried out on the Toki granite for the determination of the physical
properties (effective porosity, elastic wave velocity, density) and mechanical properties (Uniaxial
Compressive Strength UCS, triaxial compressive strength and Brazilian tests). Samples were
collected at rather uniform spacing along boreholes MIU-1 to 4 and AN-1 at Shobasama, MIZ-1 at
the Mizunami Construction Site and the adjacent borehole DH-2 (Table 1). Figure 3 shows the
variation of UCS along the boreholes at the two sites.

**Table 1. Borehole information and number of effective porosity, uniaxial compressive
tests on borehole cores and Hydro-Fracturing stress measurements.**

Borehole	Length [m]	Inclination [°]	No. of effective porosity measurements	No. of UCS tests	No. of HF stress measurements in Toki granite
MIU-1	1011.80	Vertical		90	-
MIU-2	1012.00	Vertical		30	13
MIU-3	1014.00	Vertical		10	7
MIU-4	790.10	30° from vertical		30	-
AN-1	1010.20	Vertical		20	16
MIZ-1	1300.00	Vertical to ~ 380 m, then inclined up to 14° from vertical	192	45	12
DH-2	501.00	Vertical		30	-
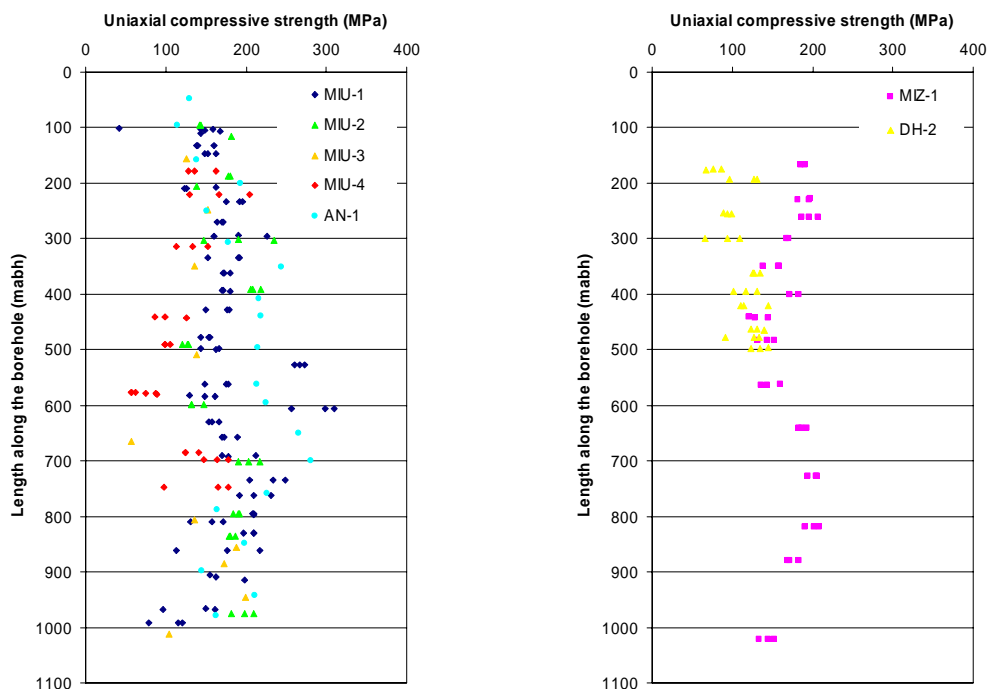
Figure 3. Plot of the uniaxial compressive strength of the Toki granite for samples taken from the boreholes at the Shobasama Site (left) and at the Mizunami Construction Site and surroundings (right). Please notice that borehole MIU-4 and MIZ-1 are not vertical.

4   Rock stress measurements

Extensive campaigns of rock stress measurements were carried out at the sites. Hydro-fracturing methods were applied to estimate the in-situ stresses in four of the seven boreholes analyzed in this study. The results are reported in Figure 4 in terms of maximum and minimum horizontal stress and vertical stress, respectively. The location of the encountered fault zones is also presented. Their position clearly affects the stress distribution by reducing the measured stresses inside or immediately close to the fault zones.

The rock mechanics model of the Shobasama Site identified three stress domains depending on the depth and the position with respect to the Tsukiyoshi Fault. In other words, two different sets of in-situ stresses were identified for the hanging wall and footwall of the fault [9]. Maximum and minimum horizontal stresses at 1000 m were found to be about 40 to 60 MPa and 20 to 30 MPa, respectively. Core discing, which is an index of high stresses relatively to the intact rock strength, was observed in some of the boreholes at the Shobasama Site (MIU-1 and MIU-3).

Also at the Mizunami Construction Site, two stress domains were recognized above and below a fault encountered at a depth of 500 m. Approximately, the same horizontal stresses were measured at the depths of 500 and 1000 m (maximum horizontal stress of 23 MPa, minimum horizontal stress of 15 MPa at 1000 m), whether the estimated vertical stress doubles between the two depths (about 26 MPa at 1000 m) [10].
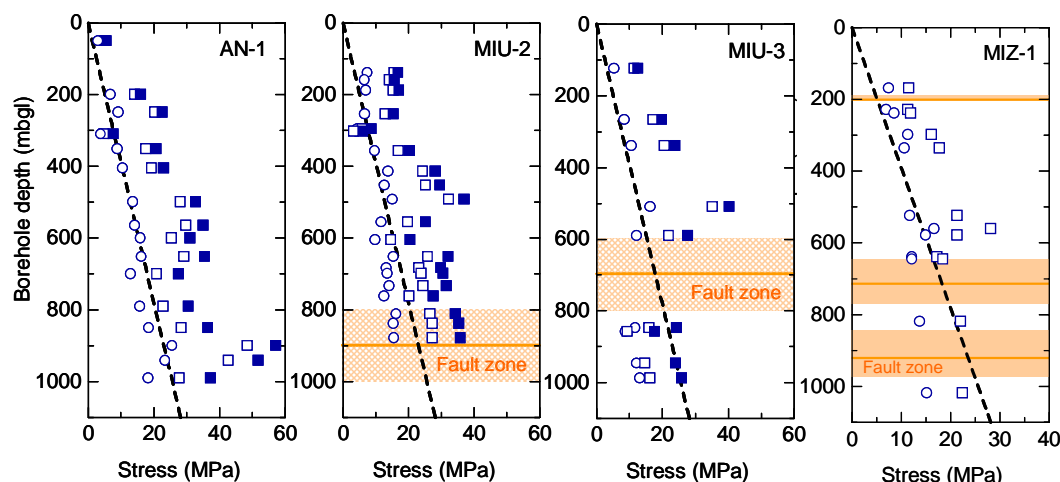
Figure 4. Summary plots of the results of hydro-fracturing measurements of the in-situ stresses. Filled squares show the maximum total horizontal stress, empty squares the maximum effective horizontal stress. Empty circles represent the total minimum horizontal stress. The dotted lines show the estimated total vertical stress calculated as the weight of the overburden. The position of the major fault zones identified along the boreholes is also indicated.

5   Spatial variability of the unconfined compressive strength

By observing the depth distribution of the uniaxial compressive strength along borehole MIU-1 to 4, AN-1, DH-2 and MIZ-1, a very well defined waviness can be observed. This can be interpreted as spatial variability of the mechanical property that might depend on:

- Different rock types and facies

- Effect of alteration and weathering

- Fracture intensity

- Vicinity to fault zones

- Damage of the core samples due to release of the in-situ rock stresses.

In the following sections, each of these causes is discussed to determine its importance for the laboratory results.

5.1   Facies of the Toki granite

According to earlier studies, the Toki granite has rather heterogeneous material properties [9]. The Toki granite presents three facies identified at the Mizunami Construction Site [8]:

- Muscovite-bearing biotite granite, medium to coarse grained

- Hornblende-bearing biotite granite, coarse grained

- Leucocratic biotite granite, medium grained.

However, Figure 5 shows that there seems not to be a clear relation between the facies and the uniaxial compressive strength of the Toki granite. In fact, the strength appears to follow a pattern irrespective of the facies occurring at different depths.
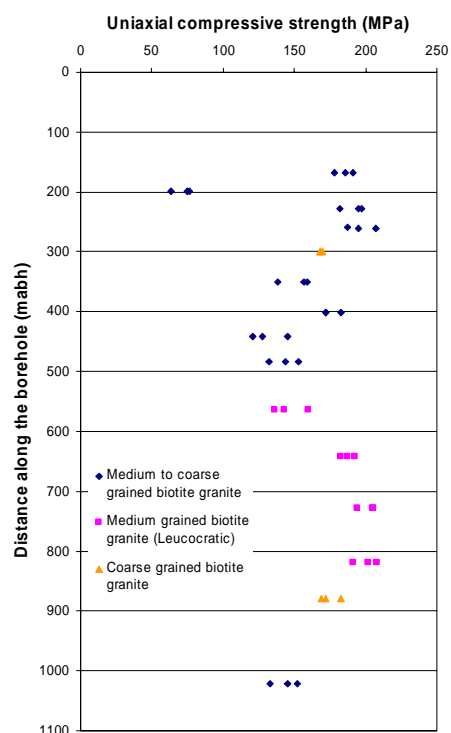
Figure 5. Variation of the uniaxial compressive strength of the Toki granite along borehole MIZ-1. The three facies (medium to coarse grained, medium grained and coarse grained) are marked with different symbols.

5.2 Alteration and weathering

At the surface of the granite basement, weathering is often observed for a thickness between 0 and 30 m (Table 2). However, most of the samples of Toki granite tested in laboratory were taken below the weathered zone and should therefore be free from the effects of strong weathering.

Table 2. Depth of the Toki granite basement, of the weathered zone and of boundary between the Upper Highly and Lower Sparsely Fractured Domain accounted from the top of the boreholes.

Borehole	Depth of the Toki granite basement [mabh]	Depth of the weathered zone [mabh]	Thickness of the weathered zone [m]	Boundary between UHFD and LSFD [mabh]	Thickness of UHFD [m]
MIU-1	88.8	103.0	14.2	350.0	261.2
MIU-2	88.6	99.0	10.4	370.0	281.4
MIU-3	87.9	97.9	10.0	317.0	229.1
MIU-4	93.0	130.8	32.7*	310.0	187.9*
AN-1	16.8	38.0	21.2	208.0	191.2
MIZ-1	109.1	-	0.0	311.0	201.9
DH-2	167.9	169.0	1.1	501.0**	333.1**

* Corrected for borehole inclination.
** To the bottom of the borehole.

5.3 Fracture frequency and fault zones

As presented in Sec. 2.1 and 2.2, the rock mechanics conceptual models of the Sites comprehend the definition of fracture domains based on the fracture frequency. Although fracture frequency accounts for macro-fractures at borehole scale, micro-fracturing or other geological processes related to macro-fractures might have affected the mechanical properties of the intact rock. In fact, the distribution of the uniaxial compressive strength with depth shows different patterns above and below the boundary between the Upper Highly Fractured Domain (UHFD) and the Lower Sparsely Fractures Domain (LSFD).

5.3.1   Upper Highly Fractured Domain

When the samples collected in the UHFD are analyzed, the values of the uniaxial compressive strength of the Toki granite appear to increase with depth with a rather linear trend. Since the thickness of the UHFD varies from borehole to borehole, the distance along the borehole from the weathered boundary of the Toki granite was normalized with respect to the total thickness of UHFD outside the weathered zone. This treatment allows discerning between two groups of boreholes, MIU-1 to 4 and MIZ-1 on one side, and AN-1 and DH-2 on the other side (Figure 6). The linear fitting of the test results for the two groups yields to the following trends:

$$UCS_{MI} = 146 \text{ MPa} + 52 \text{ MPa} \cdot d \text{ , for d} < 1 \qquad (R^2 = 0.305)$$

$$UCS_{AD} = 88 \text{ MPa} + 55 \text{ MPa} \cdot d \text{ , for d} < 2 \qquad (R^2 = 0.716)$$

where *d* is the normalized distance from the weathered boundary, MI indicates the first group of boreholes and AD the second group, respectively. Please notice that test results down to a distance of 2 times the thickness of the UHFD were taken for group AD.

The linear equation for the first group of boreholes, irrespective to the Site, has an intercept 66% larger than that of the second group. On the other hand, the slopes appear to be very consistent for the two groups since the difference is only 6%. When the maximum *d* is assumed, the same value of the uniaxial compressive strength of about 200 MPa is obtained by means of the two linear equations.

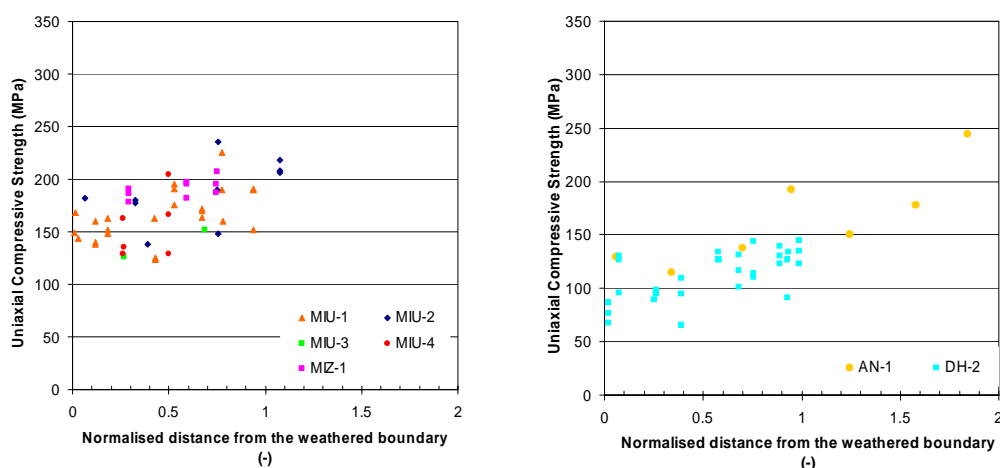**Figure 6. Variation of the uniaxial compressive strength of the Toki granite in the UHFD as a function of the normalized distance from the weathered boundary.**

5.3.2   Lower Sparsely Fractured Domain

In the LSFD, the uniaxial compressive strength of the tested samples seems to follow a rather wavy pattern when plotted against the depth (Figure 1). Although there is some spreading in the

data, the variation of the uniaxial compressive strength appears to be quite smooth and almost never abrupt in all boreholes. For this reason, polynomial interpolations were carried out as shown in Figure 7. This variation could be explained in three ways:

1) By the presence of the fault zones and the related geological processes that could reduce the intact rock strength

2) By the effect of release of the in-situ rock stresses on the samples prior to testing that would damage them by, for example, micro-cracking

3) By the effect of the drilling parameters (e.g. fluid pressure, weight on bit, torque).

Figure 7. Variation of the uniaxial compressive strength of the samples with the distance from the weathered boundary for two boreholes at the Shobasama Site. Polynomial curves are fitted to the test results to show the dominant trends with depth.

6 Correlation between the strength and the in-situ rock stresses

The following considerations can be made trying to answer question 1) to 3) in Sec. 5.3.2:

1) Contrary to what was expected, the uniaxial compressive strength of the samples seems to increase when approaching the fault zones (Figure 8). This indicates that the position of the faults is somehow correlated to the position of the peaks of the diagrams of the strength versus depth.

2) The positive correlation between the strength and the position of the fault zones suggests the hypothesis that the release of the in-situ stresses might have affected the integrity of the intact rock samples and thus their strength. In fact, the presence of the faults often produces a local decrease of the in-situ stresses, and this, in turn, would guarantee less damaged or undamaged samples. This is also supported by the plots of the polynomial fits of the difference between the in-situ maximum horizontal stress measured and the vertical stress calculated as the weight of the overburden for borehole MIU-2, MIU-3, AN-1 and MIZ-1 (Figure 8). The polynomial fits of the stress component mirror very well the shape of the polynomial fits of the uniaxial compressive strength. Please notice that the plots of the in-situ stresses have reversed y-axes.

3) The very good correlation between the troughs of the strength and the peaks of the in-situ stresses might discard the hypothesis of purely drilling induced damage. However, the damage due release of the in-situ stresses is always associated with drilling that produce a local increase of the stresses around the borehole.
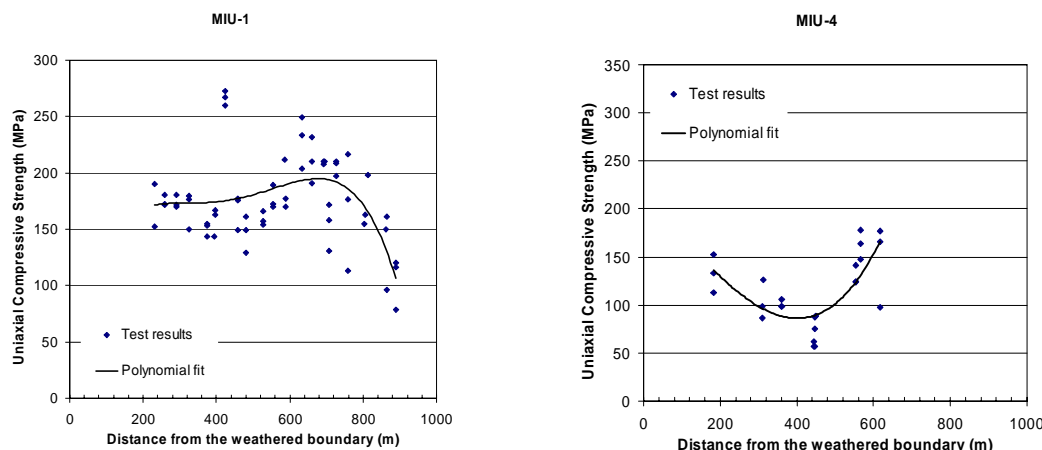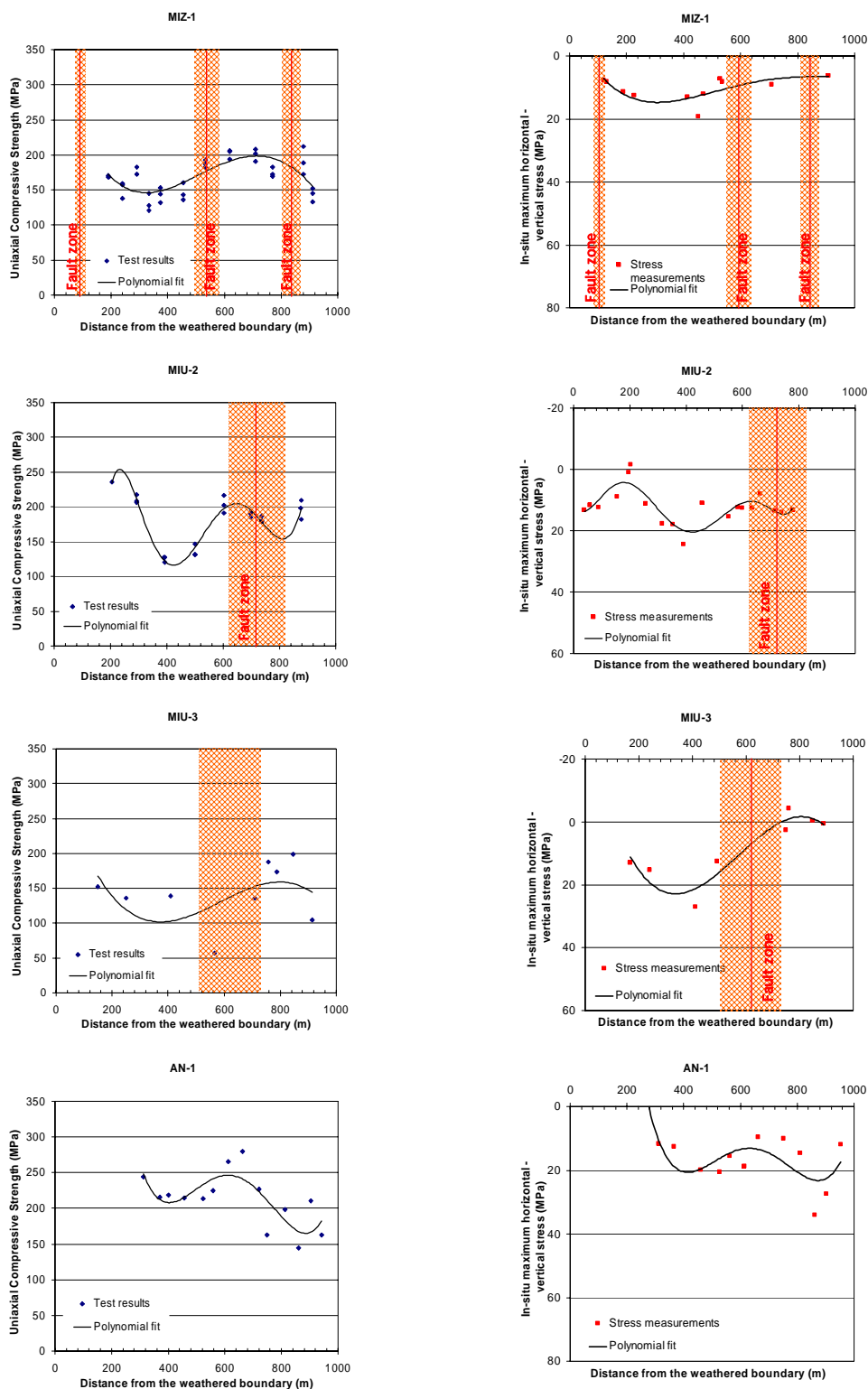
Figure 8. On the left, the variation of the uniaxial compressive strength of the samples with the distance from weathered boundary along the boreholes at the Shobasama and Mizunami Site. On the right, the variation of the difference between the maximum horizontal in-situ stress, measured by hydro-fracturing, and the vertical stress calculated, calculated as the weight of the overburden, as a function of the distance from weathered boundary. The polynomial curves are fitted to the available data to show the dominant trends with depth. Please note that the y-axes of the stress diagrams are reversed.

No clear correlation between the in-situ stresses and the uniaxial compressive strength could be observed for the core samples taken from the Upper Highly Fractured Domain.

7 Discussion

This study shows that the uniaxial compressive strength of the Toki granite varies significantly along the investigated boreholes. The attention was therefore focused on such variations trying to explain them. One of the factors playing a role in the variation of the intact rock strength seems to be the vicinity to the surface of the granite basement. Besides the weathered layer, a rather linear increase of the uniaxial compressive strength with depth was observed in the superficial Upper Highly Fractured Domain. This linearity seems to continue through the entire thickness of the UHFD. In some boreholes (e.g. AN-1), the linearity even extends beyond the lower limit of UHFD into the Lower Sparsely Fractured Domain.

Typically, in the Lower Sparsely Fractured Domain, the strength of the intact rock varies in a rather wavy fashion. It was observed that this waviness follows very well the variation of the measured in-situ stresses: the peaks of the strength are associated with the troughs of difference between the maximum horizontal in-situ stress and the vertical stress, and *vice versa*. Since in-situ stresses often decrease approaching the fault zones due to their weaker mechanical properties, it is often observed that the uniaxial compressive strength of the Toki granite increases within or around the fault zones. As this is likely to be an effect of the release of the in-situ stresses, it is only in apparent contradiction to the assumption that the faults are expressions of damage of the rock mass, and thus, the mechanical properties of the intact rock close to them should decrease or stay unchanged.

The uniaxial compressive strength of the intact rock at different depths can be inferred by means of the polynomial the fits in Figure 8 (left). In the same way, the difference between the maximum in-situ horizontal stress and the vertical stress at the same depths can be calculated by using the polynomial fits in Figure 8 (right). The estimated values of the strength can be plotted as functions of the in-situ stress component for each borehole. Such correlations are shown in Figure 9 where all the boreholes show almost the same behavior irrespective of the location (e.g. Shobasama or Mizunami) or the level of stress. Certainly, some of the patterns observed in Figure 9 might depend on the approximation by the best polynomial fittings and on the scarcity of data for some of the boreholes (e.g. MIU-3).

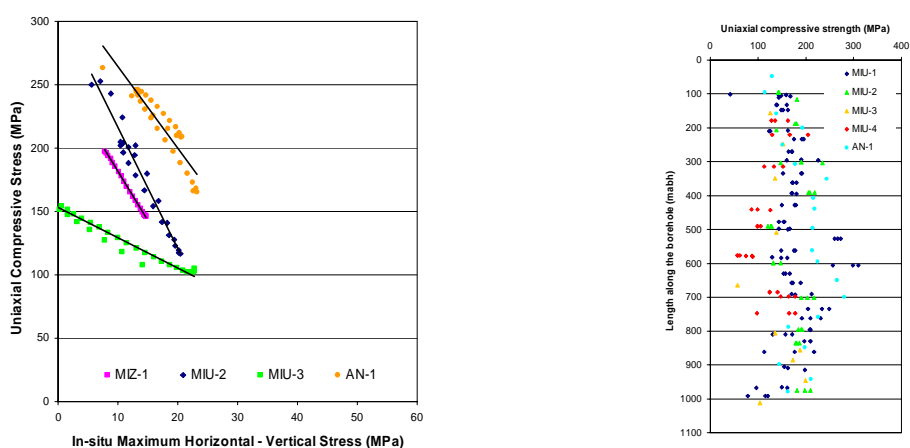**Figure 9. Correlation between the maximum in-situ horizontal stress (estimated by means of polynomial fits with depth in Figure 8, left) and the uniaxial compressive strength of the Toki granite (estimated by means of polynomial fits with depth in Figure 8, right) for the boreholes analyzed in this study. A strong negative correlation can be observed between the strength and the in-situ stress component in all boreholes.**

An explanation to the slight change in correlation from borehole to borehole could also be that the stress field is not the same in all the boreholes and some of the borehole locations have generally higher average stresses. Furthermore, depending on the angle between the borehole axis and the principal stress directions, the effect of stress release on the compressive strength of the intact rock core samples might significantly vary.

The ranges of variation of the uniaxial compressive strength seem not to coincide for all the boreholes, indicating that the strength might also spatially vary from borehole to borehole due to other reasons than stress-release related damage. Such variations should be explained by other geological and structural features.

It can be concluded that there seems to be a strong negative correlation between the uniaxial compressive strength of the Toki granite and the in-situ stresses: the higher the stresses, the lower the strength of the samples. The in-situ stress component that correlates with the strength is the difference between the maximum horizontal stress and the vertical stress. This is twice the maximum in-situ shear stress in a vertical plane, if the vertical and horizontal directions are assumed to be principal directions. The drilling of the borehole locally changes the stress conditions in the rock mass inducing much higher stresses that might affect the integrity of the cores. In fact, the stress-path experienced by the core during drilling can induce damage when approaching the failure envelope of the intact rock in triaxial conditions. Typical damage induced by drilling stress-path is micro-fracturing of the cores and in extreme cases core discing (e.g. ref. 11)).

Micro-fracturing is often associated with an increase of the porosity of the core samples. For the samples from borehole MIZ-1, in fact, a decrease of the strength is systematically associated with an increase of the effective porosity as it appears in Figure 10 (left). Thus, both strength and porosity of the intact rock appear to be affected by the in-situ stresses (Figure 10, right) resulting in the apparent drilling-induced heterogeneity of the Toki granite observed at the Shobasama and Mizunami Construction Site.

As another proof of this, the micro-cracking induced by stress release during drilling seems to have caused the estimation of the principal stresses from core deformation to fail. For measuring the stresses, the Acoustic Emission/Deformation Rate Analysis (AE/DRA) method was applied but the initiation of acoustic emission was recorded at an unexpectedly early stage during loading that disabled the stress determination [12].

It is worth to remember that drilling parameters were not considered in this study and could certainly contribute in some extend to the variations of the uniaxial compressive strength observed for the Toki granite.

The results of this study for the Upper Highly Fractured Domain and Lower Sparsely Fractured Domain can be combined to build a conceptual model that explains the variability on the laboratory results of the uniaxial compressive tests carried out on samples of Toki granite.
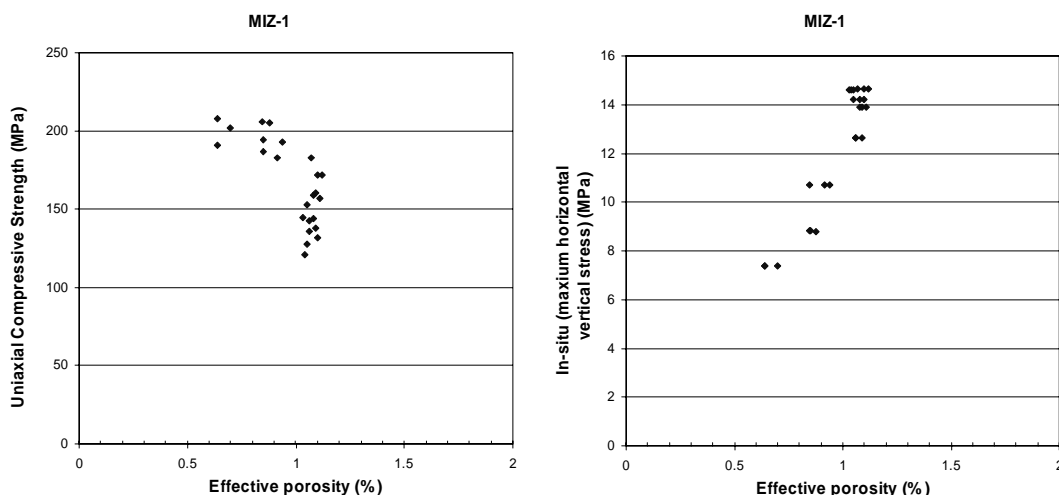
Figure 10. Correlation between the effective porosity of the samples and the uniaxial compressive strength (left) and the difference between the maximum horizontal and vertical in-situ stress (right). Stresses are obtained at the position of the samples by means of the polynomial fits in Figure 8 (right).

8 Conceptual model for the in-situ uniaxial compressive strength of the Toki granite

Based on the observations in the former sections, a conceptual model explaining the variation of the uniaxial compressive strength of the Toki granite at the Shobasama and Mizunami Construction Site can be set up (Figure 11). In this model, the in-situ uniaxial compressive strength of the intact rock is assumed to:

1) Linearly increase with depth in the Upper Highly Fractured Domain (below the superficial weathered zone) towards the values obtained in the LSFD according to a relation similar to those reported in Sec. 5.3.1;

2) Have a rather constant average value in the Lower Sparsely Fractured Domain.

The linear increase of the intact rock strength in the in the Upper Highly Fractured Domain is merely an observation of the available data. No specific explanation was attempted in this study.
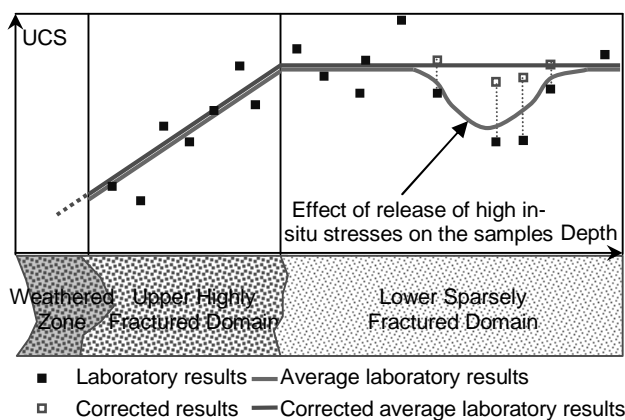
Figure 11. Conceptual model of the variation with depth of the in-situ uniaxial compressive strength of the Toki granite at the Shobasama and Mizunami Construction Site.

In the Lower Sparsely Fractured Domain, some of the large scale variations of the laboratory uniaxial strength could be explained and correlated to the damage induced by the release of the in-situ stress during drilling (Sec. 6). Based on this knowledge, it is possible to correct the laboratory results by means of the correlation between the strength and in-situ stresses in the borehole. The correlation slightly varies from borehole to borehole probably due to different angles between the borehole axis and the principal stress directions, the drilling parameters and/or to the ratio between the magnitudes of the in-situ principal stress components. However, Figure 9 shows that such correlation is very consistent for all boreholes and its linearity allows for a rather simple correction of the laboratory results to take into account the possible underestimation of intact rock strength due to the effects of the in-situ stresses on the core. This correction can only be applied on the results from boreholes where the variation of the in-situ rock stresses is known.

To apply the correction, the value of the uniaxial compressive strength of the samples unaffected by stress-release damage (i.e. from sections of borehole with low in-situ stresses) has to be estimated. Based on this value, a reference stress level (i.e. difference between the maximum horizontal and vertical in-situ stress) under which the sample should not be affected by stress-release related damage can be obtained. Based on the difference between the actual stress level in the position of core sampling and the reference stress level, an estimation of the loss of strength can be attempted through the linear relation in Figure 9.

This correction was applied to the laboratory results from borehole MIZ-1, MIU-2, MIU-3 and AN-1. Figure 12 shows the data set of laboratory results before and after the suggested correction. It is quite clear that the corrected data set appears to be much more consistent than the uncorrected laboratory result data set. The span of variation of the uniaxial compressive strength diminishes and most of the laboratory results cluster around a clear average value of about 200 MPa, except for the values from AN-1 that are generally higher (Table 3). The average value resembles very much the maximum strength estimated for the Upper Highly Fracture Domain in Sec. 5.3.1.

Table 3. Mean value and standard deviation of the uniaxial compressive strength of the intact Toki granite in the Lower Sparsely Fractured Domain before and after the suggested correction in Sec. 8.

Borehole (No. of samples from LSFD)	UCS mean (MPa)	UCS standard deviation (MPa)	Corrected UCS mean (MPa)	Corrected UCS standard deviation (MPa)	Difference of the means after correction	Difference of the standard deviations after correction
MIZ-1 (33[1])	168	25	194	23	+16%	-8%
MIU-1 (63[2])	181	45	No correction	-	-	-
MIU-2 (22[3])	180	34	207	12	+13%	-65%
MIU-3 (9[4])	143	43	187	40	+31%	-7%
MIU-4 (24[5])	115	37	No correction	-	-	-
AN-1 (14[6])	213	38	244	27	+15%	-29%

[1] Samples below 299 mabh were considered;
[2] Samples below 361 mabh were considered;
[3] Samples below 303 mabh were considered;
[4] Samples below 248 mabh were considered;
[5] Samples below 314 mabh were considered;
[6] Samples below 312 mabh were considered.
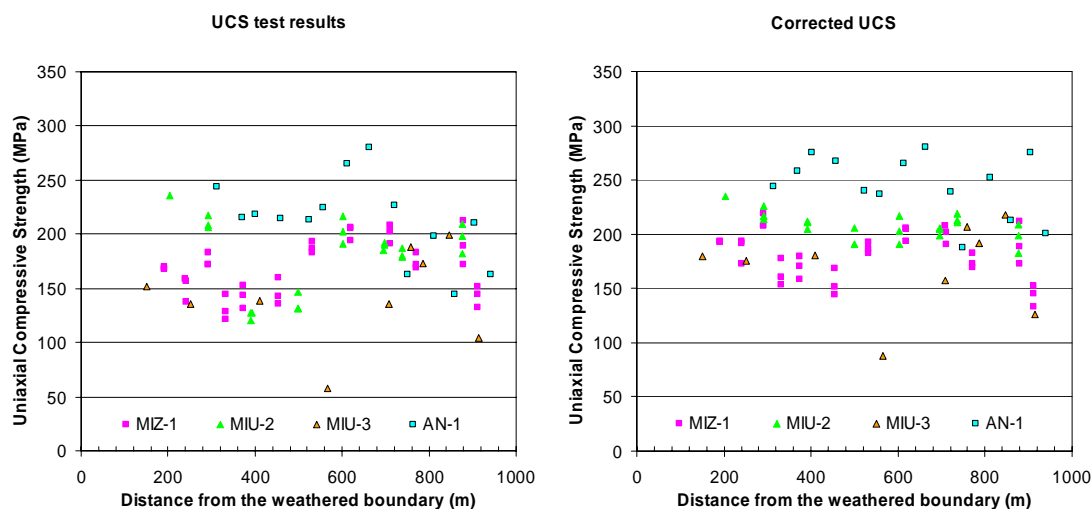
UCS test results

Corrected UCS

Figure 12. Uniaxial compressive strength of the Toki granite samples from the Shobasama and Mizunami Construction Site before (left) and after (right) the correction that takes in to account the effect of in-situ-stress release due to drilling and related core damage.

9 Conclusions

This study focused on the heterogeneities observed on some of the physical properties of the Toki granite at the Shobasama and Mizunami Construction Site. The influence of the depth, fracture intensity and rock mass stresses on the uniaxial compressive strength of the intact rock was evaluated. A positive correlation between the strength and the depth were found in the Upper Highly Fractured Domain in all analyzed boreholes. In the Lower Sparsely Fractured Domain, the correlation with depth was lost and effective porosity and strength of the intact rock seems to become negatively correlated to the magnitude of the in-situ stresses (e.g. difference between the maximum horizontal and vertical in-situ stress).

The findings in this paper, although they do not consider the drilling parameters, might be of importance in predicting the in-situ intact rock strength. In fact, if the samples tested in laboratory have been damaged, the in-situ intact rock strength is likely be higher than that obtained in laboratory. Some corrections should then be applied to the laboratory results to become representative of the in-situ conditions at the Sites.

Based on the polynomial interpolation of the variation with depth of the uniaxial compressive strength and of the difference between the maximum horizontal and vertical in-situ stress, a correction to the laboratory values of the intact rock strength is shown. This correction shows that the strength of the undamaged samples of the intact Toki granite would be much less heterogeneous than what shown by the laboratory results. Based on corrected values, a conceptual model of the variation of the uniaxial compressive strength of the Toki granite at the Shobasama and Mizunami Construction Site was developed, which takes into account the presence of the highly fractured and sparsely fractured rock domains, the magnitude of the maximum horizontal in-situ stress measured by hydro-fracturing method in the borehole and the vertical in-situ stress estimated from the weight of the overburden.

10 Acknowledgments

and Mizunami Construction Site reported in this paper. Constructive comments and suggestions by Dr K. Hashiba (University of Tokyo, Japan) and Ms A. Bäckström (Royal Institute of Technology, Stockholm, Sweden) were much appreciated.

11 References

1) Eberhardt E., Stead D., Stimpson B.: Effects of sample disturbance on stress-induced microfracturing characteristics of brittle rock, Can. Geotech. J, Vol. 36, p. 239-250,1999

2) Jaeger J.C.: Pinching off and discing of rocks, J. Geophys. Res., Vol. 68, p. 1759-65, 1963.

3) Haimson B.: Borehole breakouts and core discing as tools for estimating in situ stress in deep boreholes, in Rock Stress (eds. Sugawara K. and Obara Y.), Balkema: Rotterdam, the Netherlands, p. 35-42, 1997.

4) Lavrov, A., Vervoort, A.: Theoretical treatment of tangential loading effects on Brazilian test stress distribution, Int. J. Rock Mech. Min. Sci., Vol.39,p.275-283,2002

5) Itoigawa, J. : Geology of the Mizunami District, Central Japan. Monograph of the Mizunami Fossil Museum, No. 1, p. 1-50 (in Japanese with English abstract), 1980.

6) TODO Organisation research Group : Fault bounded inland basin of multiple blocks: an example from the sedimentary basin of the Tokai Group around Tajimi City in Gifu Prefecture, Central Japan, Earth Sciences, Vol. 53, p. 291-306 (in Japanese), 1999.

7) Yusa Y., Ishimaru K., Ota K., Umeda K. : Geological and geochemical indicators of paleohydrogology in Tono Uranium deposits, Japan, Paleohydrogeological methods and their applications, Proc. NEA Workshop, Paris (France), 9-10 November 1992, p. 117-146, 1993.

8) Tsuruta T., Ota K., Amano K., Matsuoka T., Sasaki K.: Geological investigations during the Surface-Based investigation phase of the Mizunami Underground Research Laboratory (MIU) Project. ICGM'04, JNC Report TN7400 2004-010, p. 83-95, 2004.

9) Sato T., Nakama S., Yamada A., Aoki T.: Rock mechanical studies during the surface-based investigation phase of the Mizunami Underground Research Laboratory (MIU) Project. ICGM'04, JNC Report TN7400 2004-010, p. 123-134, 2004.

10) Nakama S., Sato T., Kato H.: Status of study on in-situ stress in the Mizunami Underground Research Laboratory, 40th U.S. Symp. on Rock Mech., Alaska Rocks 2005, Anchorage, Alaska, June 25-29, 2005, ARMA/USRMS 05-887,2005.

11) Matsuki K., Kaga N., Yokoyama T., Tsuda N.: Determination of three dimensional in situ stress from core discing based on analysis of principal tensile stress. Int. J. of Rock Mech. & Min. Sci., Vol. 41, p. 1167-1190, 2004.

12) Yamada A., Seno Y., Nakama S., Sato T.: The results of the rock mechanical investigations at borehole MIZ-1, Japan Atomic Energy Agency, JAEA- Research Report (in preparation), 2007.

This is a blank page.

-51-

4. Spatial variability of the Brazilian tensile strength of the intact Toki granite at Shobasama and Mizunami Construction Site, Japan (Paper 2)

This is a blank page.

Spatial variability of the Brazilian tensile strength of the intact Toki granite at Shobasama and Mizunami Construction Site, Japan

Flavio Lanaro

Japan Atomic Energy Agency

Abstract: The extensive investigations of the Japan Atomic Energy Agency include numerous Brazilian tests on core samples from seven boreholes at Shobasama and Mizunami Construction Site, Gifu, Japan. The variation of the tensile strength from these tests is correlated to the position of the samples in the fracture domains of the granite basement. Furthermore, the tensile strength of the samples from the Lower Sparsely Fractured Domain can be correlated to the difference between the maximum horizontal stress (obtained from hydro-fracturing measurements) and the vertical stress (obtained as the weight of the overburden). The correlation appears to be linear and inverse. Based on this result, a correction of the laboratory results is designed to take into account the sample disturbance due to stress release during core drilling. The sample disturbance is explained by the microcracking that the cores experience during the loading and unloading stress-path induced by drilling, despite the applied stresses are lower than the strength of the rock material.

1 Introduction

In line with the goals of the Japan Atomic Energy Agency to improve the reliability of the deep geological disposal of high-level radioactive waste, to develop the techniques for site investigation and to provide sound technical basis for the final disposal and for regulatory guidelines, extensive investigations have been carried out in crystalline geological environment at the Shobasama and Mizunami Construction Site, Gifu Prefecture, Japan. Attention is devoted to the determination of the in-situ properties of the intact Toki granite in contrast with the physical and mechanical properties obtained in laboratory. It is known that even hard crystalline rocks might exhibit different strength properties depending on the sample alteration and disturbance (e.g. ref. 1)), loading/unloading stress path (e.g. ref. 2)) and duration of loading (e.g. ref. 3)).

It seems commonly accepted that the Brazilian strength of a rock material is governed by pre-existent flaws, grain contacts and pores. Such defects are not necessarily present in the in-situ rock matrix but might be induced by disturbance during sampling. Sample disturbance can be due to mechanical abrasion and vibration, stress concentration ahead of the drill bit and high deviatoric stresses and stress rotations during drilling. For brittle crystalline rock in highly stressed rock masses, very often the origin of the sample disturbance is related to the stress release. Stress release can induce microcraking in different directions that in turn affects the results of laboratory testing on core samples.

This study focuses on the tensile strength obtained by Brazilian testing of the intact (i.e. rock matrix) Toki granite from the Shobasama and Mizunami Construction Site. The variation of the tensile strength is studied as it varies with depth and with the level of in-situ stress. Based on the observed correlation between the strength and the difference between the maximum horizontal stress and the vertical stress, a correction of the laboratory results is proposed to determine the in-situ tensile strength of the granite.

2 Geology of the Sites

The Shobasama and the Mizunami Site are located in the Gifu Prefecture in Central Japan. The Sites are just a few kilometres apart from each other and are characterized by very similar geological conditions. A Pliocene granite basement about 65 Ma old (Toki granite) is covered by Miocene sedimentary rocks dating from 20 to 1 Ma ago. The Toki granite basement presents a surface characterized by paleo-channels. Weathering is found in the bottom of the paleo-channels but tend to significantly decrease along the slopes of the basement. Below the weathered layer, the Toki granite seems to be affected by rather heavy fracturing down to a depth varying between 100 and 500 m. This rock mass volume is addressed as the Upper Highly Fractured Domain (about 1 to 5 fractures/m). Below this domain, the fracture frequency drops in what is called the Lower Sparsely Fractured Domain (typically less than 1 fracture/m). All the geological features described here are in common for the two Sites.

2.1 Shobasama Site

The Shobasama Site lies on a valley that follows a river basin (Figure 1, left). Several boreholes were drilled at this Site. However, only borehole MIU-1 to 4 and AN-1 were sampled for rock mechanics testing. On the northern edge, the Site is interested by a large fault zone (Tsukiyoshi Fault) that trends E-W and dips about 60° to 70° at this location (Figure 1, right). The Site, originally chosen as location for the Mizunami Underground Laboratory (MIU), was abandoned on advantage of the Mizunami Site.

2.2 Mizunami Site

The Mizunami Construction Site is located on the S-E flank of a hill and limited by a river (Figure 2). Also the geological model of this Site comprehends a UHFD and a LSFD. Furthermore, the Tsukiyoshi Fault contours the N-W edge of the Site. The excavation of the Main and Ventilation Shaft of the MIU underground laboratory has reached to a depth of approximately 200 m from a gently dipping surface of the Site.
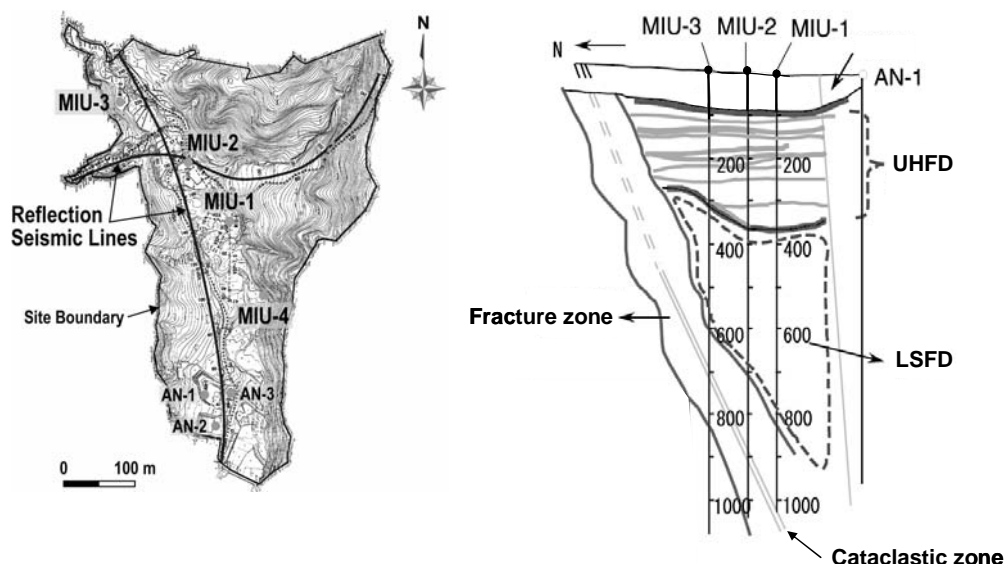
Figure 1. Map of the Shobasama Site (left) and vertical cross section of the geological conceptual model of the site along a NNW-SSE line (Tsuruta et al., 2004).
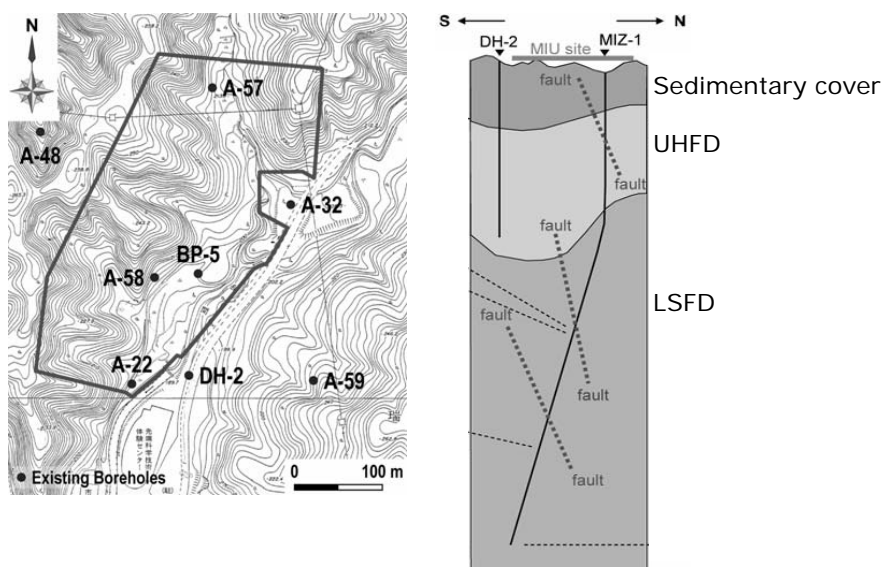
Figure 2. Map of the Mizunami Site (left) and vertical cross section of the geological conceptual model of the site along a NNE-SSW line [4].

3 Laboratory test results

Laboratory tests were carried out on the intact Toki granite for the determination of the physical (effective porosity, elastic wave velocity, density) and the mechanical properties (uniaxial compressive strength, triaxial compressive strength and Tensile Strength TS from Brazilian test). Samples were collected at rather uniform spacing along boreholes MIU-1 to 4 and AN-1 (Shobasama) and MIZ-1 and DH-2 (Mizunami) (Table 1). Hydro-fracturing methods were applied in four of the seven analyzed boreholes to determine the in-situ stress field.

Table 1. Borehole information, number of Brazilian tests on core samples of intact Toki granite and number of Hydro-Fracturing in-situ stress measurements for the analysed boreholes at the Shobasama and Mizunami Construction Site.

Borehole	Length [m]	Inclination [°]	No. of TS tests on Toki granite	No. of HF stress measurements in Toki granite
MIU-1	1011.80	Vertical	30	-
MIU-2	1012.00	Vertical	20	13
MIU-3	1014.00	Vertical	10	7
MIU-4	790.10	30° from vertical	30	-
AN-1	1010.20	Vertical	38	16
MIZ-1	1300.00	Vertical to 380 m, then inclined down to 1300 m	45	12
DH-2	501.00	Vertical	30	-

3.1 Strength

Brazilian testing was performed following the Japanese Geothecnical Society Standard (JGS 2551-2002 [5]). Figure 3 shows the variation of the indirect tensile strength obtained for samples taken along the boreholes at Shobasama (left) and at the Mizunami Construction Site (right). The plots seem to indicate that the laboratory results for samples from both sites vary with depth in a rather wavy manner. Moreover, the waviness is not the same for all boreholes at the same site.

Figure 3. Plot of the indirect tensile strength of the intact Toki granite of samples taken from the boreholes at the Shobasama (left) and Mizunami Site (right). Please notice that borehole MIU-4 and MIZ-1 are not vertical.

4 Rock stress measurements

Extensive campaigns of in-situ rock stress measurements were carried out at the Sites and are summarised in Figure 4 in terms of ma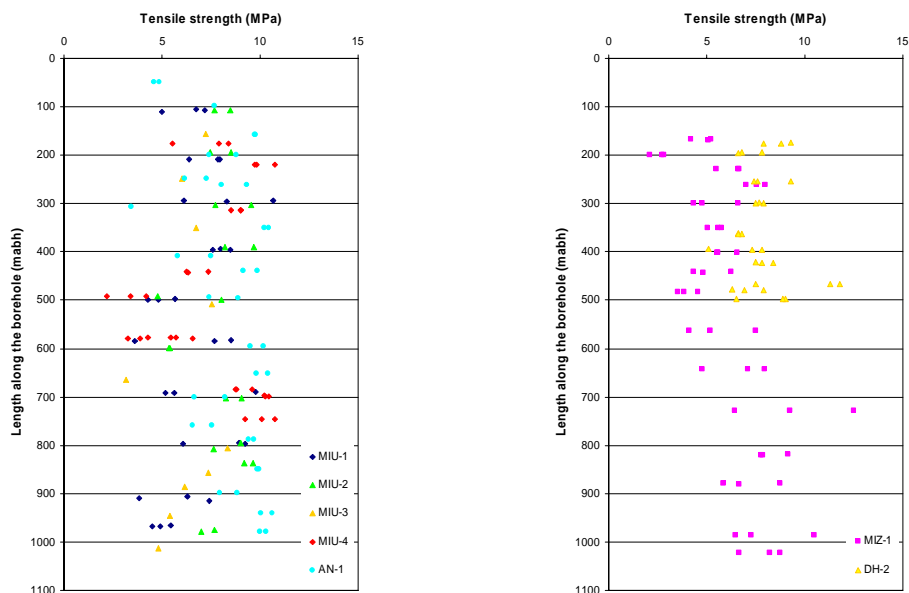ximum and minimum horizontal stress and vertical stress, respectively. The presence of the deformation zones is also indicated, which clearly affects the stress distribution by reducing the measured stresses inside or immediately closed to the fault zones.

Small-scale heterogeneities (e.g. single fractures) and large-scale heterogeneities (i.e. fault zones, see Table 2) affect the stress field at the sites, whereas the geological properties of the rock mass seem to be rather homogeneous [6]. This justifies the assumption that, if stresses are to vary, they would probably vary smoothly at the scale of the whole boreholes (between 500 and 1,000 m). The local variations are in this way attributed to the small-scale heterogeneities. On the other hand, large-scale heterogeneities should more continuously affect the stress regime due to the often gradual transition of the rock mass properties from competent bedrock to fault zones.

The rock stress measurements by hydro-fracturing returned three components of the in-situ stress tensor in the vertical direction and on horizontal planes. Since shear stress components were not determined and are assumed null, this implicitly implied that the determined stresses are also principal stresses (e.g. the vertical and horizontal directions are principal directions). This assumption, although probably rough, simplifies very much the analysis of the in-situ stresses and their variation with depth. Polynomial interpolations of the maximum total horizontal stress and of the difference between the maximum total horizontal stress and the vertical stress, here addressed as deviatoric stress, are shown in Figure 5 as a function of the distance along the boreholes from the weathered boundary of the Toki granite basement. The vertical stress is determined as the weight of the overburden (considered all in granite), thus, it increases linearly with depth according to the equation:

$$\sigma_v = \rho g z = 0.0256 z \quad \text{(MPa)}$$

where ρ is the density, g is the gravity acceleration and z is the depth, respectively.

It could be observed that the hydro-fracturing data systematically returns proportional values of the maximum horizontal stress σ_H compared to the minimum horizontal stress σ_h (σ_H/σ_h ranging between 2.1041 for AN-1 and 2.2739 for MIU-2). Therefore, the two stress components might not be considered as independent due to the method of determination. It was judged to be more relevant to study the variation of the difference between the maximum horizontal stress and the vertical stress (e.g. deviatoric stress in a core axial plane) because these components are independently determined.

Figure 4. Summary plots of the results of hydro-fracturing measurements of the in-situ stresses. Filled squares show the maximum total horizontal stress, empty squares the maximum effective horizontal stress. Empty circles represent the total minimum horizontal stress. The dotted lines show the total vertical stress calculated from the rock density. The position of the major fault zones identified along the boreholes is also indicated.

Table 2. Position of the major fault zones along the boreholes at the Shobasama and Mizunami Construction Site. The faults considered here are typically thicker than 10 m when measured along the boreholes (mabh).

Borehole	Upper Fault Zone Limit [mabh]	Lower Fault Zone Limit [mabh]
MIU-1	-	-
MIU-2	716.0	915.0
MIU-3	606.0	831.0
MIU-4	453.8	482.6
	587.6	785.3
AN-1	-	-
MIZ-1	195.3	223.2
	648.2	725.8
	918.2	982.7
DH-2	-	-
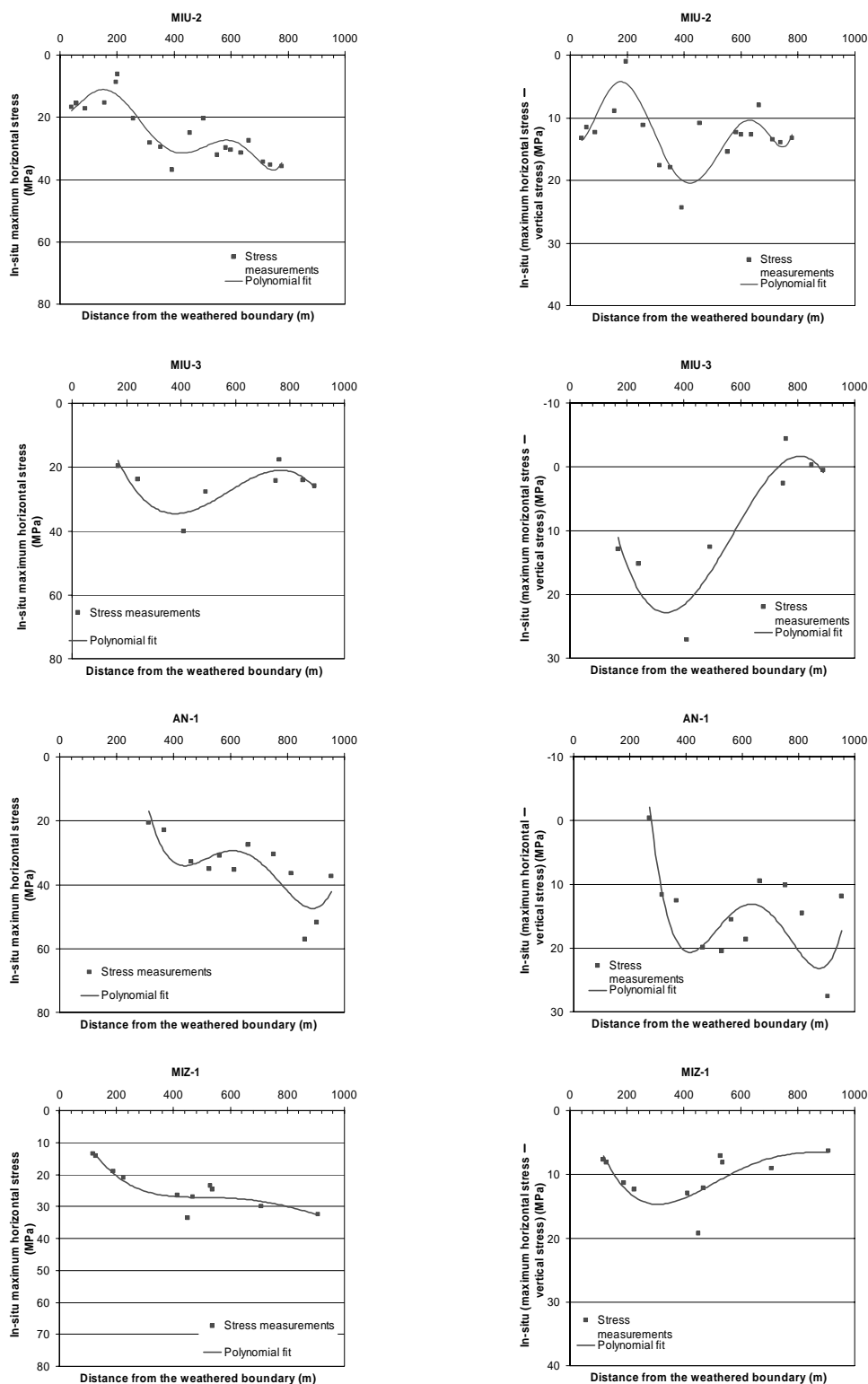
Figure 5. Polynomial fit of the variation with depth of the maximum total horizontal stress (left) and of the difference between the maximum total horizontal stress and the vertical stress for borehole MIU-2, MIU-3, AN-1 and MIZ-1. The depth is represented as the distance along the boreholes from the weathered boundary in the Toki granite basement.

5 Spatial variability of the tensile strength

Spatial variability of the indirect tensile strength obtained from Brazilian tests might depend on different causes among which we can list:

1) Mineralogical differences (e.g. facies)

2) Geological domains (e.g. fracture domains)

3) Alteration and weathering

4) Presence of fault zones

5) Effect of stress relief due to drilling.

An earlier study about the uniaxial compressive strength of the intact Toki granite at the Shobasama and Mizunami Construction Site [7] shows that the differences in mineralogy and grain size distribution could not be correlated to the variation of the strength of the samples. On the other hand, the uniaxial compressive strength would depend on the fracture domain in which the samples were taken (e.g. Upper Highly Fractured Domain and Lower Sparsely Fractured Domain). No samples were collected from altered or weathered rock volumes since the weathered zone would typically be on the surface of the crystalline basement. Moreover, a clear linear correlation could be observed between the uniaxial compressive strength and the maximum total horizontal stress extrapolated by polynomial fitting (Figure 5) to the depth at which the uniaxial test samples were taken. Thus, in the following sections, the attention will be devoted to the analysis of the tensile strength in the different fracture domains and to the dependence of tensile strength on the measured in-situ rock stresses.

5.1 *Upper Highly Fractured Domain*

The Upper Highly Fractured Domain occurs almost ubiquitously in the upper volume of the Toki granite basement. In this domain, the fracture frequency varies between 1 and 5 fractures/m. Moreover, the superficial volume of this domain is affected by weathering for a depth that reaches down to about 30 m.

Since the thickness of the upper domain varies from borehole to borehole and includes the weathered zone, a normalised distance d along the boreholes was defined as:

$$d = \text{Normalised distance} = \frac{\text{Distance from the weathered boundary}}{\text{Thickness of the UHFD (weathered zone excluded)}}$$

This definition of normalised distance is used in Figure 6 where the tensile strength results are plotted versus normalised depth in the Upper Highly Fractured Domain. For borehole MIZ-1, AN-1, MIU-1 and 4, a positive correlation with depth could be hypnotized, which cannot be observed for the tensile strength results of the samples from borehole DH-2, MIU-2 and 3.
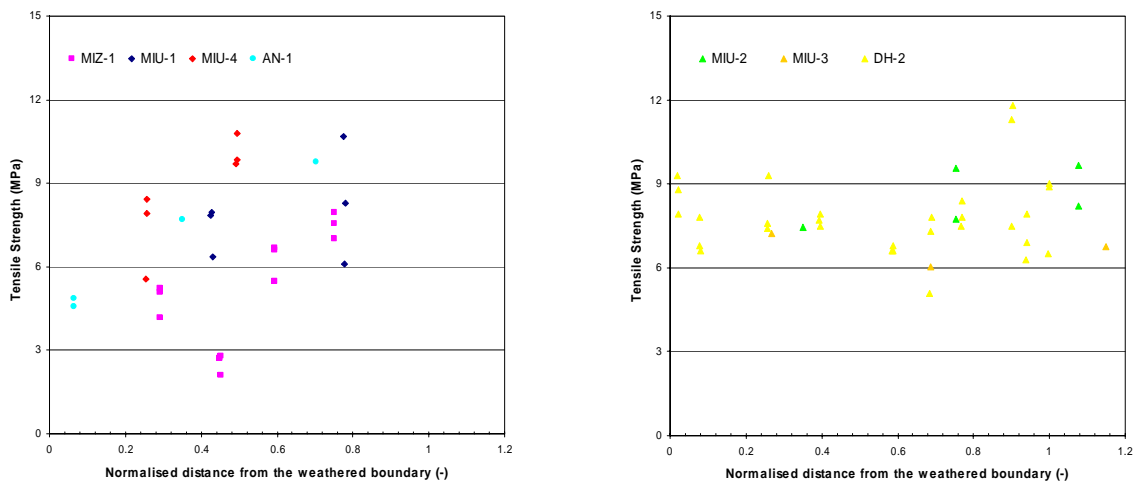
Figure 6. Plot of the tensile strength of the intact Toki granite versus normalised depth for the samples taken from the Upper Highly Fractured Domain. The results on the left (MIZ-1, MIU-1 and 4, AN-1) show an increase of strength with depth, while the results on the right (MIU-2 and 3, DH-2) seem to have a rather constant mean value.
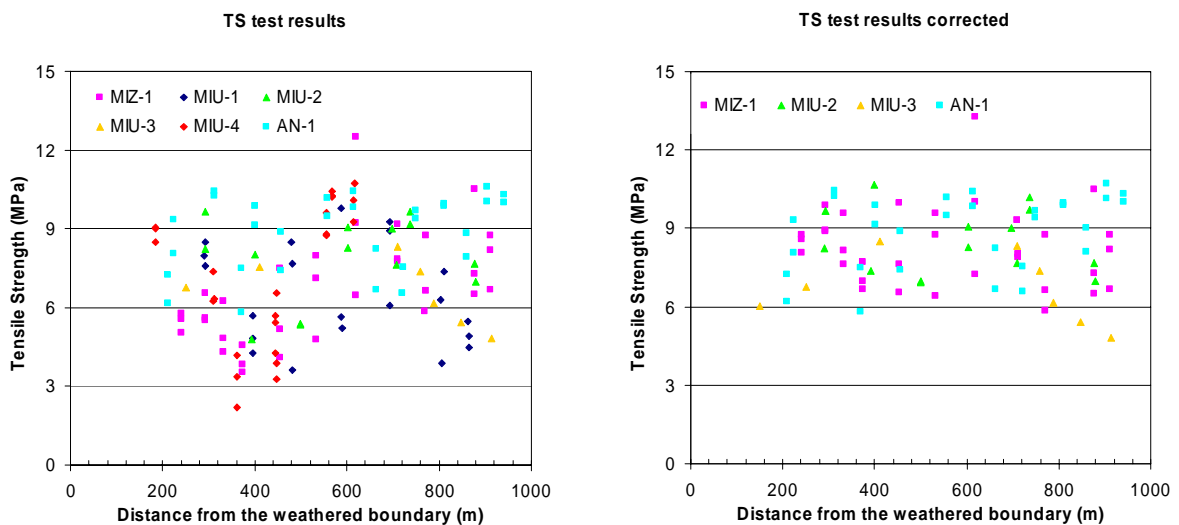
Figure 7. Plot of the tensile strength of the intact Toki granite versus depth for the samples taken from the Lower Sparsely Fractured Domain. The tensile strength values on the left are from the laboratory, while the samples on the right are corrected according to Sec. 5.2.1 for the boreholes where in-situ rock stress measurements are available.

In this fracture domain in the crystalline basement, the in-situ stresses are usually rather low and increase monotonically with depth. The stresses can therefore not be correlated to the tensile strength that either increases with depth (for borehole MIZ-1, AN-1, MIU-1 and 4; Figure 6, left) or has a rather constant mean value (for borehole MIU-2, 3 and DH-2; Figure 6, right). The increase of tensile strength with depth in the upper domain could be explained with the same fracturing processes that produced the fracture frequency in this domain.

5.2 Lower Sparsely Fractured Domain

The results of tensile strength from Brazilian tests for the samples collected in the Lower Sparsely Fractured Domain are shown in Figure 7 (left). These results show a much larger spread than the results in the Upper Highly Fractured Domain. Moreover, as observed in Sec. 3.1, rather marked waviness with depth can be seen in some of the borehole results (Figure 8).

5.2.1 Correlation with the in-situ rock stresses

In ref. 7) , the uniaxial compressive strength was found to correlate very well with the maximum horizontal in-situ stress. The same correlation with the maximum horizontal stress could not be found for the tensile strength. On the other hand, if was observed that the tensile strength correlates very well with the difference between the maximum total horizontal stress and the vertical stress (deviatoric stress in a borehole axial plane).

Assuming that the tensile strength will vary with depth according to the polynomial fittings in Sec. 5.2, the estimated strength at each depth can be correlated with the deviatoric stress at the same depth estimated by means of the polynomial fittings in Sec. 4. This results into the correlation plots in Figure 9 (left).

Also the experimental results can be plotted as a function of the in-situ stresses. Since direct measurements of the in-situ stresses are not available at each specific depths where the Brazilian test samples were taken, stresses at those depths were estimated by means of the polynomial fittings in Sec. 4 and plotted in Figure 9 (right). Also this picture, although the rather large scatter, clearly indicate the deterioration of the tensile strength obtained by means of Brazilian tests when the deviatoric in-situ stress on a vertical plane increases. Furthermore, the correlation can be considered linear in the first approximation.

No correlation could be observed for test results from samples taken from borehole AN-1. This could be explained by the fact that vertical and horizontal stresses are not principal stresses at this particular location. Another explanation could be different drilling parameters or treatment and preparation of the core samples, since this borehole was drilled much earlier than the others.
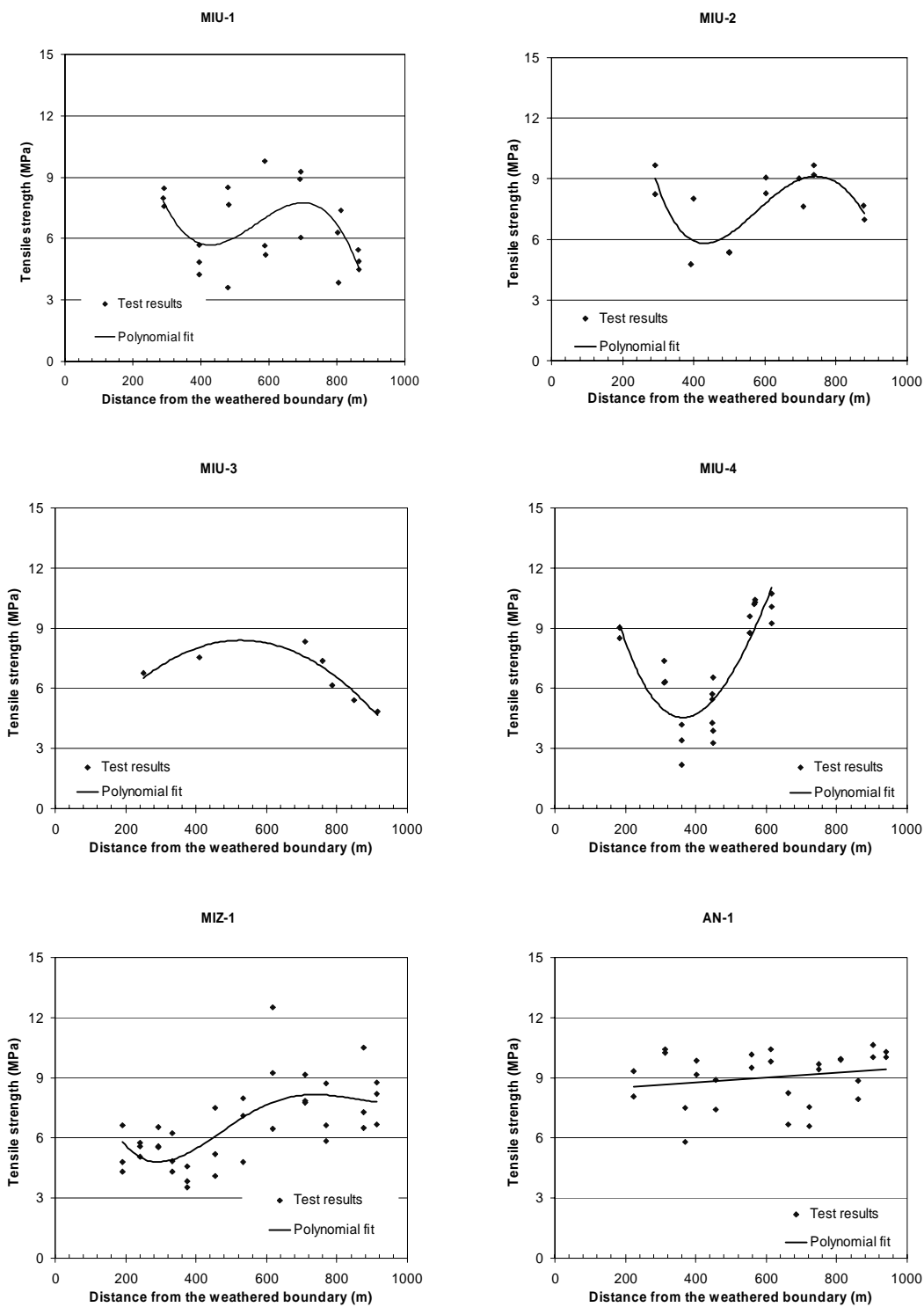
Figure 8. Polynomial fittings of the tensile strength of the intact Toki granite versus distance from the weathered boundary for the samples taken from the Lower Sparsely Fractured Domain.
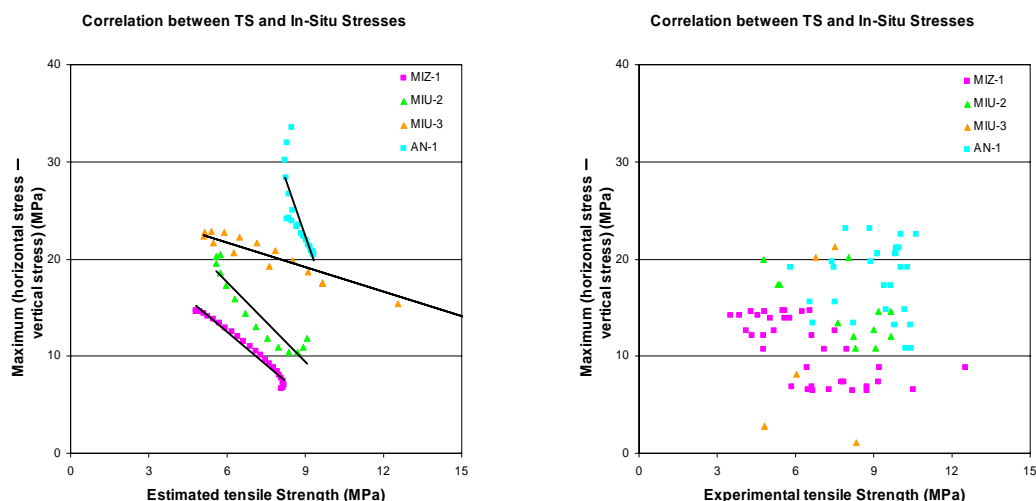
Figure 9. Correlation between the estimated values of the tensile strength and the estimated in-situ stress at each depth by means of the polynomial fittings in Sec. 4 and 5.2.1 (left); and correlation between the experimental tensile strength results and the in-situ stresses estimated at the same depth by means of the polynomial fits Sec. 4 (right). Only results from samples taken from the Lower Sparsely Fractured Domain are plotted here. The results from borehole AN-1 do not show any correlation, therefore are not presented in the right plot.

5.2.2 Correction of the experimental results

The fact that the experimental tensile strength decreases when the in-situ stress (e.g. deviatoric stress) increases might be due to the unloading stress-path induced by the drilling of the cores. Therefore, it would not be an in-situ material property of the intact Toki granite but it would be induced by different degree of stress release depending on the particular level of stress in the rock mass at the particular location where the sample was taken.

It would be then desirable to remove such in-situ stress influence on the experimental results by applying a correction. Based on the correlation found between the tensile strength and the difference between the maximum horizontal and the vertical in-situ stress, a simple correction can be designed. For the boreholes were this correlation was observed, it can be written:

$$\sigma_H - \sigma_v = MAX_{\Delta\sigma} - GRAD_{\Delta\sigma} \times TS$$

where $MAX_{\Delta\sigma}$ and $GRAD_{\Delta\sigma}$ are the intercept and the gradient of the correlation lines in Figure 9 (left), respectively. If the experimental results are assumed to be unaffected by the in-situ stress state for the lowest values of the deviatoric stress $(\sigma_H - \sigma_h)_{Low}$, the increment CORR to the experimental tensile strength values proportional to the difference between the actual and the lowest values of the deviatoric stress affecting the samples can be added:

$$CORR = \left[(\sigma_H - \sigma_h)_{ACT} - (\sigma_H - \sigma_h)_{LOW} \right] \times GRAD$$

In this way, only the samples taken from sections of the boreholes with high deviatoric stresses will be corrected. This correction results into the values of the tensile strength of the intact Toki granite shown in Figure 7 (right). The application of such correction affects the statistics of the tensile strength in each borehole according to Table 3.

6 Discussion

By the author knowledge, no papers before have considered the influence of the in-situ stress field on the mechanical properties of the samples for Brazilian testing. However, it is a well known fact that the stress release that the cores undergo during drilling might permanently damage the samples that, in turn, would exhibit mechanical properties different than the in-situ properties (e.g. ref. 8), 9)). The stress release process associated with drilling in a rock mass with deviatoric in-situ stresses mainly induces tensile damage on the cores, as numerical models of the stress distributions in the core stub show [10].

Core discing is an extreme case of such core damage when in-situ stresses are high compared to the strength of the rock material. However, for lower stresses, damage might not result into visible fractures but microcracks that can reduce the rock strength of the samples. For example, when core discing does not completely develop and the cracks do not propagate through the whole core section [11]. In this case, the sample still holds together although damage might be more uniformly distributed through the samples than when discing fractures completely develop.

Table 3. Mean value and standard deviation of the tensile strength of the intact Toki granite in the Lower Sparsely Fractured Domain before and after correction according to Sec 5.2.2.

Borehole (No. of samples from LSFD)	TS mean (MPa)	TS standard deviation (MPa)	Corrected TS mean (MPa)	Corrected TS standard deviation (MPa)	Difference of the means after correction	Difference of the standard deviations after correction
MIZ-1 (33)	6.6	2.0	8.2	1.5	+24%	-10%
MIU-1 (21)	6.5	1.9	-	-	-	-
MIU-2 (14)	7.8	1.6	8.5	1.3	+9%	-23%
MIU-3 (7*)	6.2	1.6	6.3	1.7	+2%	+6%
MIU-4 (24)	7.5	2.6	-	-	-	-
AN-1 (30**)	8.9	1.4	8.9	1.4	0%	0%

* The sample at 664.5 mabh was ignored (TS=3.18 MPa); the sample at 1012.5 mabh was corrected to 7 MPa;
** Samples below 248 m are considered. The sample at 307.13 m was ignored (TS=3.42 MPa).

For low permeability rocks, the pore pressure release during drilling is delayed in time. Thus, if drilling is fast, effective tensile stresses can develop inside the core that can also damage the core samples.

Although in weak sedimentary rocks, Holt et al. observed that core samples often show radial p-wave velocity lower than the in-situ p-wave velocity [9]. This can be explained by the development of microcracks parallel to the borehole axis during radial unloading. These microcraks, acting diametrically with respect to the core, might affect the results of the Brazilian testing that also applies diametrical loads.

Furthermore, anisotropy of the Brazilian stress results often observed (e.g. ref. 12)) might sometimes be induced by the anisotropy of the stress field that produced different degree of damage on the core in different directions [13].

Eberhardt et al. observed a degradation of the uniaxial compressive strength measured in laboratory with the increase of the deviatoric in-situ stress measured at the location of sampling at the URL in Manitoba (Canada) [8]. Samples of the Lac du Bonnet granite and granodiorite were collected at depths between 130 and 420 m, where the deviatoric stress would increase from about 5-10 MPa at the shallowest depth of 130 m to 40 MPa at 420 m, respectively. For the granite, the uniaxial compressive strength diminished by about 40% between these depths, and by 24% between the depth of 240 and 420 m. For the granodiorite, which has a smaller grain size, the uniaxial compressive strength diminished by about 6% between the depths of 240 and 420 m. Such deteriorations were attributed to the stress-induced sampling disturbance in the form of microscracking that was even visible in SEM (Scanning Electron Microscope) images taken on thin sections of the samples. This study, although not focused on the Brazilian strength, is relevant because it shows that deviatoric in-situ stresses as low as 13 MPa at 240 m might induce damage in samples of crystalline rocks that reduces the strength of the material in laboratory by about 20%.

In this paper, the variation of the tensile strength obtained from Brazilian testing could be linearly correlated to the difference between the maximum in-situ horizontal stress (i.e. measured by means of hydro-fracturing method) and vertical stress (i.e. estimated based on the weight of the overburden). The observed correlation was found to be linear, in the first approximation. Already Obert and Stephenson [14] and, more recently, Matsuki et al. [15], correlated the occurrence of core discing to the tensile strength of the rock material through a linear equation of the kind:

$$K_1 = \sigma_r - K_2 \sigma_z$$

where K_1 and K_2 are coefficients that depend on the geometry of the core, the disc thickness and the rock material properties. Thus, when discing is not occurring but the stress components are such that the linear criterion is approached, then damage of the core might develop. K_1 was found to vary between 0.59 and 0.89, while K_2 was observed to range between 6.5 and 10.5 times the tensile strength from Brazilian tests, respectively.

Let's assume that K_1 equals 6.5 times the tensile strength and K_2 equals to 0.59, respectively. According to Table 3, the mean tensile strength from Brazilian tests can be taken as 8 MPa, with a standard deviation of 1.5 MPa. If we consider that among the minimum values of the tensile strength there will be some as small as the mean values reduced by two times the standard deviation (i.e. 95% confidence level), the constant K_1 will be about 35 MPa. The criterion by Obert and Stephenson [14] will then plot as in Figure 10, were the distance between the symbols and the red line qualitatively represents the risk of development of core discing in the cores from the Shobasama and Mizunami Construction Sites. Although this analysis assumes slightly pessimistic parameter values, it is quite clear that some sections of the boreholes might be likely to experience, if not core discing, at least some damage in the form of microcracking. Thus, the correlation found in Sec. 5.2.2 can be explained in terms of potential damage of the cores due to drilling and stress release.

Also the relation between the stress level at which the Kaiser effect will occur and the previous stress level experienced by a sample in cyclic triaxial axi-symmetric compression is linear (e.g. ref. 16), 17)). Since the acoustic emission associated with the Kaiser effect is an expression of the irreversible damage and changes of the material internal structure, the Kaiser effect observed in uniaxial, triaxial and Brazilian testing supports the linearity of the relations in Figure 9. In the Brazilian testing, such changes already occur when the load reach about 50% of the final strength of the samples [18].

The linearity of the correction applied to the laboratory results also implies that an hydrostatic in-situ stress fields would not affect the laboratory results. This is in agreement with the stress distributions in the core stub obtained numerically for hydrostatic in-situ stress conditions [10]. Due to stress release, the core stub would only experience tensile stresses, and thus potential damage, in a small region of the core confined to its surface, while the centre of the core is always tension-free. Even the criterion by Obert and Stephenson will predict core discing for hydrostatic stresses

of the order of 7 to 17 times the tensile strength of the rock, thus far from the stress conditions encountered at the Shobasama and Mizunami Construction Site.
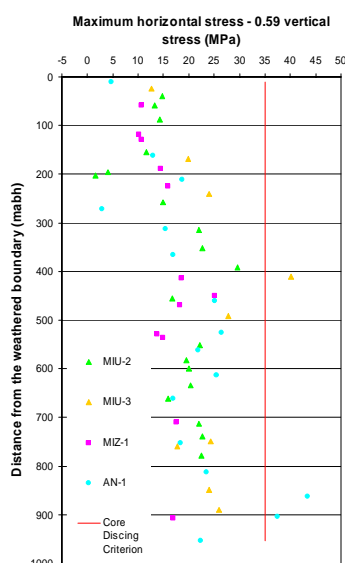

Figure 10. Plot of the left and right terms of Core Discing Criterion by Obert & Stephenson (1965) for the boreholes at Shobasama and Mizunami Construction Site.

7   Conclusions

In this study, the empirical observation of a wavy variation of the indirect tensile strength obtained from Brazilian tests could be explained in terms of spatial location of the samples and spatial variation of the local stress tensor components at Shobasama and Mizunami Construction Site. The tensile strength was found to have a rather constant mean value or to monotonically increase in the Upper Highly Fractured Domain of the Toki granite basement. This variation could not be explained other than with the fact that the same causes that produced the high frequency of macro-fractures might also be affecting the strength of the rock matrix.

In the Lower Sparsely Fractured Domain, such monotonic variation was replaced by a wavy variation. The position of the peaks and troughs of the plot of the tensile strength was observed to follow very closely the position of the peaks and troughs of the plot of the deviatoric stress calculated as the difference between the maximum horizontal stress and the vertical stress. Moreover, the values of the tensile strength were found to be inversely and linearly correlated to the values of the deviatoric stress. Based on this correlation, a correction of the laboratory results to better mirror the in-situ conditions was designed. Such correction produced in general higher mean values and lower standard deviations of the tensile strength of the intact Toki granite compared to the laboratory results.

Support to the observed linearity of the correlation was found in other studies about core discing and Kaiser Effect in brittle rock materials. However, as in many other studies on the subject of sample damage due to stress release, the nature of the correlation between the strength of the rock and the in-situ stress field was not approached by means of simulations of the stress-path that the cores undergo during drilling. Only in this way, it would be possible to identify the preferential orientation and position of the microcracks and understand their influence on the compressive and tensile strength of the core samples.

8   Acknowledgments

9   References

1) Hakami E., Johansson M. : Rock mechanics evaluation of BOREMAP data and laboratory test results. Laxemar and Forsmark – Stage 2.1. SKB P-06-267, the Swedish Nuclear Waste Management Company.,2006

2) Chen Z.H., Tham L.G., Yeung M.R., Xie H. : Confinement effects for damage and failure of brittle rocks, I. J. Rock Mech. Min. Sci., Vol. 43, p. 1262-1269., 2006

3) Eberhardt E., Stead D., Szczepanik Z. : Laboratory testing of stress-induced brittle fracture damage through incremental loading, Proc. I. Conf. Geotech. & Geo. Eng. – GeoEng2000, Melbourne, Australia, Technomic Publishing, Lancaster, Paper #UW0246, 6 pp., 2000

4) Tsuluta , T., Ota, K. , Amamo, K., Matsuoka, T. and Sesaki , K. : Geological investigations during the Surface-Based investigation phase of the Mizunami Underground Research Laboratory (MIU) Project. ICGM'04, JNC TN7400 2004-010, 83-95, 2004.

5) JGS 2551-2002. Method for splitting tensile strength test on rocks, the Japanese Geotechnical Society., 2002

6) Sato T., Imazu M., Mikake S., Tamai T., Yamamoto M., Sakamaki M. : Status of Japanese Underground Research Laboratory – Design and construction of 1000 m-deep shafts and research tunnels. Proc. ITA Annual Congr. "Underground Space Use: Analysis of the Past and Lessons for the future (eds. Erdem Y. and Solak T.), Taylor & Francis Group, London, p. 335-341., 2005

7) Lanaro F. : Spatial variability of the uniaxial compressive strength of intact Toki granite at the Shobasama and Mizunami Construction Site, Japan, in preparation., 2006

8) Eberhardt E., Stead D., Stimpson B. : Effects of sample disturbance on stress-induced microfracturing characteristics of brittle rock, Can. Geotech. J, Vol. 36, p. 239-250., 1999

9) Holt R.M., Brignoli M., Kenter C.J. : Core quality – quantification of coring-induced rock alteration, I. J. Rock Mech. & Min. Sci., Vol. 37, p. 889-907., 2000

10) Li Y., Schmitt D. : Well-bore bottom stress concentration and induced core fractures, AAPG Bulletin, Vol. 81, No. 11, p. 1909-1925., 1997

11) Kaga N., Matsuki K., Sakaguchi K. : The in situ stress states associated with core discing estimated by analysis of principal tensile stress, I. J. Rock Mech. Min. Sci., Vol. 40, p. 653-665., 2003

12) Lanaro F., Fredriksson A. : Rock Mechanics Model - Summary of the primary data. Preliminary site description Forsmark area - version 1.2, the Swedish Nuclear Waste Management Company, SKB R-05-83, p. 45., 2005

13) Lavrov A., Vervoort A., Wavers M., 2002a. Anisotropic damage formation in brittle rock: Experimental study by means of acoustic emission and Kaiser effect, Proc. 6th Conf. EUROMEC-MECAMAT'2002 (Ed. S. Cescotto), J. Phys. IV France, Vol. 105, p. 321-328.

14) Obert L., Stephenson D.E. :Stress conditions under which core discing occurs, Society of Mining Engineers of AIME Transactions, 232(3), p. 237-235., 1965

15) Matsuki K., Kaga N., Yokoyama T., Tsuda N. : Determination of three dimensional in situ stress from core discing based on analysis of principal tensile stress. I. J. of Rock Mech. & Min. Sci., Vol. 41, p. 1167-1190., 2004

16) Li C., Nordlund E. : Experimental verification of the Kaiser effect in rocks, Rock Mech. Rock Eng., Vol. 26, p. 333-351., 1993

17) Filimonov Y. L., Lavrov A. V., Shafarenko Y. M., Shkuratnik V. L. : Acoustic emission in host-rock material for radioactive waste disposal: comparison between clay and rock salt, Rock Mech. Rock Eng., Vol. 34, p. 275-291., 2001

18) Lavrov A., Vervoort A., Wavers M., Napier J. A. L. : Experimental and numerical study of the Kaiser effect in cyclic Brazilian tests with disk rotation. International Journal of Rock Mechanics and Mining Sciences, Vol. 39, p. 287-302., 2002

This is a blank page.

5. Modelling Brazilian tests with FRACOD^{2D} (FRActure propagation CODe) (Paper 3)

This is a blank page.

Modelling Brazilian tests with
FRACOD^{2D} (FRActure propagation CODe)

Flavio Lanaro*, Toshinori Sato[×], Mikael Rinne[+], Ove Stephansson[°]

*Japan Atomic Energy Agency, Japan
[×]Agency for Natural Resources and Energy, ANRE, Japan
[+] FRACOM Ltd, Finland
[°] GeoForschungsZentrum Potsdam, Germany

Abstract: This study focuses on the influence of initiated cracks on the stress distribution within rock samples subjected to tensile loading by traditional Brazilian testing. The numerical analyses show that the stress distribution is only marginally affected by the considered loading boundary conditions. On the other hand, the initiation and propagation of cracks produce a stress field that is very different from that assumed by considering the rock material as continuous, homogeneous, isotropic and elastic. In the models, stress concentrations at the bridges between the cracks were found to have tensile stresses much higher than the macroscopic direct tensile strength of the intact rock. This was possible thanks to the development of large stress gradients that can be carried by the rock between the cracks. The analysis of the deformation along the sample diameter perpendicular to the loading direction might enable one to determine the macroscopic direct tensile strength of the rock or, in a real case, of the weakest grains. The strength is indicated by the point where the stress-strain curves depart from linearity.

1 Introduction

Brazilian testing, or splitting tension test, is widely used in engineering practice to indirectly obtain the tensile strength of intact rock samples often obtained from drill cores. The standards (e.g. ref. 1), 2)) suggest using the value of the tensile stress at the centre of the sample given by the analytical solution for a continuous, homogenous, isotropic and elastic medium (e.g. ref. 3)). However, recent studies have shown that the samples loaded in Brazilian test conditions undergo cracking or activation of pre-existent flaws before the failure of the specimens (e.g. ref. 4), 5), 6), 7), 8)). Thus, the hypothesis of continuity does not hold and the stresses inside the samples may differ very much from those given by the closed-form solutions. This is particularly true for the tensile stress along the loading diameter of the sample, which is responsible for crack initiation. Despite this, several recent publications still approach the problem of tensile strength determination from Brazilian testing by using continuum analytical solutions (e.g. ref. 9)) and finite-element analyses (e.g. ref. 10), 11)). These analyses give results that only marginally differ from the closed-form solutions in the textbooks and do not address the issue of the stress concentrations induced by crack initiation and propagation inside the specimens or that of the overestimation of the tensile strength obtained from Brazilian testing compared to direct tensile testing.

Several authors (e.g. ref. 12), 13)) have suggested Brazilian tests on samples with artificially drilled holes in different positions. This allows controlling the point at which the crack propagation starts and enhances the local opening stress. These testing setups were also used to determine the toughness of the material by reloading a sample where crack propagation had been induced, stopped and measured. However, very seldom numerical models have been able to successfully replicate the magnitude of the indirect tensile strength from Brazilian testing in laboratory.

The objective of this study is to improve the interpretation of the results of Brazilian tests by studying how newly generated cracks affect the stress field in the sample during loading. This is achieved by modelling the Brazilian tests by means of a Boundary Element Method code (FRACOD^{2D} by FRACOM Ltd, Finland) that implements the Displacement Discontinuity Method and crack initiation and propagation algorithms. The code has been successfully applied to solve different problems involving fracture propagation in rocks (e.g. ref. 14),15), 16)).

In this paper, the experimental results on samples collected at the sites of Shobasama and Mizunami Underground Research Laboratory (MIU), Gifu Prefecture, Japan, are used to obtain all the necessary input parameters for the intact rock and cracks of the Toki granite (a medium to coarse biotite granite) for modelling Brazilian testing.

2   Experimental results

Laboratory tests were carried out on samples of the Toki granite for determining the physical (effective porosity, elastic wave velocity, density) and the mechanical properties: Uniaxial Compressive Strength (UCS), triaxial compressive strength and indirect Tensile Strength (TS) from Brazilian testing, fracture stiffness and toughness. Samples were collected at rather uniform spacing along boreholes MIU-1 to 4 and AN-1 (Shobasama), MIZ-1 (MIU Construction Site) and adjacent DH-2 (Table 1).

Uniaxial and triaxial testing results provide the Young's modulus, Poisson's ratio, UCS, cohesion and friction angle of the intact Toki granite. These mechanical parameters are summarised in Table 2.

Table 1. Borehole information, numbers of Brazilian tests and fracture toughness and stiffness tests on samples from borehole cores of Toki granite.

Borehole	Length [m]	Inclination [°]	No. of Brazilian tests	No. of Toughness tests
MIU-1	1011.80	Vertical	30	-
MIU-2	1012.00	Vertical	20	9 K_{IC} + 7 K_{NL}^{A} + 16 K_{IIC}
MIU-3	1014.00	Vertical	10	-
MIU-4	790.10	30° from vertical	30	-
AN-1	1010.20	Vertical	38	-
MIZ-1	1300.00	Vertical to 380 m, then inclined up to 14° from vertical to 1300 m	45	-
DH-2	501.00	Vertical	30	-

Table 2. Average rock mechanics properties of the Toki granite obtained in different investigation campaigns[17],[18].

Borehole	Young's modulus [MPa]	Poissons's ratio [-]	UCS [MPa]	Cohesion [MPa]	Friction angle [°]
MIU-1 to 4 and AN-1	51	0.34	168	34	55
DH-2	58	0.33	117	37	53
MIZ-1	54	0.26	171	39	52

2.1 Tensile strength

Brazilian testing was performed according to the Japanese Geotechnical Society Standard [2]. Typically, the diameter of the samples is 35±0.4 mm and the thickness varies between 33 and 35 mm. Figure 1 shows the variation of the indirect tensile strength (TS) obtained for samples from the boreholes at Shobasama (left) and at the MIU Construction Site (right). The term "indirect" is used here opposite to the "direct" or "macroscopic" tensile strength determined from uniaxial tensile tests. The plots seem to indicate that the laboratory results for samples from both sites vary in a rather wavy shape with depth. Moreover, the waviness is not the same for all boreholes at the same site. The average indirect tensile strength and its range of variation are summarised in Table 3 for the two rock domains at the sites, the Upper Highly Fractured Domain (UHFD) and the Lower Sparsely Fractured Domain (LSFD).

Table 3. Average values and range of variation of indirect tensile strength of the Toki granite from Brazilian tests (from the MIU Database).

Borehole	UHFD		LSFD	
	Average TS [MPa]	Min-Max TS [MPa]	Average TS [MPa]	Min-Max TS [MPa]
MIU-1 to 4 and AN-1*	8.0	4.6-10.8	7.9	4.2-10.7
DH-2	7.8	5.1-11.8	-	
MIZ-1**	6.0	4.2-8.0	6.7	4.1-12.5

* 8 samples out of 125 were removed because TS < 4 MPa,
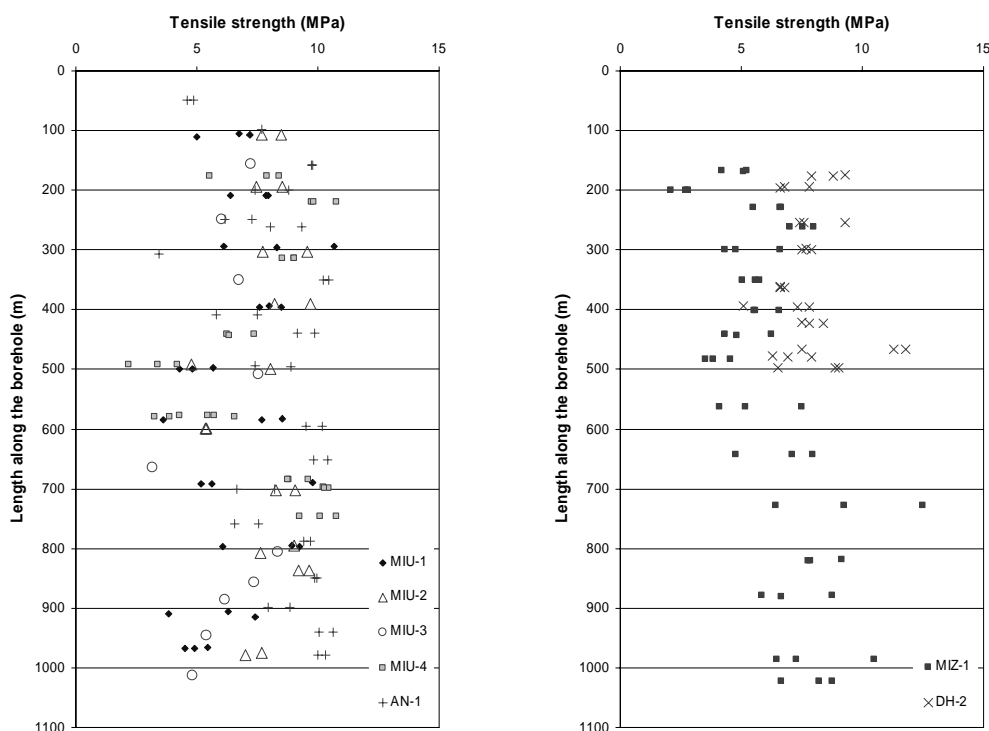** 5 samples out of 45 were removed because TS < 4 MPa.

Figure 1. Plot of the tensile strength of the intact Toki granite of samples taken from the boreholes at the Shobasama (left) and MIU Construction Site (right). Please notice that borehole MIU-4 and MIZ-1 are not vertical.

2.2 Fracture toughness

Fracture toughness and fracture stiffness determinations were performed at the GeoForschungZentrum (Potsdam, Germany) on core samples from borehole MIU-2 at Shobasama [19]. The samples were collected at three different depths (200, 500 and 950 m along the borehole). At these depths, the Toki granite has a fine-grained, porphyritic and coarse grained structure, respectively. Results are available from 9 Chevron-Bend (CB) Tests [20], 7 fracture normal stiffness tests and 16 Punch Through Shear (PTS) Tests under confinement pressures between 5 and 70 MPa [21].

The samples from 950 m, which were taken from a fractured section of the borehole, show a much lower Mode I fracture toughness than the others (Table 4). On the contrary, all samples present rather similar values of the normal stiffness K_{NL}^{A} and Mode II fracture toughness K_{IIC} at both levels of confinement. The values of the fracture normal stiffness refer to loading conditions between normal stresses of 4 MPa and 10 MPa.

2.3 Sample appearance after failure

Digital pictures and sketches as in Figure 2 were taken of the samples after failure in Brazilian tests. Typically, a neat fracture splits the samples into two parts. Sometimes, wedges are formed at the loading point but sometimes passing-trough fractures ramify and sub-parallel cracks develop.

Table 4. Summary of the average results of Mode I fracture toughness (K_{IC}), fracture normal stiffness (K_{NL}^{A}) and Mode II fracture toughness (K_{IIC}) obtained for the Toki granite samples from borehole MIU-2 (Shobasama).

Depth [mabh]	K_{IC} [MPa m$^{0.5}$]	K_{NL}^{A} [1] [GPa/m]	K_{IIC} [2] [MPa m$^{0.5}$]	K_{IIC} [3] [MPa m$^{0.5}$]
200	2.39	853	3.10	11.35
500	2.37	745	3.69	11.84
950	1.73	720	3.07	11.24

[1] For normal stress between 4 and 10 MPa;
[2] For confining pressure of 0 MPa;
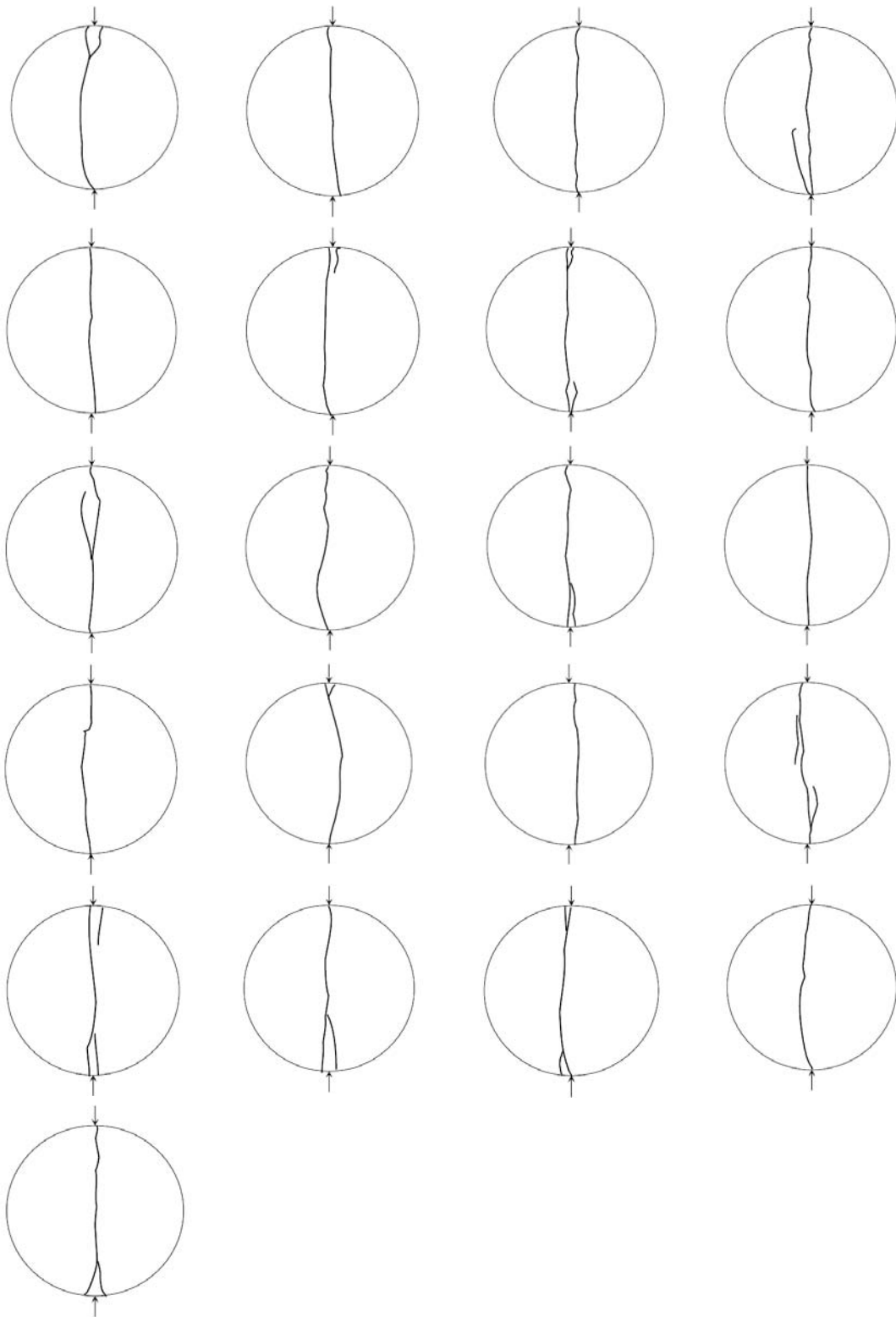[3] For confining pressure of 30 MPa.

Figure 2. Sketches of tested samples from borehole MIZ-1 (between 516.14 and 1021.40 m along the borehole) showing split in Brazilian tests.

3 FRACOD²ᴰ

FRACOD²ᴰ is a Windows based program that simulates the fracture initiation and propagation in an elastic and isotropic medium [22], [23]. To achieve this, the boundary element method called Displacement Discontinuity Method (DDM) are used. The code features the initiation of newly created fractures or the propagation of pre-existing fractures in a continuous medium in plane strain conditions. Although microcracking cannot be directly simulated, the code can simulate the process that takes place when microcrack coalescence develops into meso- and macro-scale fracture propagation.

3.1 Displacement Discontinuity Method

The DDM method is based on the stresses and displacements caused by a discontinuity with constant displacement in an infinite continuum and homogeneous elastic body. The discontinuity is assumed to be a linear segment and the displacements in the elastic body are continuous everywhere except over the linear segment where they differ for a constant value. The analytical solution of this problem was obtained by Crouch[24] and Crouch and Starfield[25]. When the stresses and displacements are caused by several discontinuities, the principle of superposition applies:

$$\left.\begin{aligned}
\{\sigma^i\} &= \left[\sum_{j=1}^{N} A^{ij}\right]\{D^j\} \\
\{u^i\} &= \left[\sum_{j=1}^{N} B^{ij}\right]\{D^j\}
\end{aligned}\right\} \text{ for i, j = 1 to N} \tag{1}$$

where $\{\sigma^i\}$ contains the shear and normal stresses, $\{u^i\}$ contains the shear and normal displacements and $\{D^j\}$ contains the elemental displacement components acting on each discontinuity segment; A^{ij} and B^{ij} are the boundary influence coefficients for stress and displacement, respectively. The expressions represent two systems of 2N simultaneous linear equations with 2N unknown. Additional constrains to the equations can be added in case:

- The i-th discontinuity is open and no stresses can be transmitted through it: the shear and normal stress components σ_s^i and σ_n^i of $\{\sigma^i\}$ are all zero;

- The i-th discontinuity behaves elastically: the stress components and the displacement components D_s^i and D_n^i are proportional through the shear and normal stiffness component K_s^i and K_n^i according to the Hook's law:

$$\begin{aligned}
\sigma_s^i &= K_s^i D_s^i \\
\sigma_n^i &= K_n^i D_n^i
\end{aligned} \tag{2}$$

- The i-th discontinuity is in failure conditions or sliding after failure: when adopting the Coulomb's failure criterion, for a compressive stress σ_n^i, we can write:

$$\left|\sigma_s^i\right| \geq c + \left|\sigma_n^i\right|\tan\phi \tag{3}$$

where the cohesion becomes zero after sliding of the fracture.

3.2 Crack initiation

The assumed continuum body is of course flawless and homogeneous. However, cracks might be initiated in the model when either the tensional or shear failure criterion is exceeded:

- In tension (Mode I), a fracture will generate perpendicularly to the orientation of the tensile stress σ that induces failure according to:

$$\sigma \geq \sigma_t \qquad (4)$$

  where σ_t is the tensile strength of the material;

- In shear (Mode II), two conjugated fractures will be symmetrically formed at an angle θ with respect to the direction of the minimum principal stress:

$$\theta = \phi / 2 + \pi / 2 \qquad (5)$$

  when the shear stress exceeds the Coulomb's failure criterion of the material.

The length of the newly formed cracks can be either assigned or determined by the spacing of the point grid where fracture initiation can be detected in the model. For dense point grids, even fracture initiation at the boundaries of the model or associated with existent fractures can be simulated. In this way, the inaccurate stress concentrations often predicted by the DDM methods close to the boundaries can be overcome. Stress concentrations at the tips of pre-existent fractures are modelled according to the fracture propagation criterion and do not necessarily give rise to crack initiation in tension.

3.3 Fracture propagation

Traditional criteria for fracture propagation usually consider tension (Mode I) and shear (Mode II) propagation separately. Shen & Stephansson [26] proposed a fracture propagation criterion based on the superposition of the resultant strain energy rates $G_I(\theta)$ in Mode I and $G_{II}(\theta)$ in Mode II respectively normalised with respect to their critical values G_{Ic} and G_{IIc} obtained in laboratory. The strain energy rates vary in different directions θ around the tip of a fracture. The fracture will (eventually) propagate when the F-Criterion is reached:

$$F(\theta) = \frac{G_I(\theta)}{G_{Ic}} + \frac{G_{II}(\theta)}{G_{IIc}} \geq 1 \qquad (6)$$

In practice, most of the cases of propagation are in pure tension or pure shear. The F-Criterion, however, can predict cases where the Mode I and Mode II propagations might collaborate to induce failure in a mixed mode.

The stain energy in a linear elastic body can be determined by integrating the work of the normal and shear stress components associated with the normal and shear displacements at the boundaries, respectively. The energy W_i associated with the presence of a fracture in the elastic body is related to the stresses acting onto the fracture and to the fracture displacements. Since the far-field stresses $\{\sigma_{i,0}\}$ are related to zero fracture displacements, they do not contribute to the strain energy of the fracture that can be written as:

$$W_i = \frac{1}{2} a_i \left[\{\sigma_i - \sigma_{i,0}\} \right] \cdot \{D_i\} = W_i^I + W_i^{II} \qquad (7)$$

where a_i is the length of the fracture, W_i^I and W_i^{II} the energy in Mode I and II, respectively. In consequence of a grow Δa of the i-th fracture in the direction θ, the strain energy rate $G_i(\theta)$ associated with the fracture propagation can be calculated as:

$$G_i(\theta) = \frac{\partial W_i}{\partial a_i} \approx \frac{W_i(a_i + \Delta a) - W_i(a_i)}{\Delta a} = G_i^I(\theta) + G_i^{II}(\theta) \tag{8}$$

In this way, the strain energy rate in tension and shear can be individually determined for each direction of growth θ. These values can then be introduced in the expression of the F-Criterion to determine whether and in which direction the fracture is supposed to grow.

4 Numerical models

The DDM numerical models represent cylindrical samples of 35 mm diameter loaded along two diametrically opposed arcs of 20° width (Figure 3, a). The models consist of 60 circumferential elements and a grid of 33×33 points. The continuum medium (e.g. intact rock) is characterised by means of elasticity properties (Young's modulus and Poisson's ratio), tensile strength and Coulomb's failure criterion parameters (cohesion and friction angle). The initiated and propagating cracks are characterised by stiffness properties (normal and shear stiffness), deformability properties (initial and residual fracture aperture) and Coulomb's failure criterion parameters (cohesion and friction angle). The required properties in Table 5 are assigned partially based on the properties of the Toki granite and partially estimated based on analogous case studies (e.g. ref. 27); ref. 28)).

The Mode I crack initiation in the models is assumed to have a "random" generation when the ratio (ran) between the stress σ and the strength σ_m would exceed 90%. The cumulative frequency distribution is assigned as follows:

$$p = \frac{1}{(1 - ran)^2} \left[\frac{\sigma}{\sigma_m} - ran \right]^2 \text{ for } ran \leq \frac{\sigma}{\sigma_m} \leq 1 \tag{9}$$

The cumulative frequency distribution is zero for a stress ratio smaller than ran, and unitary for a stress ratio larger than 1. In this way, the models take into account some heterogeneity of the continuous elastic body.

Table 5. Material properties used for modelling of Brazilian tests by FRACOD^{2D}.

Material	Parameters	Values
Intact rock	Poisson's ratio	0.33
	Young's modulus	50 GPa
	Friction angle	50°
	Cohesion	30 MPa
	Tensile strength	6 MPa
	Mode I fracture toughness	2 MPa m$^{0.5}$
	Mode II fracture toughness	11.5 MPa m$^{0.5}$
Initiated and propagating fractures	Shear stiffness	20 GPa/m
	Normal stiffness	500 GPa/m
	Friction angle	32°
	Dilation angle	0°
	Cohesion before sliding	10 MPa
	Cohesion after sliding	0 MPa
	Initial aperture	10^{-2} mm
	Residual aperture	10^{-3} mm

4.1 Boundary conditions

The load applied onto the sample (F) is considered distributed along an arc of angular width α of 20°. Since frictional effects might develop in laboratory at the contact between the loading platens and the core sample, three different sets of boundary conditions were considered (Figure 3): a) negative friction due to stiff platens inhibiting the deformation of the rock; b) positive friction due to deformable platens enhancing the deformation of the rock and; c) no friction between the platens and the rock.

In the model, the frictional forces are assumed to linearly increase in magnitude departing from the symmetry axis. Not knowing the actual entity of such frictional forces, the maximum magnitude of the applied frictional stress was chosen to be at most 1/5 of the applied normal stress.
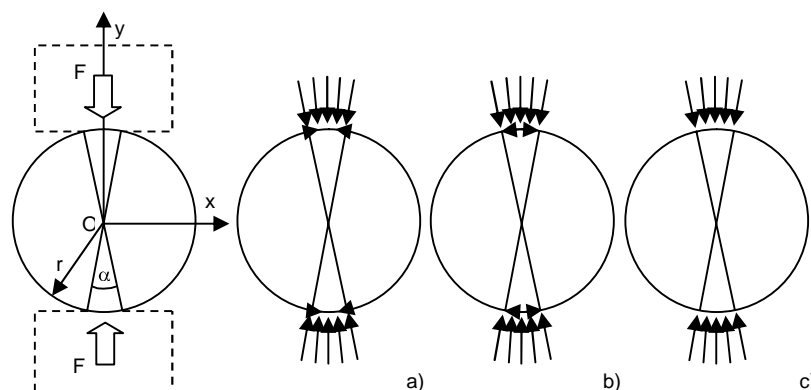

Figure 3. Geometry of the FRACOD^{2D} models (left) and applied boundary conditions (right): a) negative friction between platens and rock; b) positive friction between platens and rock; c) no friction between platens and rock.

4.2 Crack initiation element size

Although the program is designed to simulate propagation of meso- and macro-fractures, the very small size of the model makes it possible to reproduce the initiation and propagation of relatively small cracks at the border with microcrack size. In the present modelling, two sizes of the crack-initiation element were considered to study the sensitivity of the output to this parameter: element sizes of 3 and 1.5 mm. These sizes correspond to about 9% and 4% of the model diameter, respectively.

4.3 Modelling results

The models listed in Table 6 were analysed to obtain the effect of the boundary loading, element size and dilation angle on the numerical results.

Table 6. Overview of the performed numerical modelling by FRACOD^{2D}.

Model	Element size [mm]	Boundary conditions	Comments
K2	3	Negative friction	
K3	3	Positive friction	
K4	3	No friction	
H2	1.5	Negative friction	
H3	1.5	Positive friction	
H4	1.5	No friction	
K3D10	3	Positive friction	Dilation 10°

4.3.1 Validation against the theoretical solution at low stress level

An analytical solution is available for the calculation of the horizontal stress σ_θ and vertical stress σ_r in a cylinder vertically loaded along the vertical diameter (Hondros, 1959). In plain stress conditions, at the centre of the specimen, the theoretical horizontal tensile stress can be calculated as:

$$\sigma_\theta = \frac{F}{\pi \, r \, t}\left(\frac{\sin\alpha}{\alpha/2} - 1\right) \qquad (\,10\,)$$

where r is the radius of the sample and t the thickness, respectively. The vertical compressive stress in the centre of the cylinder is three times larger than the horizontal tensile stress.

In Figure 4, the theoretical values of the stresses are compared to the numerical results obtained by FRACOD[2D]. A total load of 127,215 N (per metre of thickness) is applied to the model with negative friction and element size 3 mm (K2). The comparison, which is very satisfying even thought the model is in plane strain conditions, is done for a low magnitude of the applied load that guarantees that crack initiation and propagation have not occurred in such extent to affect the stress distribution in the sample. The discrepancies approaching the boundaries are typical of all BEM models.
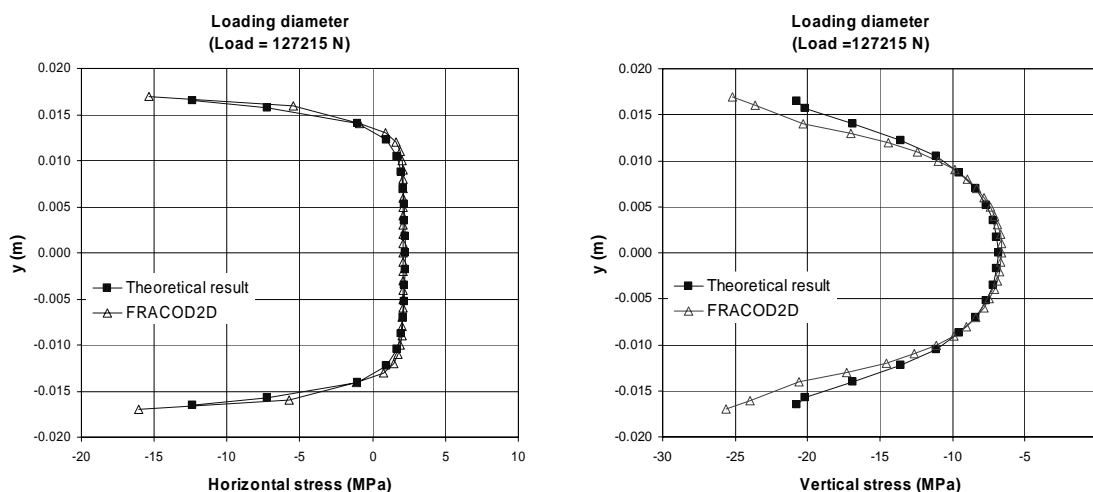

Figure 4. Comparison between the theoretical and numerical stresses in Brazilian test sample along the vertical loading diameter (x = 0). The graphs refer to a total vertical load of 127,215 N acting on the model with negative friction and element size 3 mm (K2). The horizontal stress component (left) and the vertical stress component (right) are presented. (Tensile stresses are positive.)

As also theoretically shown by Lavrov & Vervoort [4], the stress distribution inside the samples under Brazilian loading is only marginally affected by the effect of the frictional conditions at the boundary. In fact, Figure 4 shows that even the model with negative friction on the loaded arcs presents stress distributions very close to the theoretical stresses calculated according to the closed-form solution.

4.3.2 Stress distribution during loading

As shown is Section 4.3.1, the stress distribution inside the model initially follows very well the theoretically predicted stresses. However, when the average tensile stress in horizontal direction reaches the value of the tensile strength assigned to the rock material, some cracks will be initiated. As a consequence, the stress distribution inside the model changes dramatically (Figure 5, right); at the position of the initiated cracks, the tensile stress drops to zero, while at the bridges between the cracks, the tensile stress rises to values even higher than the tensile strength of the rock

material. This can be explained by the fact that at the tip of the newly initiated cracks, stress concentrations and strong stress gradients occur, which can be born although the input macroscopic strength (i.e. the direct tensile strength of the rock) is exceeded. On the other hand, the vertical stress seems to be only slightly affected by the initiation of the cracks and maintains a distribution similar to the theoretical solution (Figure 5, left).

The model also allows observing the variation of the vertical and horizontal stress along the horizontal diameter (Figure 6). The smooth distributions observed for low loads change into more ragged distributions after the crack initiation. The effect of fracture initiation is that the area with high vertical stresses (compression) tends to broaden, while the area with high horizontal stresses (tension) tends to narrow. Thus, it seems that the crack initiation and propagation induce a concentration of the stresses towards the centre leaving the rest of the model almost unloaded.
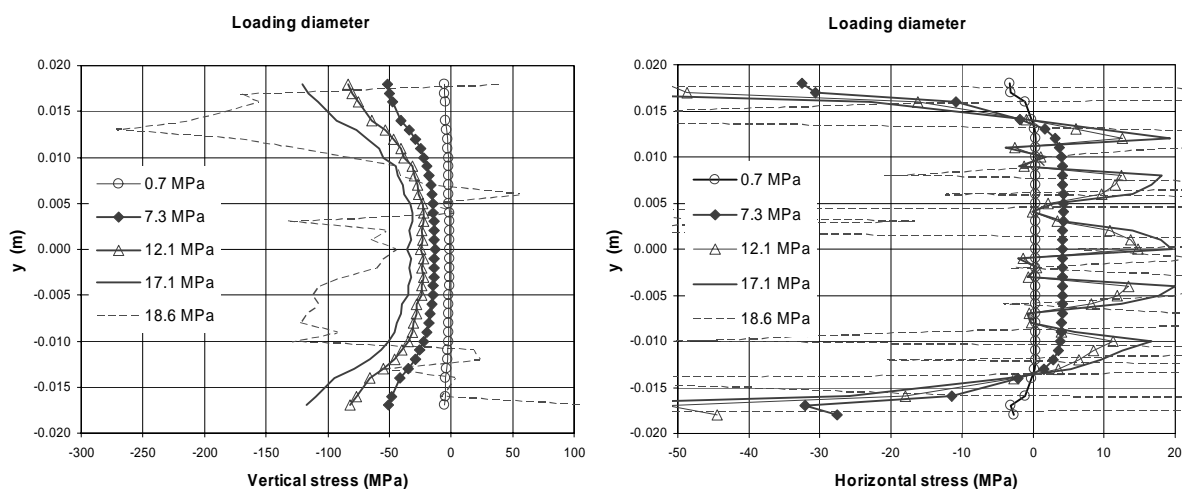
Figure 5. Variation of the vertical stress component (left) and on the horizontal stress component (right) along the vertical diameter of the FRACOD^{2D} model (x = 0) during loading. In the legend, the average vertical stress along the horizontal diameter of the model indicates the level of loading. The graphs refer to the model with negative friction and element size 3 mm (K2). (Tensile stresses are positive.)

Figure 6. Variation of the vertical stress (left) and horizontal stress (right) along the horizontal diameter of the FRACOD^{2D} model (y = 0) during loading. In the legend, the average vertical stress along the horizontal diameter indicates the level of loading. The graphs refer to the model with negative friction and element size 3 mm (K2). (Tensile stresses are positive.)
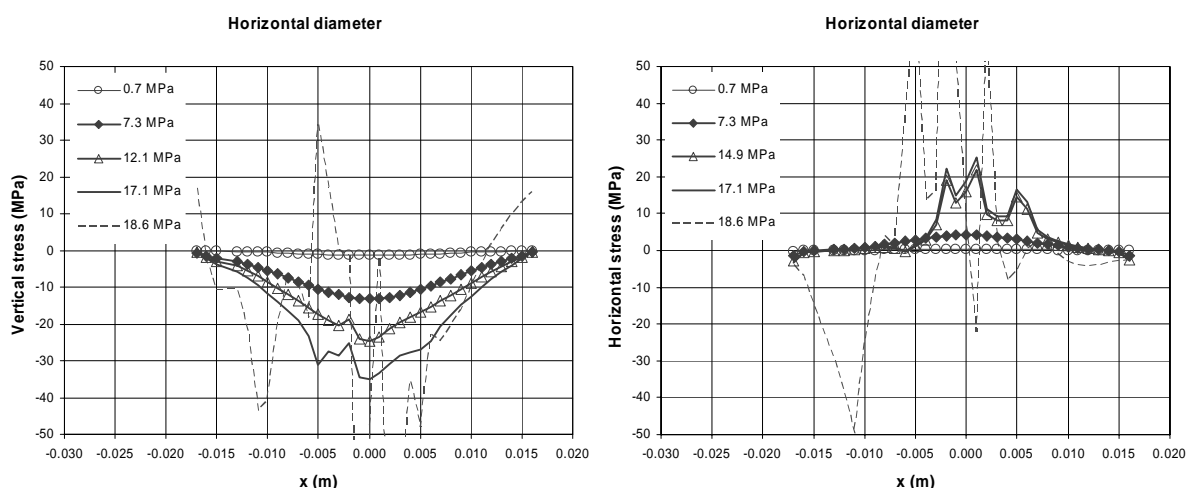
4.3.3 Stress-path

Figure 7 shows the stress-path experienced by points at the centre of the model. In the same graph, the variation of the average stresses along the loading diameter of the model is plotted together with the stresses in the centre of the model predicted by the theoretical solution by Hondros [3]. The following comments can be done about this plot:

- Local tensile failure (i.e. sub-vertical cracks) occurs in the model in an early stage of loading;

- Global failure seems to be induced by shearing of the bridges between the tensile cracks (i.e. the Coulomb's Criterion is reached);

- Average stresses along the loading diameter are low compared to local stresses induced by the cracks;

- Theoretical stresses differ significantly from the stresses numerically calculated, thus, they can unlikely describe the same failure mechanism.
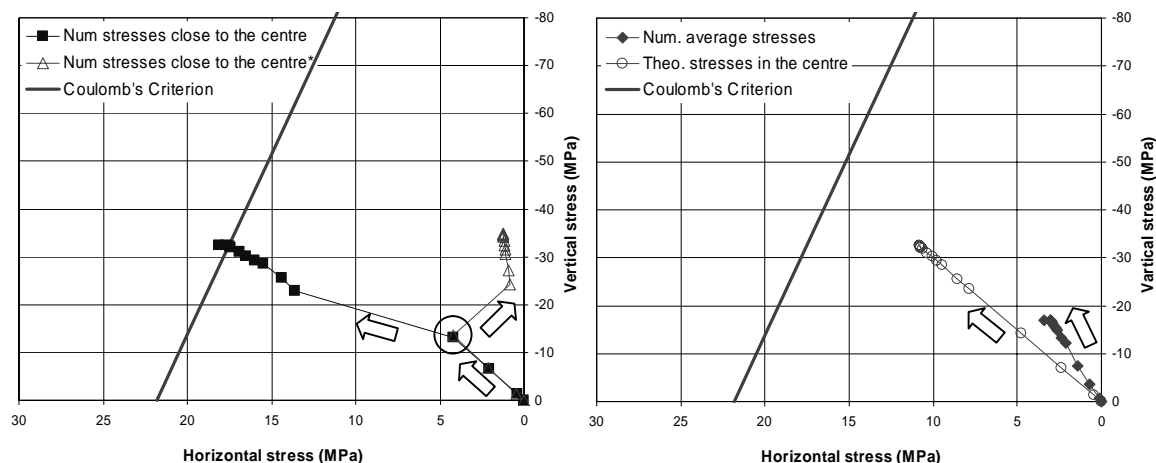

Figure 7. Stress-paths monitored in the FRACOD^{2D} model compared to the Coulomb's criterion for the rock material. On the left, stresses at two points close to the centre of the model (one marked with *): due to the initiated cracks, stresses in the model are not uniform. The circle indicates the crack initiation. On the right, average numerical stresses along the loading diameter and theoretical stresses in the centre calculated according to Hondros' solution based on the total load. Shear stresses along the vertical diameter are negligible. The graphs refer to the model with positive friction and element size 3 mm (K3).

4.3.4 Deformations

Stresses and displacements can be monitored inside the models during loading. In Figure 8 (left), the tensile stress at the centre of the models is plotted against the relative displacement of the loading platens. It can be observed that, until the tensile strength of the rock is approached, the theoretical solution by Hondros [3] is closely followed. On the contrary, as soon as some crack initiation occurs, stresses depart from the theoretical solution and can increase or decrease depending on the position of the monitoring point with respect to the tips of the cracks.

The stresses are plotted in Figure 8 (right) as a function of the change in length of the horizontal diameter of the model. The stress appears to increase non-linearly with increasing diameter length. This is an interesting effect since the rock material model is linear elastic and all the non-linear effects have to be ascribed to the geometry and behaviour of the cracks.

It can also be noticed that, although the tensile strength of the rock material was assigned to be 6 MPa, the model predicts a tensile strength of the samples around 11 MPa.
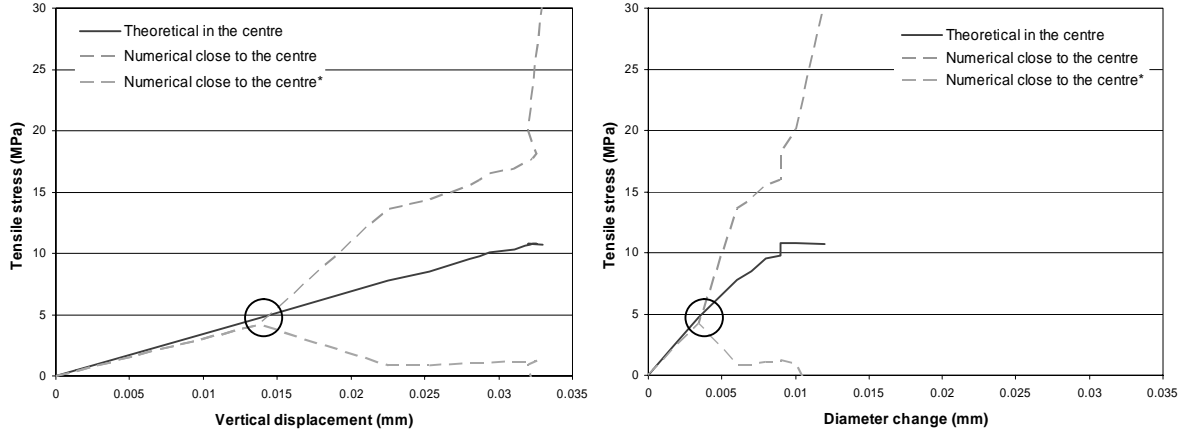

Figure 8. Horizontal tensile stress in the centre of the FRACOD^{2D} model versus the vertical displacement between the loading platens (left) and the diameter change in horizontal direction (right). The theoretical tensile stress is calculated according to Hondros' solution based on the total numerical load, this explains some slight irregularity close to failure. The circles indicate the crack initiation. The graphs refer to the model with positive friction and element size 3 mm (K3).

Hondros [3] also gives the expressions for calculating the Young's modulus (E) and Poisson's radio (ν) of the material in plane strain when the horizontal (ε_x) and vertical (ε_y) strains at the centre of the samples are monitored during Brazilian testing:

$$E = -\frac{3\,F\left(1-\nu^2\right)}{\pi\,r\,t\left(\varepsilon_y + \nu\varepsilon_x\right)}$$ (11)

and

$$\nu = -\frac{3\,\varepsilon_x + \varepsilon_y}{2\left(\varepsilon_y - \varepsilon_x\right)}$$ (12)

When extracting the values of the strains numerically obtained, the graphs in Figure 9 are obtained. These graphs show that the equivalent Young's modulus and Poisson's ratio determined based on the numerical strains are lower than the input values (50 GPa and 0.33, respectively). Moreover, the Young's modulus diminishes during loading while the Poisson's ratio generally increases with increasing vertical displacements.
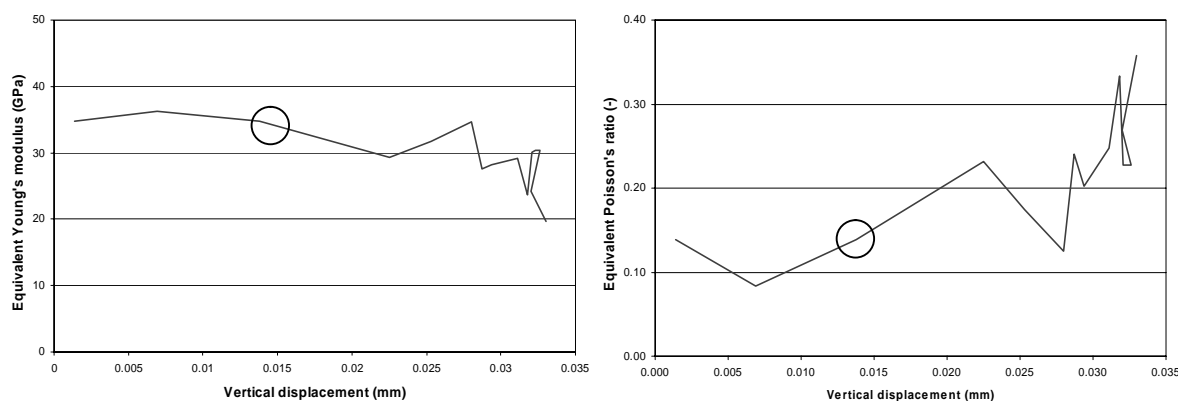
Figure 9. Equivalent Young's modulus (left) and Poisson's ratio (right) versus the vertical displacement between the loading platens from FRACOD^{2D} simulations. The circle indicates the crack initiation. The graphs refer to the model with positive friction and element size 3 mm (K3).

4.3.5 Effect of the boundary conditions

Friction was simulated at the contact between the platens and the samples. Negative and positive friction was considered, which means that the shear forces were assumed to depart from or converge toward the symmetry axis, respectively. The magnitude of the applied shear forces was assumed to decrease linearly to zero when approaching the symmetry axis.

In Figure 10, the effect of negative (K2), positive (K3) and no (K4) friction on the crack pattern during loading is shown. Weather or not there is friction at the contact between the platens and the samples, this does not seem to affect the position of the initiated cracks. On the other hand, the crack pattern at failure is influenced by friction that makes the cracks more irregular especially approaching the loading surfaces.

It can be noticed that, although the model and the boundary conditions are symmetrical, the crack patterns are not. This is probably due to the randomness of the criterion that determines where the crack initiation has to occur for stresses lower than the assigned tensile strength of the rock material (see Sec. 3.2 and 4).

The boundary conditions also drastically affect the strength of the simulated Brazilian test results. Negative and positive friction seems to have the same effect on the strength whereas the model with no boundary friction exhibited a much higher strength, although the stiffness was the same as for the other cases. Figure 11 shows the value of the theoretical tensile stress in the centre according to Hondros' solution where the total vertical load from the FRACOD^{2D} model is used as input. The displacements in the same figure were numerically determined.
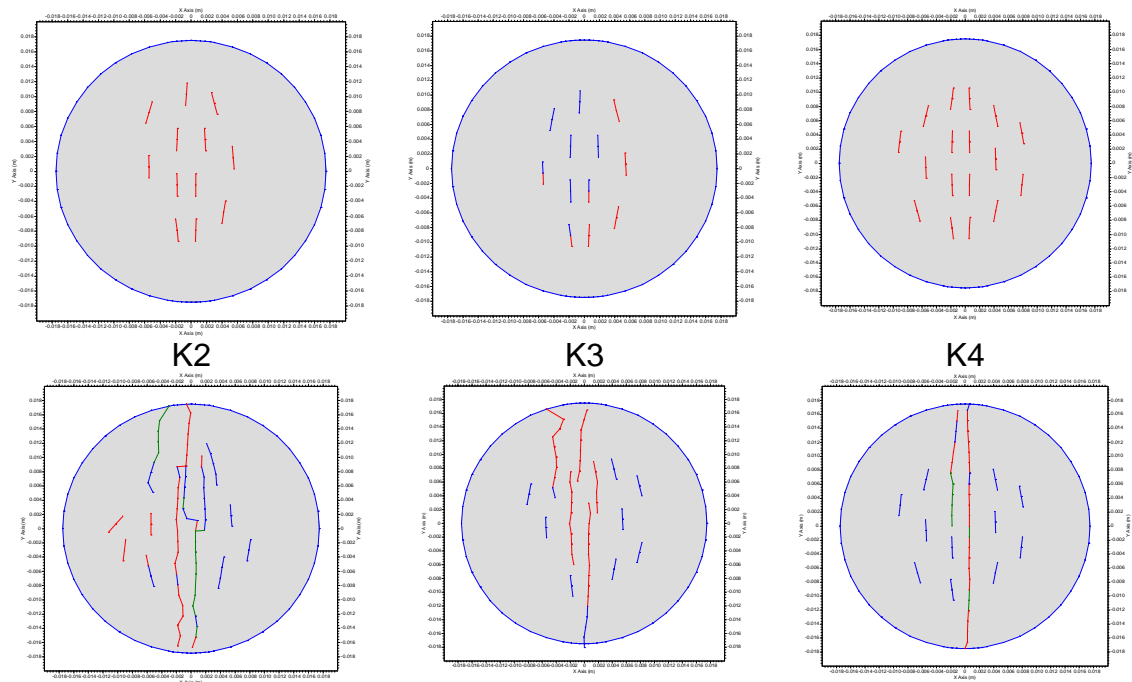
Figure 10. Shape of the initiated cracks (above) and of the crack pattern at failure (below) for the FRACOD^{2D} models K2 (with negative friction), K3 (with positive friction) and K4 (no friction), with element size 3 mm. Cracks coloured in red are in tension, in green are in shear and in blue are in elastic conditions, respectively.
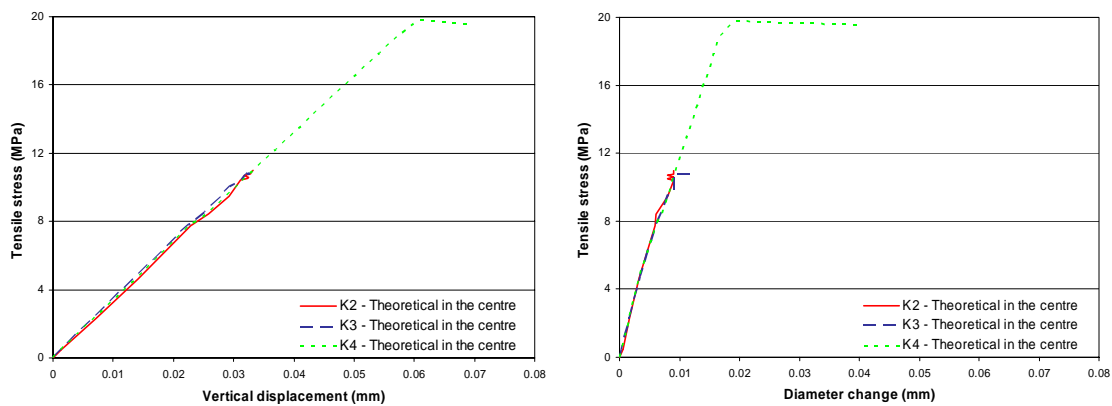
Figure 11. Effect of the boundary conditions on the tensile stress in the centre of the model. The theoretical stresses are calculated based on Hondros' analytical solution (1959) using the total load applied to the FRACOD^{2D} model. On the left, variation of the stress with the vertical displacement between the loading platens. On the right, variation of the stress with the diameter change in horizontal direction. The results are for model K2 (with negative friction), K3 (with positive friction) and K4 (no friction), with element size 3 mm.

4.3.6   Effect of the dilation

Dilation was found not to affect the numerical results because shearing of the cracks did not occur other than at the very last moment when bridges between the tensile cracks fail in shear. Therefore, the effects of dilation, such as increased horizontal stains or stiffening of the model during loading, were not observed. Model K3 (without dilation) and K3D10 (with dilation of 10°) gave exactly the same results.

4.3.7 Effects of the element size

FRACOD^{2D} is a BEM-DDM code suitable for simulation of meso- and macro-cracks rather than micro-cracks. In fact, the crack patterns for crack element size of 3 mm in Figure 10 appear to be more realistic than those for crack element size of 1.5 mm in Figure 12. This indicates that an optimization of the crack element size to match the fracture pattern experimentally obtained may be required.
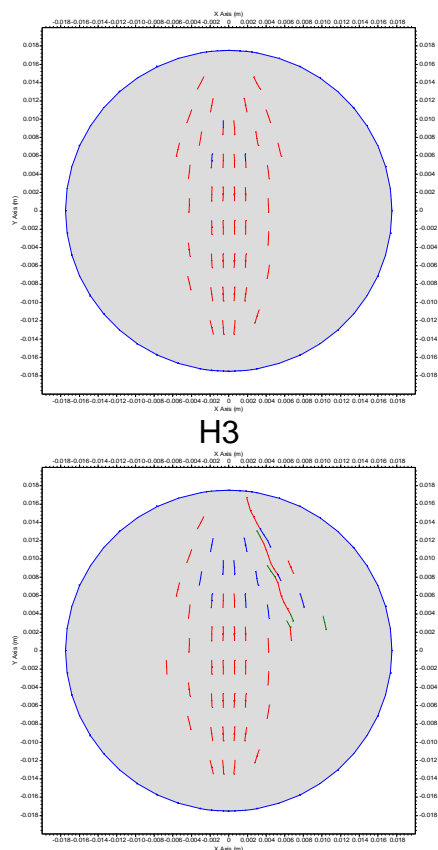
Figure 12. Shape of the initiated cracks (above) and crack pattern at failure (below) for the FRACOD^{2D} model with element size 1.5 mm and positive friction at the boundaries (H3). Please compare with model K3 with element size 3 mm in Figure 10.

5 Discussion

The modelling presented in this contribution shows that the stress distribution in the samples during Brazilian testing might not be as uniform as assumed when applying the closed-form solution by Hondros [3]. Despite this, this formula is usually used in engineering practice to obtain the tensile strength from Brazilian testing results.

If flaws exist or new cracks develop, the distribution of the stresses perpendicular to the loading direction becomes very ragged. High stress gradients develop at the tip of the flaws and cracks and the tensile stress can increase beyond the macroscopic tensile strength of the material. As result of this, the models exhibit failure loads that correspond to tensile strengths between 1.8 and 3 times larger than the input macroscopic tensile strength of the intact rock.

FRACOD^{2D} adopts the Coulomb's failure criterion for the intact rock and fractures. This criterion only takes into account the stress components acting on the section of the model. However, in plane strain conditions, an out-of-plane stress component actually exists and can be calculated as:

$$\sigma_z = \frac{\nu E}{(1+\nu)(1-2\nu)}(\varepsilon_x + \varepsilon_y)$$
(13)

For example, the out-of-plane stress at the centre of the model with negative friction and element size 3 mm (K3) can be determined based on the strains (Figure 13, left). For a vertical displacement of 0.031 mm, the out-of-plane stress at failure is -9.9 MPa which is accompanied, in the centre of the model, by a vertical and horizontal stress of -31.0 MPa and 16.9 MPa, respectively (positive stresses are tensile). These stresses are shown in Figure 13 (right).

If a true triaxial failure criterion is assumed, the same stress condition would not lead to failure. For example, the Matsuoka-Nakai's failure criterion [29] for an isotropic material in terms of principal stress components σ_1, σ_2 and σ_3:

$$\frac{(\sigma_1 - \sigma_2)^2}{(c + \sigma_1 \tan\varphi)(c + \sigma_2 \tan\varphi)} + \frac{(\sigma_2 - \sigma_3)^2}{(c + \sigma_2 \tan\varphi)(c + \sigma_3 \tan\varphi)} +$$
$$+ \frac{(\sigma_1 - \sigma_3)^2}{(c + \sigma_1 \tan\varphi)(c + \sigma_3 \tan\varphi)} = 8$$
(14)

provides stresses at failure that are larger than those obtained from the biaxial Coulomb's criterion for the same cohesion, friction angle and out-of plane stress.
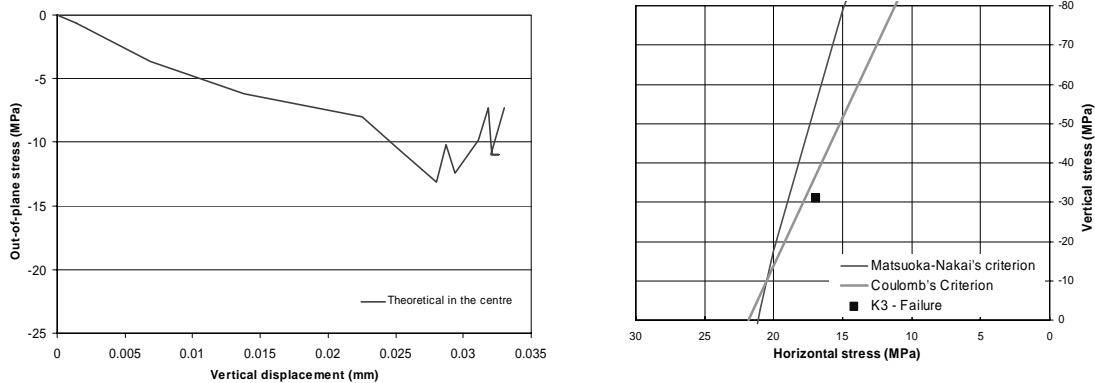
Figure 13. On the left, out-of-plane stress in the centre of the model versus the vertical displacement between the loading platens. The stress is calculated for plane strain conditions. On the right, the stresses at failure compared to the Coulomb's and the Matsuoka-Nakai's Criterion for an intermediate stress of -9.9 MPa. The graphs refer to the model with positive friction and element size 3 mm (K3).

The numerical FRACOD[2D] models seem to be capable of predicting the non-linear behaviour induced by the crack initiation. The stress calculated in the centre of the samples with the closed-form solution (theoretical) for the applied loads can be plotted against the diameter change in the direction perpendicular to loading as in Figure 14. This figure shows that it might be possible to estimate the input macroscopic tensile strength of the intact rock material by studying the point in which the curve departs from linearity.

Figure 14. Theoretical tensile stress in the centre of the model versus the diameter change in horizontal direction. An estimation of the tensile strength of the material can be given by the point at which the theoretical tensile stress in the centre departs from linearity. The graph refers to the model with positive friction and element size 3 mm (K3).

In case of a heterogeneous material, the point of deviation from linearity in Figure 14 would probably indicate the strength of the weakest mineral in the rock. Ganne & Vervoort [8] show that intra-grain damage in 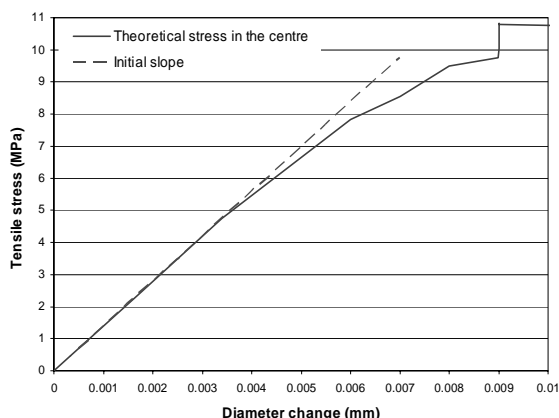tension preferentially occurs or follows pre-existent cleavage planes and flaws. Moreover, Van de Steen et al.[12] also observed that such flaws are activated in early loading stages and greatly affect the stress distribution inside the samples. Okubo & Fukui [30] sustain the hypothesis of progressive tensile failure where the strength is mobilized in different parts of the samples as the load increases even in uniaxial tension tests. They also observed that homogenous materials will exhibit more sudden development of extensive cracks because they lack the possibility of mobilizing the tensile strength in different points as loading proceeds.

The comparison between the numerically obtained crack patterns at failure agree rather well with the shape of the failure fractures observed from laboratory Brazilian testing. Figure 2 and Figure 10 show that the difference mainly consists in the short initiated cracks that cannot be seen, or might not be visible, in the laboratory samples.

In addition, the results of the simulations presented here have limitations that mainly originate from the fact that:

- The rock samples in Brazilian testing are not loaded in perfectly plane strain conditions as in the numerical models since the prescribed ratio between thickness and diameter of the samples generally should be about 0.5 [1] or chosen between 0.5 and 1.0 [2]. However, even the applicability of Eq. (10) in the two standards might be questioned because this equation is derived in plane stress conditions. The indirect tensile strength in the two cases would be underestimated between 10% and 20% (see ref. 11));

- The rock samples might show initiated or pre-existent cracks in different positions in the out-of-plane direction that might affect the pattern of the failure surfaces;

- The criterion for crack initiation in the simulations applies for pure tensional conditions, while Brazilian testing induces compressive confinement perpendicularly to the tensile loading direction;

- The presence of strong stress gradients associated with initiated or pre-existing cracks and flaws influence the sample behaviour in different ways depending on the position, dimension and shape of these flaws;

- The presence of pre-existent flaws and cracks might affect the deformability of the samples from the beginning of the loading in a Brazilian test so that the equation usually applied in practice for obtaining the macroscopic tensile strength of the rock might not be applicable. This is most likely the reason for the large variability in tensile strength obtained from Brazilian testing of the same material.

6 Conclusions

The numerical modelling in this contribution shows that the formula for calculating the indirect tensile strength from the failure load of the Brazilian test might not be applicable for rocks containing crystals with different strength, flaws and cracks. Firstly, the theoretical closed-form solution does not consider the fact that pre-existing or newly initiated flaws and cracks affect the stress distribution in the samples to such extent that it violates the hypothesis of continuity and homogeneity of the material. This can be observed when comparing the average stresses along the loading diameter and the stresses in the centre of the model in Figure 7. The difference between the average stresses and the stresses at the centre can be large; therefore, it is less likely that the sample would break when tensile strength is reached around its centre. Secondly, the closed-form solution assumes that failure occurs in pure tension. On the contrary, the numerical simulations show that the failure mechanism might occur in tension and shear, as also reported in previous studies (e.g. Van de Steen et al., 2005). In fact, the cracks developing at the centre of the model change stress state from confined tensile conditions into a pattern of stress concentrations at the bridges between the tensile cracks. Finally, the sample fails when the shear and/or tensile strength of these bridges is overcome.

Laboratory results of uniaxial tension testing (e.g. ref. 31); 30)) report that microcracking might occur in an early loading stage but macroscopic fractures only develop approaching the peak strength or even in the post-failure region. These tensile features could also be observed in the presented numerical models, although visual observations on laboratory samples might be difficult.

Figure 7 shows that the tensile stress predicted by the closed-form solution at the centre of a sample might be twice as high as the average stresses in a sample affected by cracking. This figure also shows that the value of the tensile stress is only marginally related to the tensile strength assigned to the intact rock material. For this reason, the indirect tensile strength calculated from Brazilian tests might be largely overestimated. For extreme cases, the tensile strength of the material could have no correlation with the result of the Brazilian tests. This is probably the case of materials with relatively high tensile strength.

Results presented in Figure 14 offer a way of predicting the macroscopic tensile strength of the material by studying the point at which the crack initiation starts inducing non-linearity on the plot of the theoretical tensile stress in the centre against the diameter change in the direction perpendicular to loading. In a rock material composed by minerals with different strength, the value of the input macroscopic tensile strength would probably only mirror the strength of the weakest mineral grains.

Additional Brazilian tests on samples of Toki granite are planned where the diameter change will be measured under strain controlled loading with the aim to determine the input macroscopic tensile strength according to the method of onset of non-linearity proposed here.

7 Acknowledgments

8 References

1) ISRM : Suggested methods for determining tensile strength of rock materials, International Society for Rock Mechanics, Int. J. Rock Mech. Min. Sci. & Geomech. Abstr., Vol. 15, p. 99-103, 1978.

2) JGS : Method for splitting tensile strength test on rocks, Designation JGS 2551-2002, the Japanese Geotechnical Society, 2002.

3) Hondros, G. : The evaluation of Poisson's ratio and the modulus of materials of a low tensile resistance by Brazilian (indirect tensile) test with particular reference to concrete, Aust. J. Appl. Sci., Vol. 10, p. 243-268, 1959.

4) Lavrov A., Vervoort A. : Theoretical treatment of tangential loading effects on Brazilian test stress distribution, Int. J. Rock Mech. Min. Sci., Vol. 39, p. 275-283, 2002

5) Cai M, Kaiser P.K. : Numerical simulations of the Brazilian test and tensile strength of anisotropic rocks and rocks with pre-existing cracks, Int. J. Rock Mech. Min. Sci., Vol. 41, Proc. SINOROCK2004 Symposium, Paper 2B 03, 2004.

6) Potyondy D.O., Cundall P.A. : A bounded-particle model for rock, Int. J. Rock Mech. Min. Sci. & Geomech. Abstr., Vol. 41, p. 1329-1364, 2004.

7) Zhu W.C., Tang C.A. : Numerical simulation of Brazilian disk rock failure under static and dynamic loading, Int. J. Rock Mech. & Min Sci., Vol. 43, p. 236-252, 2006.

8) Ganne P., Vervoort A. : Characterisation of tensile damage in rock samples induced by different stress paths, Pure Appl. Geophys., Vol. 163, p. 2153-2170, 2006.

.9) Claesson J., Bohloli B. : Brazilian test: stress field and tensile strength of anisotropic rocks using an analytical solution, Int. J. Rock Mech. Min. Sci., Vol. 39, p. 991-1004, 2002.

10) Wang Q.Z., Jia X.M., Kou S.Q., Zhang Z.X., Lindqvist P.-A. : The flattened Brazilian disc specimen used for testing elastic modulus, tensile strength and fracture toughness of brittle rocks: analytical and numerical results, Int. J. Rock Mech. Min. Sci., Vol. 41, p. 245-253, 2004.

11) Yu Y., Yin J., Zhong Z. : Shape effects in the Brazilian tensile strength test and a 3D FEM correction, Int. J. Rock Mech. Min. Sci., Vol. 43, p. 623-627, 2005.

12) Van de Steen B., Vervoort A., Napier J.A.L. : Observed and simulated fracture pattern in diametrically loaded discs of rock material, Int. J. Fract., 131, p. 35-52, 2005.

13) Proveti J.R.C., Michot G. : The Brazilian test: a tool for measuring the toughness of a material and its brittle to ductile transition, Int. J. Frac., Vol. 139, p. 455-460, 2006.

14) Shen B., Stephansson O., Rinne M., 2002. Simulation of borehole breakouts using FRACOD. Oil and Gas Science and Technology, Vol. 57, p. 579-590.

15) Stephansson O., Shen B., Rinne M., Backers T., Koide K., Nakama S., Ishida T., Moro Y., Amemiya K. : Geomechanical evaluation and analysis of research shafts and galleries in MIU Project, Japan, Proc. Int. Symp. Underground Environ., Environmental Rock Engineering (Saito T. & Murata S. eds.), p. 39-45, 2003.

16) Shen B., Stephansson O., Rinne M., Lee, H.S., Jing L., Röshoff K. : A fracture propagation code and its applications to nuclear waste disposal, Int. J. Rock Mech. Min. Sci., Vol. 41, p. 448-449, 2004.

17) Nakama S., Nakajima T., Aoki T., Sato T. : The results of the rock mechanical properties of the Toki granite using core specimens from DH-2 borehole, Japan Nuclear Cycle Development Institute Technical report, JNC TN7400 2003-003 (in Japanese), p. 28, 2003.

18) Yamada A., Seno Y., Nakama S., Sato T. : The results of the rock mechanical investigations at borehole MIZ-1, Japan Atomic Energy Agency, JAEA- Research Report (in preparation), 2007.

19) Backers T. : Mode I and Mode II fracture toughness testing and fracture normal stiffness estimation of Tono-Granite, Technical Report Geoframes GmbH, Potsdam, Germany, p. 18, 2002.

20) Ouchterlony F. : International Society for Rock Mechanics, Suggested Methods for determining the fracture toughness of rock, Int. J. Rock Mech. Min. Sci. & Geomech. Abstr., Vol. 26, p.13-23, 1988.

21) Backers T., Stephansson O., Rybacki E. : Rock fracture toughness testing in Model II – Punch Through Shear Test, Int. J. Rock Mech. & Min. Sci., Vol 39, p. 755-769, 2002.

22) Shen, B. : Mechanics of fractures and intervening bridges in hard rocks, PhD Thesis, Royal Institute of Technology, Stockholm, Sweden, 1993.

23) FRACOM Ltd : FRACOD^{2D} – Two dimensional fracture propagation code (Version 2.2) – User's Manual, p. 82, 2006.

24) Crouch S.L. : Solution of plane elasticity problems by the displacement discontinuity method, Int. J. Num. Methods Engng., Vol. 10, p. 301-343, 1976.

25) Crouch S.L., Starfield A.M. : Boundary element methods in soil mechanics, George Allen & Unwin Ltd, London, UK, 1983.

26) Shen B., Stephansson O. : Modification of the G-criterion of crack propagation in compression, Int. J. Engng. Fracture Mech., Vol. 51(1), p. 73-85, 1993.

27) Lavrov, A., Vervoort, A., Wavers, M., Napier, J. A. L. : Experimental and numerical study of the Kaiser effect in cyclic Brazilian tests with disk rotation, Int. J. Rock Mech. & Min. Sci., Vol. 39, p. 287-302, 2002.

28) Stephansson O., Shen B., Rinne M. : The geomechanical evaluation and analysis of surrounding rock mass response to excavation of research shafts and galleries in MIU Project, FRACOM Ltd, p. 89, 2003.

29) Matsuoka H., Nakai T. : Stress-deformation and strength characteristics of soil under three different principal stresses, Proc. Japan Society of Civil Engineers, No. 232, p. 59-70, 1974.

30) Okubo S, Fukui K. : Complete stress-strain curves for various rock types in uniaxial tension, Int. J. Rock Mech. Min Sci. & Geomech. Abstr., Vol.33, p. 549-556, 2000.

31) Peng S.S. : A note on the fracture propagation and time-dependent behaviour of rocks in uniaxial tension, Int. J. Rock Mech. Min. Sci. & Geomech. Abstr., Vol. 12, p. 125-127, 1975.

This is a blank page.

-93-

6. Drilling induced damage of core samples: evidences from laboratory testing and numerical modelling (**Paper 4**)

This is a blank page.

Drilling induced damage of core samples: evidences from laboratory testing and numerical modelling

Flavio Lanaro

Japan Atomic Energy Agency

Abstract: Extensive sample testing in uniaxial and Brazilian test conditions were carried out for the Shobasama and MIU Research Laboratory Site (Gifu Pref., Japan). The compressive and tensile strength of the samples was observed to be negatively correlated to the in-situ stress components. Such correlation was interpreted as stress-release induced sample damage. Similar stress conditions were then numerically simulated by means of the BEM-DDM code FRACOD^{2D} in plane strain conditions. This method allows for explicitly consider the influence of newly initiated or propagating fractures on the stress field and deformation of the core during drilling process. The models show that already at moderate stress levels some fracturing of the core during drilling might occur leading to reduced laboratory strength of the samples. Sample damage maps were produced independently from the laboratory test results and from the numerical models and show good agreement with each other.

1 Introduction

The knowledge of the material properties of the intact rock (i.g. the rock inside blocks isolated by fractures) are often the key parameters for the design of underground facilities. Extensive laboratory campaigns are carried out to determine the uniaxial, triaxial and Brazilian strength of core samples. However, when samples are taken at large depth, the in-situ stress field is often characterised by large stress magnitudes and sometimes by a predominant horizontal stress component. This is particularly the case of the URL Underground Research Laboratory in Canada (Atomic Energy of Canada Ltd., AECL) and the MIU Underground Research Laboratory in Japan (Japan Atomic Energy Agency, JAEA) in hard crystalline rocks. Stresses can be high due of the tectonic regime or simply due to the great depth. When drilling in a highly stressed rock masses, the stress release induced by the drill bit might be so intensive to cause tensile stresses in the core or ahead of it, stresses that can irreversibly damage the core. Eberhardt et al.[1] reported that samples of the Lac du Bonnet granite taken from a depth of 430 m at URL (where the difference between the horizontal and the vertical in-situ stress was about 40 MPa), showed a uniaxial compressive strength on average 36% lower than for samples taken from a depth of 240 m (where the difference between the horizontal and the vertical in-situ stress was only about 10 MPa). Furthermore, samples from the deeper level exhibited five times more microcracks then shallower samples. Such sample disturbance was recognized to be induced by: i) forces and vibrations during drilling; ii) stress concentrations at the contact between drill bit and the rock and; iii) by stress relief inside the drilled core. Analogous cases of sample damage were also recently reported by Holt et al.[2] and Sakaguchi et al.[3]. Holt et al. added the following causes to the list of potential damage of the cores: iv) effects of pore pressure release and; v) in-situ and drilling induce temperature release.

Several attempts of modelling the process of core drilling for investigating the occurrence of core damage and core discing were performed for example by Li and Schmitt[4], Hakala[5], Kaga et al.[6] and Lim et al.[7]. Most of the modelling, although tri-dimensional, was carried out by means of finite element analyses of continuum media or focusing on the propagation of a single "disc" surface by means of a facture propagation code implementing the Displacement Extrapolation Technique. For this reason, the models could calculate the tensile stresses occurring at the base of the core stub but did not predict the fracture pattern inside the core and ahead of the drill bit. Since the occurrence of fracturing ahead of the core stub generates high tensile stresses at the tips of the

fractures, the continuous models might not provide realistic results in terms of tensile stresses or in predicting the core damage because they cannot take into account the actual fracture pattern.

In this study, a large amount of laboratory results (uniaxial and Brazilian tests) on samples of Toki granite from two adjacent sites investigated by JAEA (MIU and Shobasama site in Mizunami Municipality, Gifu Prefecture, Central Japan) were analysed. It was observed that, although the Toki granite is considered a rather homogeneous rock type, the laboratory strength has a rather wavy variation along the boreholes. This variation could be correlated to the variation of the stresses along the boreholes. Since the peaks of the strength corresponded to the section with lower stresses, it was concluded that the laboratory strength must be negatively correlated to the magnitude of the stresses and this could be explained as a result of stress-induced sample damage. Thus, the wavy variation of the laboratory strength of the samples probably did not reflect a variation of the in-situ rock strength but the variation of the in-situ stress field.

To prove the presence of sample damage at the level of stress measured in the boreholes, numerical analyses were carried out by means of the code FRACOD^{2D} implementing the Boundary Element Method-Discrete Discontinuity Method for modelling fracture initiation and propagation. One geometrical configuration was analysed considering different applied boundary stresses to determine the occurrence and pattern of the fractures.

Based on the estimation of the difference between laboratory and in-situ rock strength in uniaxial and Brazilian test conditions, a qualitative evaluation of the level of sample damage was attempted. In a similar way, the numerical results were also classified based on the level of damage estimated from the numerical fracture patterns in the models. Since the two approaches seem to agree with each other, the negative correlation between stresses and laboratory strength was confirmed.

2 Geology of the Sites

The Shobasama and the Mizunami Site are located in the Gifu Prefecture in Central Japan [8]. The Sites are just a few kilometres apart from each other and are characterized by very similar geological conditions. A Pliocene granite basement about 65 Ma old (Toki granite) is covered by Miocene sedimentary rocks dating from 20 to 1 Ma ago. The Toki granite basement presents a surface characterized by paleo-channels. Weathering is found in the bottom of the paleo-channels but tend to significantly decrease along the slopes of the basement. Below the weathered layer, the Toki granite seems to be affected by rather heavy fracturing down to a depth varying between 100 and 500 m. This rock mass volume is addressed as the Upper Highly Fractured Domain (about 1 to 5 fractures/m). Below this domain, the fracture frequency drops in what is called the Lower Sparsely Fractured Domain (typically less than 1 fracture/m). All the geological features described in this paper are in common for the two Sites.

3 Laboratory test results

Laboratory tests were carried out on the intact Toki granite for the determination of the physical (effective porosity, elastic wave velocity, density) and the mechanical properties (uniaxial compressive strength, triaxial compressive strength and Tensile Strength TS from Brazilian test). Samples were collected at rather uniform spacing along boreholes MIU-1 to 4 and AN-1 (Shobasama) and MIZ-1 and DH-2 (Mizunami) (Table 1). Hydro-fracturing methods were applied in four of the seven analyzed boreholes to determine the in-situ stress field.

Table 1. Borehole information, number of Uniaxial Compression Tests and Brazilian tests on core samples of intact Toki granite. The number of Hydro-Fracturing in-situ stress measurements for the analysed boreholes at the Shobasama and Mizunami Construction Site is also reported.

Borehole	Length [m]	Inclination [°]	No. of uniaxial tests	No. of Brazilian tests	No. of Hydro-Fracturing stress measurements
MIU-1	1011.80	Vertical	90	30	-
MIU-2	1012.00	Vertical	30	20	13
MIU-3	1014.00	Vertical	10	10	7
MIU-4	790.10	30° from vertical	30	30	-
AN-1	1010.20	Vertical	20	38	16
MIZ-1	1300.00	Vertical to 380 m, then inclined down to 1300 m	45	45	12
DH-2	501.00	Vertical	30	30	-

3.1 Strength

Core samples were regularly taken from the core of the boreholes and tested in laboratory under uniaxial compressive conditions and Brazilian testing.

3.1.1 Uniaxial compression tests

Uniaxial compression testing was performed on samples of Toki granite following the Japanese Geothecnical Society Standar[9]. When plotted against the distance from the top of the boreholes, the Uniaxial Compressive Strength of the samples varies seems to vary in almost cyclic way.
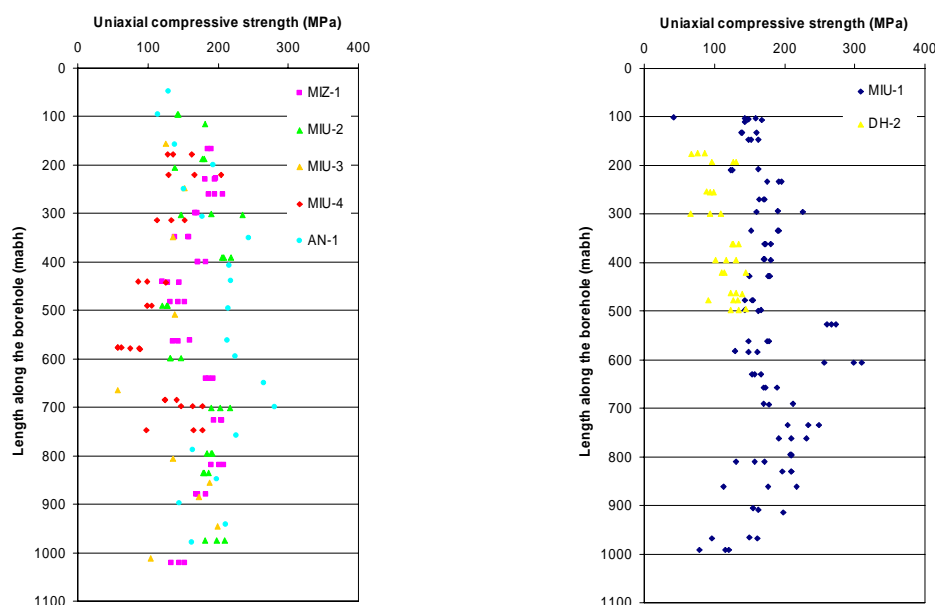

Figure 1. Plot of the uniaxial compressive strength of the Toki granite for samples taken from the boreholes at the Shobasama Site (left) and at the Mizunami Construction Site (right). Please notice that borehole MIU-4 and MIZ-1 are not vertical.

3.1.2 Brazilian tests

Brazilian testing was performed following the Japanese Geothecnical Society Standard (JGS 2521-2000[9] and JGS 2551-2002[10], respectively). Figure 2 shows the variation of the indirect tensile strength obtained for samples taken along the boreholes at Shobasama (left) and at the Mizunami Construction Site (right). The plots seem to indicate that the laboratory results for samples from both sites vary with depth in a rather wavy manner. Moreover, the waviness is not the same for all boreholes at the same site.

3.1.3 Quantification of the potential damage of the samples

It was inferred from analyses of the correlation between the strength (UCS and TS) of the samples and the in-situ stress levels [11],[12] that the observed waviness of the strength with depth might be due to the deterioration of the mechanical properties of the cores due to drilling in rock with high stresses. In fact, such oscillations of the strength could not be related to the presence of: i) different grain textures; ii) different degree of alteration, almost inexistent in the Lower Sparsely Fractured Domain, or; iii) fault zones, where the strength is usually higher. On the other hand, there high strength values were associated with samples with low porosity and *vice versa*.

By assuming that the highest values of UCS and TS would represent the properties of the rock material unaffected by stress release during drilling, a qualitative classification of the sample damage can be attempted. This classification, although quite rudimental, consists in giving six degrees of damage (from the lowest of 0 for undamaged samples to the highest of 5 for very damaged samples) depending on the difference between the actual strength and the estimated unaffected strength values. Depending on the borehole, Lanaro[11],[12] suggested the following values for the unaffected strength: i) UCS_{avg} = 168-232 MPa; ii) TS_{avg} = 6.8-8.7 MPa.

To be able to assign a degree of damage, the strength drop associated with a damaged core samples should be estimated. In this work, the decrease of UCS and TS were assumed to be 90 MPa and 4 MPa, respectively. The degree of damage is assigned proportionally to the difference between the laboratory strength and the estimated unaffected strength normalized with respect to the maximum expected strength drops.
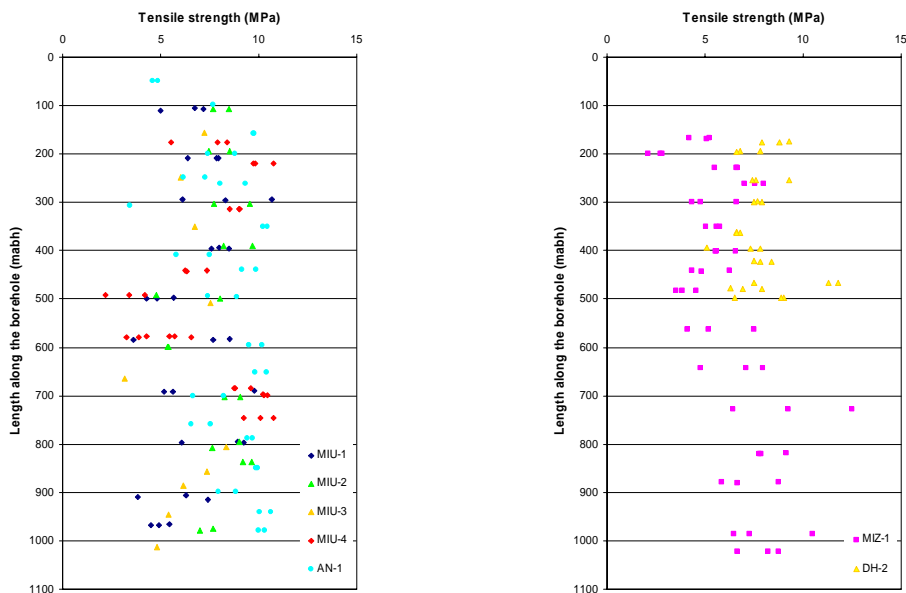

Figure 2. Plot of the indirect tensile strength of the intact Toki granite of samples taken from the boreholes at the Shobasama (left) and Mizunami Site (right). Please notice that borehole MIU-4 and MIZ-1 are not vertical.

3.1.4 Polynomial interpolation of the measured stresses with depth

The wavy variation of the strength observed in Figure 1 and Figure 2 suggests that the mechanical properties obtained from the laboratory tests vary continuously with depth. Such variation can be extrapolated from the depth of sampling to the depth where no data is available to estimate the possible laboratory strength at those depths. In Figure 3 and Figure 4, polynomial interpolations of the available laboratory results with depth along borehole MIU-2, MIU-3, MIZ-1 and AN-1 are presented.
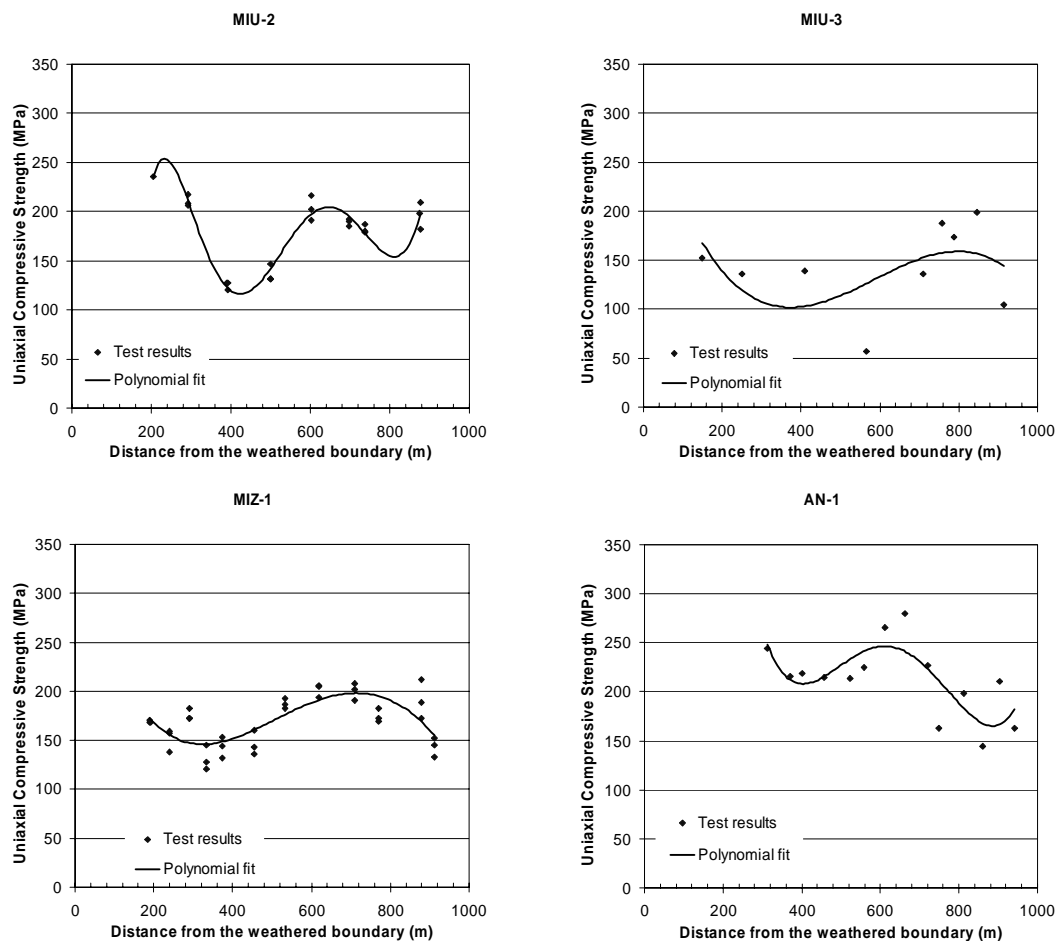

Figure 3. Polynomial fit of the variation with depth of the uniaxial compressive strength obtained in laboratory for borehole MIU-2, MIU-3, MIZ-1 and AN-1. The depth is represented as the distance along the boreholes from the weathered boundary in the Toki granite basement.
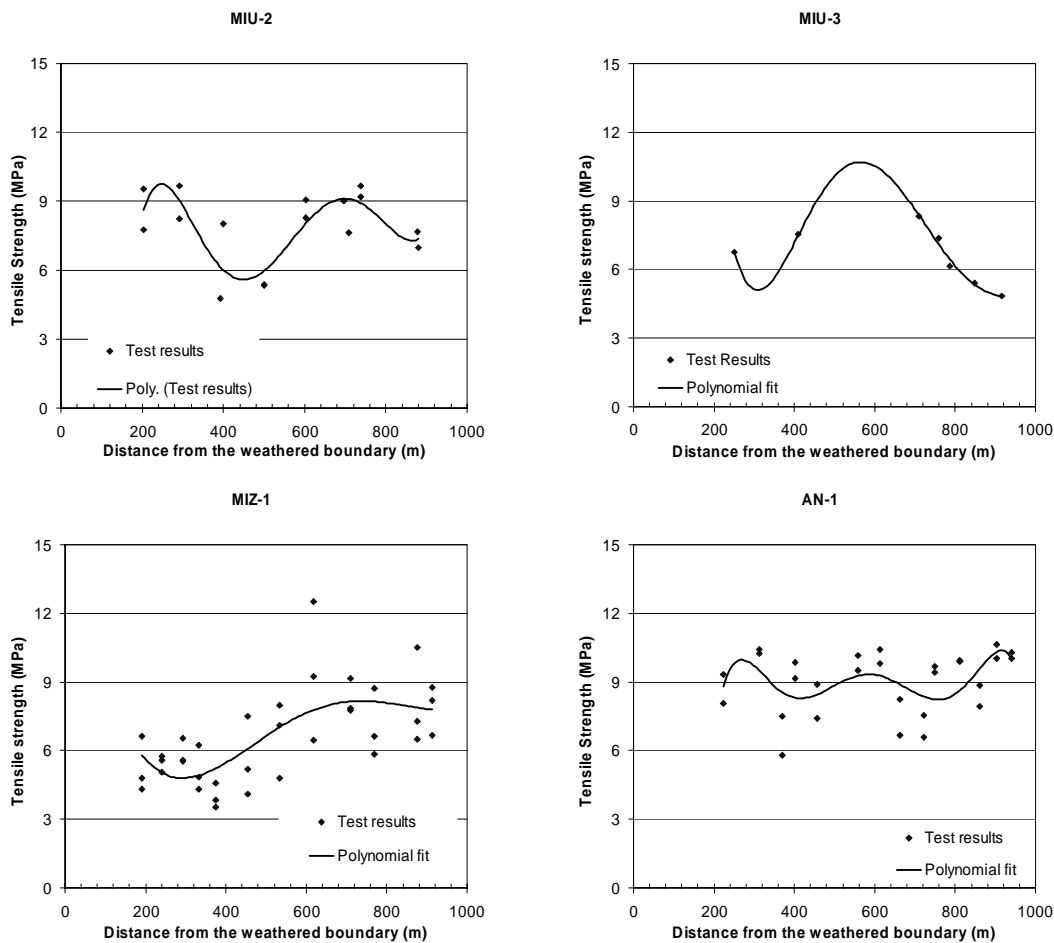
Figure 4. Polynomial fit of the variation with depth of the Brazilian tensile strength obtained in laboratory for borehole MIU-2, MIU-3, MIZ-1 and AN-1. The depth is represented as the distance along the boreholes from the weathered boundary in the Toki granite basement.

3.1.5 Other sample damage indicators

Other than reduced uniaxial compressive and tensile strength, other indications of damage were observed in the cores of boreholes at the Shobasama and MIU Construction Site. Such indicators of core damage can be listed as follows:

- Increased porosity of the samples: the porosity of the samples was observed to be negatively correlated to the strength of the samples. Since porosity in crystalline rocks is often associated to the presence of microcracks, this is a sign of potential sample damage;

- P-wave velocity measurements performed in relation to Differential Strain Curve analysis (DSCA) for stress determination on samples from the sub-vertical borehole MIU-3 show that the P-velocity is minimum in the direction parallel to the maximum horizontal stress, indicating core damage due to stress release[13];

- Acoustic Emission and Differential Strain Analysis on samples from borehole MIZ-1 failed due to the effect of microcracking believed to have been induced by drilling in the stressed rock mass[14].

4   Drilling parameters

Great effects on the core conditions are induced by the drilling parameters. The pressure of the drilling fluid is believed to induce crack propagation in a similar way as in the hydro-fracturing

testing methods for measuring the in-situ rock stresses[15]. Moreover, thermal effects due to friction under the drill bit are also believed to enhance the core damage induced by the complicated stress-path the rock undergo around the bottom of the borehole[16]. Also the shape of the kerf isolating the core might may induce different degrees of stress concentration around the bottom of borehole and thus core sample damage.

5   Rock stress measurements

Extensive campaigns of in-situ rock stress measurements were carried out at the Sites and are summarised in Figure 5 in terms of maximum and minimum horizontal stress, and vertical stress, respectively. The presence of the deformation zones is also indicated, which clearly affects the stress distribution by reducing the measured stresses inside or immediately closed to the fault zones.

It could be observed that the hydro-fracturing data systematically returns proportional values of the maximum horizontal stress σ_H compared to the minimum horizontal stress σ_h (σ_H/σ_h ranging between 2.1041 for AN-1 and 2.2739 for MIU-2). Therefore, the two stress components might not be considered as independent due to the method of determination. The vertical stress is determined as the weight of the overburden (considered all in granite), thus, it increases linearly with depth according to the equation:

$$\sigma_v = \rho g z = 0.0256z \quad (MPa)$$

where ρ is the density, g is the gravity acceleration and z is the depth, respectively.

The measured in-situ stress components can be plotted against each other in different ways as shown in Figure 6. In this figure, the following stress components were assumed to describe the stress field:

1)   The in-situ vertical stress;

2)   The in-situ maximum horizontal stress;

3)   The difference between the maximum horizontal stress (1)) and the vertical stress (2));

4)   The average stress between maximum horizontal stress (1)) and the vertical stress (2)).

In general the maximum measured horizontal stress is double than the weight of the overburden. In this case, the average stress and difference between the horizontal and vertical stress are almost in proportion 1:1. However, all the boreholes show sections were the vertical stress becomes as large as the maximum horizontal. Thus, the difference between the horizontal and vertical stress tends to zero.
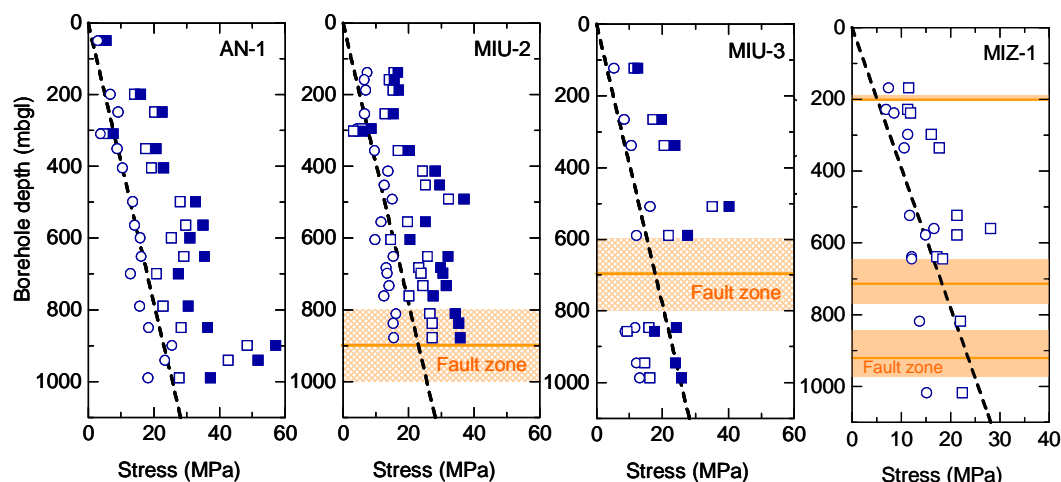
Figure 5. Summary plots of the results of hydro-fracturing measurements of the in-situ stresses. Filled squares show the maximum total horizontal stress, empty squares the maximum effective horizontal stress. Empty circles represent the total minimum horizontal stress. The dotted lines show the total vertical stress calculated from the rock density. The position of the major fault zones identified along the boreholes is also indicated.
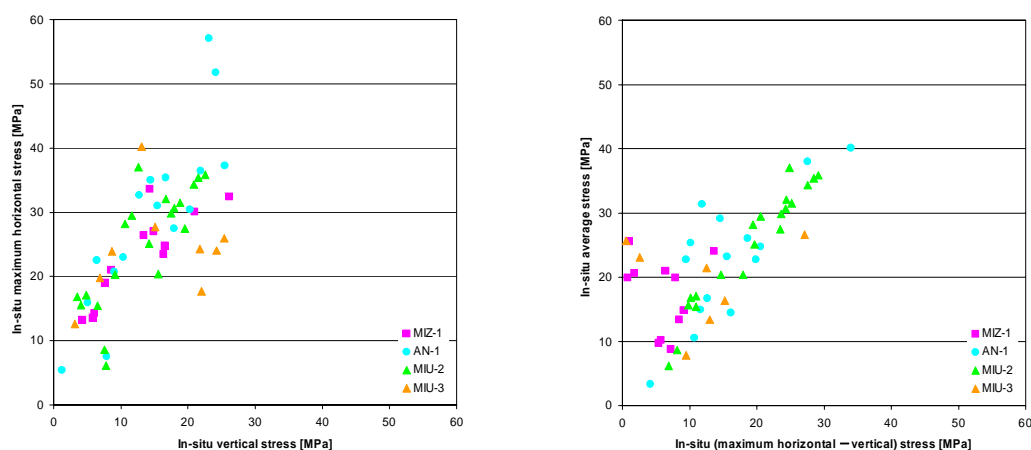

Figure 6. Measured in-situ stresses: plot of the vertical stress versus the maximum horizontal stress (left) and; plot of the difference between the maximum horizontal stress and the vertical stress versus the average stress (right).

5.1   *Polynomial interpolation of the measured stresses with depth*

Small-scale heterogeneities (e.g. single fractures) and large-scale heterogeneities (i.e. fault zones) affect the stress field at the sites, whereas the geological properties of the rock mass seem to be rather homogeneous[17]. This justifies the assumption that, if stresses are to vary, they would probably vary smoothly at the scale of the whole boreholes (between 100 and 1,000 m). The local variations are in this way attributed to the small-scale heterogeneities. On the other hand, large-scale heterogeneities should more continuously affect the stress regime due to the often gradual transition of the rock mass properties from competent bedrock to fault zones.

The rock stress measurements by hydro-fracturing returned three components of the in-situ stress tensor in the vertical direction and on horizontal planes. Since shear stress components were not determined and are assumed null, this implicitly implied that the determined stresses are also

principal stresses (e.g. the vertical and horizontal directions are principal directions). This assumption, although probably rough, simplifies very much the analysis of the in-situ stresses and their variation with depth.
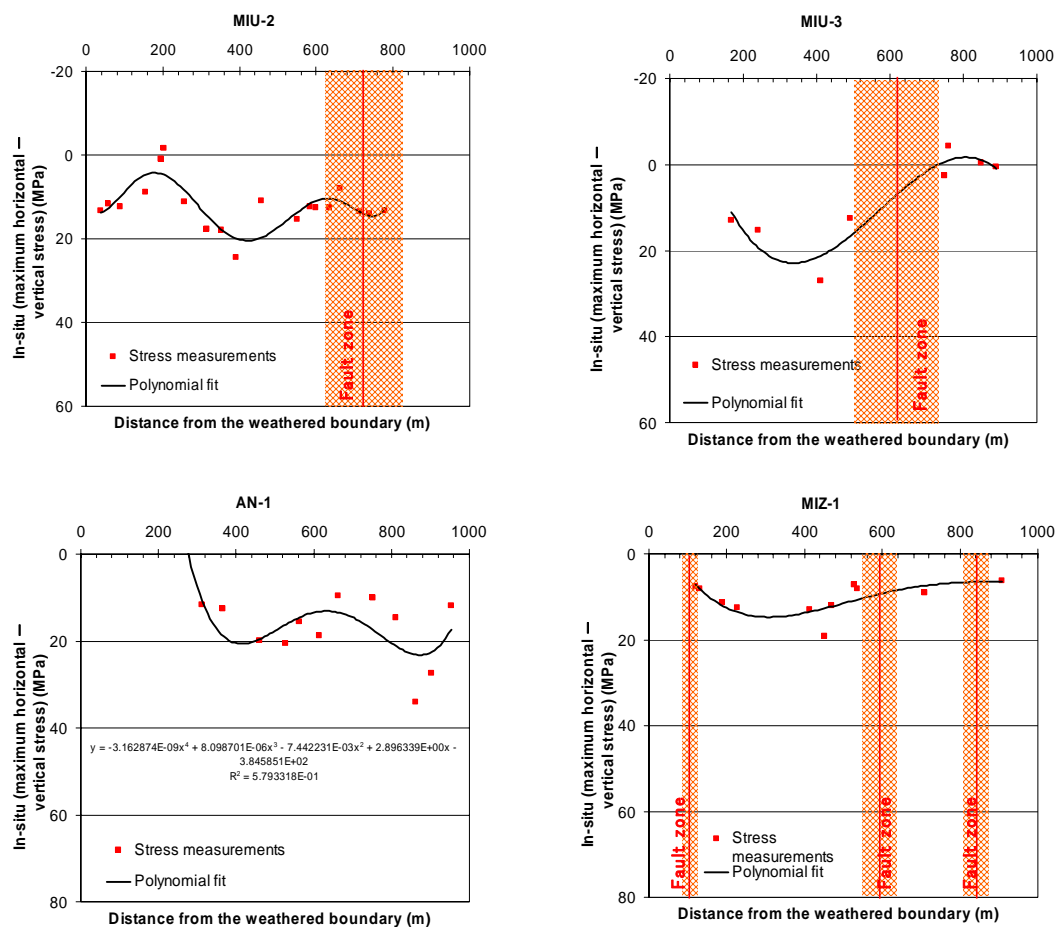

Figure 7. Polynomial fit of the variation with depth of the difference between the maximum total horizontal stress and the vertical stress for borehole MIU-2, MIU-3, AN-1 and MIZ-1. The depth is represented as the distance along the boreholes from the weathered boundary in the Toki granite basement.

Polynomial interpolations of the difference between the maximum total horizontal stress and the vertical stress, here addressed as deviatoric stress, are shown in Figure 7 as a function of the distance along the boreholes from the weathered boundary of the Toki granite basement. It was judged to be relevant to study the variation of the difference between the maximum horizontal stress and the vertical stress (e.g. twice the deviatoric stress in a core axial plane) because these components are independently determined.

5.2 Estimation of the in-situ stresses at the depth of the core sampling

Usually, the particular stress level at the location where the core samples are taken is unknown. This makes the analysis of the damage of the core difficult if not impossible even in very homogeneous rock masses. In consequence, the real nature of the variation of the strength along a borehole cannot be understood and it is often imputed to geological heterogeneity or pre-existent microcracking of the rock before drilling. At the Shobasama and MIU Site, however, the density of the rock stress measurements along the boreholes has allowed the polynomial interpolations of the stress components with depth as in Sec. 5.1. By means of these polynomial interpolations, the particular stress level at the depth of the core sampling can be determined.

5.3 Maps of potential core damage - Laboratory

Based on these data, maps of the damage level as defined in Sec. 3.1.3 as a function of the stress level can be drawn as in Figure 8 and Figure 9. These maps show that*

- The points on the stress maps are not evenly distributed and tend to cluster in particular areas. This depends on the in-situ stress distribution where a certain degree of proportionality between the vertical and horizontal stress seems to hold;

- The points with higher damage level also tend to group in certain positions. This might indicate that those particular stress levels more likely generate damage on the cores that diminishes either the compressive strength or the tensile strength;

- the areas with points with low estimated damage for the samples overlap areas with high estimated damage. This might be due to two reasons: i) possible errors in the stress determination that misplaces the points on the maps; ii) the presence of pre-existent fractures in the rock mass might locally alter the stresses field reducing the damage on samples taken from there.

- The areas of high damage obtained from uniaxial compressive and Brazilian tensile strength seem to be often overlapping or complementary. The combination of the high damage areas from the two methods might delimit an area of no stress induced damage of the cores;

- The mismatch between the results from compressive and Brazilian testing can be explained by the fact that: i) the samples for compressive tests are not taken exactly at the same position as the samples for Brazilian testing (e.g. stresses can be different); ii) the damage induced by stress release might affect the compressive and tensile tests in different ways because the loading directions are perpendicular for the two tests.

Figure 8. Maps of the core damage induced by drilling obtained from uniaxial compressive strength results. On the left, the damage level is plotted as a function of the in-situ vertical and maximum horizontal stress; on the right, damage level is plotted as a function of the difference between the in-situ maximum horizontal stress and vertical stress, and the in-situ average stress. In blue, a possible elliptical damage envelope is proposed (Eq. (1)).
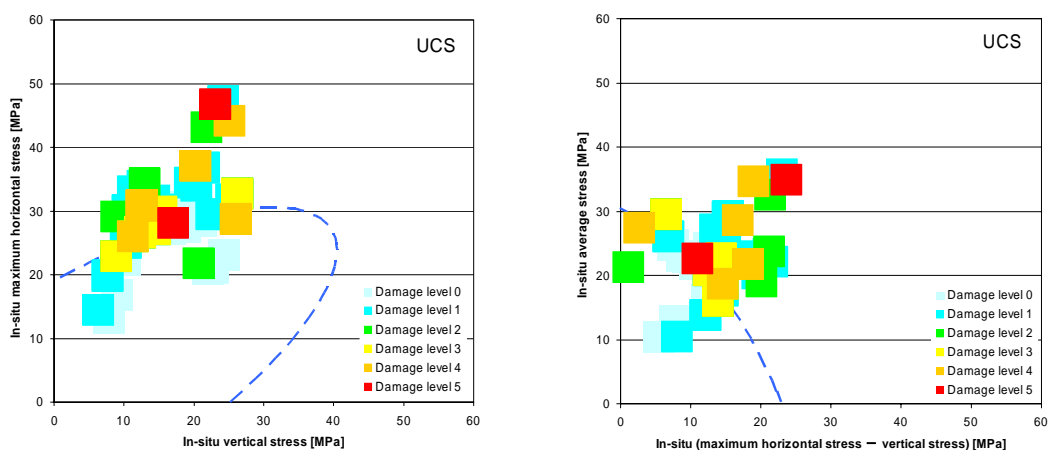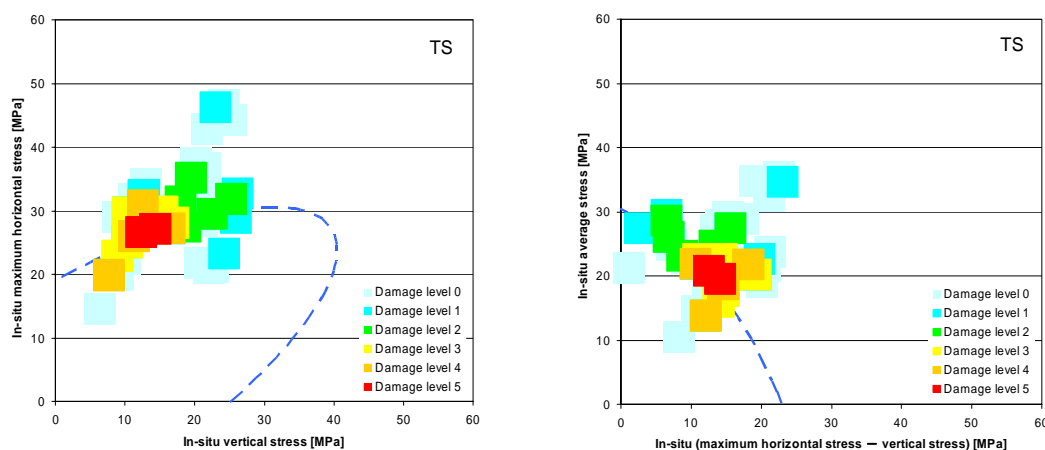
Figure 9. Maps of the core damage induced by drilling obtained from Brazilian tensile strength results. On the left, the damage level is plotted as a function of the vertical and maximum horizontal stress; on the right, damage level is plotted as a function of the difference between the maximum horizontal stress and the vertical stress, and the in-situ average stress. In blue, a possible elliptical damage envelope is proposed (Eq. (1)).

Based on these considerations, it can be hypothesised that there exist a convex area towards the lower stress levels where no damage is observed. This area is surrounded by the areas in which the damage level is high. The shape of this "no damage" convex area is different depending on the coordinate chosen for drawing the map. Sketches of such "low damage" areas are presented in Figure 8 and Figure 9. This hypothesis will be possibly confirmed by the numerical modelling of the core drilling by a BEM code implementing DDM and fracture initiation and propagation in Sec. 6.

6 Numerical modelling of core drilling

Numerical models were set up to study the fracturing effect of the stress release induced by drilling of the core.

6.1 FRACOD[2D]

FRACOD[2D] (FRActure propagation CODe) is a Windows based program that simulates the fracture initiation and propagation in an elastic and isotropic medium [18]. The code implements the boundary element method (BEM) called Displacement Discontinuity Method (DDM). The DDM method is based on the equations describing the stresses and displacements caused by a fracture with constant displacement in an infinite continuum and homogeneous elastic body [19),20)]. The effect of normal and shear deformability of the fractures is superposed to obtain a solvable system of linear equations. Additional constrains to this system are introduced for open fractures (e.g. zero normal stress), fractures in elastic conditions (e.g. linear elasticity) and fractures in failure limit conditions or sliding (e.g. Mohr-Coulomb Criterion).

Pre-existent fractures can propagate and new fractures can be generated either in tensional (Mode I) or in shear (Mode II). The propagation criterion proposed by Shen & Stephansson[21)] is implemented in which the resultant strain energy rates G_I in Mode I and G_{II} in Mode II are functions of the possible propagation direction θ around the tip of the fracture. The fracture will eventually propagate when the F-Criterion is reached:

$$F(\theta) = \frac{G_I(\theta)}{G_{Ic}} + \frac{G_{II}(\theta)}{G_{IIc}} \geq 1 \, .$$

The strain energy associated with the presence of a fracture in the elastic body can be expressed as the sum of the energy associated to tension and shear, respectively. Thus, the two strain energy rate components can independently be determined for each direction θ. These values are then introduced in the expression of the F-Criterion to determine whether and in which direction the fracture is supposed to grow.

The length of the newly formed fractures can be either assigned or determined by the spacing of the point grid where fracture initiation can detected in the model. Although microcracking cannot be directly be simulated, the code can simulate the process that takes place when microcrack coalescence develops into macro-scale fracture propagation.

The material in which the fractures can initiate and propagate (i.e. the rock) has elastic deformational properties and a Mohr-Coulomb strength criterion.

6.2   *Material properties, model geometry and boundary conditions*

The material properties of the Toki granite were determined in different laboratory test campaigns with samples from the Shobasama and MIU Construction Site. In general, the Young's modulus, Poisson's ratio, cohesion and friction angle were found to vary on average between 51 and 58 GPa, 0.26 and 0.34, 34 and 39 MPa, and 52° and 55°, respectively. The friction angle, cohesion, initial and residual aperture of the initiated or propagating fractures were estimated here based on earlier BEM-DDM simulations of the behavior of similar rock type[22]. On the other hand, experimental values of the normal stiffness and Mode I and Mode II fracture toughness were determined in laboratory on samples of Toki granite from borehole MIU-2[23]. The normal stiffness was observed to vary between 720 and 853 GPa/m; the Mode I toughness to vary between 1.73 and 2.39 MPa $m^{0.5}$; and the Mode II toughness to vary between 3.07 and 11.84 MPa $m^{0.5}$ (depending on the stress confinement). Also the shear stiffness was not determined by means of experimental tests and was estimated here based on similar studies (e.g. ref. 24)). All the experimental results and considerations above lead to the choice of the modeling parameters in Table 2.

For crack initiation in Mode I, the models are assumed to have a spatially "random" generation when the ratio between the stress σ and the strength σ_m would exceed 90%. Moreover, fracture generation is also allowed at the boundary of the model defining the borehole walls and core surface.

The models simulate a block of granite of 1 m in width and 1.5 m in height (Figure 10). The borehole diameter was chosen as for borehole MIZ-1 at about 500 m depth and is 134 mm in diameter. The kerf isolating the core has a width of 24.5 mm. The simulated core stub has an axial length of 200 mm and the bottom of the core lies 300 mm below the upper edge of the modeling rock block. The model has a vertical symmetry plane coinciding with the axis of the core.

Two dimensional modeling is performed in plane strain and the applied stress boundary conditions are compressive in vertical and horizontal direction. This means that the principal stresses acting on the model are parallel to the edges of the model (e.g. vertical and horizontal).

The model does not contain pre-existent fractures. The newly initiated fractures or the propagating portions of pre-existent fractures have a minimum length of 15 mm.

Unloading is carried out inside the borehole by step-wise proportionally reduction of the stresses from their original assigned values. Usually, the final unloading steps are performed from a hydrostatic pressure condition (e.g. pressure in the borehole between 5 and 0.5 MPa).

Table 2. Material properties used for the BEM-DDM modelling of core sample damage during drilling.

Material	Parameters	Values
Intact rock	Poisson's ratio	0.33
	Young's modulus	50 GPa
	Friction angle	50°
	Cohesion	30 MPa
	Tensile strength	6 MPa
	Mode I fracture toughness	2 MPa m$^{0.5}$
	Mode II fracture toughness	11.5 MPa m$^{0.5}$
Initiated and propagating fractures	Shear stiffness	20 GPa/m
	Normal stiffness	500 GPa/m
	Friction angle	32°
	Dilation angle	0°
	Cohesion before sliding	10 MPa
	Cohesion after sliding	0 MPa
	Initial aperture	10^{-2} mm
	Residual aperture	10^{-3} mm

Figure 10. Schematic view of the BEM-DDM model in plane strain conditions: dimensions, symmetry plane and boundary conditions.

6.3 Modelling results

The BEM-DDM modelling results look typically as the plots in Figure 11 for a model with limited damage (left) and one with extensive damage (right). The model allows the determination of the fracture pattern due to the unloading of the borehole walls and core. In turn, the fracture pattern affects the stress distribution around the borehole, which becomes more and more pervasive as the stresses and the damage increase.

Figure 11. Example of numerical results: on the left, model with limited core damage; on the right, model with extensive core damage.

6.4 Classification of core damage

Based on the results of numerical models performed with horizontal and vertical boundary stresses ranging between 10 and 40 MPa, the fracture pattern in the core stub and ahead of the bottom or the borehole could be grouped into six level of potential damage of the core, from level 0 to 5 as was done in Sec. 5.3.
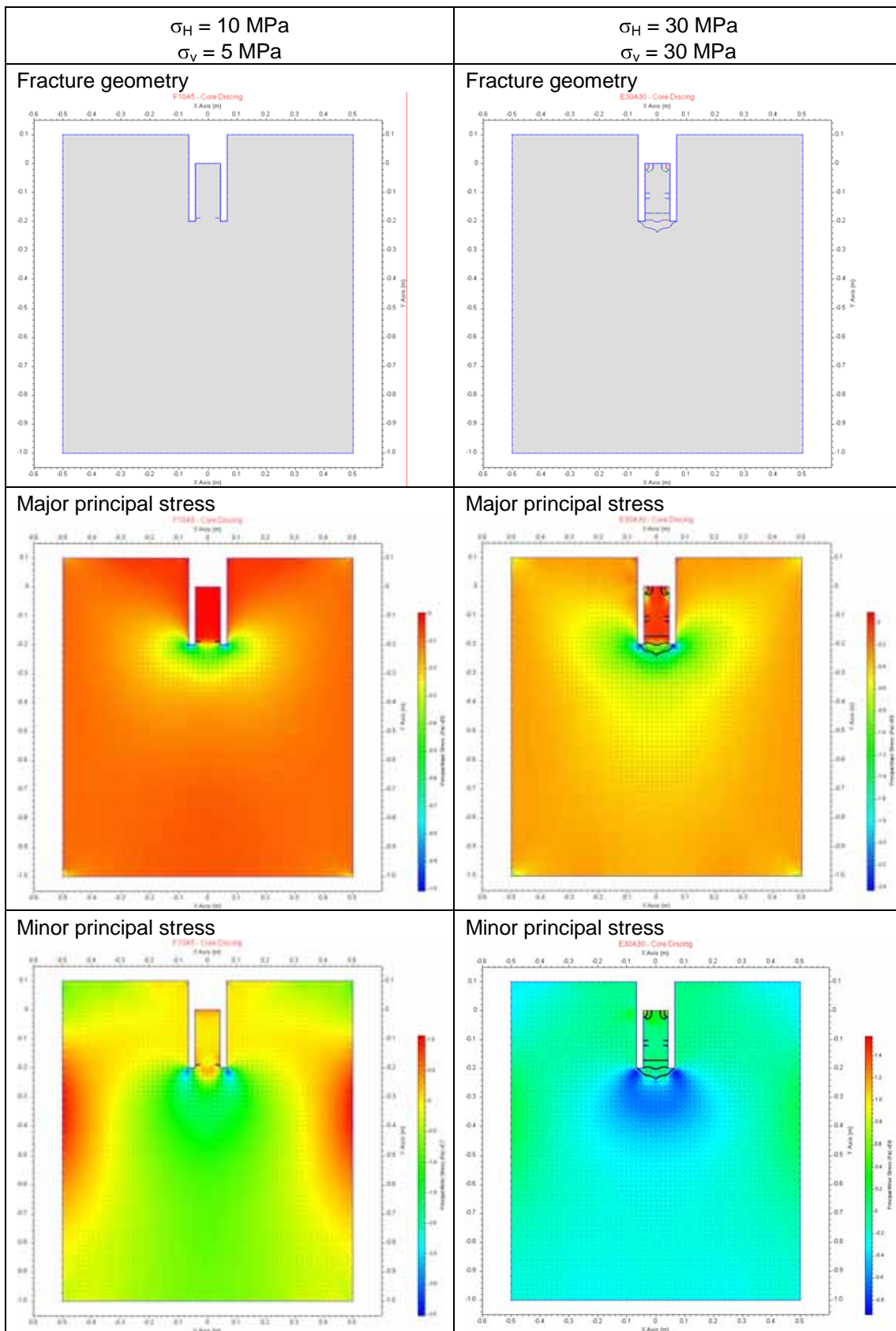
In synthesis, the levels of damage induced by the release of the in-situ stresses due to drilling can be described as follows:

- Level 0: No fractures are observed either in the core stub or in the rock around the borehole;

- Level 1: A few short fractures are generated superficially in the core stub and often in relation to the kerf;

- Level 2: Discontinuous fractures are created at the surface and inside the core stub;

- Level 3: Continuous and discontinuous fractures occur in the core, however most of the core stub is still intact (i.e. whole samples might be taken for testing);

- Level 4: The core is affected by multiple continuous fractures that cut it into disks or chips;

- Level 5: The core and the rock ahead of the bottom of the borehole are pervaded by intensive cracking indicating crushing of the core and instability of the walls of the borehole.

The fracture patterns observed in the numerical models, although realistic, suffer of the drawback that the present version of FRACOD2D does not allow to perform analysis with de-activation of areas to simulate excavation of advance of the drilling bit. Therefore, some fracture patterns might continuously or periodically occur along the core depending on the stress redistributions induced ahead of the borehole bottom as the drilling proceeds. Thus, when a single fracture perpendicular to the core axis develops, it is not possible to predict from the model at what distance next fracture will develop during drilling. Some particular fracture shapes, especially convex conical shapes ahead of the borehole, seem to stabilize the borehole contrary to concave fracture shapes that often develop into instable stress conditions. For this reason the notion of sample damage inferred from the numerical models is in some case arbitrary.
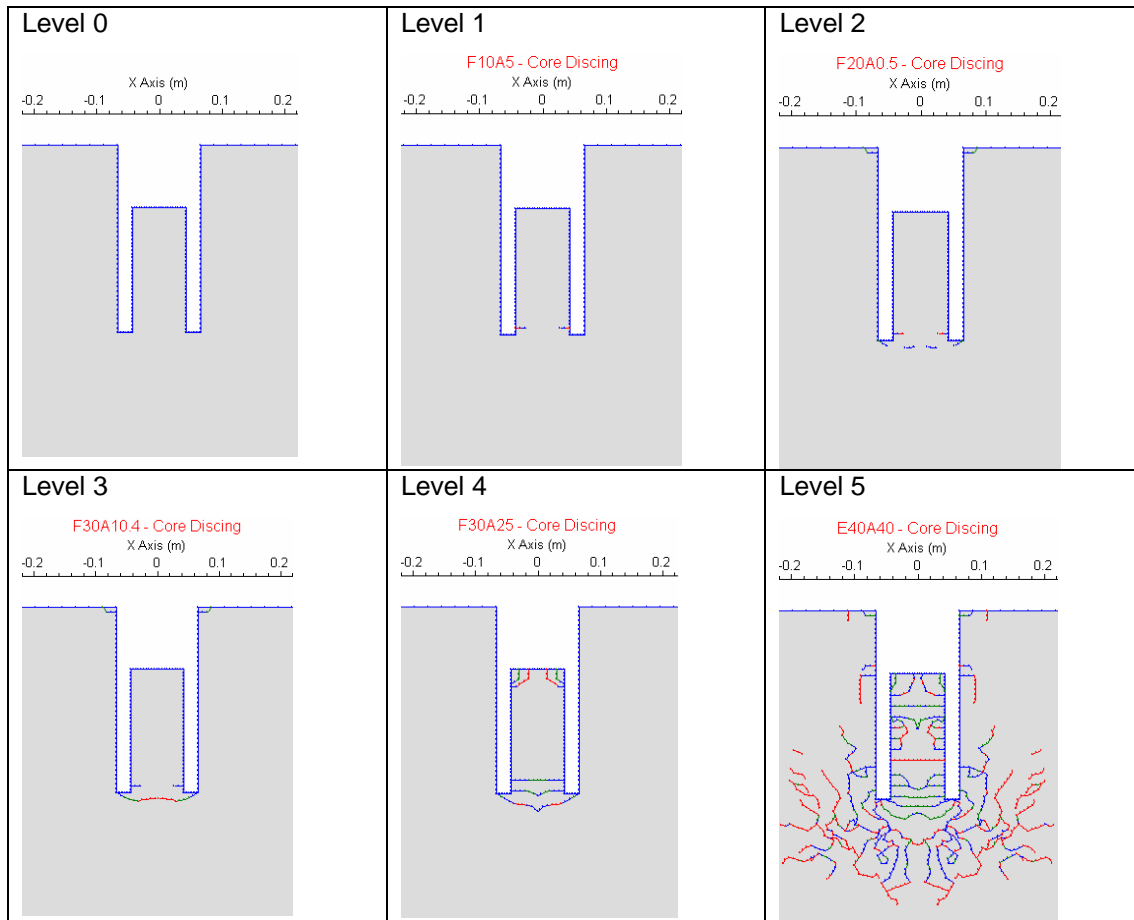
Figure 12. Examples of fracture patterns in the five levels of damage (Level 0 to 5) of the core stub and ahead of the bottom of the borehole.

6.5 Maps of potential core damage – Numerical modelling

Based on the level of damage determined in each numerical model, damage maps similar to those obtained in Figure 8 and Figure 9 are produced. Such maps can be created as a function of the boundary horizontal and vertical stresses (Figure 13, left), or as a function of the difference between the boundary horizontal and vertical stress and the boundary average stress (Figure 13, right).

In this study, attention was paid to the cases spanning between to boundary stress configurations: a) with horizontal stress larger or equal to the vertical stress and; b) with vertical stresses larger than zero. These two limit configurations are presented in Figure 13.

The analysis of the numerical results also allow to identify cases of potential cracking perpendicularly to the core axis and cases of inclined fractures, where fractures propagate from the surface of the core inwards with an angle to the core axis. Numerical models exhibiting perpendicular and inclined fractures were identified in the plots in Figure 13. It was found that:

- Perpendicular fractures seems to occur for large difference in magnitude between the boundary horizontal stresses and the vertical stresses;

- Petal fractures tend to appear when the boundary stresses are large and have rather similar magnitudes.

according to the definitions in Roegiers[26]. Centreline fractures were only observed in simulations with very small horizontal boundary stresses, not included in this study. Figure 1 shows the

evolution of fracturing for one of the numerical models (boundary horizontal and vertical stress of 20 and 15 MPa, respectively). At the beginning of the stress release in the borehole, tensional fractures generates horizontally at the base of the core stub and vertically at the periphery of the top of the core. Subsequently, some of the already initiated fractures become behaving elastically, while the vertical fractures develop into chips. Tensile fractures develop at the bottom of the kerfs. At the last unloading stage, these fractures propagate through the whole core, cutting it just ahead of the bottom of the borehole. Such fractures, resembling the fractures occurring during core discing, are generated in shear and show a slightly concave shape.
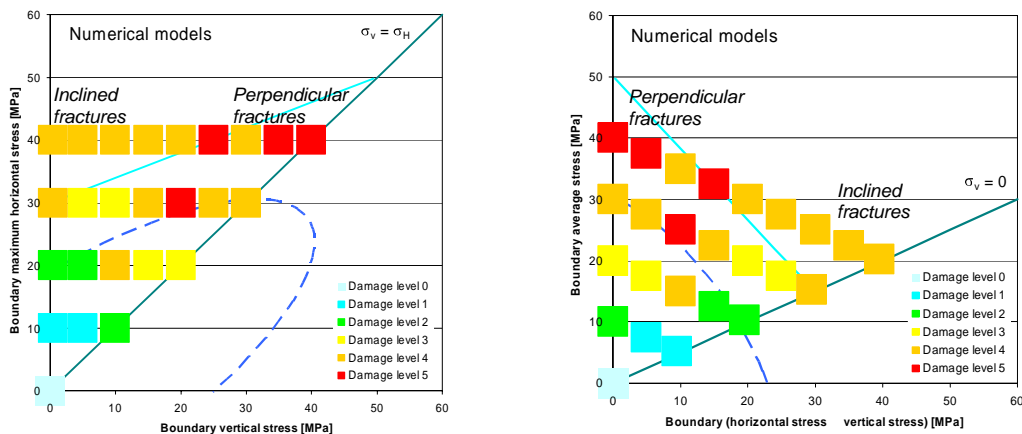
Figure 13. Maps of the core damage estimated based on numerical BEM-DDM results. On the left, the damage level is plotted as a function of the vertical and horizontal stress; on the right, damage level is plotted as a function of the difference between the horizontal stress and the vertical stress, and the in-situ average stress. In dashed blue, the same elliptical damage envelope proposed in Figure 8 and Figure 9 is shown (Eq. (1)); in cyan, the core discing criterion by Obert and Stephenson [25].
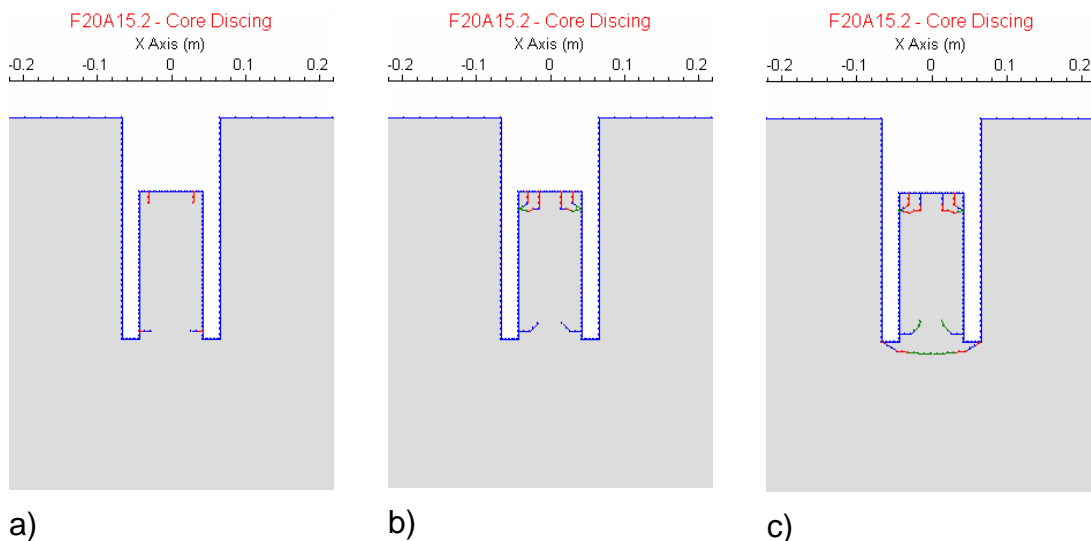
Figure 14. Different stages of fracturing for the numerical model with boundary horizontal and vertical stress of 20 and 15 MPa, respectively. The fractures colored in blue are in elastic conditions, in red are in tension and in green in shear. a), b) and c) show different levels of release of the stresses in the borehole to simulate the drilling.

In Figure 13, the samples (experimentally and numerically) showing none or little damage are grouped in the area towards the lower stresses. The border of this area, convex towards low boundary stresses, is assumed to be an empirical damage envelope. The shape of this envelope is vaguely elliptical in the plane of the boundary stress components as it could be observed in the maps of laboratory sample damage in Figure 8 and Figure 9. The analytical form of this envelope can then be written as a function of the boundary vertical and horizontal stress σ_H and σ_v, respectively, as:

$$\frac{(\sigma_v)^2}{a^2} + \frac{(\sigma_H)^2}{b^2} = 1$$

Eq. (1)

The two semi-axes a and b were determined based on all the cases of laboratory observation and numerical modelling to be equal to 16 and 48 MPa, respectively. These values, obviously, only apply for the assumed diameter of a core of Toki granite and for the material properties assumed in this study. Furthermore, such envelope is not strictly a failure envelope but only the boundary beyond which sample damage might affect the laboratory results of uniaxial and Brazilian tests.

Since perpendicular fracturing is a precursor of core discing, the empirical criterion for predicting core discing proposed by Obert and Stephenson [25] is also plotted in Figure 13. This criterion follows the equation:

$$\sigma_H = k_1 + k_2\sigma_v$$

Eq. (2)

where the coefficients k_1 and k_2 were empirically determined for different rock types. k_1 was found to vary between 6.5 to 10.5 times the Brazilian tensile strength and k_2 between 0.59 and 0.89. In this study, the two coefficients were assumed to be 30 MPa and 0.4 to roughly much the numerical models. Beside this line, also the numerical models predict damage of the core with cutting-through fractures that would not allow sampling for uniaxial and Brazilian tests.

6.6 Limitations of the modelling

The present BEM-DDM modelling of drilling of a core presents several limitations, among which:

1) FRACOD^{2D} is a two dimensional code in plane strain conditions, thus, all simulations in this study were performed in these conditions. Such planar symmetry only resembles the true axis-symmetrical geometry of the core. However, this assumption is often made when modelling uniaxial and triaxial tests by using FRACOD^{2D} [27];

2) To simulate the drilling, the stresses around the core have to be released in the two-dimensional model. The simulation of this process is somehow arbitrary because the unloading stress path corresponding to real tri-dimensional conditions is unknown;

3) The geometry of the core stub is constant and cannot be changed during the simulation of the drilling. In this study, the length of the stub was chosen to be about 2.4 times the core diameter. Although this can affect the stress release around the bottom of the borehole, Li and Schmitt[4] concluded that stress conditions are worse for long core stubs (typically more than one diameter);

4) The fracture pattern ahead of the borehole kerf affects the behaviour of the core when the drilling proceeds. Since the tips of the fractures induce stress concentrations, the actual fracture pattern in the core away from the kerf may be different than that modelled with FRACOD^{2D}.

It is auspicial that, as soon as available, a three-dimensional version of FRACOD capable of modelling complex model geometries and fracture pattern is used to perform modelling that can confirm the results presented here.

7 Discussion

By comparing the maps of the in-situ stresses (Figure 6) for the boreholes at MIU and Shobasama site, and the maps of sample damage numerically obtained (Figure 13), it can be observed that most of the values fall below the estimated limit for core discing according to Obert and Stephenson[25]. However, some of the measured stresses reach quite close to this level confirming the possibility of sample damage. This is confirmed by the maps of the sample damage estimated base on the strength of the samples in uniaxial compression and Brazilian tests (Figure 8 and Figure 9).

The maps of the sample damage also show a multitude of points for which, despite the high estimated stresses, the level of sample damage appears to be low. This could be explained in several ways:

1) By the fact that the estimated stress according to Sec. 5.1 concern variation of the stresses at the scale of the whole borehole (typically between 100 and 1000 m). Therefore, the local stresses at the particular position of the samples might significantly differ from the large scale stresses because of the presence of minor faults, fracture zones or even single fractures, which could not be considered in this study.

2) By the fact that the in-situ stress field presents principal stress orientations that can vary with depth and thus are not always horizontal and vertical. Vervoort and Govaerts[28] documented that a principal stress rotation of only 10° completely inhibits the Kaiser effect in the acoustic emission of the samples reloaded in triaxial conditions, thus limiting the core damage.

3) By the fact that the in-situ stress field is normally not biaxial (i.e. equally large horizontal stress components) as modeled with FRACOD[2D]. This implies that large differences between the two horizontal stress components results into less severe stress release of the samples that in turns exhibit higher laboratory strength values.

For these reasons, in the present study more weight was given to the samples with high damage level than to those with low damage level, especially when damage was associated with high estimated stresses.

Point 2 and 3) also imply that anisotropy and rotation of the stress field with respect to the core axis might induce anisotropy of the mechanical properties of the samples tested in laboratory that do not necessarily exists for the rock in-situ or that is superposed to the rock natural anisotropy.

Another observation consists in the fact that most of the stresses at the location of the core samples present a wide span of variation of the difference between the maximum horizontal and vertical stress components compared to the variation of average stress. This implies that, if the level of damage is directly correlated to the level of stress, the differential stress should have a much larger effect than the effect of the average stress on the experimental results from the analyzed boreholes (MIZ-1, AN-1, MIU-2 and MIU-3).

Differently than previous studies, the present gives the shape of the possible fractures generated by the stress release of the core. Even for low stresses, small fractures departing slightly above the bottom of the kerf propagate perpendicularly to the core axis. These fractures often tend to stop after a few centimetres. However, for higher stresses, the diametric fractures can merge to cut the core in two. These fractures resemble those occurring in core discing. Other fractures usually depart from the kerf cut by the drill bit downward towards the axis of the borehole. Depending on the level of stress, such fractures can sometimes propagate till they join in the middle or till they

are linked together by fractures perpendicular to the core axis. Fracture propagating at an angle with the core axis resemble to the fractures typically associated with "petal fractures". Some fracturing at the wall of the borehole could also be observed, particularly at a certain distance from the bottom of the borehole, where the principal stresses tend to return horizontal and vertical.

Some cases of core discing at the same site [29] or in similar stress conditions in a Japanese site in granite[30] are shown in Figure 15. In the first study, the level of stress was estimated based on core sample damage in boreholes (MIU-1 and MIU-4) were no stress measurements were available but core discing was observed; in the second study, an hydraulic fracturing method was applied to determine the stress components in borehole SB-1 at Sakuma (Shizuoka Prefecture). Some of the stress points in Figure 15 are rather close to the estimated core discing criterion for the Toki granite. Furthermore, it can be observed the occurrence of core discing is not univocally defined by only one stress state since stresses much larger than the material strength also induce core discing, as shown by Matsuki et al. [30].
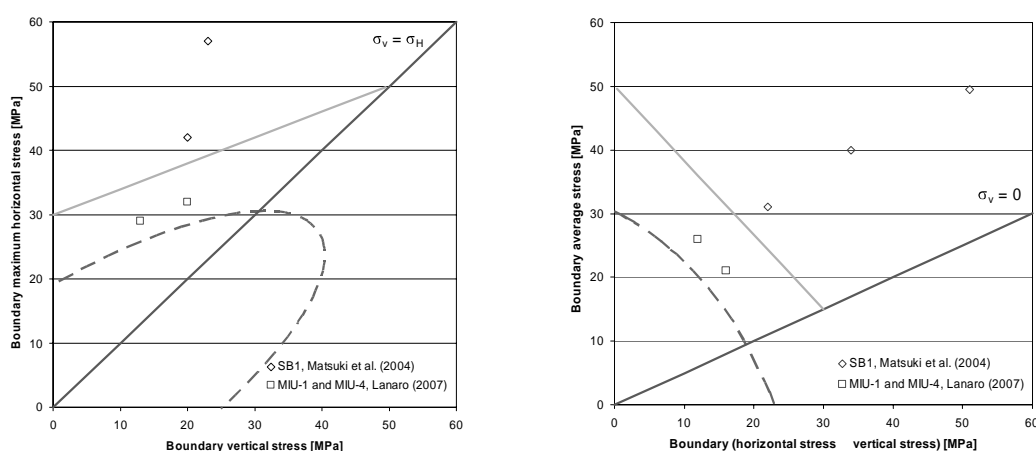

Figure 15. Two cases of core discing in granite in Japan plotted onto the damage maps in Figure 13.

The presented numerical models also allow for the determination of the disc thickness in the case core discing occurs. For the assigned core diameter of 85 mm, the observed disc thickness was found to be about 24 mm for the models with boundary horizontal stress of 30 MPa, and about 16 mm for models with boundary horizontal stress of 40 MPa, respectively. Some numerical cases, however, showed disks with different thickness down to 16 mm thickness even for horizontal stress of 30 MPa. Possibly, more detailed geometries of the numerical models and progressive simulation of the drilling could give better results from the BEM-DDM code.

Although providing hints about the shape of the propagating fractures, the present numerical models cannot simulate the effect of deepening of the kerf during drilling. The actual drilling might release the stresses more gradually as the kerf passes by the section of interest. This means that the stress state experienced by the core in the last unloading phases might be less "three-dimensional" than in the cases modelled here, where complete unloading inside the core is reached for a fixed position of the kerf. FRACOD[2D], in its present version, does not allow removal of elements, therefore, excavation or drilling in stages.

In Figure 8 and Figure 9, it can be observed that the cases of severe sample damage for the samples tested in uniaxial conditions do no exactly plot in the same position as the damage cases for Brazilian testing. Sample damage affecting the uniaxial tests results requires in general larger average stresses than for sample damage affecting Brazilian test results. This is probably due to the fact that micro fracturing of the core affects the two test results in different ways depending on the angle of the generated fractures with respect to the axis of the core, and thus, with respect to the loading direction. Preliminarily, based on the numerical results, it can be said that fractures at

an angle with the borehole axis affect prevalently the Brazilian test strength of the samples. On the other hand, fractures perpendicular to the borehole axis seem to affect more the strength in uniaxial conditions.

Eberhardt et al.[1] also commented on the fact that rock types with similar mineralogy (granodiorite and granite) exhibited larger stress-release damage if the average grain size increased, for example, from 1 mm to 3 mm. Furthermore, since about 90% of the minerals forming crystalline rocks have naturally tabular crystals, the direction of loading with respect to the preferential cleavage of the crystals will also affect the extension and orientation of damage [31]. For granite, Liu et al.[32] also assert that stronger crystals like quartz usually show higher micro-cracking prior testing than feldspar and biotite crystals. All these aspects, although not yet implemented in the BEM-DDM actual models, could be taken into account by changing the length of the shortest initiated fracture and by introducing heterogeneities in the material modelling the rock. A certain scale-dependency of the model results would also be predicted based on the considerations above.

8   Conclusions

This study shows that a realistic evaluation of the potential sample damage of a core due to drill-induced stress release can be provided by numerical modelling by means of the BEM-DDM core FRACOD^{2D}. Despite rather simple two-dimensional simulations of the drilling in plane strain conditions, the numerical results confirm many indirect indicators of sample damage observed on the core (core discing) and in the results of laboratory testing (uniaxial and Brazilian tests). The level of sample damage exhibited by the core samples could be confirmed by the fracture patterns obtained in the numerical models. Furthermore, it was observed that the fracture pattern induces stress concentrations in the core stub, leading to stress distribution quite dissimilar with those evaluated by means of continuum FEM modelling, as previously reported in the literature. Moreover, some of the fracturing occurring during stress released seems to be a result of shear and not tensile failure, differently than what commonly assumed. This calls upon the development of a BEM-DDM code capable of three-dimensional simulations of fracture initiation and propagation patterns within complex and variable geometries such as the drilling process in rocks.

9   Acknowledgments

10 References

1)   Eberhardt E., Stead D., Stimpson B. : Effects of sample disturbance on stress-induced microfracturing characteristics of brittle rock, Can. Geotech. J, Vol. 36, p. 239-250, 1999.

2)   Holt R.M., Brignoli M., Kenter C.J. : Core quality – quantification of coring-induced rock alteration, I. J. Rock Mech. & Min. Sci., Vol. 37, p. 889-907, 2000.

3) Sakaguchi K., Iino W., Matsuki K. : Damage in a rock core by induced tensile stress and its relation to differential strain curve analysis, I. J. Rock Mech. Min. Sci., Vol. 39, p. 367, 2002.

4)   Li Y., Schmitt D.R : Well-bore bottom stress concentration and induced core fractures, Am. Ass. Petrol. Geol. Bull., V. 81, No. 11, p. 1909-1925, 1997.

5)   Hakala M. : Numerical study on core damage and interpretation of in situ state of stress, Report POSIVA 99-25, Posiva Oy, Helsinki, Finland, p. 234, 1999.

6)   Kaga N., Matsuki K., Sakaguchi K. : The in situ stress states associated with core discing estimated by analysis of principal tensile stress, I. J. Rock Mech. Min. Sci., Vol. 40, p. 653-665, 2003.

7)   Lim S.S., Martin C.D., Christiansson R. : Estimating in-situ stress magnitudes from core discing, Proc. Conf. In-situ Rock Stress – Measurements, Interpretation and Application, Trondheim, Norway, (Lu, Li, Kjørholt and Dahle eds.), p. 159-166, 2006.

8)   Tsuruta, T.,Ota, K., Amano, K., Matsuoka, T., Sasaki, K. : Geological investigations during the Surface-Based investigation phase of the Mizunami Underground Research Laboratory (MIU)

project, ICGM'04, JNC Report TN7400 2004-010, p.83-95, 2004.

9) JGS 2521-2000. Method for uniaxial compression test on rocks, the Japanese Geotechnical Society, 2000.

10) JGS 2551-2002. Method for splitting tensile strength test on rocks, the Japanese Geotechnical Society, 2002.

11) Lanaro, F., Sato, T., Nakama, S. : Spatial variability of the compressive strength of the Toki granite at the Shobasama and Mizunami Construction Site, Japan, to be submitted to Rock Mech. & Rock. Eng., 2007.

12) Lanaro, F., Sato, T., Rinne, M., Stephansson, O. : Modelling Brazilian tests with FRACOM2D(FRActure propagation CODe), to be submitted to Int. J. Rock Mech. & Min. Sci., 2007.

13) Kato H. :. In situ stress measurements in MIU-3 borehole using hydraulic fracturing, the Japan Nuclear Cycle Development Institute, Report JNC TN7400 2000-005 (in Japanese with English abstract), 2000.

14) Yamada A., Sato T., Nakama S. : Rock mechanical investigations, 18th NAGRA/JNC Technical Meeting "MIZ-1 Workshop", 11-12 January 2005, MGA, Mizunami, Japan, 2005.

15) Chang C., Haimson B. : Effect of fluid pressure on rock compressive failure in a nearly impermeable crystalline rock: Implications on mechanism of borehole breakouts, Eng. Geo., Vol. 89, p. 230-242, 2007.

16) Cornet F.H., Berard Th., Bourouis S. : How close is a granite rock at 5 km depth? Int. J. Rock Mech. Min. Sci Vol. 44, p. 47-66, 2007.

17) Sato T. : Rock mechanical investigations, in MIZ-1 Workshop Phase III-VII, 29-09-2005, p. 7/1-7, 2005.

18) Shen,B : Mechanics of fractures and intervening bridges in hard rock, Ph.D Thesis, Royal Institute of Technology, Stockholm, Sweden, 1993.

19) Crouch, S.L. : Solution of plane elasticity problems by the displacement discontinuity method, I.J. Num. Methods Engng., Vol.10, p.301-343, 1976.

20) Crouch, S.L., Starfield, A.M. : Boundary element methods in soil mechanics, George Allen & Unwin Ltd, London, UK, p.79-109, 1983.

21) Shen, B., Stephansson, O. : Modificetion of the G-criterion of crack propagation in compression, I.J.Engng. Fracture Mech., Vol.51(1), p.73-85, 1993.

22) Stephansson O., Shen B., Rinne M. : The geomechanical evaluation and analysis of surrounding rock mass response to excavation of research shafts and galleries in MIU Project, FRACOM LTD, p. 89, 2003.

23) Backers T : Mode I and Mode II fracture toughness testing and fracture normal stiffness estimation of Tono-Granite, GeoForschungZentrum (Potsdam, Germany), p.18, 2002a.

24) Lanaro F. : Geometry, Mechanics and Transmissivity of Rock Fractures, PhD thesis, Royal Institute of Technology in Stockholm, KTH, Sweden, p. 60, 2001.

25) Obert, L., and Stephenson, D.E. : Stress conditions under which core discing occurs. Society of Mining Engineers of AIME Transactions, Vol. 232(3), p. 227–235, 1965.

26) Roegiers J.-C. : The petroleum approach to the state of in-situ stress, Proc. 3rd Int. Symp. On Rock Stress, RS Kumamoto '03, Japan, (Sugawara, Obara and Sato eds.), A.A. Balkema: The Netherlands, p. 99-112, 2003.

27) Shen B., Stephansson O., Rinne M., Lee H. S., Jing L., Röshoff K. : A fracture propagation code and its application to nuclear waste disposal, Int. J. Rock Mech. Min. Sci., Vol. 41, No. 3, SINOROCK2004 Symposium, Paper 2B 02, 2004.

28) Vervoort A., Govaerts A. : Kaiser effect in tri-axial tests of limestone samples, Proc. Conf. In-situ Rock Stress – Measurements, Interpretation and Application, Trondheim, Norway, (Lu, Li, Kjørholt and Dahle eds.), Taylor & Francis Group plc: London, UK, p.143-149, 2006.

29) Lanaro F., Nakama S., Sato T. : Estimation of in-situ stress field based on core sample damage, J. of the Min. Mat. Proc. Inst. Japan (MMIJ), 2007.

30) Matsuki, K., Kaga, K., Yokoyama, T., Tsuda, N. :Determination of three dimensional in-situ stress from core discing based on analysis of principal tensile stress, Int. J. Rock. Mech. Min. Sci., Vol. 41, p.1167-1190, 2004.

31) Fuenkajorn K., Daemen J.J.K. :. Drilling-induced fractures in borehole walls, J. Soc. Pet. Eng, 1992, No. 2, p. 210-216, 1992.

32) Liu S., Anwar A.H.M.F., Seiki T., Ichikawa Y. : Microcrack generation and propagation in granite during stress relaxation under water-saturated tri-axial conditions, J. Geotech. Geoenv. Eng., Japan Soc. Civ. Eng., Vol. 62, No. 3, p. 623-630, 2006.

This is a blank page.

7. Estimation of in-situ stress field based on core sample damage (Paper 5)

This is a blank page.

Estimation of in-situ stress field based on core sample damage

JAEA,　　LANARO Flavio, NAKAMA Shigeo, SATO Toshinori

1. Introduction

The Japan Atomic Energy Agency (JAEA) is in charge of the Research and Development activities to establish the technical feasibility and reliability of deep geological disposals for high-level radioactive waste (JNC, 2005). In-situ stresses and mechanical properties of the rock are important factors for the design and construction of large and deep underground facilities, such as power stations and radioactive waste disposals. In-situ stresses are also recognized as a primary cause for the development of the excavation damaged zone (EDZ) around these underground facilities. The EDZ will be less stable and essentially more permeable to groundwater than the surrounding rock, which can jeopardize the performance and safety of the facilities in the short and long term. A similar process is the potential damage of the core samples induced by the release of the in-situ stresses due to drilling. The stress release, depending on the level of stress, might induce sample damage in such an extent that the mechanical properties obtained in laboratory do not reflect the in-situ mechanical properties of the intact rock. The quantification of the damage is therefore important because, besides the effect it has on the laboratory results, it also contains precious information about the level of in-situ stress in the rock mass where the samples were taken. In this paper, some of the variation with depth of the uniaxial compressive strength and Brazilian tensile strength of samples of intact Toki granite from Mizunami Underground Research Laboratory (MIU) Construction Site and the adjacent Shobasama Site (Tono Area, Gifu, Japan; Fig. 1) is explained in terms of sample damage. Moreover, the established correlation between the strength and the measured in-situ stresses is exploited for the estimation of the in-situ stresses along boreholes where only laboratory strength results are available.

2. Variation of the strength with depth

When plotting the results of the laboratory tests of uniaxial compressive strength and Brazilian tensile strength, one can observe a rather smooth variation with depth (i.e. distance along the boreholes since most of the boreholes are almost vertical). Such variation justifies the interpolation of the strength results with polynomial functions of the depth. Local variations and heterogeneities can be neglected when considering the scale of the whole borehole that in the analyzed cases is typically around 1000 m. Such smooth variations at borehole scale could not be related to the facies of the Toki granite (medium to coarse grain leucocratic, muscovite- and hornblende-bearing biotite granite), to weathering and alteration (almost inexistent at depth). Moreover, counter-intuitively, the vicinity of the fault zones seems to imply higher values of the strength of the core samples. To reach these conclusions, data from borehole MIU-1 to -4 and AN-1 at the Shobasama Site and from borehole MIZ-1 at the MIU Construction Site were analyzed (Sato et al., 2004).

2.1 Uniaxial compressive strength

Fig. 2 shows the variation of the uniaxial compressive strength with depth along borehole MIZ-1. This borehole, 1300 m long, is vertical down to 380 m depth and then deviates from vertical less than 14°.

2.2 Brazilian tensile strength

Similarly, the variation with depth of the results of Brazilian tests performed on core samples from borehole MIZ-1 also follows a polynomial curve which shape is very similar to that in Fig. 2.

3. Variation of the in-situ stresses with depth

Hydro-fracturing technique was applied in borehole MIU-2 and -3, AN-1 and MIZ-1 to determine the horizontal maximum and minimum stresses, which are also assumed to be principal stresses (Nakama et al., 2005). When observing the plots of these components with depth,
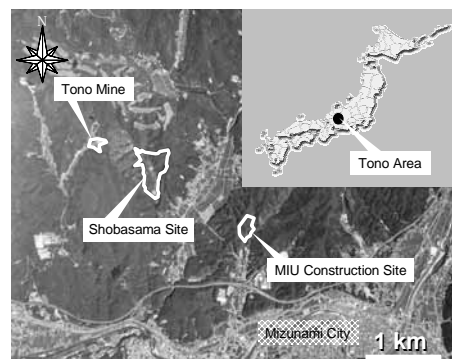

Fig. 1　Location of the MIU Construction Site and Shobasama Site, Tono Area, Gifu Prefecture, Japan
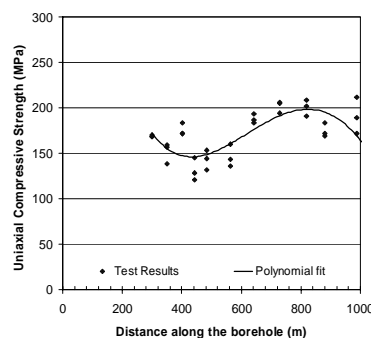

Fig. 2　Variation with depth of the uniaxial compressive strength of core samples of Toki granite along borehole MIZ-1
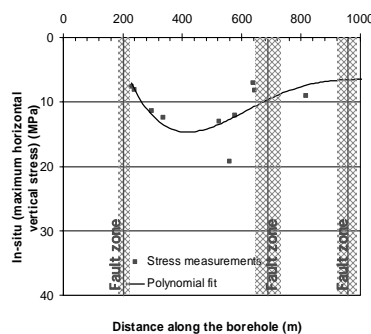

Fig. 3　Variation with depth of the difference between the measured maximum horizontal stress and the vertical stress along borehole MIZ-1

it can be observed that:

a) The ratio between the maximum and minimum stress is invariably 2. Only the maximum horizontal stress will be further considered as an independent variable;

b) The maximum horizontal stress varies rather smoothly with depth. This justifies fitting the data with a polynomial curve so that the stresses away from the measurement points can be estimated;

c) The vertical stress was estimated based on the weight of the overburden, whose density was assumed to be 2620 kg/m^3.

The difference between the in-situ maximum horizontal and vertical stress varies with depth as it is shown in Fig. 3 for borehole MIZ-1.

4. In-situ stress release and sample damage

During drilling through a stressed rock mass, the rock in and around the core undergoes a complicated stress-path. Around the walls and particularly around the bottom of the borehole the rock experiences higher radial stresses due to the removal of the core. The stress concentration at the bottom also produces extrusion of the core with associated axial tensile stresses in the core stub (Sakaguchi et al., 2002). This phenomenon is complicated by the fact that, usually, the directions of the principal stresses, besides spatially varying, are seldom aligned with the axis of the borehole, and the principal stresses have different magnitudes. The combination of high compressive and tensile stresses in the rock just ahead of the borehole bottom might very likely induce damage in the core. For this reason, although the actual level of stress experienced by the core is not known, damage of the core should intuitively depend on the level of in-situ stress preexistent the drilling (Eberhardt et al., 1999). The level of stress can be summarized by:

a) The average stress (e.g. the mean principal stress)
b) The maximum deviatoric stress (e.g. the difference between the magnitudes of maximum horizontal stress and the vertical stress).

4.1 Correlation between strength and in-situ stress

By means of the polynomial interpolations of the uniaxial compressive strength and Brazilian tensile strength, on one hand, and the polynomial interpolation of the maximum deviatoric stress component, it is possible to correlate the strength of the core and the in-situ stresses at the same depth along the boreholes. Fig. 4 shows that the relation between the uniaxial compressive strength and the maximum deviatoric stress is rather linear for all boreholes. Also the Brazilian tensile strength linearly correlates well with the maximum deviatoric stress. No clear correlation could be observed between strength and mean stress, probably because the mean stress in the boreholes varies too little.
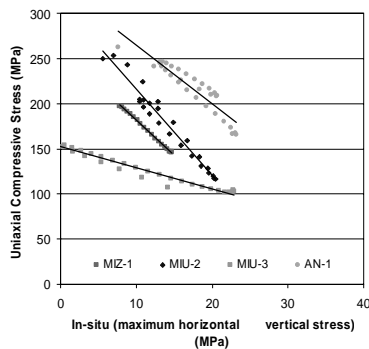

Fig. 4 Correlation between the uniaxial compressive strength and the difference between the maximum horizontal and vertical stress for several boreholes
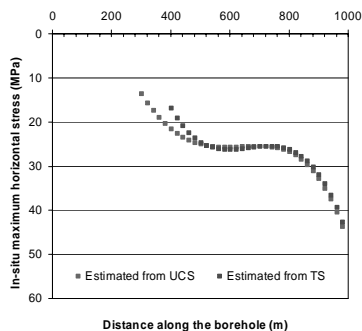

Fig. 5 Estimation of the maximum horizontal stress with depth in borehole MIU-1

4.2 Estimation of the in-situ stresses based on strength results

Knowing the correlation between strength and in-situ stress, the maximum deviatoric stress can be estimated for those boreholes where laboratory test results of intact rock strength are available but in-situ stress measurements are not. The maximum deviatoric stress can be independently obtained exploiting the correlation with the uniaxial compressive strength and the Brazilian tensile strength. Having two independent determinations, the estimation can be optimized by forcing the results of the two stress determinations to coincide by slightly adjusting the correlation parameters. If the vertical stress is assumed to equal the weight of the overburden, the maximum horizontal stress can also be obtained. This was done for borehole MIU-1 (Fig. 5) and MIU-4.

4.3 Validation of the estimated in-situ stresses

A clear sign of damage of the core due to stress release during drilling is core discing. Core discing was not observed in the boreholes where in-situ stress measurements were carried out. However, in borehole MIU-1 and MIU-4, from which uniaxial compressive strength and Brazilian tensile strength were determined in laboratory, core discing was observed on the core at the depth of 902 and 489 m, respectively. For MIU-1, this depth exactly coincides with the depth in Fig. 5 where the estimated maximum horizontal stress exceeded about 32 MPa (i.e. maximum deviatoric stress exceeding 10 MPa).

5. Discussion and conclusions

This research work shows that laboratory results of intact rock strength might differ from the in-situ strength because of the mechanical damage induced by stress release during drilling. Stress damage does not necessarily cause failure of the core as in the case of core discing. Nevertheless, core damage tangibly reduces the strength of the samples and such reduction can be directly related to the level of in-situ stress. Although assuming a rather simple configuration, where the borehole axis is one principal stress direction and the maximum stress is preferentially horizontal, the strength of the samples from uniaxial compression and Brazilian tests is observed to linearly correlate with the difference between the in-situ maximum horizontal stress and vertical stress. Such correlation can be exploited to determine the level of stress along a borehole where frequent samples were tested for strength in laboratory but no stress measurements were available. This method still suffers some limitations due to:

a) The arbitrary choice of the degree of the polynomial functions;
b) The inaccuracy of the interpolation at the end of the analyzed intervals;
c) The empirical relation between the strength of the core sample and the in-situ stress component at the same depth.

However, these limitations might be overcome by numerical modeling the drilling of the core stub in 3D by means of a code that quantitatively determine the damage (e.g. microfracturing) of the sample in different combinations of in-situ stresses.

References

Eberhardt E., Stead D., Stimpson B., 1999. Effects of sample disturbance on stress-induced microfracturing characteristics of brittle rock, Can. Geotech. J, Vol. 36, p. 239-250.

JNC, 2005. H17: Development and management of the technical knowledge base for the geological disposal of HLW, JNC TN1400 2005-022, 68.

Nakama S., Sato T., Kato H., 2005. Status of study on in-situ stress in the Mizunami Underground Research Laboratory, 40th U.S. Symp. on Rock Mech., Alaska Rocks 2005, Anchorage, Alaska, June 25-29, 2005, ARMA/USRMS 05-887.

Sakaguchi K., Iino W., Matsuki K., 2002. Damage in a rock core by induced tensile stress and its relation to differential strain curve analysis, I. J. Rock Mech. Min. Sci., Vol. 39, p. 367-380.

Sato T., Nakama S., Yamada A., Aoki T., 2004. Rock mechanical studies during the surface-based investigation phase of the Mizunami Underground Research Laboratory (MIU) Project. ICGM'04, JNC Report TN7400 2004-010, 123-134.

8. Sample damage investigation by laboratory testing and DDM modelling by FRACOD2D of Brazilian tests on Toki granite (Paper 6)

This is a blank page.

Sample damage investigation by laboratory testing and DDM modelling by FRACOD^{2D} of Brazilian tests on Toki granite

Flavio Lanaro*, Toshinori Sato[×], Akio Funato[+]

* Japan Atomic Energy Agency
[×] Agency for Natural Resources and Energy, ANRE, Japan
[+] Oyo Corporation, Saitama, Japan

Abstract: Numerical scooping calculations by means of FRACOD^{2D} had shown that Brazilian test models present a bend in the relation between the sample deformation perpendicularly to the loading direction and the load itself. The input "direct" tensile strength of the rock could be re-obtained based on the numerical load at the bend. In this study, a similar technique is applied to specially designed Brazilian tests on Toki granite (Gifu, Japan) which also exhibits such bend for a tensile stress in the centre of the samples of about 2.6 MPa. However, the samples show a wide range of Brazilian tensile strengths that appear to be negatively correlated to the level of in-situ stress at the depth where the samples were taken. The correlation was interpreted as an effect of sample damage due to drilling in a stressed rock mass. Numerical models were designed with various pre-existent crack patterns to simulate the sample damage. The numerical results show Brazilian peak strength results ranging between 6.7 and 13.0 MPa, which are very realistic considering that the laboratory Brazilian tensile strength was observed to vary between 4.1 and 11.3 MPa. These values are all larger than the stress at the bend which is then interpreted as the tensile strength of the weakest grains in the granite. It is also shown that the occurrence of newly initiated cracks at the bend completely changes the stress distribution and failure mechanism of the samples: this explains why the Brazilian tensile strength should be higher than the "direct" tensile strength of the rock from uniaxial tests.

1 Introduction

The Japan Atomic Energy Agency (JAEA) is conducting the Mizunami Underground Research Laboratory (MIU) Project in order to develop comprehensive geological investigation and engineering techniques to be applied to deep underground repositories for high level nuclear waste (HLW).

Rock mechanics laboratory testing was carried out on samples of the Toki granite for determining its physical and mechanical properties. Samples were collected at rather uniform spacing along boreholes MIZ-1 at the MIU Construction Site (Mizunami, Gifu Pref., Japan). Brazilian tests were performed for obtaining the "indirect" tensile strength of the Toki granite, in opposition to the macroscopic "direct" strength obtained from uniaxial tensile tests.

Several circumstances, however, seem to indicate that the tested core samples are affected by some degree of damage due to drilling in a stressed rock mass. The in-situ stress release is actually a process of loading that subjects the core to stresses much higher than the in-situ ones. Some evidences of damage can be listed as follows:

- The samples taken from rock mass volumes of better rock quality classes (A and B according to the rock mass classification system by the Central Research Institute of Electric Power Industry, Japan [1] systematically exhibit lower uniaxial compressive and Brazilian strength than samples from the other rock classes (see ref. 2));

- A negative correlation could be observed between the uniaxial compressive and Brazilian strength and the difference between the maximum recorded in-situ horizontal stress and the vertical stress (σ_H - σ_v) at the same depth (see Lanaro et al., 2007a);

- Samples taken at levels with high stress difference (σ_H - σ_h) also show significantly reduced radial P-wave velocity (in this study);

- Micro-cracking of the core samples was also documented during in-situ stress measurements in the vicinity of the site [3),4),5)].

In the literature, several attempts to model the strength and deformability of rock specimens loaded in Brazilian test conditions can be found (e.g. ref. 6), 7), 8)). However, very few cases report the comparison of the numerical results with the experimental results in terms of peak strength. This is symptomatic of the fact that most published numerical simulations of the Brazilian strength greatly overestimate the laboratory strength. Among the reasons, one is the fact that failure in Brazilian conditions is often approached by means analytical methods or finite element models for of continuous media that cannot take into account the formation of cracks appearing inside the rock samples during loading. The drastic change in stress distribution due to crack initiation explains why the assumption of continuity is not suitable for these analyses. Another reason of the mismatch of the peak strength is the weak control over the geometrical and mechanical modelling parameters that characterize for example the Displacement Discontinuity Method applied to Voronoi tessellation meshes [9)] or the Bound-Particle Method [10)].

The present study aims to make a further step validating the numerical code FRACOD^{2D} [11)], which implements the Displacement Discontinuity Method (DDM) and the Boundary Element Method (BEM), by applying it to the simulation of Brazilian tests. Since the reliability of a numerical code lies in its capability of reproducing simple and constrained laboratory test results on natural materials, the case of the Brazilian testing seems an excellent benchmark [12)]. However, potential sample damage slightly complicates the picture. In the numerical models, core sample damage is introduced in the shape of pre-existent micro-cracks of different patterns and length.

2   Brazilian testing

At the MIU Construction Site, different rock and fracture domains are recognised in the Toki granite basement. Such domains identify volumes of granite with approximately the same mechanical properties. In this study, only core samples taken from the Lower Sparsely Fractured Domain (LSFD) are considered for the analyses of previous and new laboratory test results.

2.1 Previous tests

Brazilian testing was performed according to the Japanese Geothecnical Society Standard [13)] on samples with diameter of 35±0.4 mm and length between 33 and 35 mm. Figure 1 shows the variation with depth of the indirect tensile strength obtained for samples of Toki granite from the LSFD in borehole MIZ-1 at the MIU Construction Site. The strength varies rather smoothly with depth and seems to decrease away from the fault zones observed in the borehole. In Figure 1, such variation, observed in many geographically close boreholes, was interpolated with a polynomial curve that consents to estimate the values of the strength for the depth where no samples are available. The indirect tensile strength of samples from LSFD in borehole MIZ-1 has an average value of 6.7 MPa and varies between the extreme values of 4.1 and 12.5 MPa.

At the Site, a negative correlation has been observed between the Brazilian tensile strength and the in-situ stresses [14)]. In particular, this correlation is strongest between the strength and the difference (i.e. deviatoric stress) between the maximum horizontal stress, measured by hydro-fracturing method, and the vertical stress, calculated as the weight of the overburden. The correlation is also proved by the matching of the polynomial interpolation of the deviatoric stress with that of the Brazilian strength with depth (plotted in reversed order). This correlation was interpreted as an effect of sample damage due to the stress-path undergone during drilling. For this

reason, higher deviatoric stresses might cause larger sample damage that in turn reduces the sample strength.

These considerations brought to the design of new Brazilian tests on samples from those depths were the previous laboratory results were not available.
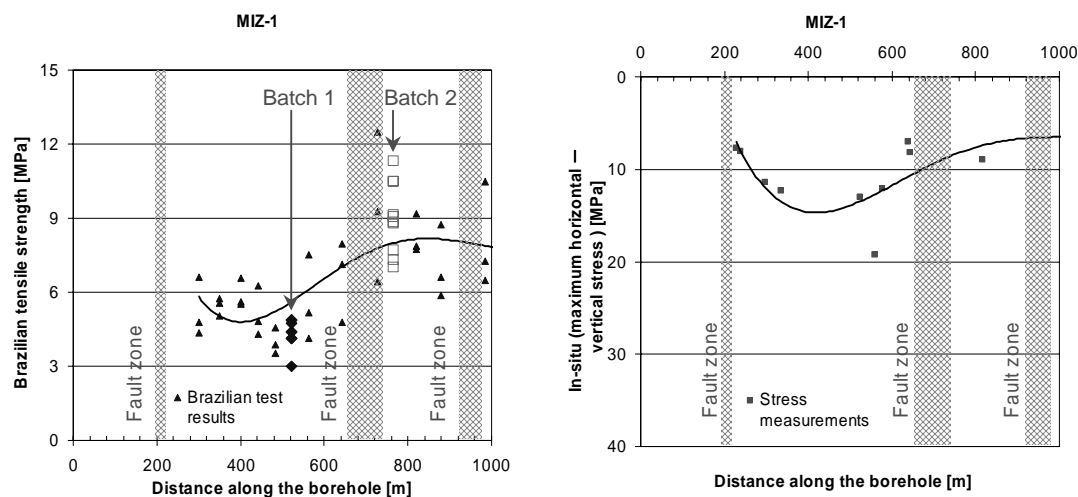

Figure 1. Plot of the tensile strength of the intact Toki granite from MIU Construction Site (left). The position of new samplings is indicated by the red arrows. Plot of the difference between the in-situ maximum horizontal stress and the vertical stress along the same borehole (right). Please notice that the axis of the stress difference is reversed.

2.2 New tests

Samples were selected from those depths in borehole MIZ-1 were the previous laboratory results were not available: between 522 and 523 m (batch 1) and between 765 and 766 m (batch 2), respectively (Figure 1, left). Effective porosity measurements yield values of 0.899% and 0.740% for batch 1 and 2, respectively, clearly indicating different conditions of the samples. The core of borehole MIZ-1 is oriented. The purpose of the tests was:

- To confirm the validity of the polynomial interpolations of the strength with depth;

- To study more in detail the differences of laboratory behavior between the samples taken at the two depths (i.e. between samples with different level of potential damage).

Before testing in Brazilian test conditions, the P-wave velocity in radial and axial direction was measured for all samples.

2.2.1 P-wave velocity measurements

The travel time of P-waves with frequency 200 kHz across the core samples was measured by means of Acoustic Emission receivers with a data sampling interval of 0.1 μs. Seven transversal measurements (at even intervals of 30°) and one axial measurement according to the JGS standard [15] were taken for each sample. Anisotropy of the transversal P-wave velocity was observed for all samples, although it is much stronger for the samples taken at 522 m than for those from 765 m. The ratio between the maximum and minimum P-wave velocity is on average 1.23 for samples from 522 m and 1.04 for samples from 765 m, respectively. Furthermore, the average P-wave velocity for the samples from 522 m (3.49 km/s) is 36% less than the average P-wave velocity for the samples from 765 m depth (5.38 km/s). The azimuth of the maximum P-wave velocity was found to be N17W for samples from 522 m and N32E for the samples from 765 m, respectively.

Plots of the measured P-wave velocity as a function of the orientation with respect to the direction of the maximum P-wave velocity are given in Figure 2 for all samples. The axial P-wave velocity was observed to be rather similar to the average transversal velocity for the sample batch from 522 m. For the sample batch from 765 m, the axial P-wave velocity was 4% lower than the average transversal velocity, which is more than the maximum range of variation of the transversal P-wave velocity (i.e. 3.7% of the average value).
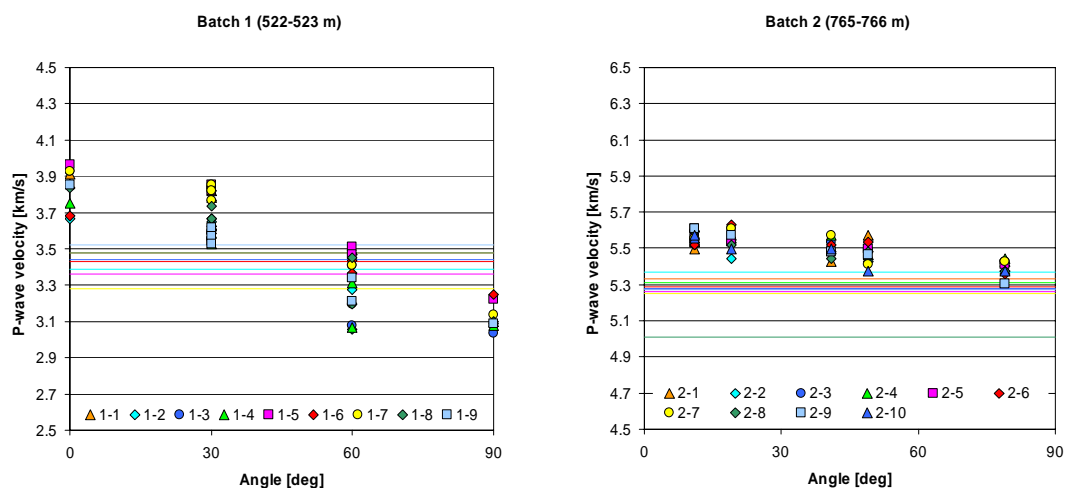

Figure 2. Transversal and axial P-wave velocity of the samples. The symbols show the variation of the transversal P-wave velocity with different angles with respect to the direction of the maximum P-wave velocity. The solid lines show the axial P-wave velocity values. On the left, test results for samples from 522 m depth and, on the right, test results for samples from 765 m depth, respectively.

2.2.2 Testing set-up and sample preparation

Brazilian testing was performed on the two sample batches at the Oyo Corp laboratories, Saitama, Japan. Sample preparation, loading equipment and data acquisition fulfilled the requirements of the JGS standard [13]. The loading equipment was displacement-controlled. Furthermore, the data acquisition system for high frequency measurement allowed a sampling interval of 5 to 10 ms. Lateral expansion of the core with respect to the loading direction was measured by two non-contact optical distance gauges with targets attached onto the sides of the samples. Testing was performed along three directions with respect to the direction of the maximum P-wave velocity previously measured: at 0°, 45° and 90°, respectively.

The core diameter was in all cases about 82.7±0.04 mm while the length varied between 82.7 and 84.5 mm. The core in the first sample batch (depth of 522 m) presented surface waviness. For this reason, the samples were grounded at the diametrical loading points to flatten the surfaces to avoid deleterious stress concentrations. This operation resulted into loading surface areas of various widths between 0 and 12 mm, with an average value of 7 mm. One sample from batch 2 (i.e. 2-7) was also prepared to obtain a loading area of width of about 0.07 mm to study the effect of the sample preparation on the test results.

2.2.3 Test results

The laboratory tests returned the curves of the change of the vertical diameter (i.e. vertical shortening) and of the change of the horizontal diameter (i.e. horizontal lengthening) of the samples from batch 1 (522-523 m, Figure 3) and from batch 2 (765-766 m, Figure 4), respectively.

For the samples from batch 1, Figure 3 shows that the samples tested without grounding of the loading surfaces (1-1, 1-2 and 1-3) seem to behave more softly than the samples with grounded

surfaces. The grounding of the surfaces, however, does not appear to influence the horizontal diametrical displacement of the samples that all fall within the same range of values and have similarly shaped curves. What is particular of the grounded samples is that they actually exhibit two peaks of strength (Figure 5), one relative, and one absolute. Since the Brazilian strength of the samples is defined based on the "maximum" load the sample can support, we are facing an ambiguity in the strength determination. Such ambiguity could not be noticed for the samples without grounded surfaces because of their more brittle behaviour that led to uncontrolled failure before the possible second peak was reached.

For the samples of batch 2, the grounding of the loading surfaces was carried out only on one sample for comparison (Figure 5). This sample (2-7) exhibited almost exactly the same behaviour of sample 2-6 that did not have surface grounding. Therefore, for this batch the influence of grounding can be considered negligible. All the curves of the vertical load versus the change in vertical diameter (i.e. vertical displacements) are very similar to each other. They also exhibit only one maximum value that is used to determine the Brazilian strength of the samples in Figure 5. On the other hand, the curves of the horizontal diameter change show a wide variety of shapes from initially concave, almost linear or convex.

A comparison between the two possible values of the Brazilian strength of the samples from batch 1 is shown in Figure 5 together with the results for batch 2. From this figure, the following remarks can be made:

- The Brazilian strength, whichever peak load is used, vary quite significantly within the results of the same batch (at most between -31 and +38% for batch 1 and between -22 and 24% for batch 2);

- The Brazilian strength calculated for the maximum peak load values for batch 1 very closely approaches the values obtained for batch 2, although the strength calculated based on the first peak is almost half the strength calculated based on the maximum peak load;

- There is no clear dependency of the Brazilian strength of the samples on the angle of loading with respect to the direction of diametrical maximum P-wave velocity measured on the samples. This is despite the very strong anisotropy of the transversal P-wave velocity revealed by the samples in batch 1.

A closer analysis of the curves of vertical load versus horizontal diameter change discloses an interesting feature: all curves show a more or less sharp bend (e.g. change in slope) in the load interval between 20 and 35 kN. Usually, the slope decreases for samples in batch 1, while it might likely increase or decrease for samples in batch 2. Whichever the shape of the curve is, however, the change occurs almost at the same loading level for both sample batches as shown in Figure 7. Moreover, although the results from batch 2 do no show any variation of the load at the bend with the angle of loading with respect to the direction of the maximum P-wave velocity of the samples, the results from batch 1 exhibit clearly decreasing loads at the bend for increasing angles. Thus, the load at the bend also mirrors the anisotropy in of the samples observed in laboratory. This particular load, which could not be exclusively related to any of the particular features of the samples (e.g. batch, grounded surfaces) nor to the loading characteristics (e.g. velocity, step size), could be interpreted as a material feature being more invariant than the Brazilian strength itself. This topic will be called upon in the following sections about numerical modeling.
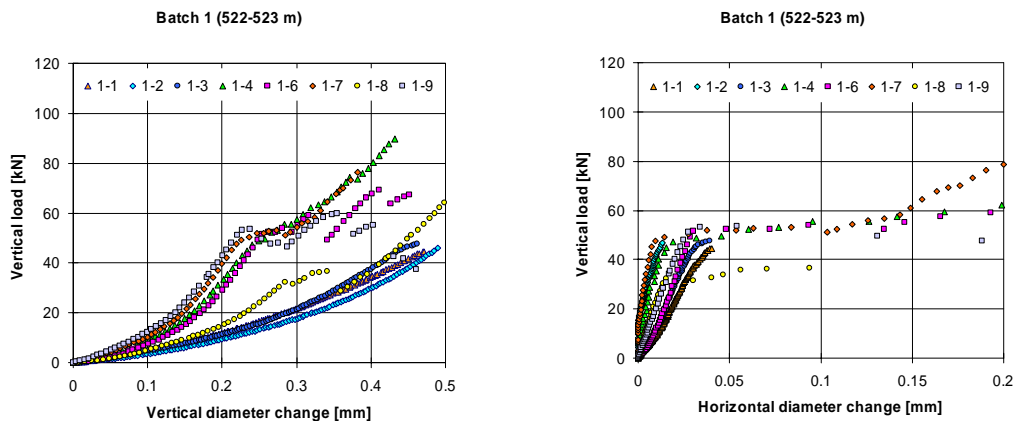
Batch 1 (522-523 m)

Batch 1 (522-523 m)

Figure 3. Vertical diameter change (i.e. vertical displacement) versus vertical load (left) and horizontal diameter change versus vertical load (right) for all samples in batch 1 (from depth 522-523 m).

Batch 2 (765-766 m)
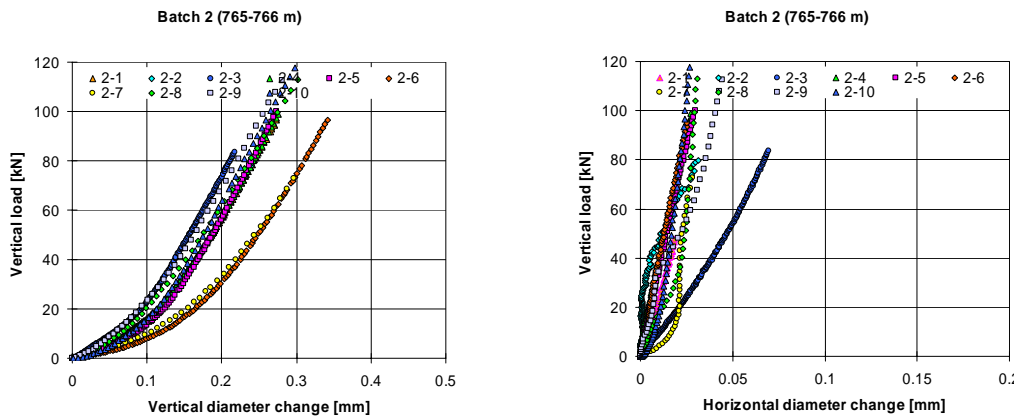
Batch 2 (765-766 m)

Figure 4. Vertical diameter change (i.e. vertical displacement) versus vertical load (left) and horizontal diameter change versus vertical load (right) for all samples in batch 2 (from depth 765-766 m).
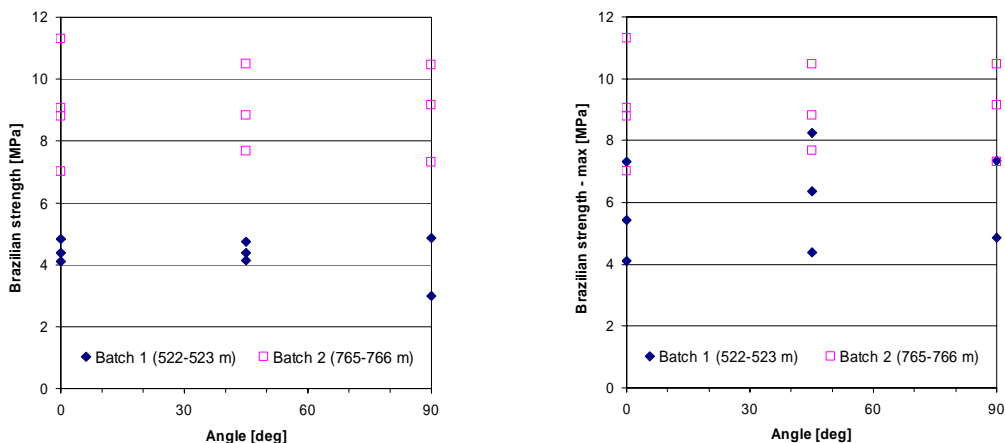
Figure 5. Brazilian strength of the samples from borehole MIZ-1: batch 1 (from depth 522-523 m) and batch 2 (from depth 765-766 m). On the left, the Brazilian strength values as interpreted by the laboratory operators at Oyo Corp.; on the right, the Brazilian strength values as calculated from the maximum applied load on the samples.

Batch 1 (522-523 m)

Batch 2 (765-766 m)
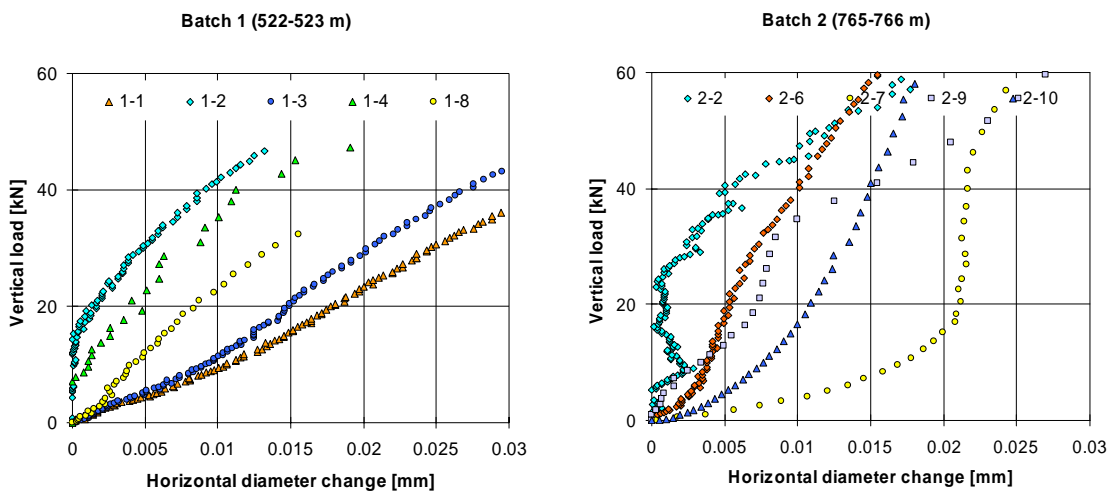
Figure 6. Curves of the horizontal diameter change versus the vertical load for selected samples from batch 1 and batch 2, respectively.

Batch 1 (522-523 m)
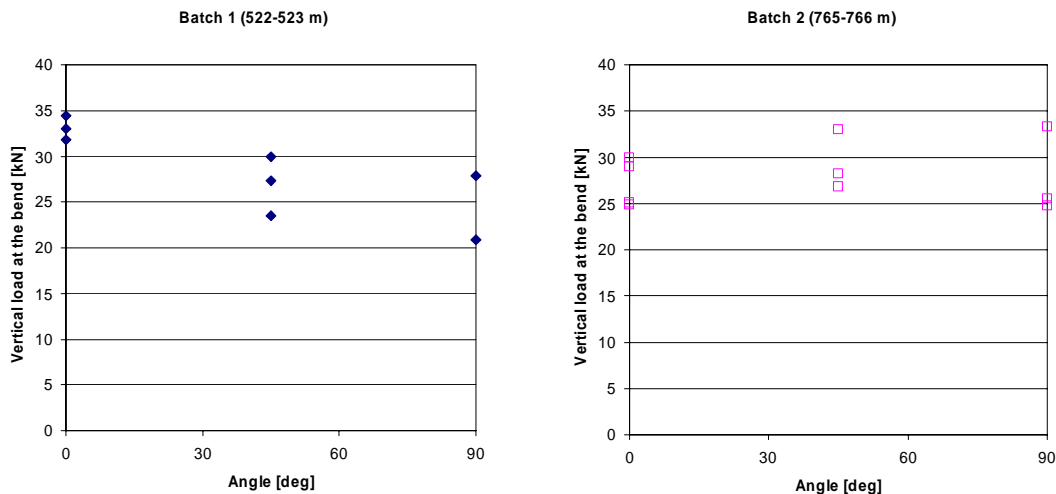
Batch 2 (765-766 m)

Figure 7. Vertical loads evaluated at the bend (i.e. change in slope) of the curves of horizontal diameter change versus vertical load in Figure 6 for all samples in batch 1 (522-523 m, left) and batch 2 (765-766 m, right), respectively.

2.2.4 Sample appearance after failure

Digital pictures, movies and sketches of the sample as in Figure 8 s were taken during and after failure in Brazilian test conditions. Typically, a neat fracture splits the samples into two parts. Sometimes, wedges are formed at the point of application of the loads but sometimes passing-trough fractures ramify and/or sub-parallel cracks develop.

Figure 8. Sketches of the samples from borehole MIZ-1 split in Brazilian tests (samples 1-1 to 1-9 belong to batch 1 from 522-523 m; samples 2-1 t 2-10 belong to batch 2 from 765-766 m). The position of the reference line on the core is indicated by a red dotted line. Its azimuth is N47W for batch 1 and N21E for batch 2, respectively.

3 FRACOD²ᴰ

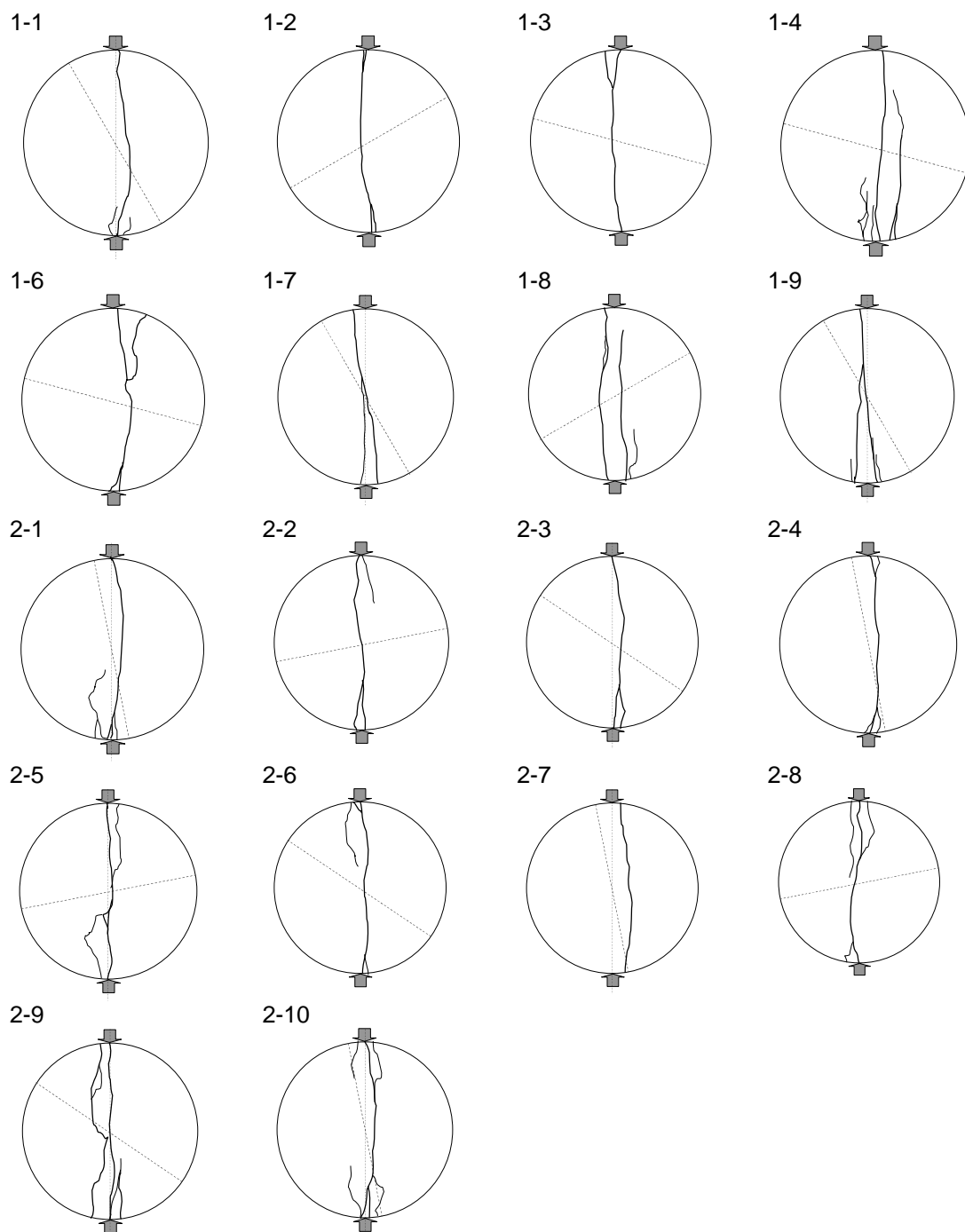FRACOD²ᴰ (FRActure propagation CODe) is a Windows based program that simulates the fracture initiation and propagation in an elastic and isotropic medium [16),11)] . The code implements the boundary element method (BEM) called Displacement Discontinuity Method (DDM). The DDM method is based on the equations describing the stresses and displacements caused by a fracture with constant displacement in an infinite continuum and homogeneous elastic body [17),18)]. The effect of normal and shear deformability of the fractures is superposed to obtain a solvable system of linear equations. Additional constrains to this system are introduced for open fractures (e.g. zero normal stress), fractures in elastic conditions (e.g. linear elasticity) and fractures in failure limit conditions or sliding (e.g. Mohr-Coulomb Criterion).

Pre-existent fractures can propagate and new fractures can be generated either in tension (Mode I) or in shear (Mode II). The propagation criterion proposed by Shen & Stephansson [19)] is implemented where the resultant strain energy rates G_I in Mode I and G_{II} in Mode II are functions of the possible propagation direction θ around the tip of the fracture. The fracture will eventually propagate when the F-Criterion is reached:

$$F(\theta) = \frac{G_I(\theta)}{G_{Ic}} + \frac{G_{II}(\theta)}{G_{IIc}} \geq 1 .$$

where G_{Ic} and G_{IIc} are the critical strain energy rates in Mode I and II, respectively. In other words, the strain energy associated with the presence of a fracture in the elastic body can be expressed as the sum of the energy associated to tension and shear, respectively. Thus, the two strain energy rate components can independently be determined for each direction θ. These values are then introduced in the expression of the F-Criterion to determine whether and in which direction the fracture is supposed to grow.

The length of the newly formed fractures can be either assigned or determined by the spacing of the point grid where fracture initiation can detected in the model. Although microcracking cannot be directly be simulated, the code can simulate the process that takes place when microcrack coalescence develops into meso- and macro-scale fracture propagation. The material in which the fractures can initiate and propagate (i.e. the rock) has elastic deformational properties and a Mohr-Coulomb strength criterion.

3.1 *Material properties, model geometry and boundary conditions*

The material properties of the Toki granite were determined by different laboratory test campaigns with samples from the adjacent Shobasama and MIU Construction Site. In general, the Young's modulus, Poisson's ratio, cohesion and friction angle were found to vary on average between 51 and 58 GPa, 0.26 and 0.34, 34 and 39 MPa, and 52° and 55°, respectively. The friction angle, cohesion, initial and residual aperture of the initiated or propagating fractures were estimated here based on earlier BEM-DDM simulations of the behavior of similar rock types [20)] . On the other hand, experimental values of the normal stiffness and Mode I and II fracture toughness were determined in laboratory on samples of Toki granite from borehole MIU-2 at Shobasama [21)] . The normal stiffness was observed to vary between 720 and 853 GPa/m; the Mode I toughness to vary between 1.73 and 2.39 MPa m$^{0.5}$; and the Mode II toughness to vary between 3.07 and 11.84 MPa m$^{0.5}$ depending on the stress confinement. The shear stiffness was not determined by means of experimental tests and was estimated here based on similar studies (e.g. ref. 22)). All the experimental results and considerations above lead to the choice of the modeling parameters in Table 1.

For crack initiation in Mode I, the models are assumed to have a spatially "random" generation when the ratio between the stress σ and the strength σ_m would exceed 43%. This means that the grid points in the models exhibit randomly generated direct tensile strength values that vary between 2.6 and 6 MPa. The lower value of 2.6 MPa was determined based on the observed bend

in the graph of the total applied load versus the change in horizontal diameter. Fracture generation is also allowed at the boundary of the model defining the borehole walls and core surface. The upper value of 6 MPa was chosen based on previous Brazilian tests.

The models simulate cylindrical specimens of granite of radius 41.5 mm like in the laboratory tests (Figure 9). Some of the analyzed models contain pre-existent fractures of length of 6 mm and various inclinations and patterns. Newly initiated fractures or the propagating portions of pre-existent fractures have a minimum length of 5 mm.

Table 1. Material properties used for the DDM modelling of Brazilian tests.

Material	Parameters	Values
Intact rock	Poisson's ratio	0.33
	Young's modulus	50 GPa
	Friction angle	50°
	Cohesion	30 MPa
	Tensile strength	ranging between 2.6 and 6 MPa
	Mode I fracture toughness	2 MPa m$^{0.5}$
	Mode II fracture toughness	11.5 MPa m$^{0.5}$
Initiated and propagating fractures	Shear stiffness	20 GPa/m
	Normal stiffness	500 GPa/m
	Friction angle	32°
	Dilation angle	0°
	Cohesion before sliding	10 MPa
	Cohesion after sliding	0 MPa
	Initial aperture	10^{-2} mm
	Residual aperture	10^{-3} mm

3.2 Boundary conditions

The load F applied onto the sample is considered uniformly distributed along an flat horizontal edge corresponding to a total angular width α of 10° (Figure 9). This is of course an approximation considering that some of the samples had flattened contact surfaces and some were not flattened (the force was almost punctually applied). Since this angle corresponds to a very little loading surface and due to the symmetry of the section, we assume that frictional effects are negligible. An earlier study, however, showed that the model without friction overestimated the Brazilian strength [12]. On the light of the experimental results presented in this contribution, the overestimation in the earlier analyses might be due to the fact that a tensile strength was assumed to vary between 5.4 and 6 MPa instead of the values assigned here between 2.6 and 6 MPa. The assumption of frictionless contact also gets around the problem of determining the frictional parameters of the contact.
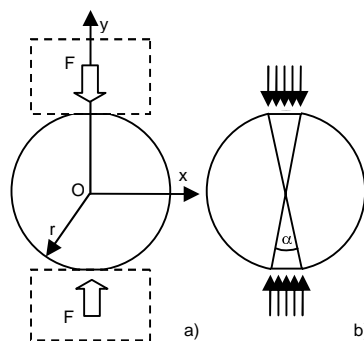

Figure 9. Geometry of the DDM numerical models (a) and the applied boundary conditions (b): no friction is assumed between platens and rock.

3.3 Modelling results

The anisotropy of the P-wave velocity can be explained, other than by intrinsic anisotropy of the rock material, by pre-existing pours and cracks or by some degree of damage of the core during to drilling through a rock with relative high in-situ stresses. Thus, the anisotropy is interpreted as micro-voids or cracks in a preferential direction. Such damage cracks in the rock samples were simplified as parallel discrete fractures in the FRACOD^{2D} models considering the following aspects:

- Influence of the presence of pre-existing cracks

- Influence of the orientation of the pre-existing cracks with respect to the loading direction

- Influence of the pattern of the pre-existing crack

- Influence of the length of the pre-existing cracks.

One model was run with no pre-existing cracks for comparison (Figure 10). Models with pre-existing crack length of 6 mm were designed with six different crack patterns: three with the same geometry loaded along three directions (3°, 45° and 87° between the crack traces and the loading direction); one considered denser cracks at an angle of 45° and; two models featured perpendicular cracks at 30° and 60° with respect to the loading direction (Figure 11). Three models with pre-existing crack of length of 12 mm were analyzed considering angles between the cracks and the loading direction of 3°, 45° and 87° (Figure 12).

No cracks

3 deg A

45 deg A

87 deg A
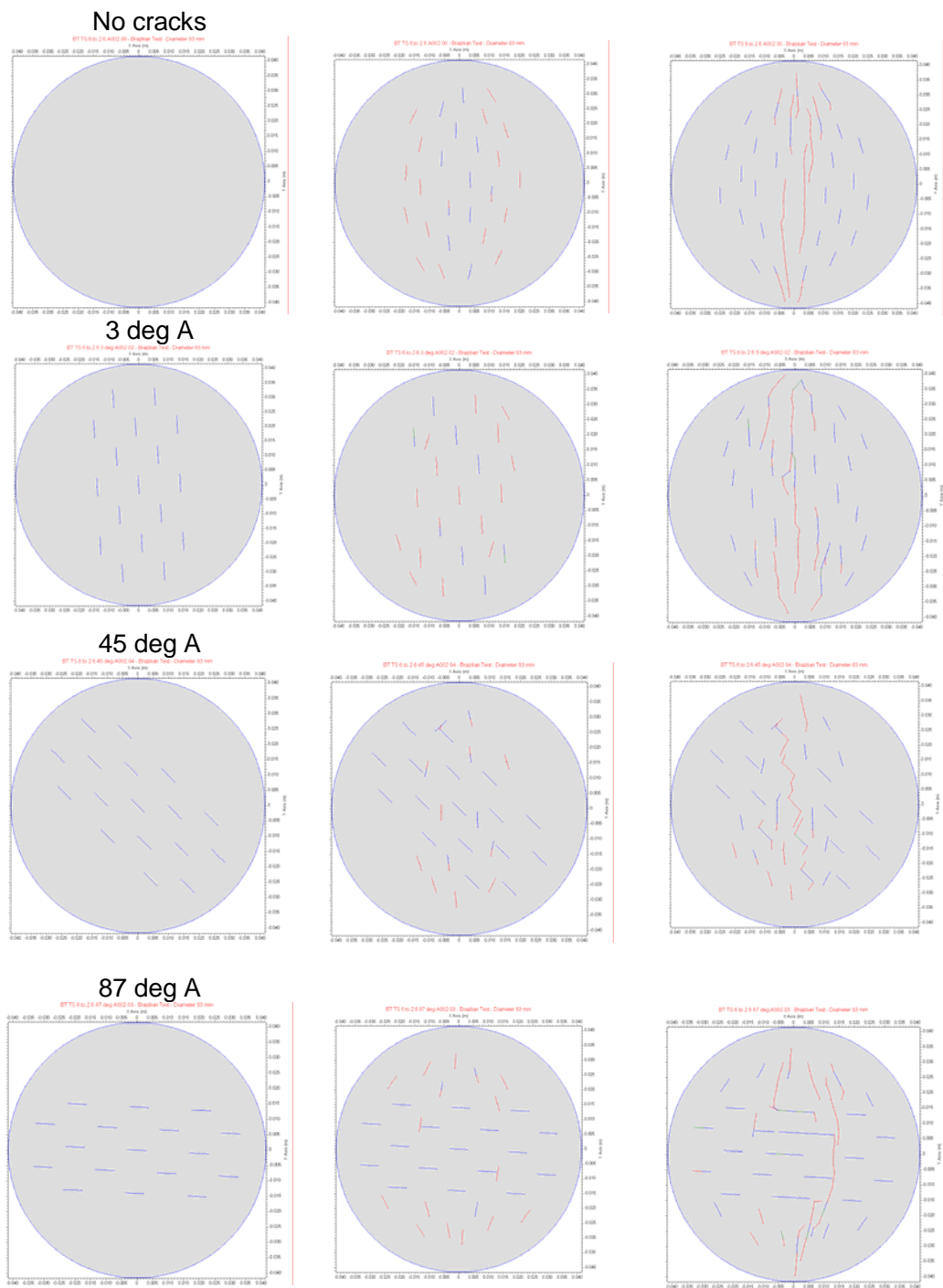
Figure 10. Initial crack geometry and its evolution at an intermediate loading stage and at failure for the FRACOD^{2D} models of Brazilian tests (the length of the pre-exiting and initiated cracks is 6 mm). In blue cracks in elastic conditions, in red cracks in tension and in green cracks in shear failure, respectively.

45 deg B

30 deg A

30 deg B

Figure 11. Additional initial crack patterns and their evolution at an intermediate loading stage and at failure in Brazilian test conditions modelled with FRACOD[2D] (the length of the pre-exiting and initiated cracks is 6 mm). In blue cracks in elastic conditions, in red cracks in tension and in green cracks in shear failure, respectively.
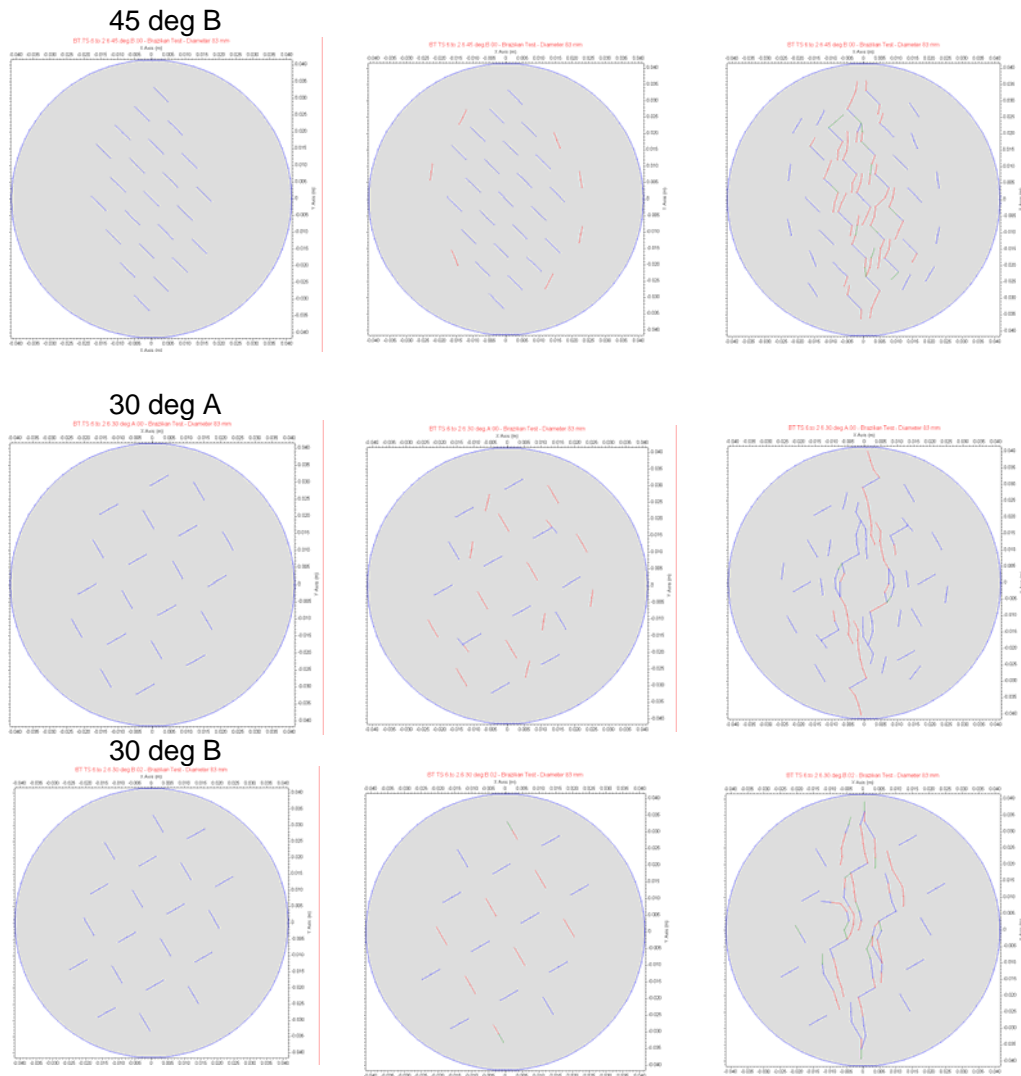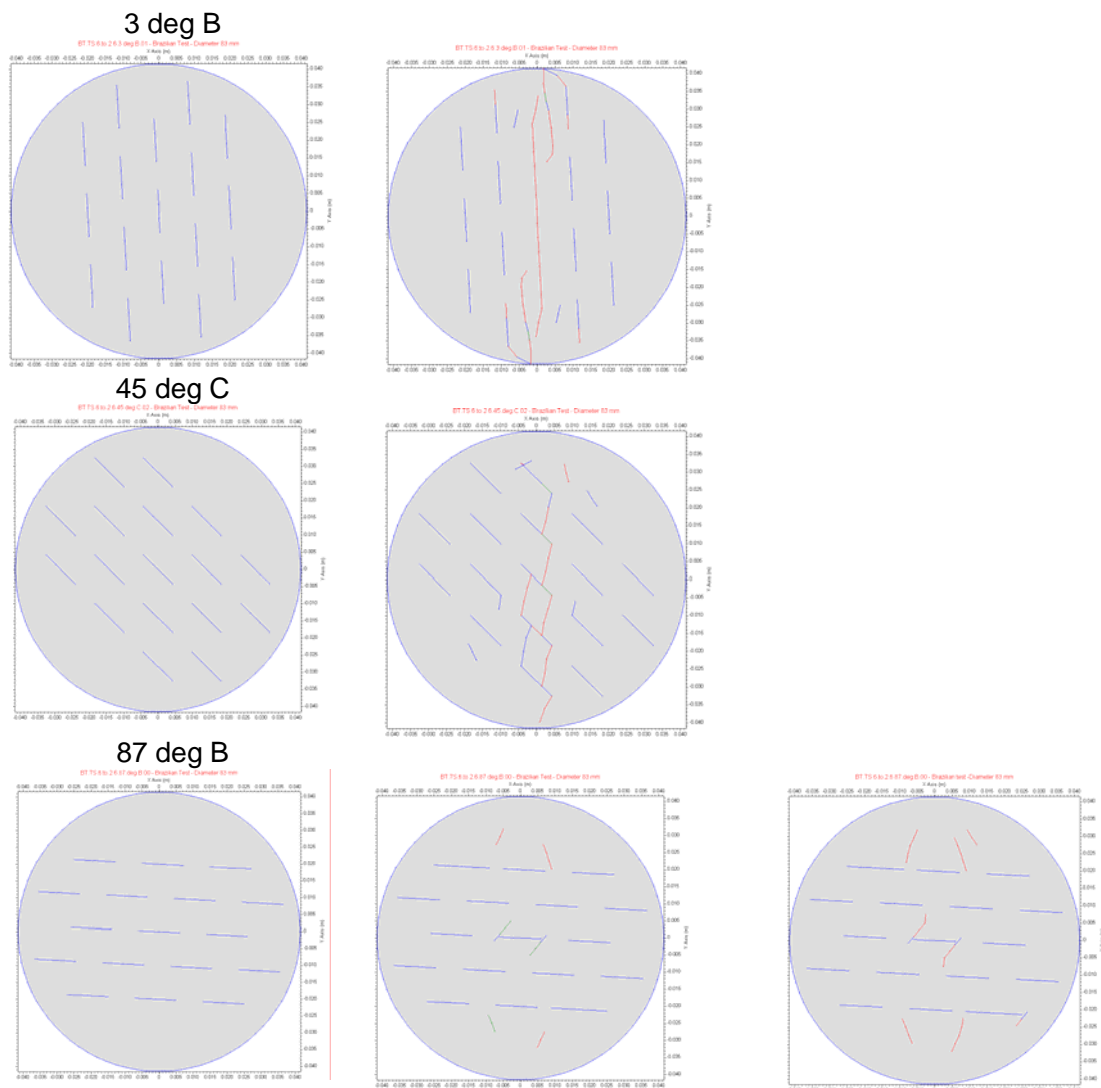
Figure 12. Initial crack geometry and its evolution at failure for the FRACOD^{2D} models of Brazilian tests (the length of the pre-exiting and initiated cracks is respectively 12 and 6 mm). In blue cracks in elastic conditions, in red cracks in tension and in green cracks in shear failure, respectively.

Figure 10, Figure 11 and Figure 12 also show the evolution of the crack pattern during loading. The more numerous the pictures, the larger the strength of the samples. The crack patterns at failure are rather realistic compared to the experimental patterns in Figure 8 considering the simplicity of the initial geometry of the models.

In all models, the initiated fractures avoid the area where pre-existing fractures are located, leading however to stable configurations until the models fail through the propagation of the pre-existing or initiated cracks located along the loading diameter or forming a little angle with it. The propagation starts in tensile conditions, but towards the last steps of the analyses shearing of some material bridges between cracks occur.

Pre-existent cracks inclined at 45° produce echelon-like failure patterns splitting the models into two parts. Pre-existent cracks at a large angle with the loading direction tend to merge with each others at the centre of the model and shift the diametric split of the model in a more peripheral position.

4 Discussion

This section will comment on the laboratory results, on the numerical results and on the comparison of the two results giving some interpretation of the reasons for their matching or mismatching.

4.1 Laboratory results

When plotted together with previous laboratory results, the new Brazilian tests on samples from borehole MIZ-1 confirm the wavy variation of the strength with depth. The polynomial interpolation of the available data predicts well the strength of the samples at the depth where no data were available (see Figure 1, left). This is true irrespective to sample size that in the previous tests was only 35 mm compared to 83 mm in the test campaign. Thus, for the particular grain size of the Toki granite, there seems to be little influence on the Brazilian test results from samples with the two different diameters used at the MIU Construction Site.

The results of effective porosity and P-wave velocity tests indirectly confirm that samples taken from a depth of 522-523 m might present more extensive microcracking that is not shown by the samples taken at the much higher depth of 765-766 m. This confirms the suggested negative correlation between the in-situ differential stress and the strength of the samples that was hypothesized before the tests. Moreover, it seems correct to conclude that the fault zone between 648 and 726 m affects the differential in-situ stress by reducing its magnitude. Therefore, the samples taken in the vicinity of this fault show comparatively higher Brazilian strength values.

The P-wave velocity measurements allowed the determination of the anisotropy directions in the core samples. This was rather marked for samples from batch 1, while the deeper samples from batch 2 seem to be more isotropic transversally to the core axis. The direction of the maximum P-wave velocity was compared to the direction of the in-situ maximum horizontal stress obtained from hydro-fracturing method in the borehole. Figure 13 (left) shows that the difference between the two orientations is between 50° and 67°, which means only 40° and 23° from perpendicularity.

Similarities can be also found in the granitic to granodioritic rock at Forsmark, Sweden. Figure 13 (right) compares the orientation of the maximum horizontal stress obtained from hydro-fracturing methods in borehole DBT-1 [23] and KFM01B [24] with the orientation of the maximum P-wave velocity measured on core samples from the adjacent borehole KFM01A [25] . The two orientations can differ from almost zero for some points at depth between 200 and 300 m to roughly 90°. This would also explain why a tentative correlation with the foliation observed on the core, which is rather constantly oriented at Forsmark, could not explain the variation of the orientation of the maximum P-wave velocity transverse to the samples with depth [26] . This is because the anisotropy of P-wave velocity was probably rather an effect of the release of the in-situ stresses during drilling.

Anisotropy of the samples from batch 2 can be seen when comparing the P-wave velocity transversally to the core axis with that P-wave velocity parallel to it. In this direction, the P-wave velocity is even lower than the minimum one measured transversally. This can also be due to stress release effects that, for more uniform horizontal stresses, might manifest preferentially as micro-fracturing at a right angle with the core axis (analogous to core disking).
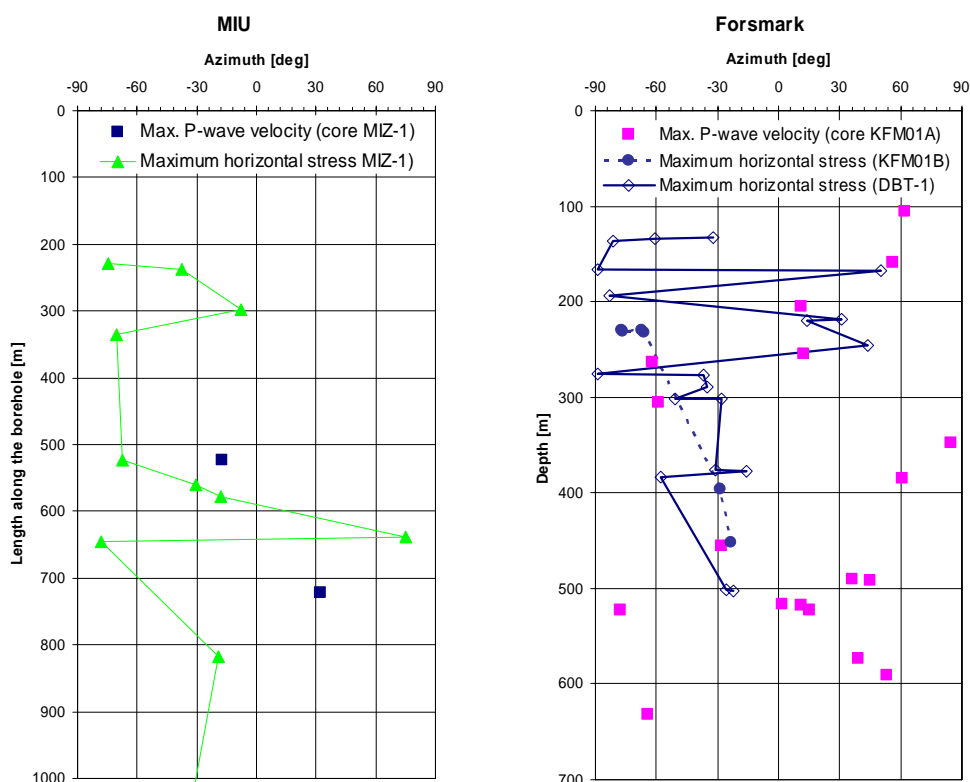
Figure 13. Plot of the orientation of the in-situ maximum horizontal stress and the orientation of the maximum P-wave velocity in the samples from borehole MIZ-1 at the MIU Construction Site (left). For comparison, the same kind of data are shown for adjacent boreholes KFM01A, KFM01B and DBT-1 at Forsmark, Sweden (right).

4.2 Comparison between laboratory and numerical results

The performed analyses aim to reproduce the experimental behaviours presented in Sec. 2.2. It was observed that the models with pre-existing crack length of 12 mm compare well with the experimental results from sample batch 1, while results for pre-existing crack length of 6 mm better reproduce the behavior of sample batch 2.

The following features could be observed analyzing the shape of the curves of the total vertical load versus the change in length of the vertical sample diameter (Figure 14, where positive values of the diameter change represent shortening of the distance between the loading platens):

a) The experimental results show a stiffening behavior of the samples for the initial loading steps up to a total load of about 30 kN (for batch 1) and 20 kN (for batch 2). This is probably due to the closure of cracks and voids in the direction perpendicular to loading. However, the numerical results do not exhibit any stiffening but rather a constant secant stiffness. This is a consequence of the assumption in FRACOD[2D] of linear deformability of the pre-existent cracks that are characterized by only one value of the normal and shear stiffness K_n and K_s for all stress levels. Since the input values in the models are taken from laboratory results with normal stresses acting on the fractures of the order of 4 to 10 MPa, it is clear that the deformability of the laboratory samples during the first loading steps cannot be followed by the numerical models.

b) Beside the non linear portion of the diagrams, the experimental results show that the vertical load is linearly related to the change in vertical diameter length. This evidence is

confirmed by the numerical results that also show a secant slope of the curves (stiffness) very similar to that of the laboratory results.

c) The Brazilian tensile strength in laboratory does not show a clear variation with respect to the angle of loading with respect to the direction of the maximum recorded P-wave velocity. On the other hand, the numerical peak vertical load is larger for pre-existing cracks that form a little angle with respect to the loading direction. Among the analyzed direction, the lowest peak load is recorded for pre-existing cracks oriented at 45° with respect to the loading direction and it is only marginally different from the case with cracks perpendicular to the loading direction, at least for short pre-existing cracks.

d) Both the models simulating samples from batch 1 and 2 reach a peak load similar to the experimental results, confirming the soundness of the choice of material parameters and geometries of the numerical models. This also means that longer pre-existing cracks might be equivalent to the crack and void patterns of the potentially damaged samples of batch 1.

Figure 14. Comparison between the numerical and experimental results of total vertical load versus vertical change in diameter of samples in Brazilian test conditions (positive values indicate shortening of the distance between the platens): sample batch 1 (left) and sample batch 2 (right), respectively.
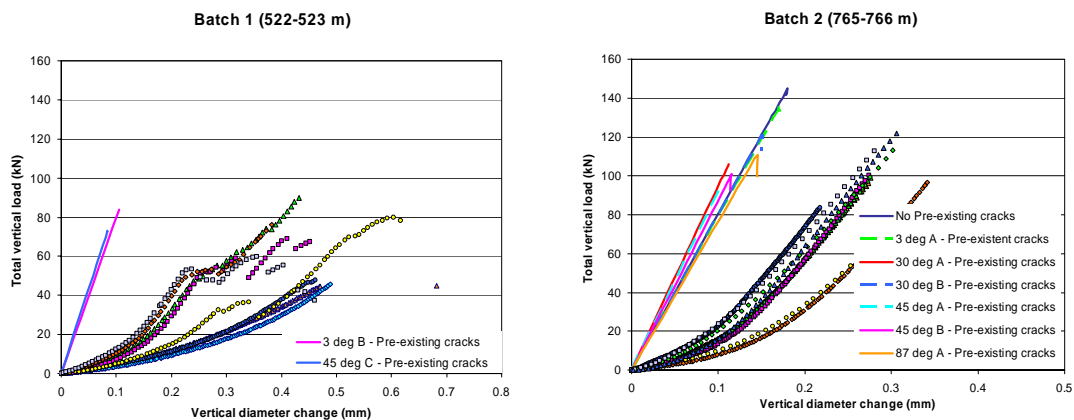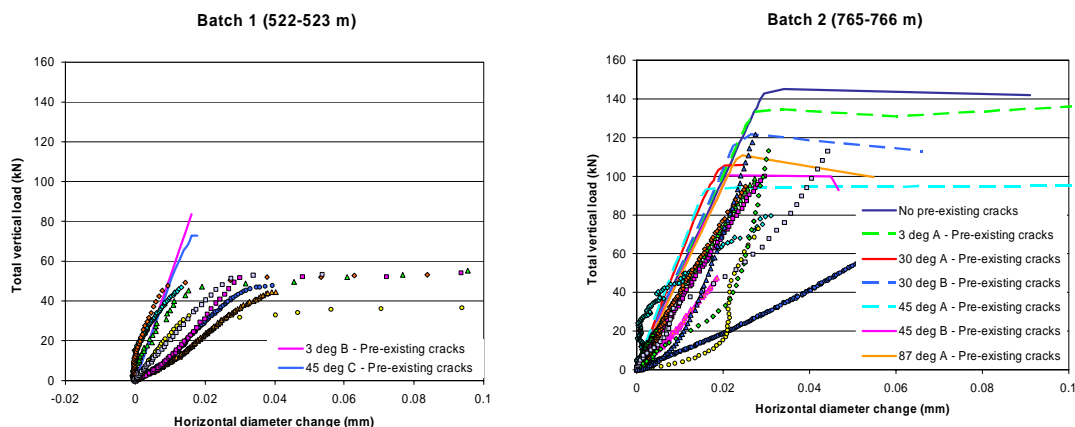

Figure 15. Comparison between the numerical and experimental results of total vertical load versus horizontal change in diameter of samples in Brazilian test conditions (positive values indicate lengthening of the horizontal diameter): sample batch 1 (left) and sample batch 2 (right), respectively.

As for the laboratory results, the variation of the diameter length in the direction perpendicular to loading could be monitored in the numerical models (Figure 15, where positive values of the displacement represent lengthening of the horizontal diameter). The following remarks can be made:

1) Stiffening of the samples during the first stages of the loading was not observed in the direction perpendicular to loading for both the numerical and the experimental results (with some exceptions). The increase in length of the horizontal diameter follows quite linearly the variation of the vertical load. The slope of the curves for the two cases is very similar.

2) In laboratory, the diameter perpendicular to the loading direction show a quite clear and consistent bend for all samples and batches at a loading force between 20 and 35 kN (Figure 7). This bend, that does not seem to be correlated to the stiffening of the sample in the vertical loading direction, can occur either in relation to stiffening or a weakening of the samples in the horizontal direction. However, only the numerical models with no pre-existing cracks or cracks at a right angle with the loading direction show such a clear bend although not as clearly as in laboratory. Furthermore, the bend in the numerical results is always a weakening of the samples (i.e. the slope of the curves diminishes). For the models with bend, this is predicted for a total force of 28 kN that corresponds to the appearance (i.e. initiation) of the first tensional cracks. For this reason the lowest value of the randomly generated tensile strength in the numerical models was assigned to be 2.6 MPa.

3) Although the relation between the vertical load and vertical diameter change maintains its linearity until the last loading step, the relation between the vertical load and the horizontal diameter change reaches a plateau of the vertical load where increasing displacements are measured in relation to the propagation of the cracks at failure. This also represents the release of deformational energy into cinematic energy due to the formation of new crack areas that corresponds to the explosive behavior recorded in laboratory for all samples.

4.3 About the verisimility of the model crack patterns

To reproduce the anisotropy of the core samples, pre-existent crack patterns were designed to affect the strength and deformability of the models in different ways depending on the loading direction. Thus, the reduction of the strength between the two sample batches was assumed to depend on different levels of damage and micro-cracking due to different level of stresses arising inside the core due to drilling. The models succeeded in reproducing a reduction of the peak strength with respect to the model with no cracks by means of a lengthening of the pre-existent cracks (from 6 to 12 mm). This could re-conduct the peak strength of the models to values comparable to the results in laboratory.

However, the peak strength of the models, as for the laboratory results, does not show the same anisotropy as for the P-wave velocity. In fact, the minimum peak strength occurs for pre-existent cracks oriented 45° with respect to the loading direction. This means that, even if the assumed crack patterns would probably provide similar anisotropy of the deformability and P-wave velocity, they don't seem to behave the same way as the crack patterns of the real core samples. This could be explained by the tri-dimensionality of the stress field around the core stub during drilling that would produce more complex crack patterns than those assumed in this study.

The stress pattern in the core stub during drilling has been shown to depend on the direction and magnitude ratio of the principal stresses (e.g. ref. 27)). Moreover, some rock types show preferential direction of the natural micro-cracks that seems to depend on geological factors other than the drilling (e.g. ref. 28)). For this reasons, the crack patterns assumed in this study failed to reproduce the real distribution of the flaws and micro-cracks of the core samples. If cracks are opened or generated by drilling, then they could probably be located peripherally to the core and

mainly perpendicularly to the direction of the maximum in-situ compressive stress component in the plane of the cross-section of the core. The presence of such localised fractures would, other than affect the P-wave velocity in different directions, also change the position at which new micro-cracking is first experienced by the numerical models. This would also imply that superficial micro-cracking of the core could make the Brazilian tests more prone to failure in the vicinity of the loading platen, departing from the general opinion that the split of the samples should start from the centre.

To test these hypotheses, three new FRACOD^{2D} models were designed with parallel and peripheral pre-existent cracks as it is shown in Figure 16. These fracture patterns would satisfy the condition of anisotropy of the P-wave velocity but also that of localized damage in the form of pre-existing cracks. Despite the length of the pre-existing cracks is only 10 mm, the new models show lower peak strength than the models with crack length of 12 mm presented in Figure 12 (except for pre-existing cracks parallel to the loading direction). Furthermore, the most important feature shown by the laboratory results, which is the bend in the graph of the total load versus the diameter change in the perpendicular direction, is also exhibited by these new numerical models. The bend might therefore be related to the tensile strength of the rock material and not to pre-existing crack patterns in the core samples. The high peak strength of the model with cracks parallel to the loading direction (3 deg N) would suggest that the real core samples probably present patterns of pre-existing microcracks that are combinations of the three basic cases presented here in different proportions. This would guarantee at the same time anisotropy of the P-wave velocity across the core and a reduced peak tensile strength with respect to an intact rock sample. Moreover, these crack configurations would imply that the centre of the core samples should not be affected by cracking due to drilling as much as the perimeter. The model with peripheral cracks parallel to the loading direction also shows that peripheral cracks do not seem to affect the peak strength compared to a model without pre-existing cracks (as for the no-crack model in Figure 10). It should be reminded here that the two-dimensional models only consider cracks parallel to the core axis.
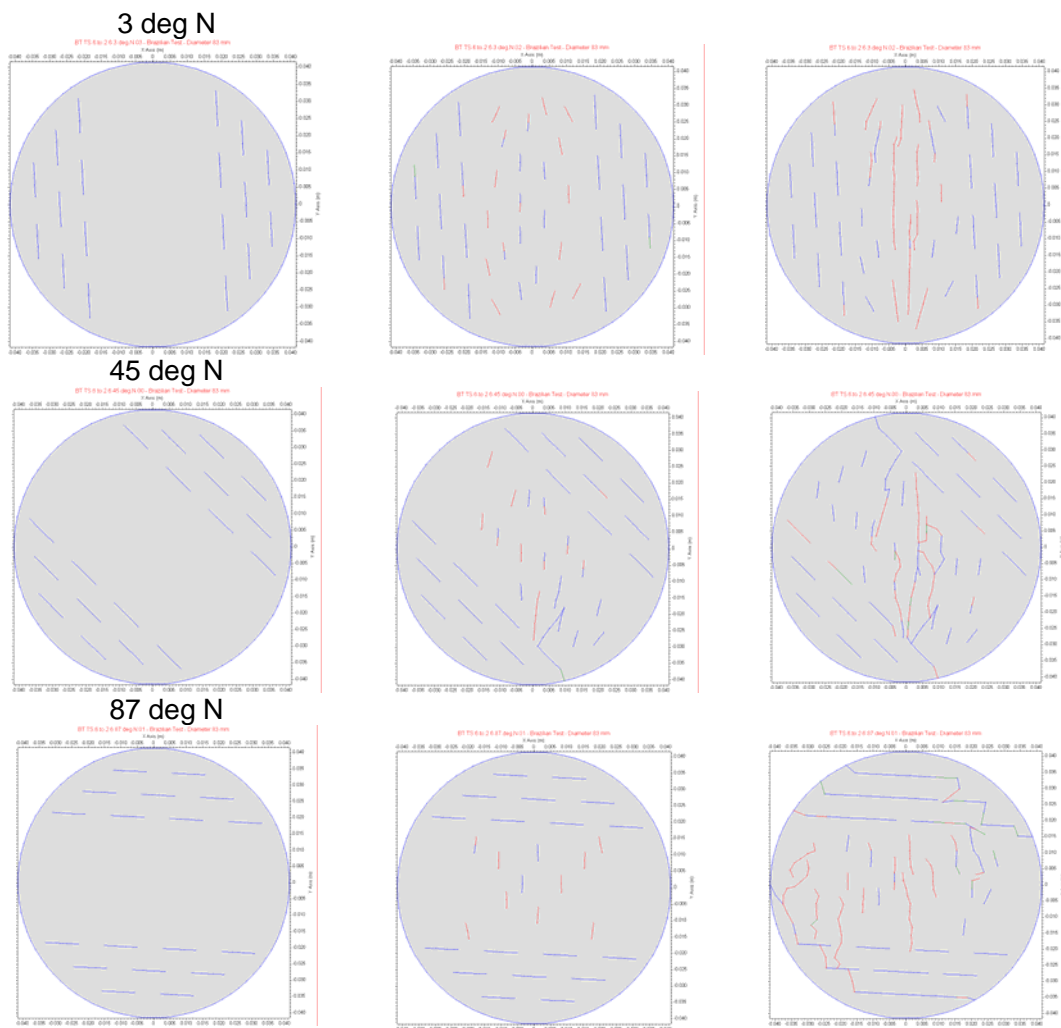
Figure 16. New crack patterns designed based on the comparison between laboratory and previous modelling results with FRACOD^{2D} and their influence on the failure mechanism (the length of the pre-exiting and initiated cracks is 10 mm). In blue cracks in elastic conditions, in red cracks in tension and in green cracks in shear failure, respectively.
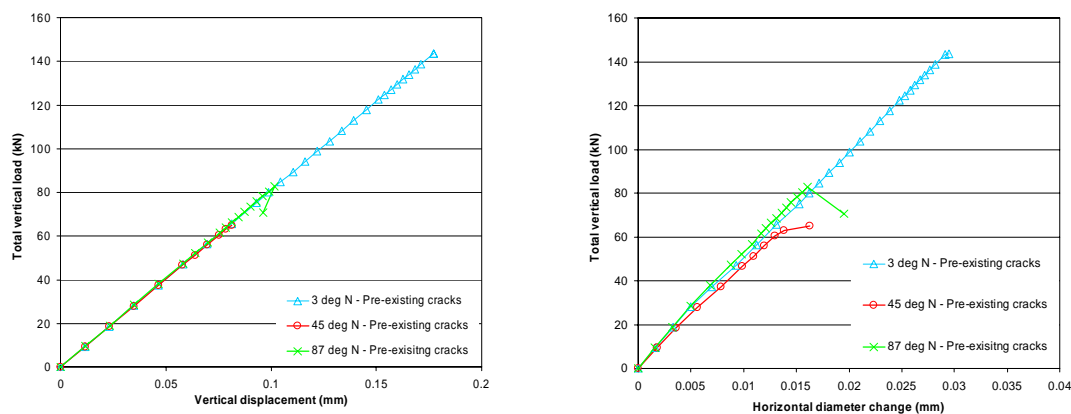
Figure 17. Total vertical load versus horizontal change in diameter of samples in Brazilian test models with new crack patterns (positive values indicate lengthening of the horizontal diameter): sample batch 1 (left) and sample batch 2 (right), respectively.

More accurate studies on the distribution of micro-cracks in core samples of different diameter taken from rock masses with relatively low and high in-situ stresses are needed. Even tri-dimensional modelling of the core behaviour during drilling by means of a fracture propagation code is recommended (e.g. ref. 29)). Studies of visible micro-cracks in thin sections of core samples are ongoing but yet not available to this study.

5   Conclusions

The new laboratory results on core samples of Toki granite confirm the hypothesis made based on scooping calculations by FRACOD[2D] carried out in a previous study [12] . That study predicted a bend in slope in the graphs of the change in length of the sample diameter in the direction perpendicular to loading versus the total load. This was also observed in the laboratory results (Figure 6). In all laboratory results, such bend was observed approximately at the same level of load (30 kN) that corresponds to a tensile stress perpendicular to the loading diameter in the centre of the sample of about 2.6 MPa. This value was assumed as the minimum tensile strength of the grains composing the Toki granite and input into the numerical models.

Besides having a lower Brazilian test strength and average P-wave velocity in the direction perpendicular to the core axis than the other samples, samples from 522 to 523 m along borehole MIZ-1 (batch 1) also showed a very strong anisotropy of the P-wave velocity. Pre-existent crack patterns were introduced in the numerical models to take into account anisotropy and sample observed in the form of reduced P-wave velocity. As expected, pre-existent cracks reduced the peak load of the numerical models. However, the intuitive assumption that a larger Brazilian strength would be observed parallel to the direction of the maximum P-wave velocity could not be confirmed for all models. This mismatch may indicate that the crack patterns initially assumed for the numerical models are different than those present inside the core samples. Based on this result, additional fracture patterns compatible with the P-wave velocity measurements and with the assumed peripheral core damage due to drilling were considered. The new analyses show that the fracture patterns with peripheral cracks, other than providing a peak strength very similar to that of the tested samples, also show the well defined bend observed in laboratory in the graph of the total load versus the diameter change in the direction perpendicular to loading. In laboratory, this tensile stress in the centre of the samples slightly diminished when the loading direction was varied from parallel to perpendicular to the direction of the maximum radial P-wave velocity.

The value of the input tensile strength of the intact rock in the models was assumed to be randomly assigned in the interval between 2.6 and 6 MPa. Contrary to the expectations, such low values of the tensile strength occurring at some grid points in the models did not significantly affect the peak strength of the models. On the other end, this was the cause of the early initiation of cracks around the centre of the samples that completely changes the stress distribution and the failure mechanisms exhibited by the models. Such initiated cracks lead to stress concentrations and gradients that allow the sample to resist load larger than that corresponding to the input tensile strength of the rock, despite the presence of crack patterns accounting for sample damage. The numerical models provide peak strengths varying between 6.7 and 13.0 MPa that are rather close to the laboratory results between 4.1 and 11.3 MPa. This also confirms the commonly accepted believe that the Brazilian strength overestimates the "direct" tensile strength of the material obtained from uniaxial tests.

This study shows, beside the validation of the code, that FRACOD[2D] could also be used to gain precious insights on the possible patterns of cracks inside the core samples from borehole MIZ-1 at JAEA's MIU Construction Site. Such crack patterns are probably due to sample disturbance and damage due to the drilling processes in a stressed rock mass. The values of the Brazilian tensile strength could also be successfully estimated by means of their negative correlation with an in-situ stress component (i.e. difference between the maximum horizontal stress and the vertical stress) as proposed in a previous study [14] .

6   Acknowledgments

7   References

1) Kikuchi K., Fujieda M., Oka N., Kobayashi, T. : Geotechnically integrated evaluation on the stability of dam foundation rocks, Journal of the Japan Society of Engineering Geology, Special Edition, Japan Society of Engineering Geology, p.103-118 (in Japanese), 1984.

2) Hashiba H.: Personal communication, JAEA, 2006.

3) Kato H.: In situ stress measurements in MIU-3 borehole using hydraulic fracturing, the Japan Nuclear Cycle Development Institute, Report JNC TN7400 2000-005 (in Japanese with English abstract), 2000.

4) Xue Z. : Experimental study on characterisation of microcracks in Toki granodiorite using Differential Strain Curve Analysis, the Japan Nuclear Cycle Development Institute, Report JNC TN7400 2000-003 (in Japanese with English abstract), 2000.

5) Kato H.: Differential Strain Curve Analysis on Toki granite for evaluationg the rock mechanical effects of Tsukiyoshi fault, the Japan Nuclear Cycle Development Institute, Report JNC TN7400 2002-006 (in Japanese with English abstract), 2002.

6) Cai M, Kaiser P.K. : Numerical simulations of the Brazilian test and tensile strength of anisotropic rocks and rocks with pre-existing cracks, Int. J. Rock Mech. Min. Sci., Vol. 41, Proc. SINOROCK2004 Symposium, Paper 2B 03, 2004.

7) Zhu W.C., Tang C.A.: Numerical simulation of Brazilian disk rock failure under static and dynamic loading, Int. J. Rock Mech. & Min Sci., Vol. 43, p. 236-252 , 2006.

8) Ganne P., Vervoort A. : Characterisation of tensile damage in rock samples induced by different stress paths, Pure Appl. Geophys., Vol. 163, p. 2153-2170, 2006.

9) Lavrov, A., Vervoort, A., Wavers, M., Napier, J. A. L. : Experimental and numerical study of the Kaiser effect in cyclic Brazilian tests with disk rotation, I. J. Rock Mech. & Min. Sci., Vol. 39, 3, p. 287-302, 2002.

10) Potyondy D.O., Cundall P.A. : A bounded-particle model for rock, Int. J. Rock Mech. Min. Sci. & Geomech. Abstr., Vol. 41, p. 1329-1364, 2004.

11) FRACOM Ltd : FRACOD^{2D} – Two dimensional fracture propagation code (Version 2.2) – User's Manual, p. 82 ,2006.

12) Lanaro F., Sato T., Rinne M., Stephansson O.: Modelling Brazilian tests with FRACOD^{2D} (FRActure propagation CODe), to be submitted to Int. J. Rock Mech. & Min. Sci, 2007b.

13) JGS : Method for splitting tensile strength test on rocks, Designation JGS 2551-2002, the Japanese Geotechnical Society ,2002.

14) Lanaro F., Sato T., Nakama S. :. Spatial variability of the compressive strength of the Toki granite at the Shobasama and Mizunami Construction Site, Japan, to be submitted to Rock Mech. & Rock Eng., 2007a.

15) JGS :. Method for Laboratory Measurement of Ultrasonic Wave Velocity of Rock by Pulse Test, JGS 2110-1998, the Japanese Geotechnical Society, 1998.

16) Shen, B. : Mechanics of fractures and intervening bridges in hard rocks, PhD Thesis, Royal Institute of Technology, Stockholm, Sweden, 1993.

17) Crouch S.L. : Solution of plane elasticity problems by the displacement discontinuity method, I. J. Num. Methods Engng., Vol. 10, p. 301-343, 1976.

18) Crouch S.L., Starfield A.M. : Boundary element methods in soil mechanics, George Allen & Unwin Ltd, London, UK, p. 79–109, 1983.

19) Shen B., Stephansson O. : Modification of the G-criterion of crack propagation in compression, I. J. Engng. Fracture Mech., Vol. 51(1), p. 73-85,1993.

20) Stephansson O., Shen B., Rinne M. : The geomechanical evaluation and analysis of surrounding rock mass response to excavation of research shafts and galleries in MIU Project, FRACOM Ltd, p. 89, 2003.

21) Backers T. : Mode I and Mode II fracture toughness testing and fracture normal stiffness estimation of Tono-Granite, GeoForschungZentrum (Potsdam, Germany), p.18, 2002.

22) Olofsson I., Simeonov A., Stephens M., Follin S., Nilsson A.-C., Röshoff K., Lindberg U., Lanaro F., Fredriksson A., Persson Lars. : Site descriptive modelling Forsmark, stage 2.2. A fracture domain concept as a basis for the statistical modelling of fractures and minor deformation zones, and interdisciplinary coordination, the Swedish Nuclear Fuel and Waste Management Co, SKB R-07-15, 2007.

23) Sjöberg J., Lindfors U., Perman F., Ask D. : Evaluation of the state of stress at the Forsmark site. Preliminary site investigation Forsmark area - version 1.2, the Swedish Nuclear Fuel and Waste Management Co, SKB R-05-35, 2005.

24) Lindfors, U., Perman, F., Sjöberg, J. : Evaluation of the overcoring results from borehole KFM01B – Forsmark site investigation, the Swedish Nuclear Fuel and Waste Management Co, SKB P-05-66 , 2005.

25) Tunbridge L., Chryssanthakis P. : Forsmark site investigation – Borehole KFM01A. Determination of P-wave velocity, transverse borehole core, the Swedish Nuclear Fuel and Waste Management Co., SKB P-03-38, 2003.

26) SKB : Preliminary site description – Forsmark area – Version 1.2, the Swedish Nuclear Fuel and Waste Management Co, SKB R-05-18, 2005.

27) Li Y., Schmitt D.R. : Effects of Poisson's ratio and core stub length on bottomhole stress concentrations, Int. J. Rock Mech. Min. Sci., Vol. 34, p. 761-773, 1997.

28) Chen Y., Nishiyama T., Kusuda H., Kita H., Sato T. : Correlation between microcrack distribution patterns and granitic rock splitting planes, Technical Note, Int. J. Rock Mech. Min Sci., Vol. 36, p. 535-541, 1999.

29) Shi J., Shen B., Rinne M. : FRACOD^{3D} – Developing 3-Dimensional Displacement Discontinuity Code with Cracks Growth, FRACOM Ltd, Report in preparation, 2007.

This is a blank page.

9.   Modelling the formation of sheeting joints with FRACOD2D (FRActure propagation CODe)

(Paper 7)

This is a blank page.

Modelling the formation of sheeting joints
with FRACOD²ᴰ (FRActure propagation CODe)

Flavio Lanaro°, Kiyoshi Amemiya⁺, Atsuo Yamada⁺

°Japan Atomic Energy Agency, Japan
⁺Hazama Corporation, Japan

Abstract: This contribution shows an application of the newly developed gravity acceleration function in the BEM-DDM code FRACOD²ᴰ. The influence of the model geometry, material parameters and boundary stresses on the initiation and propagation of sheeting joints due to rebound by removal of the overburden is studied. The models seem to capture the pattern of sheeting joints and the depth of their occurrence. The influence of the sheeting joints on the stress distributions in the rock mass also seem to be realistic and in agreement with field observations. The results indicate that the stresses measured in-situ at several sites in crystalline rock might exhibit the same features as the numerical results by FRACOD²ᴰ. For example, the horizontal stress is found to be rather high at the surface of the models as it was observed in Forsmark, Sweden. Moreover, stresses where sheeting joints are developing are so severe to justify damage and fracturing of the intact rock observed in terms of fracture frequency and laboratory sample damage close to the surface at the Shobasama and MIU Construction Site, Mizunami, Japan.

1 Introduction

Reconstructing the genesis of formation of the fractures in the rock mass constitutes one of the most challenging tasks in Geology and Rock Mechanics. This is mainly because the exact entity of the forces involved, the strength of the rock, the sequence of loading and unloading and, finally, the influence of the boundary constrains on the process of failure of the rock are largely unknown [1]. Moreover, time dependent processes such as stress relaxation, stress corrosion, creep and thermal changes affect the deformability and strength of the rock sometimes radically [2]. For these reasons, before approaching the phenomenon of rock fracturing as a whole, it is useful to study and understand the processes involved one by one. This study focuses attention on the rebound processes imputed to produce sheeting joints. The boundary conditions in terms of allowed displacements and applied stresses are identified as key factors affecting the process.

Sheeting joints seem to be caused by the "stress-exfoliation" phenomenon that usually follows the topography of the site [3),4),5)]. "Exfoliation" occurs very often in plutonic rocks [6]. These rocks usually cool down and crystallize at depth under high pressures. When the overburden is removed, plutonian rocks tend to depressurize and peel parallel to the free surface. Such exfoliation joints and fractures are usually addresses as "sheeting joints". Sheeting joints are sometimes observed to be gently inclined with respect to the basement surface and can appear in conjugated directions (authors' experience)

There are several theories explaining the mechanism behind the formation of sheeting joints in plutonic hard crystalline rocks. All of them, however, involve gravity acceleration. Two of these theoretical models for sheeting joint are as follows:

1) Compression along a curved surface: Sheeting joints are explained as effect of the vertical component of prevalently horizontal forces acting parallel to the convexly shaped topography of the bedrock (e.g. ref. 7),8));

2) Rebound stresses and strains: Sheeting joints are explained as result of removal of the overburden/ice cover due to erosion/melting that induce failure of the rock. Although not considered in this contribution, the effect of the groundwater pressure can be determinant in this failure mechanism.

The lithostatic vertical stress due to gravity inhibits the occurrence of sheeting joints with increasing depth. This also means that gravity acceleration is the key parameter in determining the depth at which the phenomenon of sheeting joints gradually stops.

At the Shobasama and MIU Construction Site (Mizunami, Gifu Prefecture, Japan), a higher degree of fracturing with prevalent sub-horizontal joints is observed in the upper part of the granitic basement, the Upper Highly Fractured Domain. Although fracturing might originate from different tectonic events, one of the causes can be the removal of the overburden due to erosional phenomena. The eroded granitic cover at the Sites is estimated to have been about 4 km thick based on reconstruction of the cooling temperature history and dating of the mineral crystals in the granite [9].

The main questions that this contribution will try to answer by means of numerical analyses are:

- Reproduce the extension with depth and pattern of the fractures in the Upper Highly Fractured Domain at the Shobasama and MIU Construction Site: Can gently dipping fractures be generated by rebound due to removal of the overburden?

- Study the stress distribution induced by the sheeting joints: Can rebound alone explain some of the features of the stress distribution with depth measured in-situ in hard crystalline rocks?

- Explain the linear increase with depth of the experimental strength from uniaxial and Brazilian testing of samples from the Upper Highly Fractured Domain: Can this be explained by the mechanism of failure observed in the models?

2 Conceptual model

The theoretical model that explains sheeting joints as result of compression along convexly curved surfaces (Sec. 1, point 1) might be contradicted by the fact that also bedrocks with concave topography experience sheeting joints. This model also implies the hypothesis that high stresses run perfectly parallel to the curved surface of the bedrock which seems slightly unrealistic because natural stresses usually avoid convex surfaces leaving the topographical tops less stressed. Furthermore, this model cannot predict the depth where the formation of sheeting joints should cease. For this reason, sheeting joints might be explained with another mechanism like the release of lithostatic pressure by removal of the overburden.

Intuitively, only the removal of the lithostatic stress alone would not explain the formation of sheeting joints. In elastic conditions, a body compressed to a certain level of stress recovers its shape with no damage when the stress is removed. However, the process of uneven unloading from high stresses can alone, in some cases, produce stresses and/or deformations such to induce failure of the rock. For sheeting joints, tensile failure is often considered as the governing failure mode.

Another possibility to explain sheeting joints could be that cooling and crystallization of the rock occurs under high in-situ stresses. Thus, crystal bounds are formed in compressive conditions. The removal of the overburden pressure would actually apply a new constrain onto the bedrock by tearing apart such crystal bounds, which can actually lead to their failure in tensile mode. This hypothesis would imply the concept of "locked-in stresses", which will not be developed in this paper.

In this paper, the process of uneven unloading by removal of the overburden is simulated with FRACOD^{2D}. The following unloading process is considered to be realistic for the generation of sheeting joints:

- The model is consolidated under rock stresses corresponding to a rock cover of 4 km with different horizontal to vertical stress ratios (K);

- The vertical stress is removed stepwise with unchanged horizontal stress until the upper surface of the model is completely unloaded ($\sigma_V = 0$ MPa);

- The vertical boundaries of the models are allowed to deform due to the applied horizontal stresses: the combination of high horizontal stresses, unloading deformations and gravitational field can actually induce failure in the rock material. Also the influence of the Poisson's ratio seem to be determinant because it governs the ratio between the bulk and shear deformation modulus of the rock;

- The influence of pre-existent faults with different inclination and location is also studied.

3 Numerical models

To the authors' knowledge, there have been no attempts to model surface rebound and sheeting joints due to removal of the overburden by means of a numerical code that can take into account the initiation and propagation of the fractures in intact rock. This was made possible by the implementation of gravity in one of the few available BEM-DDM codes, FRACOD^{2D}, Version 2.3.1 [10].

3.1 FRACOD^{2D}

FRACOD^{2D} (FRActure propagation CODe) is a Windows based program that simulates the fracture initiation and propagation in a continuous, homogeneous, elastic and isotropic medium [11]. The code implements the boundary element method (BEM) called Displacement Discontinuity Method (DDM). The DDM method is based on the equations describing the stresses and displacements caused by a fracture with constant displacement in an infinite continuum and homogeneous elastic body [12],[13]. The effect of normal and shear deformability of the fractures is superposed to obtain a solvable system of linear equations. Additional constrains to this system are introduced for open fractures (e.g. zero normal stress), fractures in elastic conditions (e.g. linear elasticity) and fractures in failure limit conditions or sliding (e.g. Mohr-Coulomb Criterion).

Pre-existent fractures can propagate and new fractures can be generated either in tensional (Mode I) or in shear (Mode II). The propagation criterion proposed by Shen & Stephansson [14] is implemented where the resultant strain energy rates G_I in Mode I and G_{II} in Mode II are functions of the possible propagation direction θ around the tip of the fracture. The fracture will eventually propagate when the F-Criterion is reached:

$$F(\theta) = \frac{G_I(\theta)}{G_{Ic}} + \frac{G_{II}(\theta)}{G_{IIc}} \geq 1 .$$

The strain energy associated with the presence of a fracture in the elastic body can be expressed as the sum of the energy associated to tension and shear, respectively. Thus, the two strain energy rate components can independently be determined for each direction θ. These values are then introduced in the expression of the F-Criterion to determine whether and in which direction the fracture is supposed to grow.

The length of the newly formed fractures can be either assigned or determined by the spacing of the point grid where fracture initiation can be detected in the model. Although microcracking

cannot be directly be simulated, the code can simulate the process that takes place when microcrack coalescence develops into macro-scale fracture propagation.

The material in which the fractures can initiate and propagate (i.e. the rock) has elastic deformational properties and a Mohr-Coulomb strength criterion.

3.2 Geometry, material properties and boundary conditions

The material properties of the Toki granite were determined in different laboratory test campaigns with samples from the Shobasama and MIU Construction Site [15]. In general, the Young's modulus, Poisson's ratio, cohesion and friction angle were found to vary on average between 51 and 58 GPa, 0.26 and 0.34, 34 and 39 MPa, and 52° and 55°, respectively. The friction angle, cohesion, initial and residual aperture of the initiated or propagating fractures were estimated here based on earlier BEM-DDM simulations of the behavior of similar rock types [16]. On the other hand, experimental values of the normal stiffness and Mode I and Mode II fracture toughness were determined in laboratory on samples of Toki granite from borehole MIU-2 [17]. The normal stiffness was observed to vary between 745 and 853 GPa/m; the Mode I toughness to vary between 2.37 and 2.37 MPa m$^{0.5}$; and the Mode II toughness to vary between 3.10 and 11.84 MPa m$^{0.5}$ (depending on the stress confinement). The shear stiffness was not determined by means of experimental tests and was estimated here based on similar studies (e.g. ref. 18)). All the experimental results and considerations above lead to the choice of the modeling parameters in Table 1.

For crack initiation in Mode I, the models are assumed to have a spatially "random" generation when the ratio between the stress σ and the nominal tensile strength σ_m would exceed 50%. The lower threshold of the tensile strength of the rock is assigned based on the results of recent Brazilian tests carried out on core samples from borehole MIZ-1. Moreover, fracture generation is also allowed at the boundary of the model. This sometimes leads to the formation of fractures at the corners of the model that are due to the vicinity of the boundaries. These fractures often cease to propagate during the numerical iterations, contrary to the fractures directly induced by the rebound phenomenon.

The models simulate a large-scale block of granite of 500 m in width and 500 m in height (Figure 1). Two configurations are considered:

- Same boundary conditions at the vertical boundaries of the block (Figure 1, a). These models simulate the condition where the vertical boundaries are close to each other (500 m) and the model has no symmetry;

- Symmetry about one of the vertical boundaries (Figure 1, b). Thanks to the symmetry, these models consider a larger volume of bedrock with double distance (1000 m) between the vertical boundaries.

Initial stresses are applied to one (symmetrical model) or two vertical (non-symmetrical model) boundaries and to the horizontal upper surface. On the horizontal lower surface, vertical displacements are inhibited.

Two dimensional modeling is performed in plane strain and the applied stress boundary conditions are compressive in vertical and horizontal direction. This means that the initial principal stresses act on the model parallel to its edges (e.g. vertical and horizontal).

The analyzed models contained no pre-existent fractures or one or two symmetrical cracks simulating fault planes. The newly initiated fractures or the propagating portions of initiated fractures have a minimum length of 20 m (about 4% the model edge length).

To simulate rebound due to removal of the overburden, the vertical stress acting on the horizontal upper surface is removed from its initial value of 102 MPa to zero in three stress increments:

50 MPa, 50 MPa (in one case this increment is split into two) and 2 MPa. The horizontal stress is left unchanged according to Table 2.

Table 1. Material properties used for the FRACOD^{2D} models simulating sheeting joints due to rebound caused by removal of the overburden.

Material	Parameters	Values
Intact rock	Poisson's ratio	0.33
	Young's modulus	50 GPa
	Friction angle	50°
	Cohesion	30 MPa
	Tensile strength	6 MPa
	Mode I fracture toughness	2 MPa m$^{0.5}$
	Mode II fracture toughness	11.5 MPa m$^{0.5}$
Initiated and propagating fractures	Shear stiffness	20 GPa/m
	Normal stiffness	500 GPa/m
	Friction angle	32°
	Dilation angle	0°
	Cohesion before sliding	10 MPa
	Cohesion after sliding	0 MPa
	Initial aperture	10^{-2} mm
	Residual aperture	10^{-3} mm
Fault zones	Shear stiffness	2 GPa/m
	Normal stiffness	50 GPa/m
	Friction angle	25°
	Dilation angle	0°
	Cohesion	0 MPa

Table 2. Initial stresses acting on the FRACOD^{2D} models simulating sheeting joints due to rebound caused by removal of the overburden.

| Case	Stress components	Values
K = 0.5	Vertical stress on the upper surface	102 MPa
	Horizontal stress on the upper surface	51 MPa
	Horizontal stress on the lower surface	57.5 MPa
	Gradient of the horizontal stress with depth	0.013 MPa/m
K = 0.3	Vertical stress on the upper surface	102 MPa
	Horizontal stress on the upper surface	31 MPa
	Horizontal stress on the lower surface	35 MPa
	Gradient of the horizontal stress with depth	0.008 MPa/m
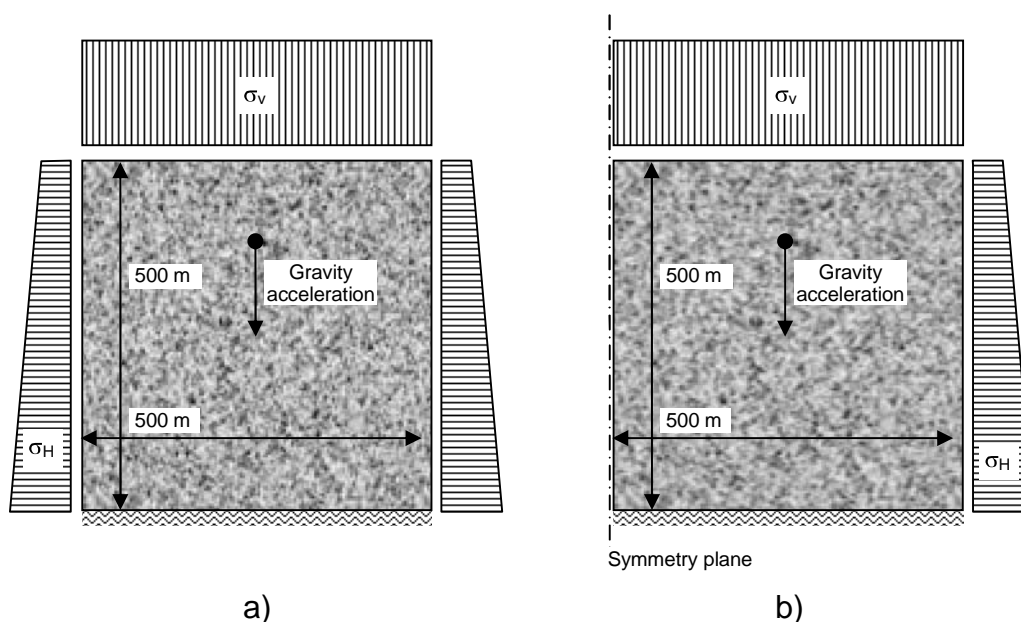
Figure 1. Schematic view of the FRACOD^{2D} models, dimensions and boundary conditions for: a) model with no symmetry plane; b) model with symmetry plane. Plane strain conditions apply in all cases. Rebound is simulated numerically by setting σ_V to zero.

4 Sheeting joints: numerical results

In the following sections, the numerical results are presented to highlight the different fracture patterns and stress distributions due to the assumed boundary conditions, in-situ stress ratio, material properties and geometry of the models. In particular, attention is paid to:

- The influence of the boundary conditions;

- The influence of the ratio between the initial vertical stress and the horizontal stress;

- The effect of the Poisson's ratio of the intact rock on the numerical results;

- The effect of the presence of fault planes (pre-existent weakness zones);

- The effect of the topography of the ground surface;

- The stress-path at points with different depths inside the models and the effect of water pressure.

In the following sections, tensile stresses are assumed positive and depth negative. In the text, shallow depths are above -250 m, while large depths are between -250 and -500 m.

4.1 Effect of the boundary conditions

In Figure 2, the results for a non-symmetrical model and a symmetrical model for initial stresses with K = 0.3 are shown. The results indicate that the vicinity of the horizontally loaded boundary affects the pattern of the fractures and the stress distributions. The different stages of rebound shown in the figure might correspond to different times (e.g. Rebound 1, 2 and 3, respectively) during the development of the process of sheeting joints, but strictly speaking, only correspond to different stages of the fracture generation and propagation through the models. The dominant inclination seems to go from the loaded boundary towards the ground surface of the model leading to converging fractures in the non-symmetrical model, and preferably parallel fractures in the symmetrical model. The spacing of the fracture, however, seems to be very similar in the two models, although the fractures in the non-symmetrical model appear to have rougher traces than

the fractures in the symmetrical model. The spacing varies between 20 and 40 m, values that are certainly affected by the grid spacing of the models that was 20 m. Probably, denser fracturing would have occurred in the models if the grid spacing was smaller.

The two models agree, not only for what concerns the fracture spacing, but also for the depth at which the fracturing ceases with depth that is about -150 m. Observation of the fracture propagation indicate that the propagation occurs prevalently from the loaded boundary inwards. Deepening of the fractures during rebound was much less marked than lateral propagation.

Due to fracture propagation, the distribution of the horizontal stress with depth is rather different than that of the applied horizontal boundary stress. The linearity of the boundary stress with depth is lost. Horizontal stresses between -100 and -200 m depth appear to be much lower than the boundary stresses at the same depth. On the other hand, stresses above -100 m are in general high. This seems to depend on the fracturing and deformations that concentrate the horizontal stresses close to the surface.

The vertical stress calculated by the models follows a linear increment with depth due to the effect of gravity. However, the values along the investigated vertical line are on average about 3.5 MPa lower than the weight of the overburden. Please notice that the gradient of the vertical stress is not applied to the grid points inside the model but only at the boundaries of the model. The profiles with depth of the vertical stress also show that stresses depart from linearity for depths shallower than about -200 m. Above this depth, the vertical stress starts to oscillate giving rise to tensile stresses in some rebound phases. This might explain the process of fracturing rather parallel to the horizontal surface of the models. In other cases, the vertical stress can be higher than the weight of the overburden. The tensile stresses observed in Figure 2 are large. This can be explained in two ways: i) the grid density of the model does not allow the generation of more fractures, thus the stresses between the initiated fractures can become very large; ii) at the tips of the newly initiated fractures, stress concentrations are always present leading to tensile stresses several times larger than the tensile strength of the rock without actually induce failure in the material.

Although the boundary conditions applied imply null shear stresses on vertical and horizontal planes, approaching the surface of the models the shear stress is not zero. This explains why the generated fractures are not perfectly horizontal because the minor principal stress is not exactly vertical.
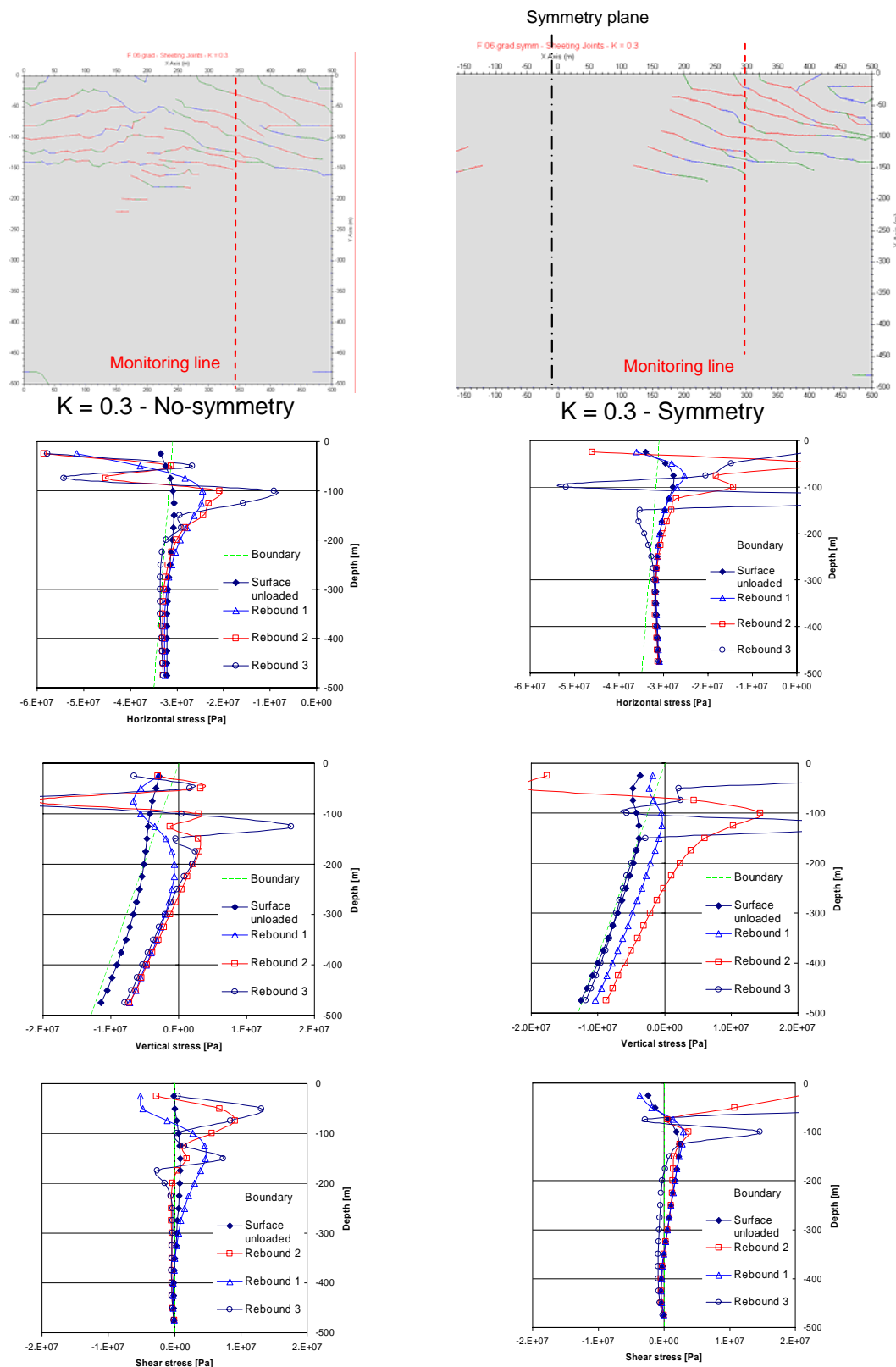
Figure 2. FRACOD²ᴰ models with K = 0.3. On the left, results for the non-symmetrical geometry; on the right, results for the symmetrical geometry. Three different phases of the rebound process are named "Rebound" 1 to 3 and indicate the evolution of the stresses for propagating fractures. For "Rebound stage 3", the fracture pattern, horizontal stress distribution, vertical stress distribution and shear stress distribution with depth along a horizontal line located at x = + 300 m from the left vertical edge are shown.

In general, the stress distributions of the symmetrical models are less ragged than those of the non-symmetrical model, certainly due to the stronger effect of the boundary conditions on the latter model.

Figure 3 compares the vertical displacements numerically calculated close to the surface of the non-symmetrical (left) and symmetrical (right) models. It can be observed that, just after the removal of the vertical load at the surface, the vertical rebound calculated by the two models is exactly the same since it only depends on the elastic behaviour of the intact rock. However, the initiation and propagation of the fractures produce other than dilation behaviour also rigid displacements of the blocks between the fractures that change the displacement profiles approaching the boundaries. The maximum displacements are very similar in the two models and the centre of the non-symmetrical model seems to behave as a fixed boundary like the symmetry axis in the symmetrical model. A change in the Poisson's ratio might also drastically change the magnitude and profiles of the rebound displacements since it affects the fracture patterns (Sec. 4.3).

The calculated vertical displacements and shear displacements along the fractures for the symmetrical model with $K = 0.3$ are shown in Figure 4. It can be seen that the vicinity of the boundary induces the maximum vertical rebound displacement. On the other hand, large shear displacement along the initiated fractures in the model occurs at depth shallower than -100 m and not necessarily very close to the boundary of the model. Normal displacements of the fractures are also large in this area due to low vertical stresses and dilation effects along the sheared fractures.
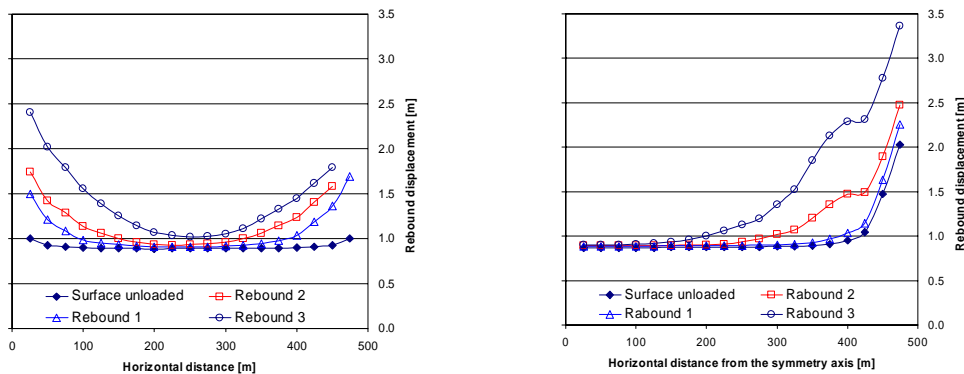

Figure 3. Vertical rebound displacements for the numerical models with $K = 0.3$ and no-symmetry (left) and symmetry (right). The displacements are calculated at a depth of -10 m from the surface of the models.
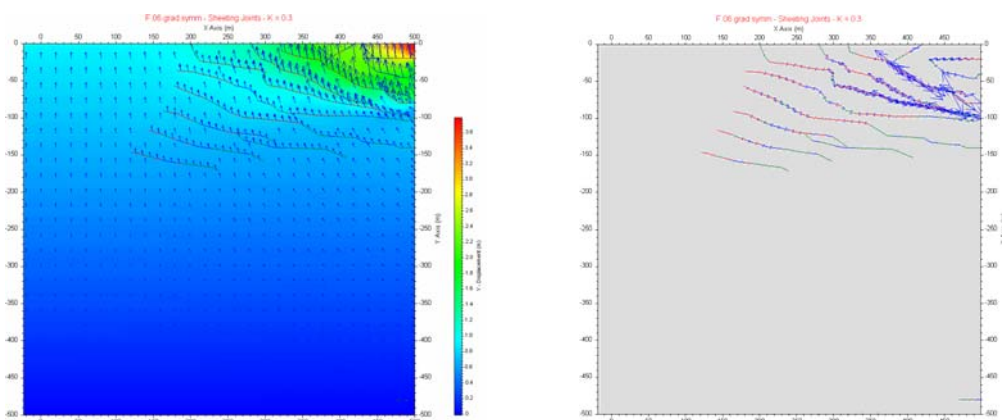

Figure 4. Vertical rebound displacements (left) and shear displacements along the fractures (right) for the numerical model with symmetry and $K = 0.3$. The maximum vertical displacement is 3.8 m while the maximum shear displacement is 0.54 m, respectively.

4.2 Effect of the ratio between initial horizontal and vertical stress

The immediate effect of the ratio between the vertical and horizontal stress is that for K = 0.5 stresses are generally higher than for K = 0.3, as shown in Figure 5 for the symmetrical model. The fracture patterns of the two models also differ consequently: the model with higher stresses presents deeper sheeting joints (down to about -200 m) than the model with lower stresses (down to about -150 m). Furthermore, the spacing of the fractures in the model with higher stresses is also larger (between 25 and 50 m). The fractures of this model reaching the surface present conjugated orientation that isolate large triangle-shaped rock blocks. The fractures of the model with lower stresses have generally more irregular traces. The fractures also seem to be slightly more inclined (about 16°) than the fractures occurring in the model with higher stresses (about 12°).

In this Figure 5, another vertical line crossing at x = +100 m is considered for the comparison of the stress components (cf. Figure 2). The position of this line is relatively distant from the fractured volume, but despite this, it seems to be affected by the presence of the initiated sheeting joints. Along this line the horizontal stress appear to be close to the assigned boundary stress below about -200 m. Shallower than -200 m, the horizontal stresses markedly decrease in both models for then drastically increase again approaching the ground surface. At -500 m, the calculated stress in the models only differs about 2 to 4 MPa from the assigned boundary stress.

The two models also present different gradients of the horizontal stress as it can be seen in Table 2. However, the gradient of the vertical stress is the same and it is governed by the weight of the overburden, at least when the process of sheeting jointing is not so advanced. For late rebound phases, the vertical stress seems to decrease up to 4 MPa compared to the weight of the overburden. This is probably due to stress rotations and deformations of the models and to the stress concentrations induced by fracturing.

Such stress rotations and concentrations are also confirmed by the shear stresses on a vertical or horizontal plane that, although they are zero at the boundary, have magnitudes up to about 8 MPa. The model with higher boundary stresses shows only marginally higher maximum shear stresses than the model with lower boundary stresses.

The shape of the curves of the stress components varies with the rebound phase probably depending on the influence of newly formed fractures or propagating fractures. The changes of the horizontal stress principally occur in the interval between -100 and -200 m depth. On the other hand, changes of the vertical stress imply, not only oscillations at the same interval of depth, but also a decrease of the vertical stress of up to about 6 MPa at all depths larger than -200 m. Consequently, tensile stresses can be observed for some rebound phases between -150 and -250 m depth.
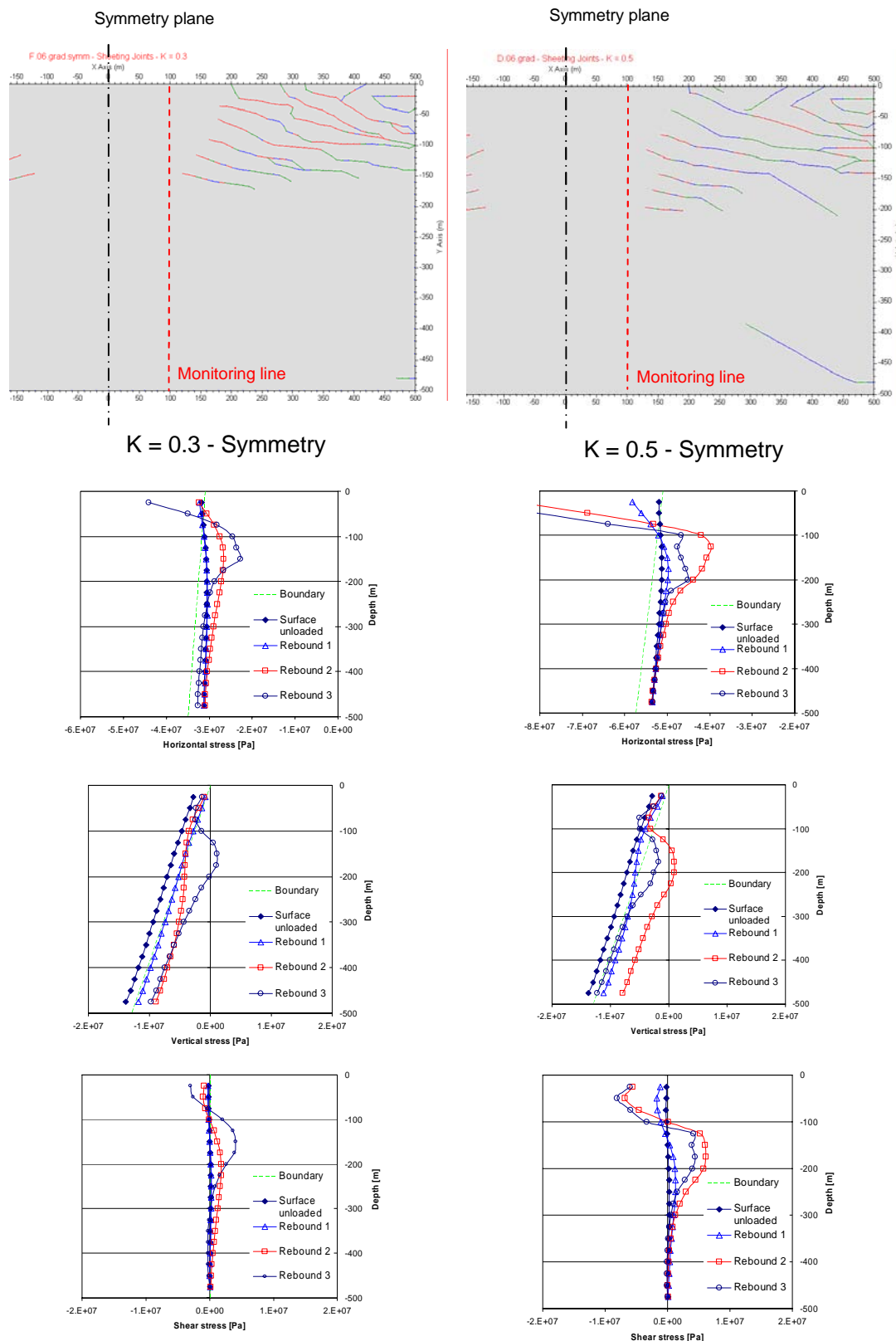
Figure 5. Comparison of the FRACOD^{2D} models symmetrical geometry and K = 0.3 (left) and K = 0.5 (right), respectively. Three different phases of the rebound process are named "Rebound" 1 to 3 and indicate the evolution of the stresses due to propagating fractures. For "Rebound stage 3", the fracture pattern, horizontal stress distribution, vertical stress distribution and shear stress distribution with depth along a horizontal line located at x = + 100 m from the left vertical edge are shown.

4.3 Effect of the Poisson's ratio

The Poisson's ratio plays an important role in the stress distributions and deformability of rock masses subjected to static or dynamic loads [19]. The Poisson's ratio influences the deformability of the rock because it determines the ratio between the bulk modulus and the shear modulus and, in turn, it determines the ability of the rock to resist shear deformations. Moreover, in plane-strain problems like those treated in this study, the Poisson's ratio and the presence of body forces (e.g. gravity acceleration) greatly affect the stress distribution in the rock especially close to an opening and at shallow depth [20]. The ratio between the horizontal and vertical stress components might also be related to the Poisson's ratio, typically in geologically undisturbed sedimentary formations [21].

The Poisson's ratio of the rock in the model was changed for the purpose of studying how this parameter affects the fracture pattern. Besides the laboratory value of the Poisson's ratio of the Toki granite (0.33), the values of 0.25 and 0.4 were also input in the symmetrical model with ratio K between horizontal and vertical stress of 0.3.

By comparing the fractures patterns in Figure 5 (left) and Figure 6 for the symmetrical model and the same unloading phase and number of numerical cycles, it can be observed that an increase of Poisson's ratio seems to:

- Reduce the depth at which the fracturing ceases. For the model with Poisson's ratio of 0.25 the fracturing reach a depth of -200 m while with the experimental value of the Toki granite reaches only about -150 m. The Poisson's ratio also seems to inhibit the lateral extension of the fractured area;

- Increase the inclination and roughness of the fracture traces;

- Promote the development of planar fractures dipping 30° towards the symmetry axis of the model. Since the model is symmetrical, fractures in conjugated directions appear.
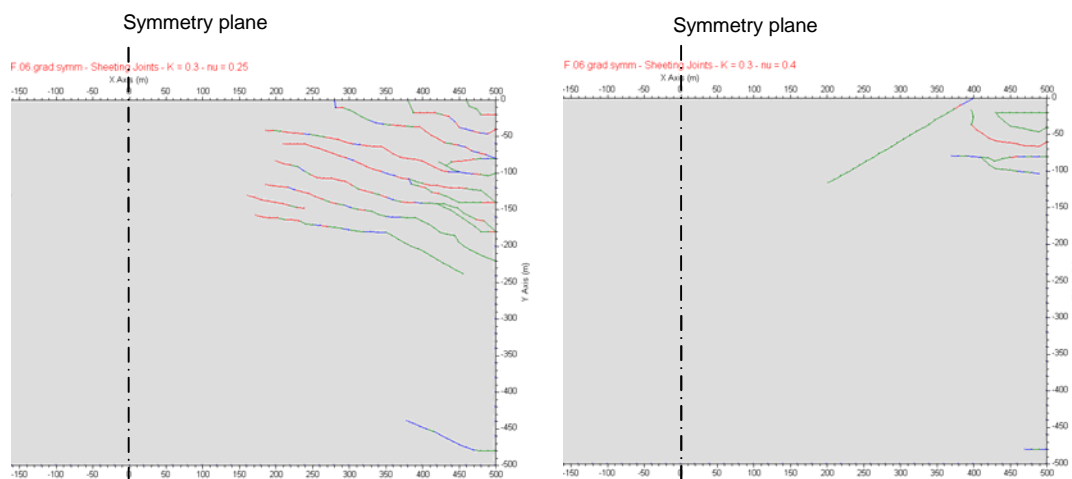

Figure 6. Effects of the Poisson's ratio on the FRACOD^2D model with symmetrical geometry, K = 0.3: fracture pattern for the model with Poisson's ratio of 0.25 (left) and 0.40 (right), respectively.

4.4 Effect of the faults

Weakness planes were introduced into the models to simulate the presence of fault zones with different inclinations. The material properties assigned to these fault zones are summarised in Table 1. Three inclinations of the faults were considered: a fault dipping 75° towards the boundary,

a fault dipping 75° towards the symmetry plane, a fault dipping 30° towards the boundary, respectively.

The numerical results show that the presence of the sub-vertical fault zones (dip ±75°) effectively inhibits the propagation of the sheeting joints through the model (Figure 7). All newly formed fractures stops against the faults and the fracture pattern is almost identical in the two cases.

Although the fracture patterns of the two models in Figure 7 are very similar, the distributions of the stress components with depth along a line crossing the middle height of the faults are rather different. For the model with fault dipping toward the boundary (+75°), the horizontal stress distributions is not as linear as for the model with fault dipping towards the symmetry plane. The former also exhibits rather large spread of values of the horizontal stress component approaching the ground surface.

Also the vertical stress components differ in the two models. In the model with fault dipping towards the symmetry plane (dip -75°), the vertical stress component is almost perfectly linear with zero value at the surface as for lithostatic pressure. On the other hand, the model with fault dipping towards the boundary (dip +75°), the vertical stress is linear below -100 m depth and, above, it varies from small compressive values to tensile values of approaching the tensile strength of the rock.

While for the model with fault dipping towards the symmetry plane (dip -75°) the shear stress component is almost zero at all depths, the other model (dip +75°) shows shear stresses linearly varying up to a depth of -100 m; above this depth, the shear stresses start to increase conspicuously in magnitude.
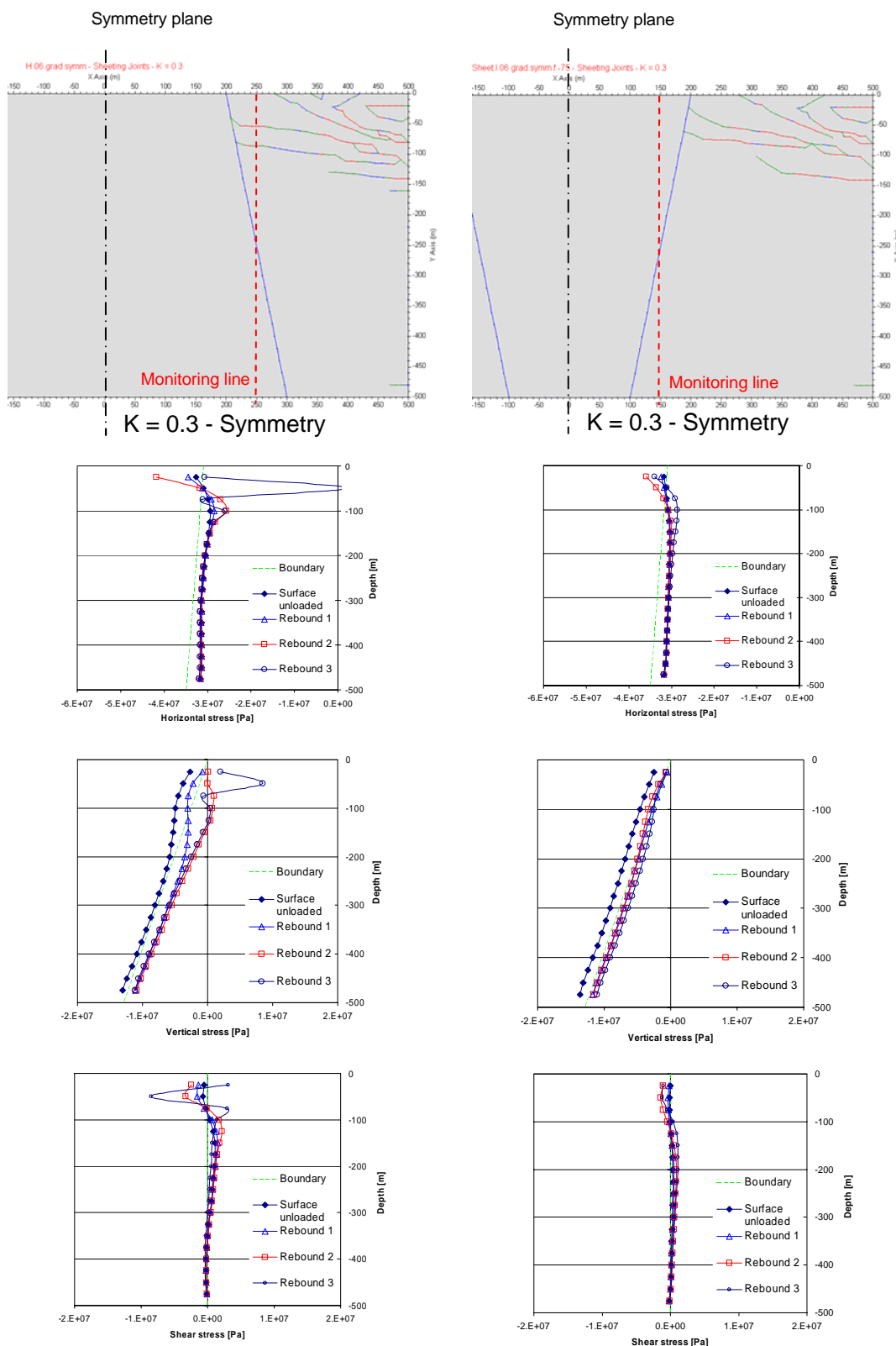
Figure 7. Comparison of the FRACOD[2D] models with symmetrical geometry, K = 0.3 and a fault plane dipping towards the boundary (dip +75°, left) and towards the symmetry plane (dip -75°, right), respectively. Three different phases of the rebound process are named "Rebound" 1 to 3 and indicate the evolution of the stresses for propagating fractures. For "Rebound stage 3", the fracture pattern, horizontal stress distribution, vertical stress distribution and shear stress distribution with depth along a vertical line located at x = + 250 m (dip +75°, left) and x = +150 m (dip -75°, right) from the symmetry plane are shown.

Another interesting case study is the presence of a gently dipping fault zone isolating a wedge at the surface of the model. Figure 8 shows the variation of the stresses along two monitoring lines in the model with a planar zone dipping 30° towards the boundary of the model. For numerical reasons, this model was run with vertical stress unloading increments of 50, 25, 25 and 2 MPa.

The fault zone intercepts "monitoring line 1" at a depth of about -30 m. At this depth, the horizontal stress slightly increases and the vertical stress drops down about 3 MPa. The stress profiles, however, differ from the stress profile applied at the boundary for the horizontal stress and from the lithostatic vertical stress shown with a dashed line in the diagrams. The horizontal stress is generally rather constant despite the boundary horizontal stress has a gradient of 8 kPa/m. On the other hand, probably to counterbalance the low horizontal stresses, the vertical stress is generally larger than the weight of the overburden and seems to have a lower gradient than that due to gravity. Shear stresses are generally low along this line.

Less uniform is the variation of the stress components along "monitoring line 2" due to the presence of the zone and to the vicinity of the model boundary. The fault zone intercepts monitoring line 2 at about -150 m depth. At this level, the horizontal stress experiences a drop in magnitude of about 3 MPa. On the other hand, from this depth, the vertical stress inverts its gradient and raise about the same amount (3 MPa) at a depth of about -50 m. The gradient of the vertical stress is slightly lower than the lithostatic gradient. Shear stresses are negligible below -250 m, and increase up to about 3 MPa at the depth of the fault zone.

The fracture pattern produced by the rebound presents sub-horizontal fractures departing from the boundary and extending only within the wedge formed by the fault zone. These fractures, differently than for the other analyzed models, are not systematically continuous but exhibit rock bridges. One large fracture, with the same inclination as the fault but dipping in the opposite direction, reaches the fault zone at a depth of about -200 m. When the fracture pattern inside the symmetrical model in Figure 8 is compared with the non-symmetrical model in Figure 9, it can be noticed that sub-horizontal fractures appear in the latter at the top of the footwall of the fault. Those fractures have a rather rough trace and occur only in the upper -90 m of the model. On the hanging wall of the fault, on the other hand, fractures are also rougher than for the symmetrical model and have a preferential inclination towards the fault zone that they reach before stopping. Moreover, these fractures occupy the whole wedge identified by the fault, leading to a difference in depth at which fracturing ceases between the footwall and hanging wall of the fault.
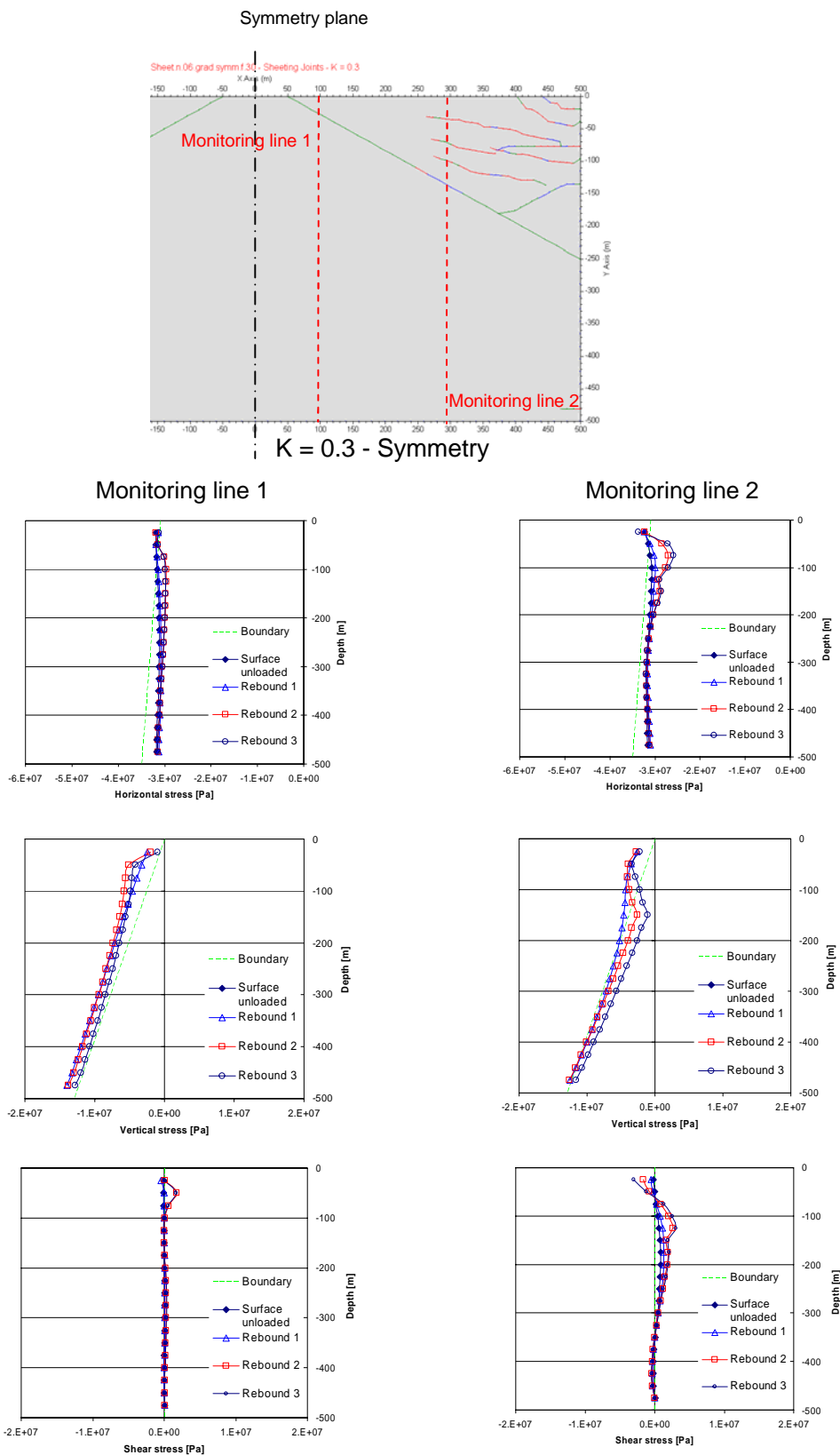
Figure 8. Effects of a gently dipping fault zone inclined 30° on the FRACOD^{2D} model with symmetrical geometry, K = 0.3. Three different phases of the rebound process are named "Rebound" 1 to 3 and indicate the evolution of the stresses due to propagating fractures. For "Rebound 3", the fracture pattern, horizontal stress distribution, vertical stress distribution and shear stress distribution with depth along two vertical lines located at x = + 100 m and x = +250 m from the symmetry plane are shown.
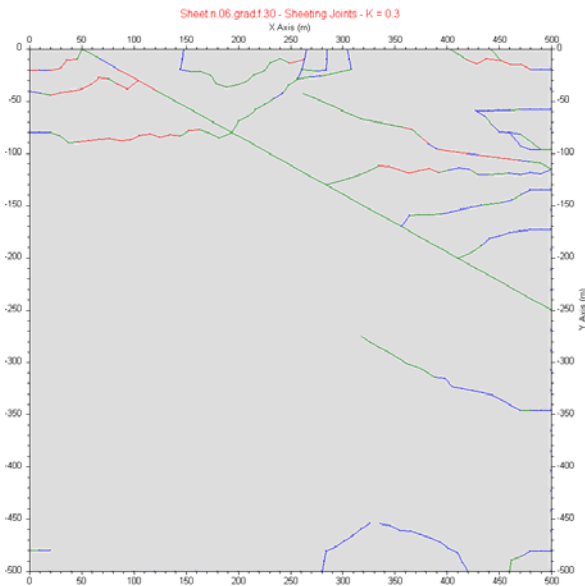
Figure 9. Effects of a gently dipping fault zone inclined 30° on the fracture pattern inside the FRACOD^{2D} model with non-symmetrical geometry, K = 0.3.

4.5 Effect of the topography of the ground surface

Even a slight curvature of the ground surface of the models induces great effect on the fracture initiation and propagation induced by rebound. Figure 10 shows that a concave ground surface almost totally inhibits the formation of sheeting joints in the model. On the contrary, a concave ground surfaces enhances the fracturing process for the same boundary stress conditions. This seems to depend on the vicinity of the model boundary to the topographical top of the ground surface: the farer the smaller the fracturing. Furthermore, the few fractures observed for the convex ground surface are nearly parallel to the surface, while for the convex ground surface, the fractures have a steep and discordant dip with respect to the slope of the surface. In this case, irregular fractures are observed down to a depth of -300 m.
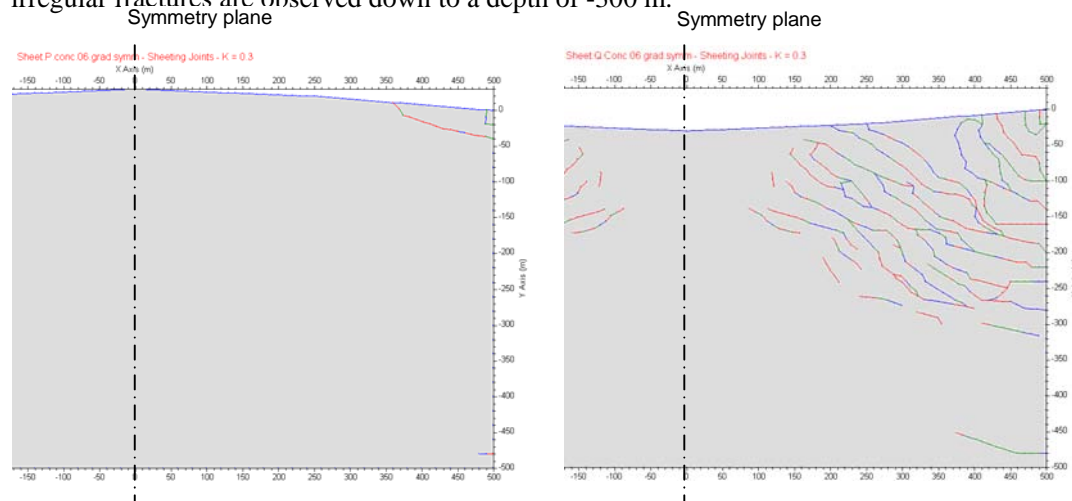

Figure 10. Effects of a convex (left) and concave (right) topography of the ground surface for the numerical model with symmetry and K = 0.3.

4.6 Stress-paths and the effect of water pressure

In Figure 11, the stress-path of points located along a vertical monitoring line in the models presented in Figure 5 is shown. It can be observed that for the most superficial points, the stress-path tend to cross the Mohr-Coulomb's criterion. This means that at these depths, not only the rock breaks and large cracks are initiated, but also the rock between the newly formed cracks is in

failure conditions or very close to it. The fact the stress-paths sometimes do not stop at the Mohr-Coulomb's criterion depends on the fact that crack initiation is only allowed at certain grid-points spaced 20 m in the models. Thus, if a crack has already departed from those points in the models, the rock around it cannot break and stresses might exceed the assigned strength of the rock. In other words, this depends on the chosen grid-point density that for practical reasons cannot be too high. However, the calculation tends to re-conduct the stresses to the failure criterion causing the oscillation of the stress-path around the failure criterion.

A more detailed analysis of the stress-paths (Figure 12) also shows that sometimes the stress-path reach the tensile strength of the intact rock (e.g. between 3 and 6 MPa) and, after crack generation, turns back towards compressive stresses. Afterwards, other approaching cracks propagating from other grid-points might raise the stresses beyond the tensile strength of the material. However, since such stresses are due to the vicinity of a crack tips, they can actually overcome the tensile strength of the material without causing local failure according to Griffith's crack model (e.g. ref. 22)). These observations might indicate that where the numerical models show the initiation of a single fracture/joint, in reality the rock mass could be subjected to ubiquitous cracking in the form of fracture clusters as observed at the MIU Construction Site [23].

For points located deeper in the rock, the stress-path tends to remain unchanged from the initial stress state. Due to the stabilizing effect of gravity, these points do not experience failure.

The models were run in terms of total stresses, thus the presence of groundwater pressure is not considered in this study. However, the stress-path in the normal and shear stress graph in Figure 11 allows commenting on the effect of water pressure. If a certain water pressure is introduced in the models, the effective stresses in the rock will diminish accordingly, but not the shear stresses. In consequence, the stress-path would rigidly translate towards lower compressive stresses, approaching in this way the Mohr-Coulomb's stress criterion and/or the tensile stress of the rock. It can be observed that a very small water pressure would already induce additional failure at the most superficial points in some areas of the models. For increasing depth, also increasing pore pressures are required for the stress-paths to approach the failure criterion for tension or shear. For the model with $K = 0.5$, a pressure of about 10 MPa is needed at 100 m depth. On the other hand, for the model with $K = 0.3$, points as deep as 150 m are already so close to the failure envelope that minor changes of the groundwater pressure (of the order of 1 MPa) would already induce failure. Thus, the stress conditions in the model with $K = 0.3$ would be prone to extensive failure if a large rise of the water table would take place due for example to marine submersion or to a glacial ice shield. Water pressure would probably induce a deepening of the volume affected by sheeting joints compared to the model with zero water pressure.
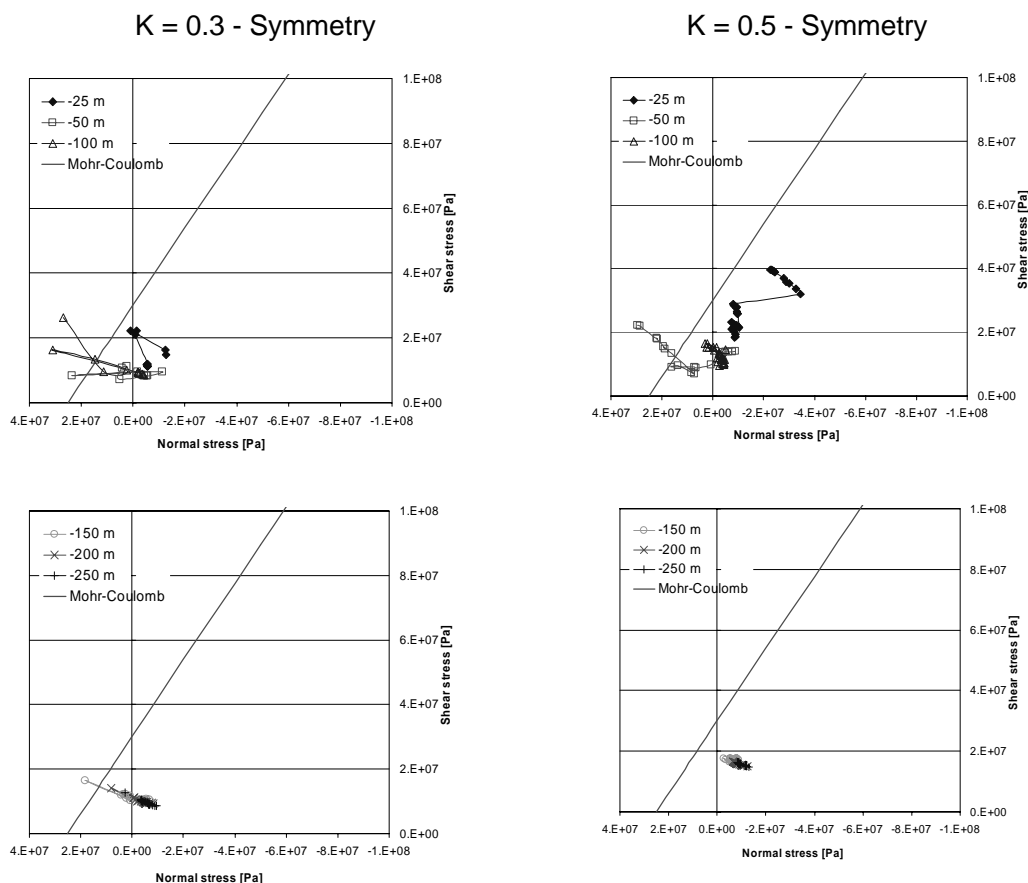
Figure 11. Stress-paths in terms of normal and shear stress for points located at -25, -50, -100, -150, -200 and -250 m depth along the models and monitoring lines shown in Figure 5 (K = 0.3, left; K = 0.5, right). For clarity, the stress-paths are stopped after the stresses cross the Mohr-Coulomb criterion the first time.
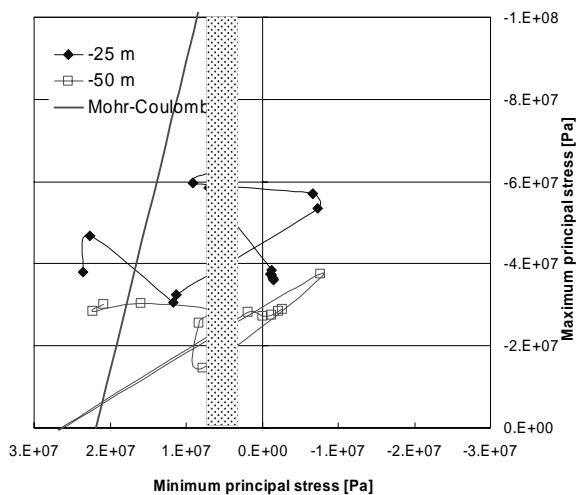

Figure 12. Stress-paths in terms of maximum and minimum principal stresses for two points located at -25 and -50 along the monitoring line shown in Figure 5 for the symmetrical model with K = 0.3. For clarity, the stress-paths are stopped after the stresses cross the Mohr-Coulomb criterion. The masked area shows the range of variation of the tensile strength of the material.

5 Discussion

This study shows that besides tectonic forces and gravity, also the rebound process due to erosion and removal of the overburden might result into failure of the rock and generation of extensive fracturing. Fracturing due to overburden removal, besides the horizontal forces applied to the rock, seems to be markedly affected by the vicinity of the model boundary. The vicinity of the deformed boundary in the models produces more pervasive fracture patterns than for fixed boundaries (e.g. symmetry plane) that produce heterogeneous fracturing increasing with the distance from the fixed boundary. Considering that both configurations are realistic, they are expected to apply to different part of the rock mass and thus, to give raise to different fracture patterns from place to place. Besides being a cause of fracturing, rebound also affects the distribution of stresses in the rock mass. For this reason, depending on the sequence of occurrence of the loading/unloading and fracturing processes of the rock mass, rebound might sometimes be the main mechanism governing the actual in-situ stress distribution at a certain site.

Sheeting joints due to rebound were observed in models characterised by different material properties (i.e. Poisson's ratio), spatially variable tensile strength (i.e. random generation of the tensile strength between two assigned extreme values) and different initial stress magnitudes. Fracturing in the models can be either basically inexistent (i.e. the rock remains intact) or can be characterized by rather regularly spaced fractures. When fracturing occurs, it extends to a certain depth that seems to be governed by the applied horizontal stresses. Thanks to the stabilizing effect of gravity, fracturing ceases at a certain depth that in the models with input parameters similar to the Toki granite at the adjacent Shobasama and MIU Construction Site was observed to vary between -100 to -250 m from the granitic basement surface. At these Sites, the shallowest part of the granitic basement is affected by more intensive and prevalently sub-horizontal fracturing than the rest of the deeper rock. The thickness of what is defined as the Upper Highly Fractured Domain (UHFD) observed in seven deep boreholes drilled was found to vary between 188 and 281 m with an average thickness of 225 m. If the thickness of the weathered zone located at the surface of the granitic basement is removed, these values decrease of about 15 m, and they are therefore comparable with the depth of the observed fracturing in the numerical models. Since the thickness of the present sedimentary cover above the granitic basement is almost in all cases about 90 m for the boreholes around the two Sites, there seems not to be a correlation with the thickness of UHFD. Thus, it can be concluded that the numerical models might capture the mechanism of formation of the gently dipping fractures in UHFD. Fracture clusters observed at the Sites in the shallowest part of UHFD might be explained with more extensive fracturing due to the low confinement.

In the superficial granitic basement down to a depth of -100 to -150 m, the numerical models show that stresses due to rebound are large enough to cause tensile and shear failure of the intact rock. Moreover, the appearance of the fractures changes the stress distribution in the rock causing the stresses to become high and heterogeneous in this area. Besides the fracturing that the model is capable to generate depending on the assigned grid-point spacing, the high stresses could induce more cracks and damage of the rock in the superficial granitic basement. The analysis of the laboratory results of uniaxial compressive and Brazilian tests shows that the strength of the Toki granite increases rather monotonically with depth across UHFD to become almost constant in the Lower Sparsely Fractured Domain located immediately below UHFD (Figure 13). This monotonic increase can very likely be explained with stress conditions due to rebound that induce damage and failure of the intact rock. Drilling through the rock in such stress conditions in presence of water pressure might also enhance the phenomenon and produce additional damage of the samples.
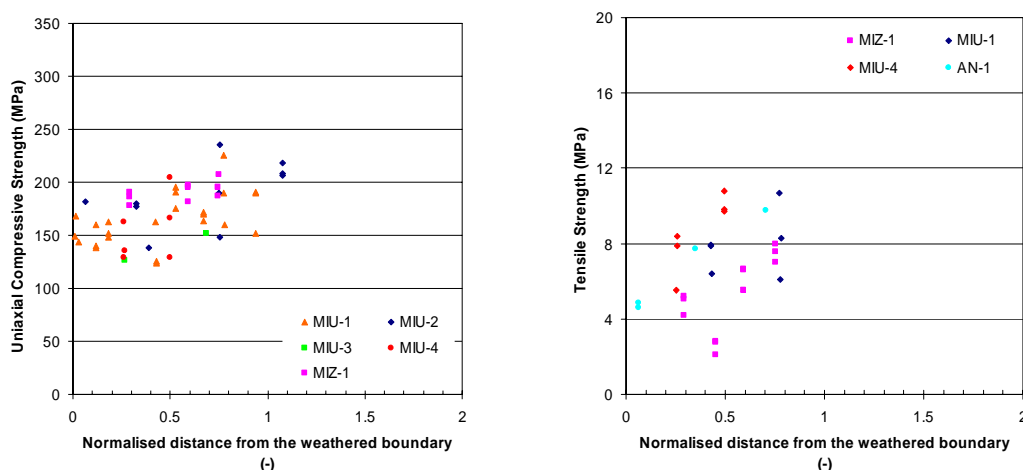
Figure 13. Variation of the uniaxial compressive strength (left) and Brazilian tensile strength (right) within the Upper Highly Fractured Domain at the Shobasama and MIU Construction Site. The vertical distance from the superficial weathered surface is normalised with respect to the thickness of UHFD in each borehole (e.g. the normalised distance is zero at the top and one at the bottom of UHFD).

The numerical analyses also constitute a source of information about the possible variation of the stress components with depth due to the presence of superficial sheeting joints in the rock mass. Considering that the maximum horizontal stress at the Shobasama and MIU Construction Site is about 30 MPa in magnitude and rather constant for depths below about 400 m (borehole AN-1, MIU-2, MIU-3), the numerical models with $K = 0.3$ appear to be realistic analogous of the two Sites (Figure 2). These models show that:

- Horizontal stress:

  1) Might be very high at shallow depth (down to about -50 m);

  2) Decrease markedly between -50 and -200 m;

  3) Increase gently with the same gradient as for the boundary stresses for depth below -200 m.

- Vertical stress:

  1) Might be larger in magnitude than the weight of the overburden at shallow depth (down to about -50 m), but in general can greatly vary between tensile and compressive values;

  2) Decreases towards tensile values between -50 and -200 m;

  3) Increases linearly according to the lithostatic gradient for depth larger than -200 m.

The findings reported above agree well with many field observations carried out in crystalline rocks at the AECL's URL (Canada) and SKB's Forsmark Site (Sweden). In the same order as presented above, the following field observations were done at these sites:

- Horizontal stress:

  1) Carlsson and Christiansson [24] reported that spalling in the roof of the Unit 3 discharge tunnel at Forsmark was observed during construction due to large horizontal stress concentrations at shallower depth than about -50 m;

  2) Stresses at the AECL's URL are low to a depth of about -200 m in relation to the presence of a superficial volume of fractured granite [25] that might correspond to the volume of rock interested by sheeting joints in the numerical models presented here;

3) Below about -200 m at the Shobasama and MIU Construction Site, the gradient of the horizontal stress is generally gentle except in the vicinity of the fault zones [15].

- Vertical stress:

1) The stress measurements by overcoring technique in borehole DBT1 and DBT2 at Forsmark show widely varying vertical stresses in a range between -10 to +15 MPa down to a depth of -80 m [26]. In this rock volume, no correlation seems to hold between vertical stress and depth. Larger vertical stresses than the weight of the overburden were also reported by Carlsson and Christiansson [27] for the same site at very shallow depths. Stress concentrations at the asperity of the sheeting joints might explain such wide variations;

2) Stresses are generally compressive between -80 and -120 m but lower than for the level above [26]. If the actual variation of the stresses resembles the numerical results, in-situ measurements results might be difficult to interpret at this depth interval as recurrent comments occurring in the literature seem to indicate;

3) In engineering practice [1], a lithostatic gradient of the vertical stress is assumed at all depth. The numerical results show that, besides oscillating, the vertical stress appears to be linear only for depth larger than about -200 m. Moreover, depending on the vicinity to the boundary and the degree of development of sheeting joints, the values can be significantly lower than the weight of the overburden. The linear lithostatic gradient from about -150 m is observed in the numerical models along lines very close to the model boundaries (symmetrical model in Figure 2).

The presence of fault zones previous the occurrence of sheeting joints affects the evolution of the fracturing and the distribution of the stresses. Usually, the presence of faults limits the propagation of the sheeting joints to only one side of the fault (the side towards the boundary of the model). A distinction must be made between sub-vertical faults and gently dipping faults. For sub-vertical faults:

- On the fractured side of the fault, the horizontal and vertical stress drop towards smaller compressive stresses while the shear stress increases;

- On the non-fractured side of the fault, the horizontal stress assumes higher compressive values while the vertical stress becomes almost lithostatic. Shear stresses are not particularly affected by the presence of the fault;

- At the depth of the fault, the stresses do not exhibit any abrupt variation.

For gently dipping faults:

- Horizontal stresses are markedly lower above the fault;

- Vertical stresses have a minimum in magnitude in relation to the fault and increase away from it (above and below the fault);

- At the depth of the fault, the stresses exhibit a jump in their values.

The fact that many indirect observations on the rock stresses, strength, deformation of crystalline rock masses seem to agree well with the results of the presented numerical modeling, one might conclude that the assumption made on the boundary conditions and boundary stress distributions (i.e. K, gradients and magnitudes), unloading sequence and material properties must be rather realistic and verisimilar. Also the fracture patterns resulting from the calculation look realistic and several features of these patterns can be observed in the field.
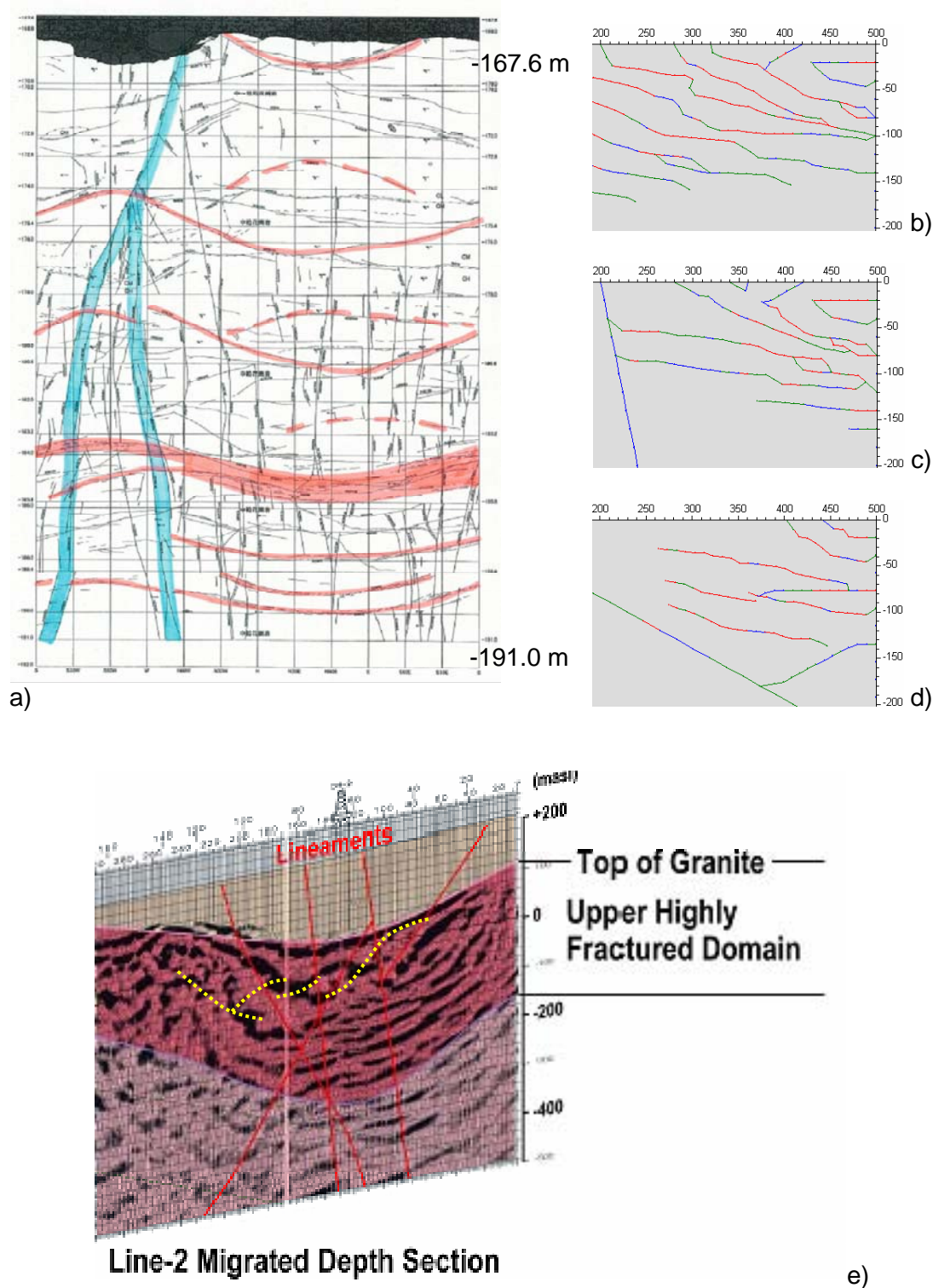
-167.6 m

-191.0 m

a)

b)

c)

d)

e)

Line-2 Migrated Depth Section

Figure 14. Similarities between the fracture patterns observed in-situ and the fracture patterns obtained by FRACOD[2D] modelling: a) unfolded fracture map of top of the granite basement of the Ventilation Shaft walls at the MIU Construction Site (steep fault in blue and sheeting joints in red); b, c, d) typical fracture patterns obtained by FRACOD[2D] models with and without fault zones; e) seismic SW-NE cross section adjacent to the MIU Construction Site in correspondence of borehole DH-2 where probable sheeting joints (dotted yellow lines) and fault zones (red lines) are indicated.

Some of the in-situ evidences are presented in Figure 14. The mapping of granite basement as it appears on the walls of the Ventilation Shaft of the MIU Construction Site shows that gently dipping fractures believed to be sheeting joints are abundant (red lines). Such fractures tend to stop against a vertical fault located at the SW side of the wall (blue lines). Sheeting joints also appear to be quite evenly spaced but in some location are rather clustered. Weaker gently dipping fractures with the same strike but opposite dip direction can also be observed on the walls (dashed red lines). The same features can be observed in the FRACOD[2D] models in Figure 1: case b) shows the presence of fractures with the same dip but opposite strike at the surface of the rock basement; case c) shows how the sheeting joints tend to stop against pre-existing steeply dipping fault zones and; case d) shows that the sheeting joints tend to run parallel to pre-existing gently dipping fault zones. All these schematic cases can be also observed in a seismic section adjacent to the MIU Construction Site (Figure 1 e) were lineaments (e.g. fault zones) inferred from surface and borehole observations are also marked.

The numerical models show that the effect of the boundary conditions on the pattern of the generated fractures is determinant. However, there is a close similarity between the effect of steeply dipping fault zones and the external boundary of the models in the sense that both features transfer preferentially normal loads but also allow a certain degree of deformation in the both the vertical and horizontal directions. This also implies that, if the boundary of the models can be assimilated to steep faults, sheeting joints might also be confined between the steep faults and could leave the rock on the other side of the faults untouched. This will consequently affect the stress regimes inside and outside the rock volume affected by sheeting joints as earlier observed for example in granite at Mount Valdo, Maine, USA [28].

6 Conclusions

In this study, an attempt to simulate the phenomenon of formation of sheeting joints in crystalline rocks by numerical modelling seem to have provided very useful and original results. This was made possible by the recent implementation of gravity acceleration in the BEM-DDM code FRACOD[2D] that was used for the analyses. The code, differently than most of the previous studies reported in the literature about rock stress modelling (e.g. ref. 29),30)), offers the unique possibility of analyzing the effect of fracture initiation and propagation on the stress distribution in the rock mass. The results presented here show that the final configuration of the models gives completely different results than the elastic solutions which only correspond to the initial steps of the BEM-DDM calculation. This result is reached without the need of unrealistic assumption about the material properties, model geometry or loading conditions (e.g. ref. 31)). In other words, the evolution of fracturing can significantly change the pattern of deformations and stresses.

Large uncertainties remain about most of the choices to be made in order to determine the input parameters, geometry, boundary conditions and sequence and mode of loading/unloading of the rock in the models. However, the analyses seem to show that beside tectonic forces and pure gravity, also rebound by removal of the overburden is a process that induces damage and/or failure of the rock. Thus, this phenomenon is of major importance when trying to reconstruct the fracturing history of a site. Sheeting joints are important, not only for the mechanical implications highlighted in this study, but also because they offer preferential pathways to the water in the superficial bedrock. The features of the fracture patterns obtained here by numerical modelling provide interesting information about the frequency, continuity, length, inclination and intersection of the gently dipping fractures due to rebound. This study also shows how the sheeting joints are affected by the presence of pre-existent faults.

This study provides the stress distributions due to the development of the sheeting joints and gives explanations to several features of the stresses observed, but not always understood, in many stress measurement campaigns in crystalline rocks. The verisimilitude of the numerical results with the field measurements, especially in the upper part of the bedrock, might also indicate that the field results are probably mainly showing the effect of rebound on the rock mass other than precedent geological processes (e.g. tectonic, faulting).

The main conclusions of this study can be summarized as follows:

- Vertical stresses do seldom follow a lithostatic distribution especially in the superficial part of the models. This is due to rebound that produces tensile stresses and sheeting joints close to the surface;

- Horizontal stresses tend to concentrate at the surface of the bedrock where they can also induce shear failure (typically above -100 m depth). Their concentration diminishes with depth and the horizontal stresses become rather low in magnitude between -100 and -200 m for increasing again for larger depths.

- An increase of the ratio between the vertical and horizontal stress (K) produce a deepening of the rock volume that experience sheeting joints. For K changing from 0.3 to 0.5, the volume interested by sheeting joints move from a depth of about -150 to about -200 m. In the field, intensive gently dipping fracturing is often observed in crystalline rocks down to similar depths (e.g. AECL's URL, SKB's Forsmark, JAEA's Shobasama and MIU Construction Site). The inclination of the sheeting joints diminishes and their spacing increases for increasing values of K.

- For increasing values of the Poisson's ratio of 0.25, 0.33 and 0.4, the depth until which sheeting joints appear decreases from -200, to -150 and -100 m, respectively.

- The presence of sub-vertical fault zones stops the horizontal propagation of the sheeting joints. Consequently, the stress regimes on the overhanging wall and footwall of the fault are different, although no abrupt stress variation can be observed along a profile crossing the fault.

- A gently dipping fault zone also affects the stresses but prevalently above of it. Vertical stresses seem to diminish in the vicinity of the fault. Fracturing is also limited to the hanging wall of the fault.

- The stresses experienced by the rock in the upper -100 to -200 m depth are severe enough to cause failure. However, the models have a finite grid-point spacing that limits the fracture occurrence to long fractures. Due to stress concentrations at the tips of the fractures or to the fact that the code cannot initiate denser fractures, stresses in the rock can become very high. This might explain the occurrence of frequent shorter sheeting joints in real rock masses and/or the damage of the core samples of intact rock (as observed superficially at the Shobasama and MIU Construction Site). The effect of an additional groundwater pressure can also trigger further fracturing.

Further studies should be carried out to consider the effect of a denser point-grid, of the groundwater pressure and of the size of the model. Time dependent phenomena causing stress relaxation and stress corrosion would also need to be checked upon to evaluate their impact on the fracture initiation and propagation. Furthermore, thermal stresses, which can reduce the tensile strength of the rock to very low values especially in quartz-reach rock types (Kranz, 1983), were not considered in this study.

7 Acknowledgments

8 References

1) Fairhurst C. : Stress estimation in rock: a brief history and review, Int. J. Rock Mech. Min. Sci., Vol. 40, p. 957-973,2003.

2) Kranz R.L. : Microcracks in rocks: A review, Tectonophysics, Volume 100, Issues 1-3, p. 449-480 (Abstract), 1983.

3) Barnes F.A. : Canyon country geology: Salt Lake City, Utah, Wasatch Publishers, p. 160, 1978.

4) Blair R.W.Jr. : Development of natural sandstone arches in south eastern Utah, in Gardiner, V., eds., International Geomorphology 1986, University of Manchester, p. 597-604, 1987.

5) Hunt C. : Cenozoic Geology of the Colorado Plateau, United States Geological Survey Professional paper 279, p. 99, 1956.

6) EIU : Mechanical and Chemical Weathering, Eastern Illinois University, http://www.ux1.eiu.edu/~cfjps/1300/weathering.html, 2006.

7) Martel S.J. : Effect of topographic curvature on near-surface stress and application to sheeting joints, Geoph. Res. Lett., Vol. 33, Paper L01308, 2006.

8) Martel S.J., Larin P. : Formation of sheeting joints in concave slopes, Eos Trans. AGU, 87(52), Fall Meet. Suppl., Abstract T11A-0423, 2006.

9) Amano K. : Personal communication, 2006

10) Shen B., Rinne M., Stephansson O. : FRACOD^{2D} - Two dimensional fracture propagation code (Version 2.3.1), FRACOM Ltd., Finland (www.fracom.fi), 2007.

11) Shen B. : Mechanics of fractures and intervening bridges in hard rocks, PhD Thesis, Royal Institute of Technology, Stockholm, Sweden, 1993.

12) Crouch, S.L.: Solution of plane elasticity problems by the displacement discontinuity method, I. J. Num. Methods Engng., Vol. 10,p.301-343, 1976.

13) Crouch, S.L., Starfield, A.M. :Boundary element methods in soil mechanics, George Allen & Unwin Ltd., London, UK, p.79-109, 1983.

14) Shen B., Stephansson O., 1993. Modification of the G-criterion of crack propagation in compression, Int. J. Engng. Fracture Mech., Vol. 51(1), p. 73-85.

15) Nakama S., Sato T., Kato H., 2005. Status of study on in-situ stress in the Mizunami Underground Research Laboratory, 40th U.S. Symp. on Rock Mech., Alaska Rocks 2005, Anchorage, Alaska, June 25-29, 2005, ARMA/USRMS 05-887.

16) Stephansson O., Shen B., Rinne M. : The geomechanical evaluation and analysis of surrounding rock mass response to excavation of research shafts and galleries in MIU project, FRACOM LTD, p.89,2003.

17) Bakers T. : Mode I and Mode] II fracture toughness testing and fracture normal stiffness estimation of Tono-Granite, GeoForcschungZentrum(Posdam, Germany), p.18, 2002.

18)Lanaro F. : Geometry, Mechanics and Transmissivity of Rock Fractures, Ph.D thesis, Royal Institute of Technology in Stockholm, KTH, Sweden, p.60, 2001.

19) Gercek H. : Poisson's ratio values for rocks, Int. J. Rock Mech. Min. Sci., Vol. 44, p. 1-13, 2006.

20) Mindlin R.D. : Stress distribution around a tunnel, Trans. ASCE, Vol. 105, p. 619-642, 1939.

21) Terzaghi K., Richart R.E. : Stresses in rock about cavities, Geotéchnique, Vol. 3, p. 57-90, 1952.

22) Fairhurst C. : Fundamental considerations relating to the strength of rock, Veröff. Inst. Bodenmechanik und Felsmechanik, Karlsruhe, Germany, Vol. 55, p. 1-56, 1971.

23) Amano K. : JAEA-NAGRA Workshop at MIU Construction Site, July 4-5, 2007.

24) Carlsson A., Christiansson R. : Construction experiences from underground works at Forsmark: Compilation Report, the Swedish Nuclear Fuel and Waste Management Co, SKB Rapport R-07-10, 2007.

25) Thompson P., Chandler N. :In situ rock stress determinations in deep boreholes at the Underground Research Laboratory, Int. J. Rock Mech. Min. Sci., Vol. 41(8), p. 1305-1316, 2004.

26) Sjöberg J., Lindfors U., Perman F., Ask D. :Evaluation of the state of stress at the Forsmark site – Preliminary site investigation, Forsmark area - version 1.2, Swedish Nuclear Fuel and Waste Management Co, Tech. Rep. SKB R-05-35, 2005.

27) Carlsson A., Christiansson R. : Geology and tectonics at Forsmark, Sweden, the Swedish State Power Board, Vattenfall, Technical Report U(B) 1987/42, 1987.

28) Engelder T. : Stress regimes in the lithosphere, Princeton University Press: Princeton, New Jersey, USA, p. 457, 1993.

29) Hakami E., Hakami H., Christiansson R. : Depicting a plausible in situ stress distribution by numerical analysis – examples from two candidate sites in Sweden, Proc. Int. Symp. on In-Situ Rock Stresses – Measurement, Interpretation and Application, Trondheim, Norway (Lu M., Li C., Kjørholt H., Dahle H. eds.), Taylor & Francis/Balkema, the Netherlands, p. 473-481, 2006.

30) Baek S.-H., Moon H.-K., Park S.-C., Moon S.-H., Kim C.-Y., Kim K.-Y. : Analysis of the distribution of rock stress ratio and its influence on the behaviour of underground opening, Proc. Int. Symp. on In-Situ Rock Stresses – Measurement, Interpretation and Application, Trondheim, Norway (Lu M., Li C., Kjørholt H., Dahle H. eds.), Taylor & Francis/Balkema, the Netherlands, p. 279-287, 2006.

31) Hakami H. : Numerical studies on spatial variation of the in situ stress field at Forsmark - a further step. Site descriptive modelling Forsmark - stage 2.1, Swedish Nuclear Fuel and Waste Management Co, Tech. Rep. SKB R-06-124, 2006.

This is a blank page.

10. Thin-sections and x-ray spectroscopy of Toki granite samples from borehole MIZ-1 (Paper 8)

This is a blank page.

Thin-sections and x-ray spectroscopy
of Toki granite samples from borehole MIZ-1

Flavio Lanaro, Kenji Amano, Kiminori Nakamata

Japan Atomic Energy Agency

Abstract : Samples of Toki granite were collected from the core of borehole MIZ-1 at the Mizunami Underground Laboratory (MIU) Construction Site for performing Brazilian tests. The test results integrate the already available laboratory results for two depths that previous testing did not cover. These two depths were chosen to correspond to high and low in-situ stresses, according to the available results of the hydro-fracturing method. Two samples batches of 8 and 10 samples were respectively taken at about 522 and 765 m along the borehole. One sample for each batch was also taken for producing a thin-section to be observed with a microscope and to be subjected to x-ray spectroscopy. Additional information is also provided here about grain size, mineral composition and microcracks patterns visible at the microscope or found in the literature about the Toki granite. The first sample, from a section of borehole MIZ-1 with relatively large in-situ stresses, shows extensive cracking. This sample also presents a much larger grain size than a second sample taken from larger depth in a section of borehole with lower in-situ stresses. The second sample presents cracks filled with sericite and quartz. The presence of open microcracks in the first sample could be imputed to the higher in-situ stresses at the position the sample was taken and can be interpreted as sample damage. Alteration was not observed in any of the samples.

1   Sampling of Toki granite from MIZ-1 for Brazilian testing

Two batches of 8 and 10 core samples each were collected from the core of borehole MIZ-1 to be tested in Brazilian test conditions. Two sampling locations were chosen considering the following aspects:

- Samples were taken outside the fault zones (see Table 1)
- Samples were taken from sections of borehole not sampled for Brazilian testing before (see Figure 1)
- Samples were taken from a macroscopically intact section of core (no preexistent or drill-induced visible fractures)
- Samples were taken from the Lower Sparsely Fractured Domain
- One batch of samples should come from a depth where the difference between the maximum horizontal stress and the vertical stress (σ_H-σ_v) is expected to be *high* (see Figure 3)
- One batch of samples should come from a depth where the difference between the maximum horizontal stress and the vertical stress (σ_H-σ_v) is expected to be *low* (see Figure 3)
- The samples in each batch should be taken consecutively.

The sampling depths are as shown in Table 2.

Table 1. Position of the fault zones in borehole MIZ-1.

Borehole	Upper Fault Zone Limit [mabh]	Lower Fault Zone Limit [mabh]
MIZ-1	195.3	223.2
	648.2	725.8
	918.2	982.7

Table 2. Sampling position along borehole MIZ-1 for Brazilian testing.

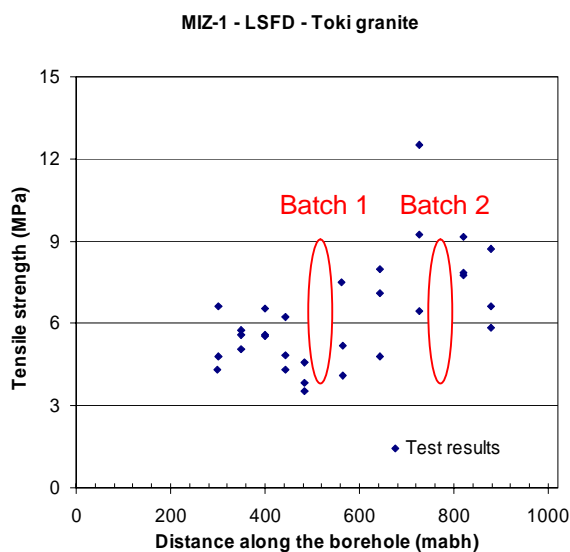| Sample batch No.	Length along the borehole [mabh]	Depth [masl]	Comments
	483.07	*-276.51*	*Previous sampling*
1 (8 samples)	521 – 522	-314.45 / -315.45	(Figure 2, left)
	563.14	*-356.58*	*Previous sampling*
	773.43	*-520.85*	*Previous sampling*
2 (10 samples)	765 – 766	-558.44 / -560.44	(Figure 2, right)
	819.44	*-612.88*	*Previous sampling*

Figure 1. Available Brazilian test results in the Lower Sparsely Fractured Domain (LSFD) in borehole MIZ-1.
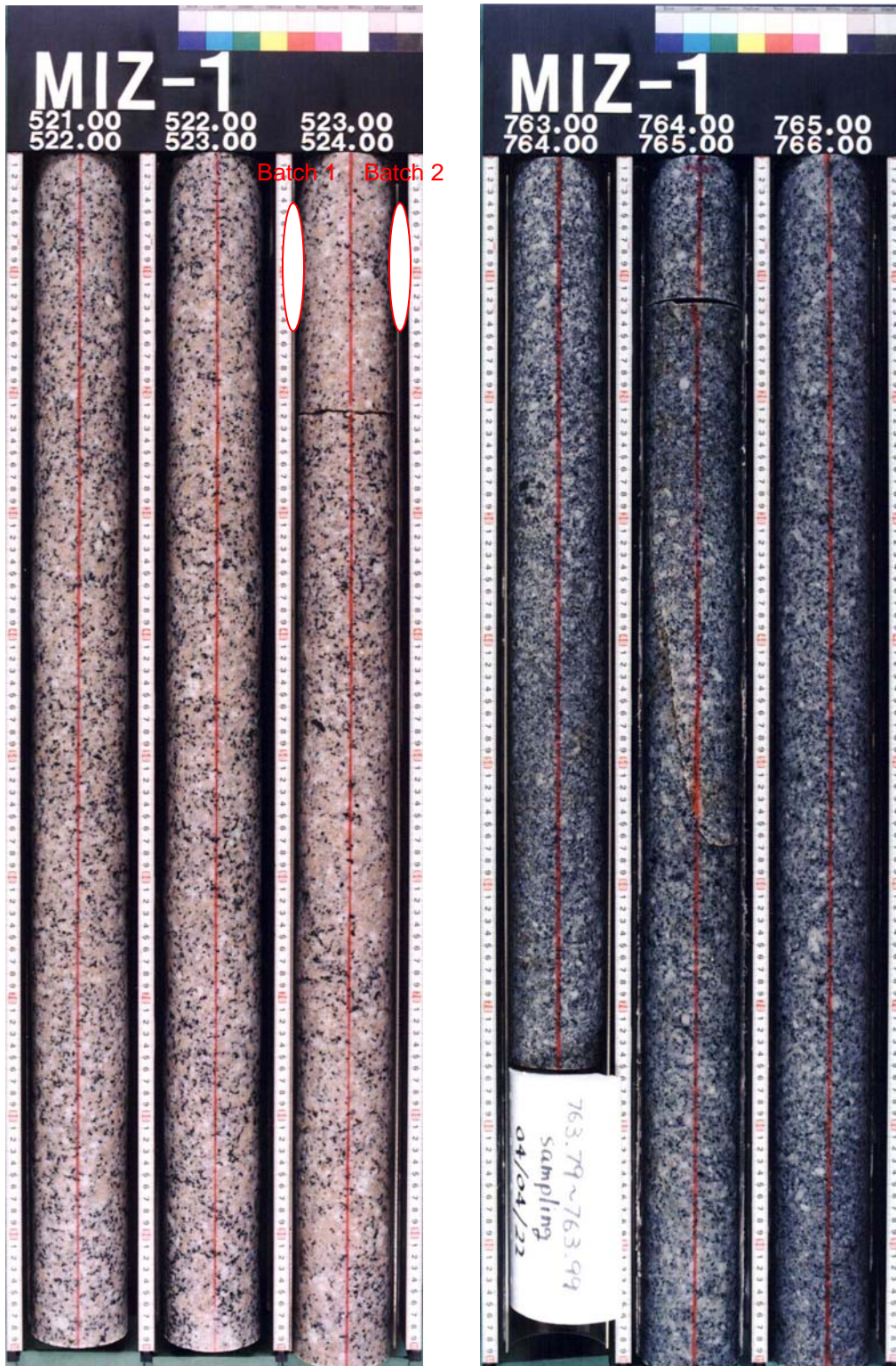
Figure 2. Picture of the core box from MIZ-1 where sample batch No. 1 was taken (522-523 mabh) (left); picture of the core where sample batch No. 2 was taken form the same borehole (765-766 mabh)(right).
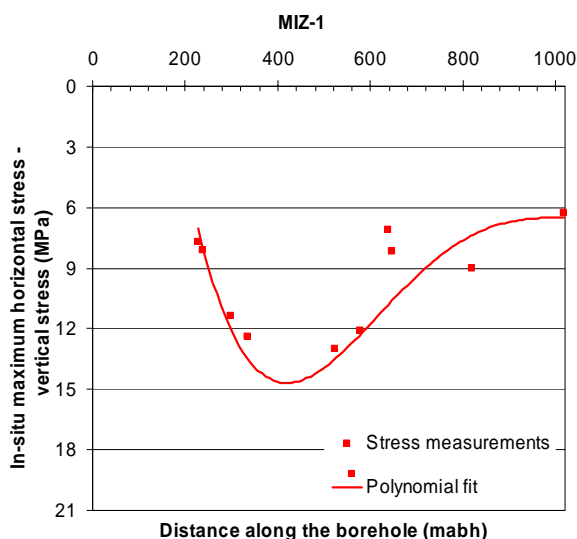
Figure 3. Estimated variation of the difference between the maximum horizontal stress and the vertical stress (σ_H-σ_v) along borehole MIZ-1 based on in-situ hydro-fracturing measurements.

2 Samples for thin-sections and x-ray spectroscopy

Two samples were provided for thin-section and x-ray spectroscopy analysis. The microscope pictures were taken indicating the orientation with respect to two reference lines so that microfracture orientation can be determined. On the core samples, a red line indicates the orientation of the core. A blue line indicates which is the upper and lower flat surface of the core sample. If the blue line appears on the right hand side of the red line, then the upper flat surface of the core was also the upper surface in the borehole (e.g. lower depth).
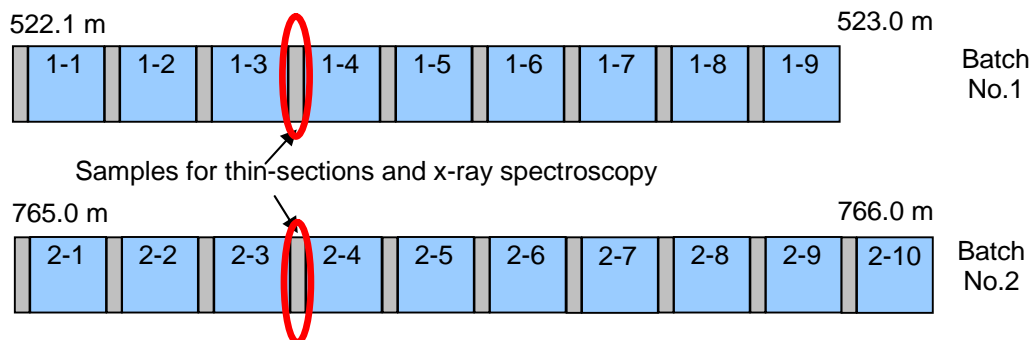

Figure 4. Position of the samples for thin-section and x-ray spectroscopy along the core of borehole MIZ-1.

Table 3. Sample identification.

MIZ-1 – Sample ID	Length along the borehole [mabh]
1-4	522.40 - 522.50
2-4	765.30 - 765.40

3 Sample appearance

The samples were photographed and cut to obtain thin-sections of size 24×30 mm. The surfaces prepared for the thin section and their location with respect to the core reference system are shown in Figure 5. This figure also shows that the grain size for sample 1-4 varies typically between 0.1 and 10 mm (average about 4 mm), while the grain size of sample 2-4 ranges between 0.1 and 6 mm (average about 2 mm).

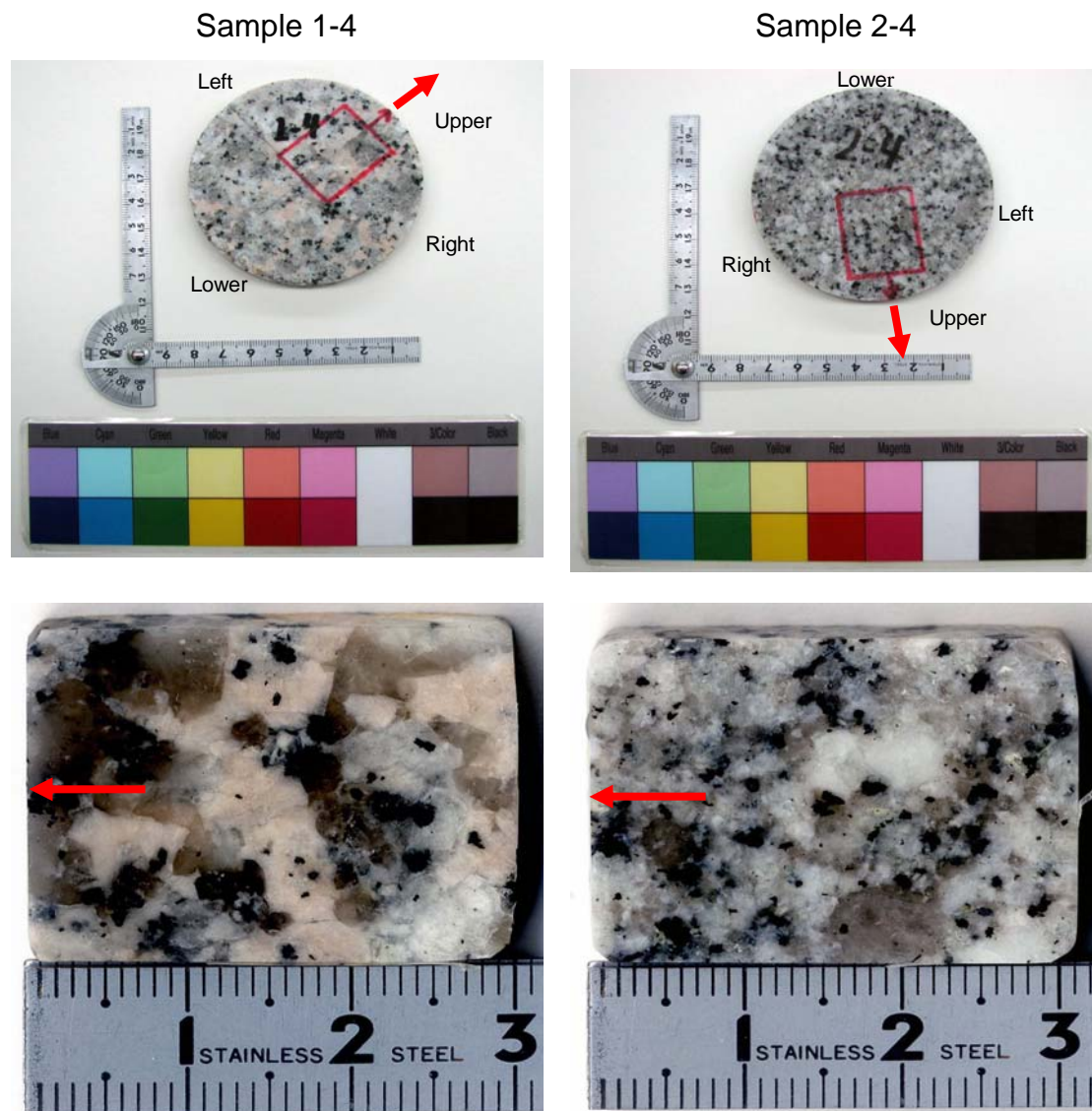Sample 1-4   Sample 2-4

Figure 5. Sample 1-4 and 2-4 from borehole MIZ-1 and their surfaces prepared for thin-sections and x-ray spectroscopy. The red arrow shows the edge close to the contour of the core.

4 Typical element and oxide composition of the Toki granite (MIZ-1)

The x-ray spectroscopy of the polished surface of the samples in Figure 5 returned the qualitatively element composition in weight presented in Table 4 and Figure 7 (based on the count-per-second/mA recorded by the spectroscopy). Sample 1-4 and both samples were scanned. The element and compound composition of sample 2-4 was obtained by difference because the samples had exactly the same size.

Accurate measurements of the total mass of elements lighter than manganese are difficult due to weakness of x-ray intensities. Errors of the mass concentrations of sodium and manganese reflect on those of aluminium and iron because these mass concentrations are calculated as remnant fractions of the total. Also the determination of the percentage of mass of the oxides suffers similar uncertainties.

The element composition of the two samples is almost identical for what concerns silicon and oxygen content, but differs 25% for calcium, 20% for aluminium, 7% for sodium content. The difference for the other dominant elements is smaller than 5% with respect to the total weight. The element spatial distributions inside the samples are shown in Figure 6, where the shape of the grains can also be analysed. Here, iron is localised exclusively in the biotite grains (dark in colour) and its distribution is similar in both samples. Moreover, the boundaries of the crystals of potassium-feldspar are better defined in sample 1-4 probably because of its coarseness.

Concerning the oxide composition, silica is dominant (approximately 80% in weight; Table 4 and Figure 7). Other compounds are sodium, aluminium and potassium oxides (all below 10%). The values obtained in this study differ from the results published by Ishihara & Wu[1] and obtained from outcrop samples.

Table 4. Element and oxide concentrations in weight from the X-ray spectroscopy of sample 1-4 and 2-4 of Toki granite. All figures are only qualitative estimations.

Elements	Sample 1-4 Conc.* [%]	Sample 2-4 Conc.* [%]	Oxides	Sample 1-4 Conc.* [%]	Sample 2-4 Conc.* [%]	Ishihara & Wu, 2001
Na (11)	6	6	Na_2O	9	9	3
Mg (12)	0	0	MgO	0	0	0
Al (13)	4	4	Al_2O_3	7	7	14
Si (14)	38	38	SiO_2	81	80	73
K (19)	2	2	K_2O	3	3	4
Ca (20)	1	1	CaO	1	1	1
Mn (25)	0	0	MnO	0	0	0
Fe (26)	0	0	Fe_2O_3	0	0	2
O (8)	49	49				

- Accurate measurements of elements lighter than Mg are very difficult due to weakness of x-ray intensities. This also mirrors on the concentrations of the oxides.
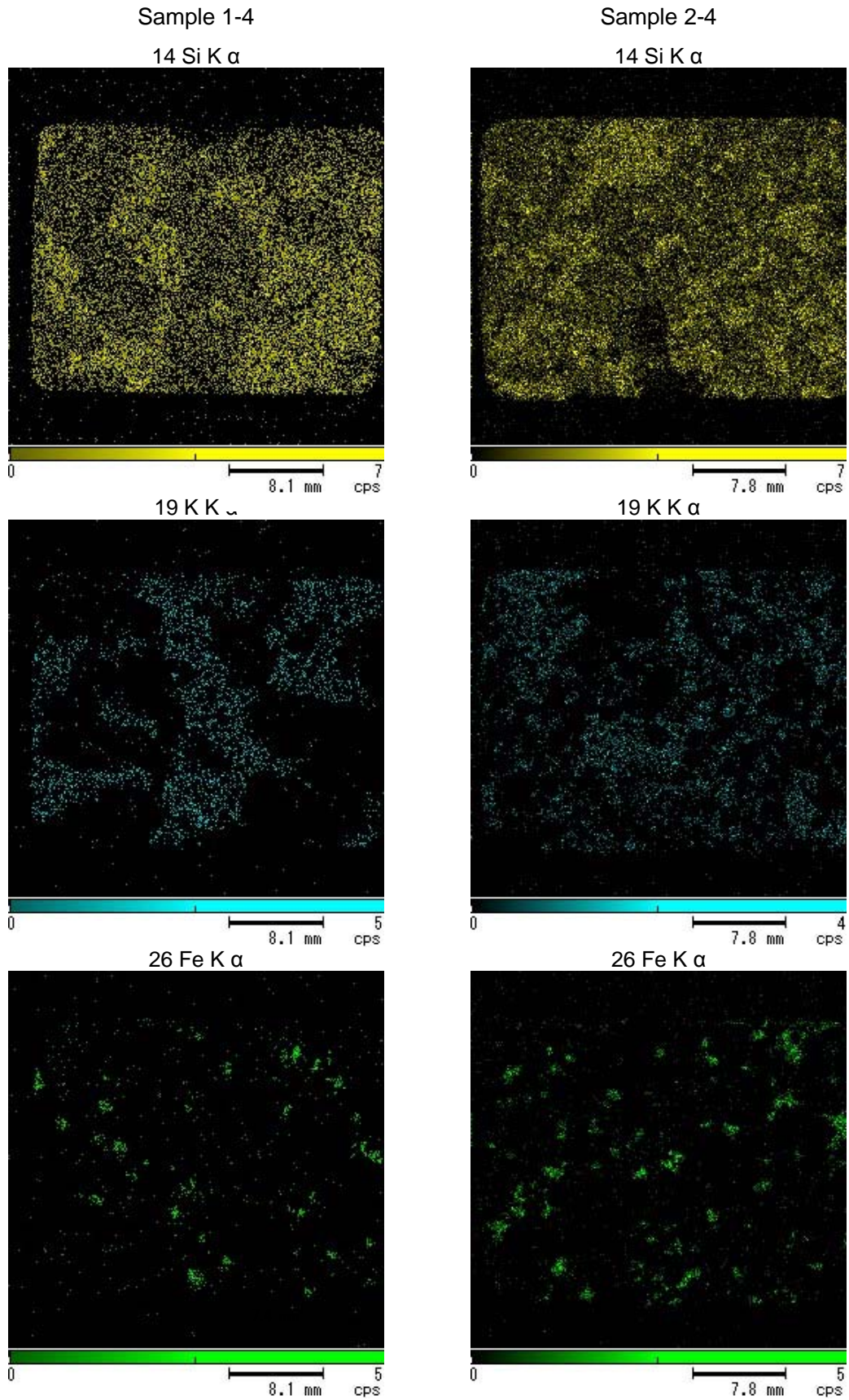
Sample 1-4

14 Si K α

Sample 2-4

14 Si K α

19 K K α

19 K K α

26 Fe K α

26 Fe K α

Figure 6. Distribution of silicon, potassium and iron inside sample 1-4 (left) and 2-4 (right) as obtained by means of x-ray spectroscopy.
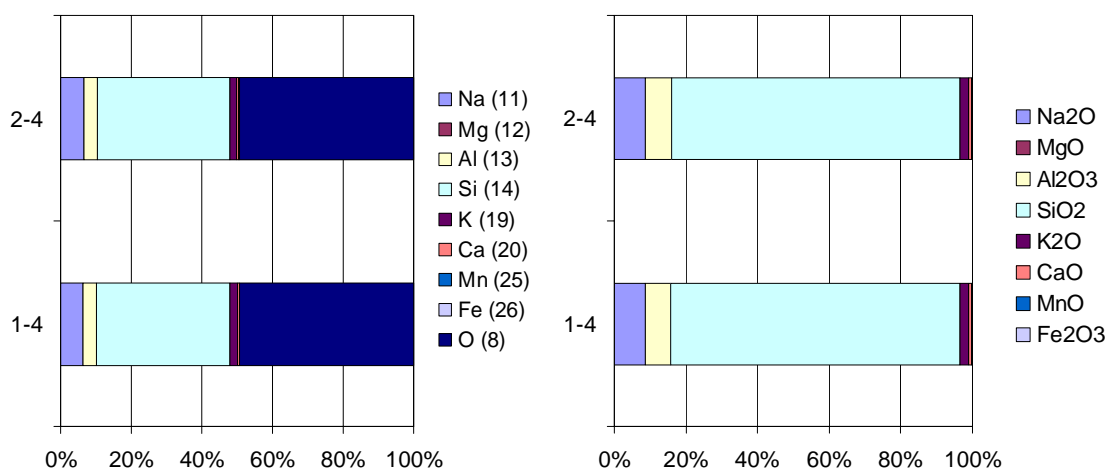
Figure 7. Element and oxide concentrations in weight obtained by x-ray spectroscopy of sample 1-4 and 2-4 of Toki granite. (Data from Table 4.).

5   Typical mineral composition of the Toki granite (general)

The Toki pluton, which has a circular exposure of about 140 km^2, predominantly presents a monzogranite composition except on its North-Western corner where it becomes granodioritic[2] . The Toki granite contains only a few pegmatite intrusions and almost totally lacks of any economic grade of metallic mineralization [1].

The modal analysis results of Ishihara & Terashima[2] were also confirmed by the results from borehole DH-5 belonging to the Regional Hydrogeological Study[3] and distant about 5 km from borehole MIZ-1. The modal analysis results locate the Toki granite from borehole DH-5 in the field of monzogranite[4]. The low sodium-oxide content also ascribes the Toki granite to the group of biotite granites[1].

Table 5. Modal analysis of the Toki granitoids (after Ishihara & Terashima[2]).

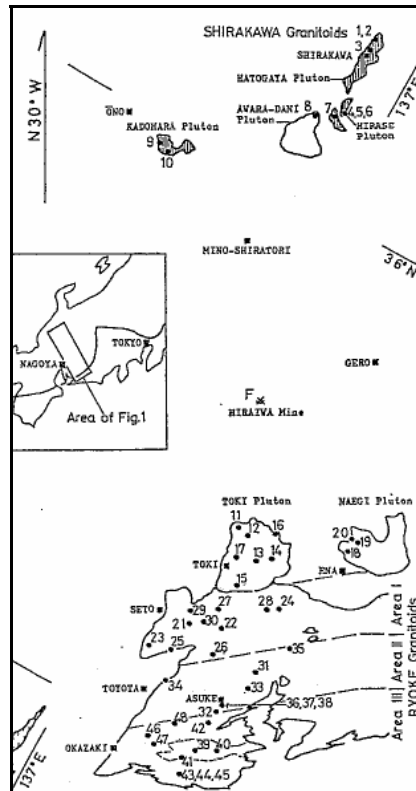| Analysis No.	P Plagioclase	A Potassium feldspar	Q Quartz	Hb Hornblende	Bt Biotite	Mus Muscovite	Others
11	45.4	17.1	26.8	0.2	9.2	-	1.3
12	35.6	17.8	40.1	0.2	6.0	-	0.3
13	32.3	30.7	32.3	-	4.1	-	0.6
14	33.3	30.3	33.6	-	2.6	traces	0.2
15	37.7	29.5	28.6	-	3.9	0.1	0.2
16	38.3	26.3	33.6	-	1.2	0.2	0.4
17	27.3	27.0	43.8	-	1.3	-	0.6

Figure 8. Location of the samples for modal analysis reported in Table 5[2]**.**
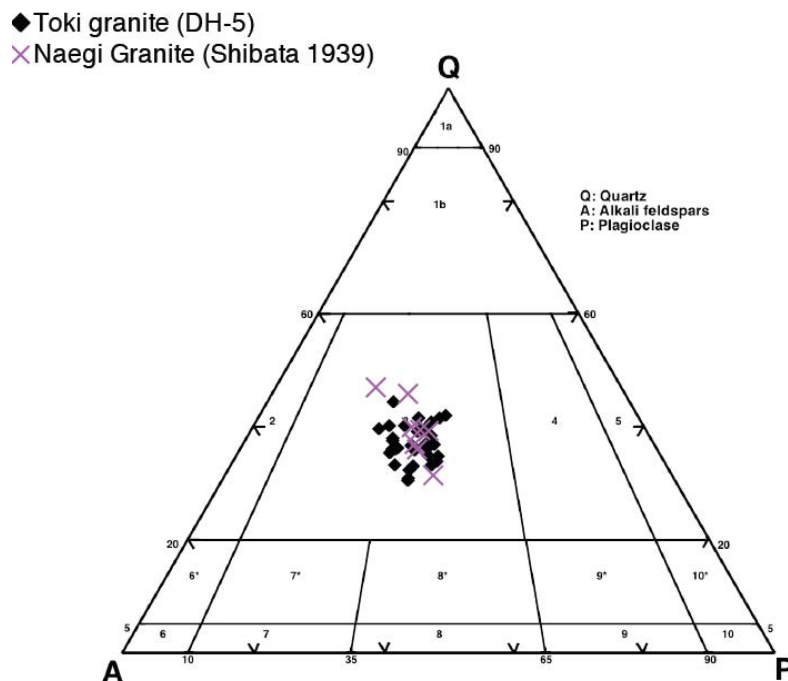

Figure 9. Modal analysis of the samples of Toki granite from borehole DH-5 according to the general classification for igneous rocks by Streckeisen (% in volume of quartz, plagioclase, alkali feldspar; modal mineral content)[4]

6 Microscope observations on thin-sections (MIZ-1)

Thin-sections from sample 1-4 and 2-4 were analysed with an optical microscope with magnification 100 times. Some pictures were also taken and are shown in Figure 10   and Figure 11. From the pictures, both samples show no alteration of the biotite grains, which implies that the rock is "fresh".

The pictures from sample 1-4 clearly show that the grain size is larger than 1 mm on average. The plagioclase crystals (striated gray sometimes showing twinning – Figure 11, ④[5]) also show some cleavage with an angle with the picture vertical edge (that is radial with respect to the core section). Crystals of quartz (plane light or dark gray) and alkali feldspar (banded light gray) show quite intensive microcracking. This is more randomly oriented at the centre of the sample and it aligns itself to the radial direction by approaching the contour of the core. Close to the contour of the core, microcracks have millimetric size, and some of them continue outside the pictures (length larger than 1 mm). Figure 10 ③ shows perthitic texture of the K-feldspar, where the potassium reach phase is the host from which the sodium-rich phase exsolved forming bands and strings[6].

Sample 2-4 shows larger abundance of sericite (fine-grained potassium mica[6]) and quartz filled cracks. Often, also the boundaries of the crystals show the presence of sericite veins. However, their length is often shorter than the grain size, which for this sample varies between 0.1 and 6 mm. These filled microcracks are found to be intragranular in the large grains, and intergranular around the small grains. Almost no open microcracks are observable in the pictures and the infilled microcracks have a typical length between 0.1 and 0.3 mm.

This analysis shows that the conditions of sample 2-4 are generally better than for sample 1-4 when microcracking is concerned. It should be pointed out here that no particular attention was taken to avoid the appearance of microckracks during preparation of the thin-sections. However, sample 2-4 does not show any noticeable signs of cutting induced microcracking.

Biotite crystals were not so common in the pictures taken. However, Figure 10 ⑤ a typical biotite crystal protruding into quartz with a very sharp corner.
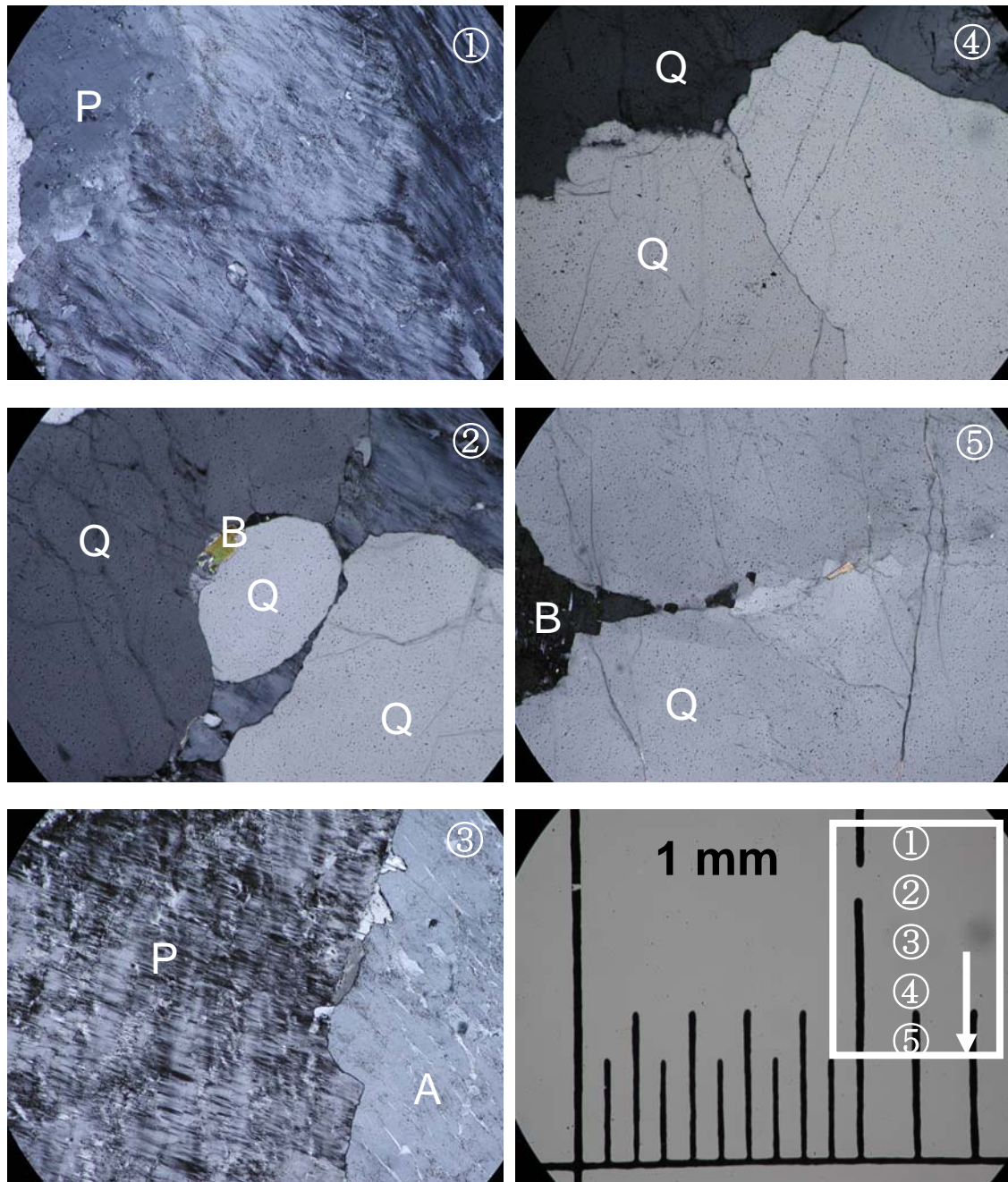
Sample 1-4

Figure 10. Microscopy pictures of the thin-section of sample 1-4 at different positions with respect to the outer contour of the core (indicated by the arrow). The letters indicate the type of crystals: A for alkali-feldspar, B for biotite, P for plagioclase and Q for quartz.
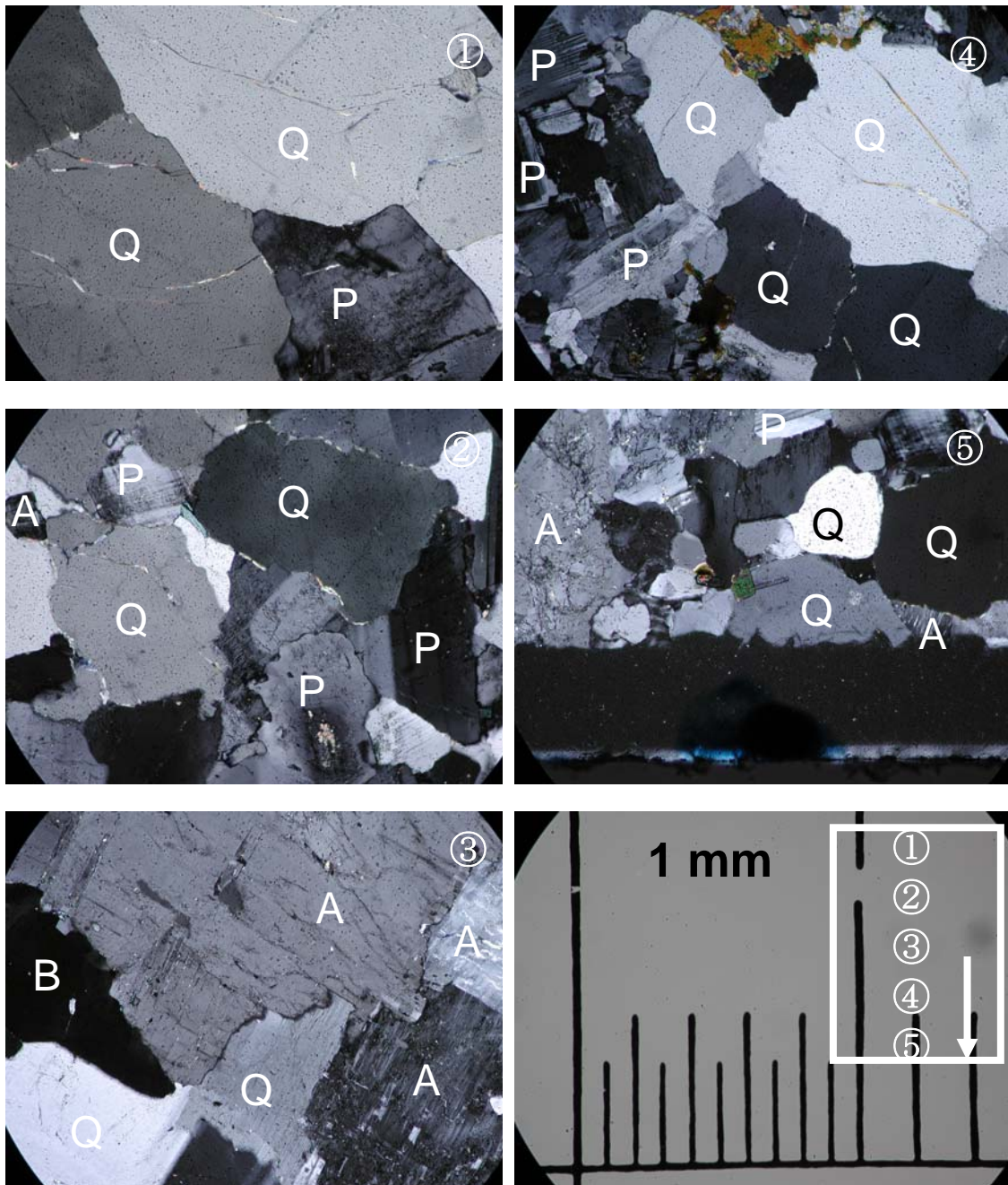
Sample 2-4

Figure 11. Microscopy pictures of the thin-section of sample 2-4 at different positions with respect to the outer contour of the core (indicated by the arrow). The letters indicate the type of crystals: A for alkali-feldspar, B for biotite, P for plagioclase and Q for quartz.

7   Conclusions

From previous studies it can be concluded that the Toki granite has a monzogranite composition. Furthermore, the mineralogy does not vary much in a large area (the Toki pluton has a diameter of about 13 km).

Also this brief study shows that the element and mineralogical composition of the samples from borehole MIZ-1 at the MIU Construction Site, which were tested in Brazilian conditions, is rather constant although the samples were taken from locations 242 m apart from each other. Despite the mineral composition is the same, the grain size distribution is different for the two samples, quite coarse for sample 1-4 (from 522.3 mabh) and medium-to-fine grained for sample 2-4 (from 765.3 mabh). In both samples, alteration is not present.

Sample 1-4 presents longer and more frequent microcracks of millimetric length. Most of the cracks appear to be open and tend to become radial approaching the contour of the core. On the other hand, most of the microcracks in sample 2-4 seem to be filled with sericite and quartz, thus, should not be open. The size of the microcracks for sample 2-4 is smaller than 0.3 mm. Preferential cracking direction could not be observed.

This study confirms earlier observations on microphotographs carried out by Liu et al.[7]. They observed that quartz usually contains the largest number of cracks, followed in order by biotite and feldspar. According to their observations, stress concentrations arose inside the samples in correspondence of the sharp corners of laminar mineral such biotite against quartz and feldspar. When the fracture propagation during loading is concerned[8], quartz grains act as obstacle for fracture propagation. Biotite, on the other hand, facilitates the propagation. Feldspar usually induces a change in the direction of propagation thanks to its directions of preferential cleavage.

It could be concluded that the level of in-situ stress might be the cause of more microcracking in sample 1-4 compared to sample 2-4. Those microcracks would be an indication of damage of the core sample.

In the future, it would be interesting to analyze samples of Toki granite after testing in uniaxial compression and/or Brazilian test conditions so that the initiation and propagation of the microcracks can be studied in detail and compared with the sample conditions before testing.

The analysis of the frequency distribution of the cracks calculated by the "box counting" method (e.g. ref. 9)) could also be carried out to verify the fractal nature of the sample microcracks. The same technique could be applied to study core sample damage in induced in laboratory under uniaxial, triaxial and Brazilian test conditions.

8   Acknowledgments

9　References

1) Ishihara S., Wu C. : Genesis of late Cretaceous-Paleogene granitoids with contrasting chemical trends in the Chubu District, Central Japan, Bull. Geo. Surv. Japan, Vol. 52 (10), p. 471-491, 2001.

2) Ishihara S., Terashima S. : Chemical variation of the Cretaceous granitoids across Southwestern Japan, J. Geol. Soc. Japan, Vol. 83(1), p. 1-18, 1977.

3) Takeda, S. : Current status of R&D activities at Tono Geoscience Center – Mizunami Underground Research Laboratory Project and Regional Hydrogeological Study Project. ICGM'04, JNC TN7400 2004-010, p.83-95, 2004.

4) Nishimoto S. : Personal communication, Nagoya City Science Museum, Nagoya, Aichi Pref., Japan, 2007.

5) Vernon R. H. : A practical guide to rock microstructure, Cambridge University Press: UK, p. 594, 2004.

6) Bates R.L, Jackson J.A. : Glossary of geology, American Geological Institute: Alexandria, Va, USA, p. 788, 1987.

7) Liu S., Anwar F., Seiki T., Ichikawa Y. : Microcrack generation and propagation in granite during stress relaxation under water saturated tri-axial condition, Journal of the Japan Society of Engineering Geology, Special Edition, Japan Society of Engineering Geology, p. 623-630, 2006.

8) Nara Y., Koike K., Yoneda T., Kaneko K. : Relation between subcritical crack growth behavior and crack paths in granite, Tech. Note, Int. J. Rock Mech. Min. Sci., Vol. 43, p. 1256-1261, 2006.

9) Zhao Y. : Crack pattern evolution and a fractal damage constitutive model for rock, Int. J. Rock Mech. Min. Sci., Vol. 35(3), p. 349-366, 1998.

11.   Discussion and conclusions

This is a blank page.

Discussion and conclusions

Flavio Lanaro

Japan Atomic Energy Agency

Abstract: In this chapter, the issues treated in this report concerning variability, predictive capability and crack patterns are discussed. Linear elastic fracture mechanics and its intrinsic scaling properties are also analysed with respect to scale dependency of the geometry and strength of crack/fracture patterns. The conclusions of this study can be summarised as: i) damage permeates core sampling; ii) understanding of core damage can lead to more reliable estimations of the in-situ stresses; iii) scaling properties of fracture mechanics and crack/fracture patterns should be carefully considered in modelling; iv) the concept of "weakest crack" is introduced and; v) gravity seems to be the driving force of sheeting joint patterns.

1   Natural and numerical variability

Variation of the geological settings, boundary conditions, sampling and testing technique can cause variability of the measured strength of the rock. Also numerical modelling involving random generation of the mechanical properties for modelling heterogeneity shows variability of the results. In this section, some aspects of variability encountered in this study are examined.

1.1   Variability of the Toki granite

The geoscientific studies at the Shobasama and MIU Construction Site show that the Toki granite has mainly three facies: muscovite-bearing, biotite-bearing and leucocratic (Figure 1; Tsuruta et al.[1]). All three facies occur in borehole MIZ-1 within rather persistent volumes of rock. The mechanical properties of the Toki granite, however, were not found to correlate well with the occurrence of the three facies, which mineralogy and grain size distribution differences do not seem to affect the strength of the core samples. On the other hand, the rock mass classification (which takes into account the strength of the rock, the occurrence of the fractures and other geological parameters[2]) along borehole MIZ-1[3] shows an interesting feature: the rock mass classes of better quality (A and B) also show lower uniaxial compressive strength of the intact rock compared to the middle rock mass quality classes (CH and CM). This is evidently a contradiction that could be explained as follows. Rock masses of better quality are probably stiffer than the surrounding rock, thus, are more likely to be prone to stress concentrations (e.g. ref. 4)).
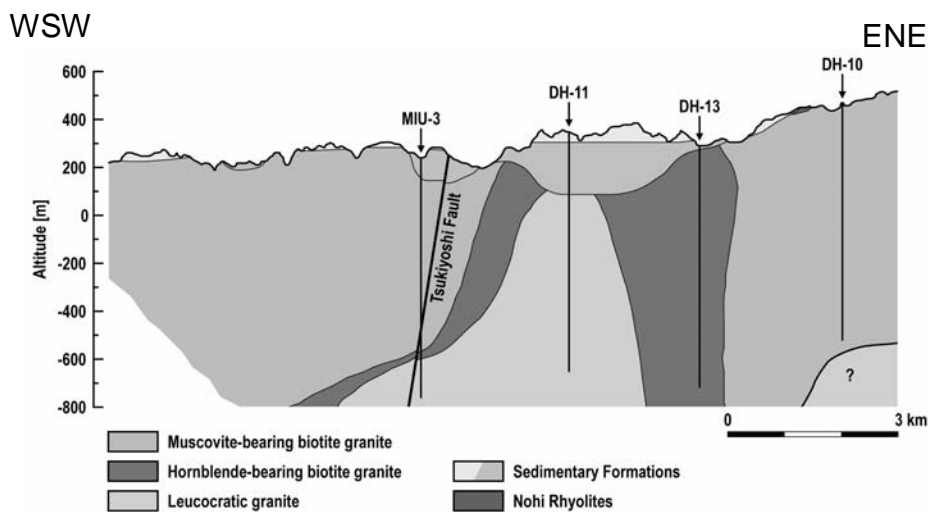
Figure 1. Geological WSW-ENE cross section of the Tono Area at Mizunami, Gifu Pref., Japan, with indication of the recurrent types of Toki granite (muscovite-bearing, hornblende-bearing, leucocratic). The Shobasama and MIU Construction Site are located in the central part of the section. (After Tsuruta et al., 2004.)
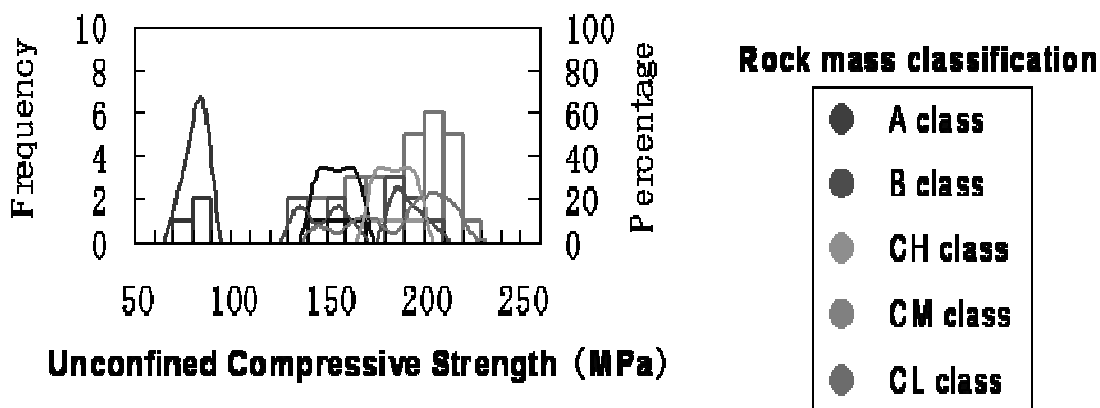

Figure 2. Frequency distribution of the rock mass quality classes for the rock along borehole MIZ-1 at the MIU Construction Site (Yamada et al., 2005).

In-situ stress concentrations together with drilling induced mechanical and thermal stress concentrations (e.g. ref. 5), 6), 7), 8)) can result into "disturbance" and "damage" of the drill-cores with reduction of the laboratory strength compared with the in-situ strength.

1.2 *Variability of the laboratory test results*

Non negligible spatial variation of the strength of the Toki granite was observed for the uniaxial compressive strength and Brazilian tensile strength of core samples from several boreholes at the Shobasama and MIU Construction Site. Initially, such spatial variation was imputed to geological heterogeneity of the rock type, influence of the drilling parameters and diameter, sampling and testing techniques, but in more accurate investigations (PAPER1 and PAPER2) it was shown that such spatial variability would be strongly correlated to the level of in-situ stresses at location in the rock mass where the samples were taken. Although the other causes of heterogeneity could not be completely excluded, the sample "disturbance" or "damage" seemed to be the most plausible reason. Disturbance or damage would rise due to the complex stress-path the borehole core goes through during drilling which involves stresses much more severe than the stresses in-situ.

A technique for estimating the entity of the disturbance and damage was developed based on the observed correlation between the strength (from uniaxial and Brazilian testing), and some stress component (i.e. difference between the maximum horizontal and vertical stress). It can be argued that the assumption of the strength being linearly correlated with the deviatoric stress in the vertical plane is quite simplistic. In fact, depending on the relation between the magnitude of the principal stresses and the orientation of the core, different patterns and level of damage would be predicted as it will be shown in Sec. 2. However, there are some limitations: a) in the knowledge about the relation between the stresses during drilling and the micro-cracking of the samples; b) in the way the in-situ stresses are measured.

The relations between drilling stresses and sample cracking shown in Sec. 2, despite being rigorously determined and convincing, suffer of the major limitation that all relations are obtained by means of numerical models that do not explicitly consider fracture initiation and propagation. Thus, no quantitative relations can be established between the magnitude of the stress components and the density and exact location of cracking.

Hydraulic fracturing method, on the other hand, seems to provide plausible results about the minimum stress perpendicular to the borehole axis (if inclined fractures are involved). Furthermore, the method for determining the maximum stress perpendicular to the borehole axis often returns values that are doubles of the minimum stress on the same plane. Hydraulic fracturing usually cannot determine the stress component parallel to the borehole axis (unless testing fractures perpendicular to it). Thus, this component (e.g. the vertical stress fro sub-vertical boreholes) is often simply determined as the weight of the overburden. The stress measurement results available for the Shobasama and MIU Construction Site all suffer of such limitations. Moreover, the minimum horizontal stress is often very similar to the vertical stress estimated from the weight of the overburden. For this reasons, the difference between the maximum horizontal stress (proportional to the minimum horizontal stress) and the weight of the overburden was assumed to be a good indicator of the level of (differential) stress in the a vertical plane containing the borehole axis.

An attempt to quantitatively determine the level of disturbance or damage of the samples is presented in PAPER4, where contour maps provide the level of damage in terms of reduced strength of the laboratory samples as a function of the axial and radial stress component of the hypothetical axis-symmetrical in-situ stresses. Since these results and the empirical relation between strength and stresses observed in PAPER1 and PAPER2 point in the same direction, they seem to independently confirm each other.

After removing the variation attributed to the damage effects due to drilling, the average and standard deviation of the uniaxial compressive strength and of the Brazilian tensile strength becomes more stable and differences between the boreholes also diminish. The remnant standard deviation of the population of laboratory test results must be interpreted to account for all effects other than in-situ stresses. In general, even assuming a homogeneous rock mass, local differences might occur due to sampling (when the size of the mineral grains is large with respect to the sample size), presence of alteration, sealed cracks, porosity and hidden flaws typical of natural materials. Such variability should also be taken into account when modelling the behaviour of the rock samples.

1.3 Variability of the modelling results

The successful validation of the numerical models against the laboratory results shown in PAPER6 seems to derive from the ability of describing the possible variability of the tensile strength of the continuum body representing the rock. This is implemented in FRACOD^{2D} by randomly generating the values of the tensile strength in each grid point of the model according to a parabolic probability distribution (see PAPER3). This parabolic distribution applies between a minimum and maximum limit values. Although successful, the technique applied in FRACOD^{2D} has two major limitations:

- There is not experimental support to a parabolic probability distribution of the tensile strength in natural rocks. Usually, parameters like the tensile strength are statistically treated in rock mechanics as Gaussian distributions;

- FRACOD[2D] generates one realisation among the possible tensile stress distributions across the models. However, in the present version[9], there is no function that allows to generate several realisations of property distributions for the same model geometry (i.e. one has to change the coordinate reference system to be able to obtain a new realisation). This precludes statistical analyses of the results that are the base of, for example, the Monte-Carlo method.

The previous comments can be generalised to all mechanical input parameters in the model such as: Young's modulus, Poisson's ratio, fracture toughness in Mode I and II, fracture stiffness in normal and shear loading conditions, etc.

Mechanical parameters as fracture normal and shear stiffness and fracture toughness are very sensitive to the level of stress at which they are observed or calculated (Figure 3). If a mechanical parameter can change one order of magnitude within the range of stresses involved in the same model calculation, an approach that considers constant model parameters as a function of stress is not satisfactory.
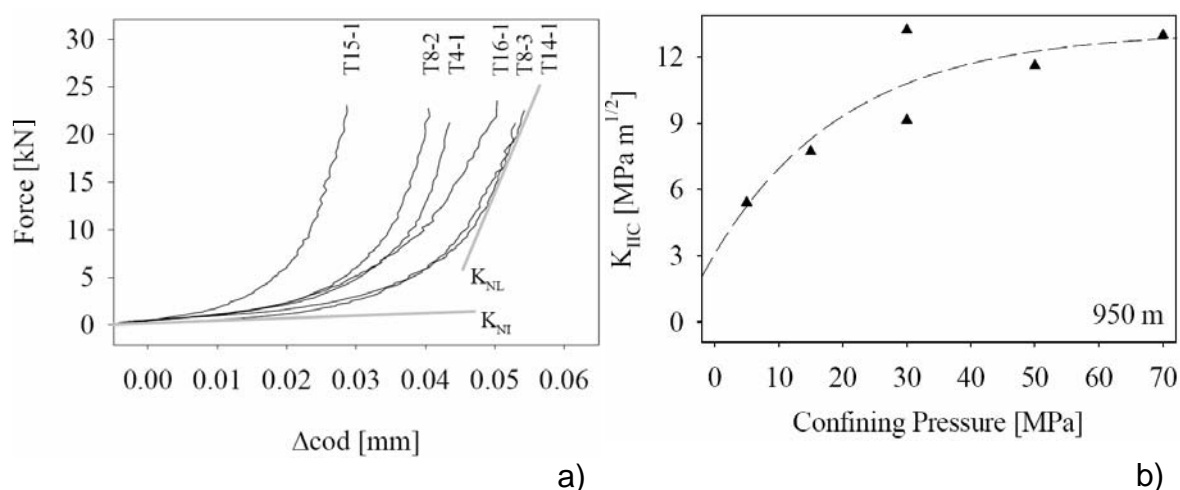

a) b)

Figure 3. Laboratory testing of samples of Toki granite from borehole MIU-2 at Shobasama. a) Normal deformability of a rock fracture sample: total applied force versus normal displacement during loading. K_{NI} (about 20 GPa/m) and K_{NL} (about 1300 GPa/m for a normal load between 10 and 25 kN) are the fracture initial and tangential normal stiffness, respectively. b) Fracture toughness in Mode II determined from Punch Trough Shear Test versus the confinement pressure. (After Backers[10] .)

2 Prediction performance

The performance of a technique or numerical modelling method resides in their capability of making correct predictions of phenomena outside the scope of data on which they were based on and developed from. In this section, the ability of predicting newly acquired data as presented in PAPER1 to PAPER7 is overviewed.

2.1 *Predicting laboratory Brazilian tensile strength*

PAPER1 and PAPER2 have shown that the variation of the uniaxial compressive strength and the Brazilian tensile strength of samples of Toki granite taken from the Lower Sparsely Fractured Domain (LSFD) at the Shobasama and MIU Construction Site follow rather smooth polynomial curves when plotted against depth (or distance

along the borehole from the top of the casing). These polynomial curves (Table 1) help to predict the average material properties that would be obtained from laboratory tests if additional core were available from non-investigated borehole sections. Such polynomial curves disregard the causes of the smooth polynomial variation and just describe that fact that they approximate well the data from all analysed boreholes at Shobasama and MIU Construction Site.

A polynomial curve approximating the Brazilian tensile strength of the core samples from borehole MIZ-1 was proposed in PAPER1. In PAPER6, additional Brazilian tensile tests were carried out on additional samples taken from untested section of core. Two sections of core were chosen based on the prediction of the polynomial curve so that low tensile strength (sample batch 1 from 522-523 m) and high tensile strength (sample batch 2 from 765-766 m) were expected. The new laboratory tests confirmed the good quality of the prediction as shown in Figure 4, despite the tests were conducted on core samples of different diameter.

Table 1. Parameters of the polynomial fits for all analysed boreholes.

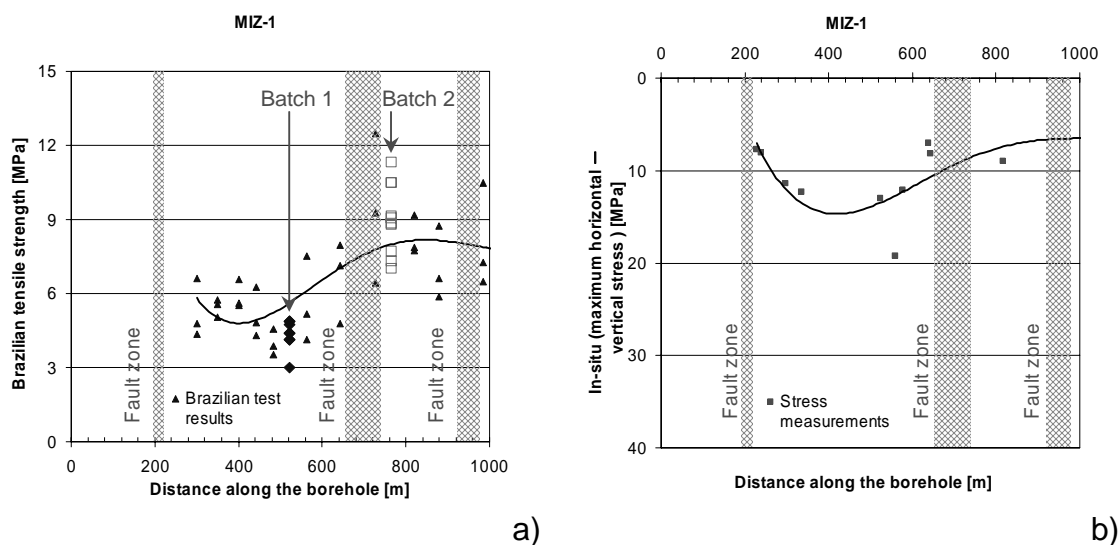| Parameters	Polynomial fit	R^2
	Borehole MIU-1	
UCS	$= -1.6999440E-09z^4 + 9.2961815E-07z^3 + 1.4893201E-03z^2 - 1.1555813E+00z + 3.6443752E+02$	$R^2 = 0.487721$
TS	$= -2.0550584E-07z^3 + 3.4746042E-04z^2 - 1.8441387E-01z + 3.7081836E+01$	$R^2 = 0.335640$
$(\sigma_H-\sigma_v)$	Estimated as shown in Figure 6	
$(\sigma_H-\sigma_v)$	Estimated as shown in Figure 6	
UCS-$(\sigma_H-\sigma_v)$	UCS=$-6.5789(\sigma_H-\sigma_v)$+ 236.8421 (Estimate)	
TS-$(\sigma_H-\sigma_v)$	TS=$-0.3333(\sigma_H-\sigma_v)$+9.6667 (Estimated)	
	Borehole MIU-2	
UCS	$= -1.2688777E-13z^6 + 5.2389233E-10z^5 - 8.3464798E-07z^4 + 6.5613812E-04z^3 - 2.6650283E-01z^2 + 5.2374924E+01z - 3.6605331E+03$	$R^2 = 0.942399$
TS	$= -1.144966E-15z^6 + 6.878646E-12z^5 - 1.375624E-08z^4 + 1.270321E-05z^3 - 5.834785E-03z^2 + 1.264915E+00z - 9.299387E+01$	$R^2 = 0.635730$
$(\sigma_H-\sigma_v)$	$= -3.025661E-14z^6 + 7.300426E-11z^5 - 6.533158E-08z^4 + 2.622280E-05z^3 - 4.437380E-03z^2 + 2.265470E-01z + 1.012338E+01$	$R^2 = 0.627180$
UCS-$(\sigma_H-\sigma_v)$	UCS = $-9.554436(\sigma_H-\sigma_v)$ + 311.711240	$R^2 = 0.961987$
TS-$(\sigma_H-\sigma_v)$	TS = $-0.299990(\sigma_H-\sigma_v)$ + 11.414458	$R^2 = 0.906645$
Borehole	**Borehole MIU-3**	
UCS	$= -1.5085255E-06z^3 + 2.6527516E-03z^2 - 1.3520307E+00z + 3.1522804E+02$	$R^2 = 0.249336$
TS	$= -1.475098E-12z^5 + 5.131964E-09z^4 - 6.772028E-06z^3 + 4.165898E-03z^2 - 1.172969E+00z + 1.269468E+02$	$R^2 = 0.984721$
$(\sigma_H-\sigma_v)$	$= 4.734386E-07z^3 - 8.124102E-04z^2 + 3.863263E-01z - 3.319024E+01$	$R^2 = 0.877673$
UCS-$(\sigma_H-\sigma_v)$	UCS = $-2.382401(\sigma_H-\sigma_v)$ + 152.804562	$R^2 = 0.972099$
TS-$(\sigma_H-\sigma_v)$	TS = $-1.137809(\sigma_H-\sigma_v)$ + 30.794067	$R^2 = 0.954468$
	Borehole MIU-4	
UCS	$= 1.5207517E-06z^3 - 4.4481160E-04z^2 - 3.7625639E-01z + 2.1056485E+02$	$R^2 = 0.550984$
TS	$= -9.9722107E-08z^3 + 2.3516012E-04z^2 - 1.3124280E-01z + 2.5966714E+01$	$R^2 = 0.77156$
$(\sigma_H-\sigma_v)$	Estimated as shown in Figure 6	
$(\sigma_H-\sigma_v)$	Estimated as shown in Figure 6	
UCS-$(\sigma_H-\sigma_v)$	UCS=$-2.5641(\sigma_H-\sigma_v)$+125.6410 (Estimated)	
TS-$(\sigma_H-\sigma_v)$	TS=$-3.3333(\sigma_H-\sigma_v)$+100.0000 (Estimated)	
	Borehole MIZ-1	
UCS	$= 7.9415951E-10z^4 - 3.4077624E-06z^3 + 3.9593426E-03z^2 - 1.5990411E+00z + 3.5562575E+02$	$R^2 = 0.536235$
TS	$= 1.3474548E-10z^4 - 3.5354604E-07z^3 + 3.1835013E-04z^2 - 1.0887364E-01z + 1.7268457E+01$	$R^2 = 0.450473$
$(\sigma_H-\sigma_v)$	$= -2.0531910E-10z^4 + 5.7417552E-07z^3 - 5.5607278E-04z^2 + 2.0360579E-01z - 1.0200313E+01$	$R^2 = 0.516626$
UCS-$(\sigma_H-\sigma_v)$	UCS = $-7.716560(\sigma_H-\sigma_v)$ + 258.604231	$R^2 = 0.998763$
TS-$(\sigma_H-\sigma_v)$	TS = $-0.429173(\sigma_H-\sigma_v)$ + 11.373621	$R^2 = 0.973232$
	Borehole AN-1	
UCS	$= 1.6966649E-08z^4 - 4.2956908E-05z^3 + 3.8797857E-02z^2 - 1.4783158E+01z + 2.2285659E+03$	$R^2 = 0.565646$
TS	$= -8.9729646E-15z^6 + 3.1674587E-11z^5 - 4.4794648E-08z^4 + 3.2336488E-05z^3 - 1.2502361E-02z^2 + 2.4408782E+00z - 1.7803499E+02$	$R^2 = 0.230229$
$(\sigma_H-\sigma_v)$	$= -3.162874E-09z^4 + 8.098701E-06z^3 - 7.442231E-03z^2 + 2.896339E+00z - 3.845851E+02$	$R^2 = 0.579332$
UCS-$(\sigma_H-\sigma_v)$	USC = $-6.485916(\sigma_H-\sigma_v)$ + 329.599122	$R^2 = 0.863455$
TS-$(\sigma_H-\sigma_v)$	TS = $-0.081262(\sigma_H-\sigma_v)$ + 10.721281	$R^2 = 0.625782$

a)

b)

Figure 4. Prediction of the results of Brazilian tensile tests on core samples from borehole MIZ-1 at the MIU Construction Site (PAPER6): a) variation of the Brazilian tensile strength along the borehole; b) variation of the difference between the maximum horizontal stress and the vertical stress along the borehole.

2.2 Predicting in-situ stresses

In PAPER1 and PAPER2, polynomial approximation of the uniaxial compressive strength and Brazilian tensile strength were calculated. Analogous polynomial fitting curve were also calculated for the difference between the maximum horizontal stress and the vertical stress along the boreholes (Figure 4). It was observed that, without exceptions, the two sets of polynomial curves were very similar in shape so that a correlation between the strength of the core samples and the in-situ stresses could be established.

When plotting the values of strength against the values of stresses for the same distance along the boreholes, the correlations in Figure 5 could be obtained. These correlation lines are a powerful tool because they allow predicting the strength when knowing the in-situ stresses and vice-versa. Predicting the level of in-situ stresses when knowing the strength of the core samples obtained in laboratory is a novel achievement. This was tested on the data from two boreholes were stress measurements were not available. An equivalent correlation line was chosen based on each of the plots in Figure 5. From each correlation line, the values of the difference between the maximum horizontal stress and the vertical stress could be estimated independently from the data of uniaxial compressive strength and Brazilian tensile strength. The two estimations of stress could be optimized by slightly adjusting the parameters of the correlation lines. Assuming that the vertical stress is given by the weight of the overburden (2620 kg/m^3), the maximum horizontal stress along borehole MIU-1 and MIU-4 could be obtained as also presented in PAPER5 (Figure 6).
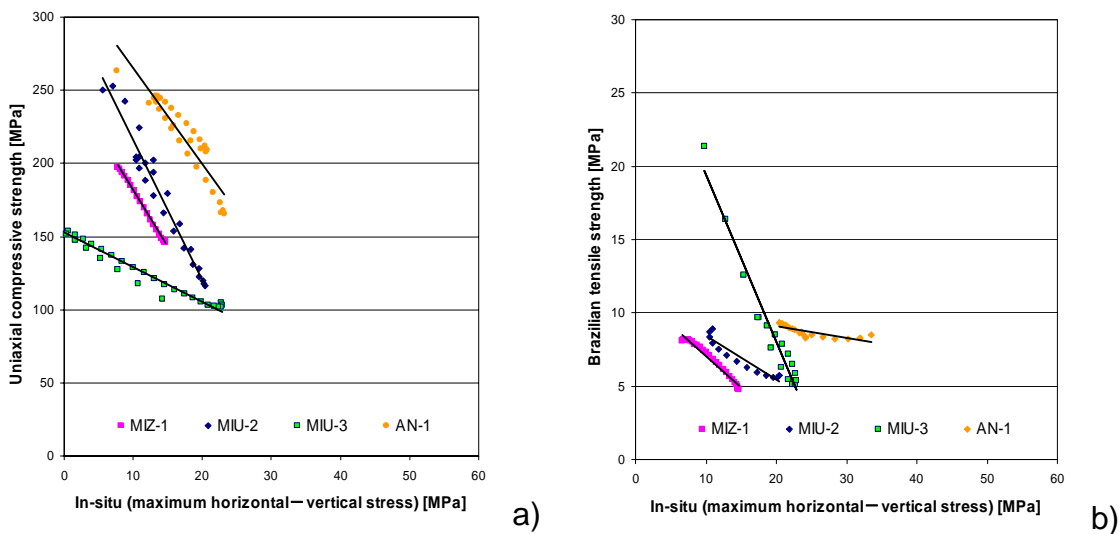
Figure 5. a) Correlation between uniaxial compressive strength and in-situ stresses (PAPER1); b) correlation between the Brazilian tensile strength and in-situ stresses (PAPER2; no correlation could be observed for the data from borehole AN-1).
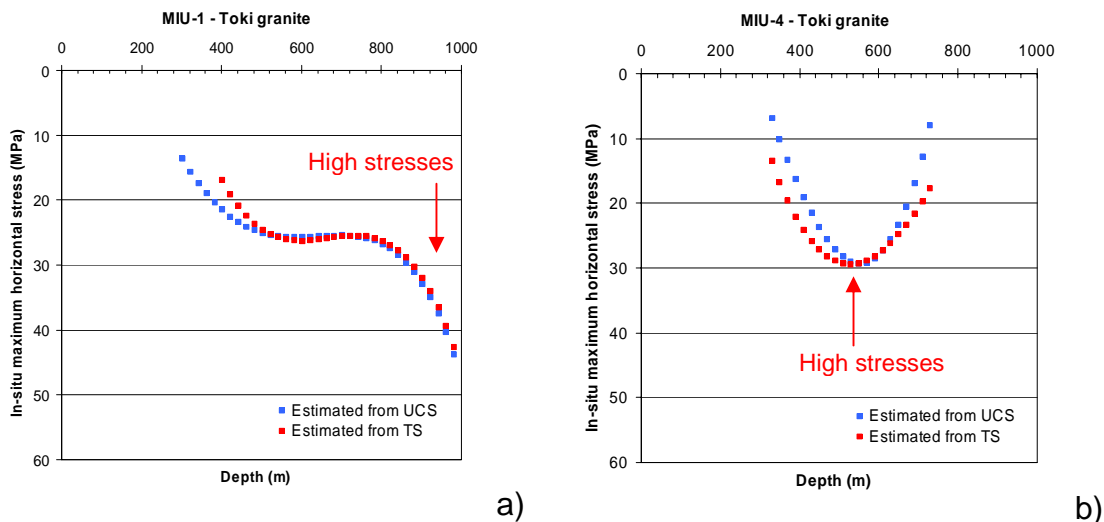

Figure 6. Prediction of the maximum horizontal stress for two boreholes where in-situ stress measurements were not available. Borehole MIU-1 (a; PAPER5) and MIU-4 (b) at the Shobasama site are shown.

Figure 7. Prediction of the maximum horizontal stress for two boreholes where in-situ stress measurements were not available. Borehole MIU-1 (a; PAPER5) and MIU-4 (b) at the Shobasama site are shown.

Stresses are particularly high below about 900 m in borehole MIU-1 and around 480 m in borehole MIU-4. At these depths, the estimated maximum horizontal stress maybe larger than 30 MPa, while the overburden pressure should be around 12 and 24 MPa, according to the depth. Such stresses are likely to cause damage of the core. In fact, the survey of the core shows that core discing, an unequivocal sign of core damage, was found at the depth of 902 m in borehole MIU-1 and 489 m in MIU-4, respectively (Figure 7).

2.3 Predicting in-situ rock strength

The correlations between the strength of the core samples from uniaxial compressive and Brazilian tests and the estimated in-situ stresses (i.e. strictly, twice the deviatoric stress) in Figure 5 indicate that almost systematically strength is lower when stress is higher (PAPER1 and PAPER2). This is not likely to occur in-situ in the same extent. In this study we have attributed the cause of this strength reduction to sample damage during drilling. Thus, by knowing the strength of the samples for low levels of stress we can estimate the "undisturbed" or in-situ strength of the rock. The laboratory strength values for samples taken from higher in-situ stress conditions can then be corrected of an amount proportional to the in-situ stress. To make the correction, a

minimum level of stress not causing sample damage has to be hypothesized, usually around the lower stresses shown in Figure 5.

When the correction is applied to the laboratory results, most of the wavy variations with depth disappear leading to rather constant in-situ uniaxial compressive and Brazilian strength of the Toki granite as shown in Figure 8. Compared to the laboratory results, the estimated in-situ uniaxial compressive strength for the analysed boreholes could be 13 to 31% higher while the Brazilian strength could be 0 to 24% higher, respectively.

a)

c)

b)

d)
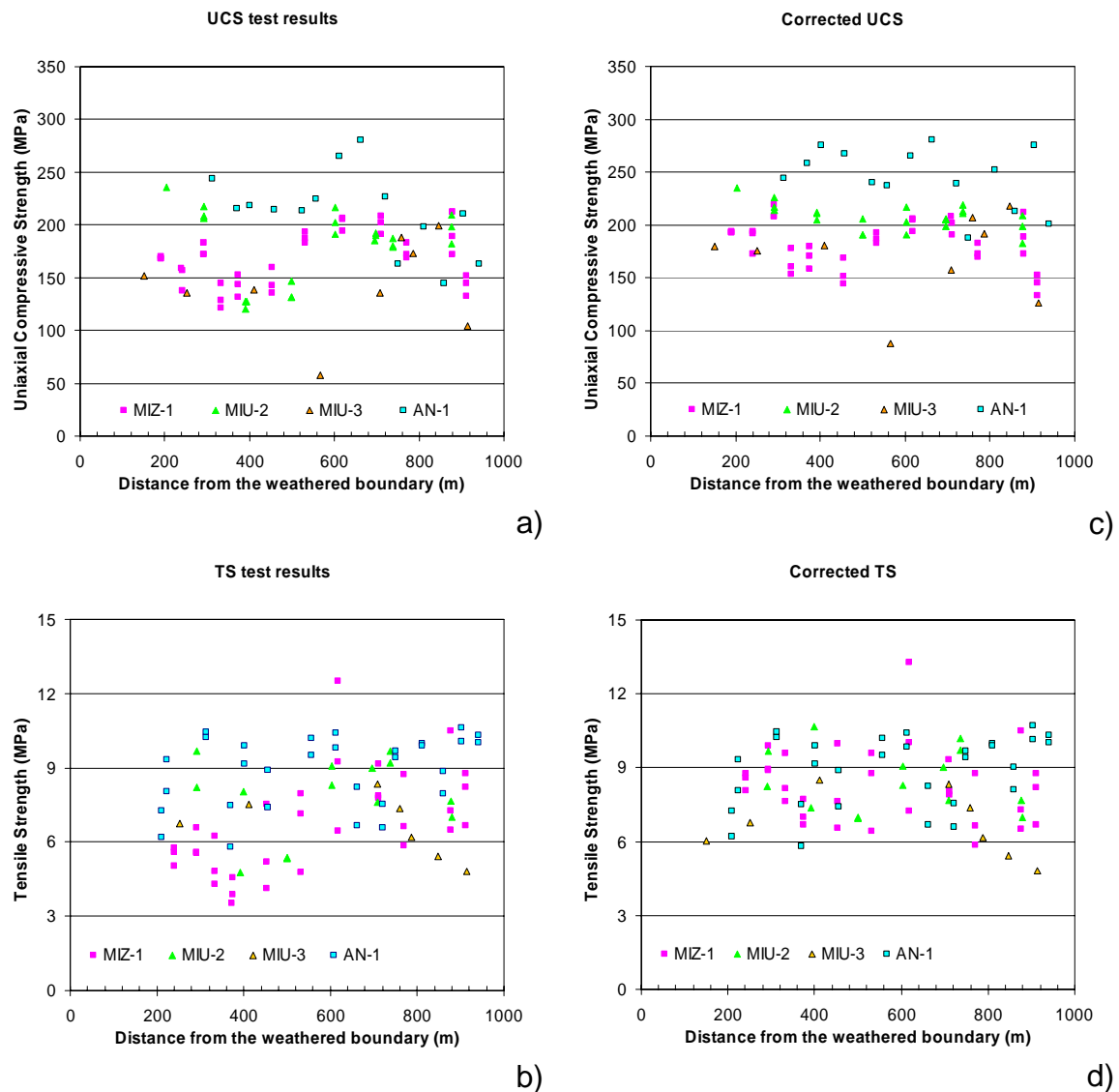
Figure 8. Variation of the laboratory uniaxial compressive strength (UCS) and Brazilian tensile strength (TS) with depth for four boreholes at the Shobasama and MIU Construction Site (a and b); variation of the corrected uniaxial and Brazilian strength with depth for the same boreholes (c and d). The corrected strength is believed to better represent the in-situ strength of the Toki granite.

2.4 *Predicting Brazilian tensile strength by modelling*

Scooping analyses were carried out by means of FRACOD^{2D} to obtain a suitable set of modelling material parameters for the Toki granite to be used to study core sample damage (PAPER3). For

this purpose, Brazilian tests were simulated to reproduce the values of tensile strength available for samples from borehole MIZ-1. This study concluded that FRACOD^{2D} models without any pre-existent cracks would slightly overestimate the Brazilian strength of the samples measured in laboratory between 35 and 100%. This conclusion was extrapolated by affirming that probably, due to the complex stress distribution inside the sample just after the development of the first tensile cracks, there was only a weak correlation between the "direct" tensile strength of the rock material (i.e. in uniaxial conditions) and its Brazilian tensile strength. This is because, inside the loaded samples, tensile stresses occur together with compressive stresses changing the onset of failure. Furthermore, the development of tensile cracks in the samples would introduce high stress concentrations at the tips of the cracks and stress gradients that exceed the "direct" tensile strength of the material but are still under its failure limit. In fact, the "direct" tensile strength of the model was assigned to vary between 5.4 and 6 MPa, but failure of the model occurred for an average tensile stress of about 11 MPa (Figure 9 a).

Another conclusion of the scooping calculations in PAPER3 was that the onset of tensile cracking beyond which the models become discontinuous could be observed by a clear bend in the graph of the total load versus the lateral expansion of the sample perpendicularly to loading. The stress at which this bend occurred in the models coincided with the lower limit of possible variation of the "direct" tensile strength. This result inspired a new test campaign where core samples from borehole MIZ-1 (batch 1 and 2 in Figure 4) were tested in laboratory under Brazilian conditions and presented in PAPER6. During these testes, the lateral expansion of the samples was measured by means of non-contact optical extensometers.

In agreement with the numerical predictions, also the real core samples showed the described sudden bend of the graph of the total load versus the lateral expansion. Interestingly, all the real samples showed this feature for a total load between 20 and 40 kN, corresponding to an average tensile stress in the samples of about 2.6 MPa (Figure 9 b). This stress value was interpreted as the "direct" tensile strength of weakest grains in the rock material and was input in some of the FRACOD^{2D} analyses in this report (PAPER6 and PAPER7). The fact that the Brazilian tensile strength overestimate the "direct" tensile strength was also recently confirmed by a study on granite to granodiorite from Forsmark, Sweden [11]. That study show that the ratio between the direct tensile strength of that rock type is only 58% of the indirect tensile strength from Brazilian testing.

PAPER6 shows that although the "direct" tensile strength of the model was given a value between 2.6 and 6 MPa, still the model would overestimate the laboratory results. Considering the samples from borehole MIZ-1 at 522-523 m were drilled under in-situ stress conditions non dissimilar from those shown for borehole MIU-4 at 489 m, the hypothesis that the samples are affected by some degree of disturbance and damage is reasonable. Based on this, different pre-existing cracks patterns were introduced in the FRACOD^{2D} to simulate an equivalent sample damage for the samples from batch 1 (cracks with length of 10 or 12 mm) and batch 2 (cracks with length 6 mm).
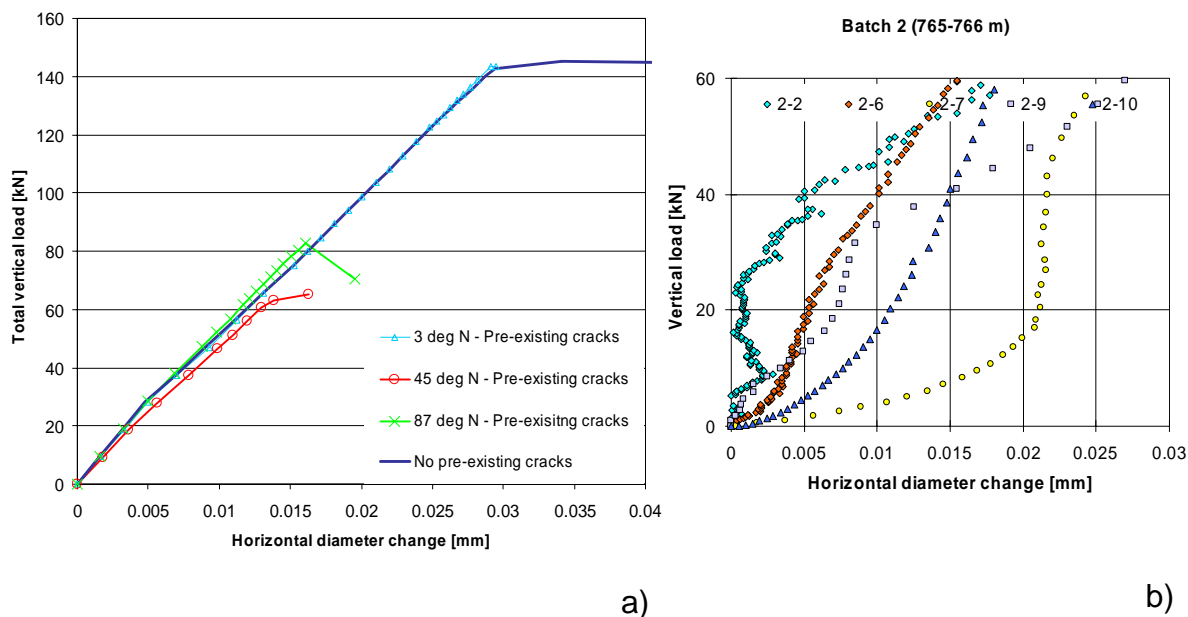
a)

b)

Figure 9. Numerical and experimental results of Brazilian testing (PAPER6): a) behaviour of FRACOD[2D] models where the bend of the graph of the tensile stress versus the lateral expansion perpendicularly to the loading direction and the peak strength of the model can be seen for a force of 35 kN; b) experimental Brazilian test results for the samples taken between 765 and 766 m along borehole MIZ-1 at the MIU Construction Site. Please notice that the peak load is not shown in the graphs. The bend can also been recognized between 20 and 45 kN.

Some of the crack patterns shown in Figure 17 provided results very similar to the laboratory tests by showing the bend of the diameter change and by giving very similar peak tensile strength. Some more comments about these crack patterns are given in Sec 3.3 and the concept of "weakest crack" length is also introduced in Sec. 5.3.

The analyses in PAPER3 and PAPER6 provide a good example of validation of the FRACOD[2D] models against experimental results. Moreover, the achieved understanding of the mechanism of failure allows improving the determination of the fracture toughness in Brazilian testing as presented by Proveti & Michot [12].

2.5 Predicting sample damage

PAPER1 and PAPER2 have shown that the negative correlation between the laboratory strength of the samples and the in-situ stresses is likely to exist. Based on such correlation, it was possible to correct the laboratory strength results to make an estimation of the in-situ uniaxial compressive and Brazilian strength as in Sec. 2.3. The variations of the laboratory strength with respect to the estimated in-situ average strength, which was consistently higher, were interpreted a sign of damage. Based on the magnitude of such variations, six levels of damage could be determined.

Thanks to the polynomial interpolations of the in-situ stress measurement data, the stresses at the location of each sampling point could be determined. Thus, the levels of damage could be plotted on a map of the in-situ stresses as presented in Figure 10 a. It can be observed that the points with higher level of damage preferentially plot towards higher in-situ stress components.

In PAPER4, FRACOD[2D] models were set up to simulate drilling in the rock subjected to a series of boundary stress fields to recreate the conditions in Figure 10 a. Examples of the plane strain models analysed are shown in Figure 16, where the crack pattern induced by drilling is predicted around the borehole and in the core stub. The numerical models were also qualitatively assigned a

level of damage based on the estimated influence of the crack patterns on the strength of hypothetical samples taken from the core. Cracks occurring at an angle with the core axis were considered to affect the Brazilian strength, while cracks almost perpendicular to the borehole axis to affect the uniaxial compressive strength. Based on the boundary stress field and the level of damage, damage maps could be constructed as in Figure 10 b. This figure shows a certain agreement with the correspondent damage map obtained from the laboratory data. As expected, larger magnitude of the stresses correspond to higher levels of damage. Furthermore, both maps show that even stresses of the order of 20 to 30 MPa could already cause damage of the cores. In particular, the two maps agree in predicting the same enhanced damage for values of the horizontal and differential stress of 20 MPa and 10 MPa, as shown by the red squares in the centre of the maps.

The fact that the agreement between the two maps is only qualitative can be explained as follows: i) in-situ stresses may greatly vary from point to point, even if the large scale behavior can be described by rather smooth polynomial functions as in Figure 4b; ii) the in-situ stresses are not necessarily symmetrical with respect to the borehole axis and their difference in magnitude and rotations affect the core crack patterns; iii) mineral composition and grain size can also greatly influence the level of damage experienced by the cores.

Based on the results of PAPER4, it can be inferred that anisotropy of the in-situ stress field might cause different crack patterns in different directions with respect to the core axis. This certainly explains the anisotropy of the P-wave velocity across the core samples presented in PAPER6. Furthermore, the stress distributions obtained by FRACOD[2D] are quite dissimilar to those reported in the literature (e.g. ref. 6),13),14)) since the former are largely affected by the initiation of the cracks ahead of the drilling bit or inside the core stub. The BEM-DDM analyses also show that besides tensile failure also shear failure may occur inside the cores due to drilling. In this study, fluid pressure and thermal effects on the core damage were not considered although they are believed to have an important role in core damage and borehole breakouts (e.g. ref. 8); 15)).

a)   b)
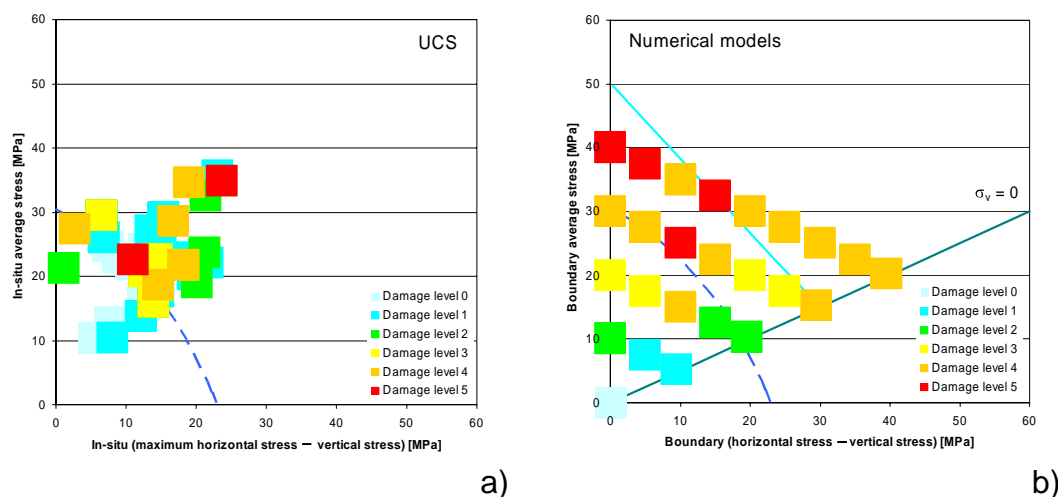
Figure 10. Damage maps as obtained from the laboratory results with polynomial estimation of the stress level at the sampling depth (a); damage maps resulting from FRACOD[2D] models of the process of core drilling under different stress conditions. Pictures from PAPER4.

2.6 Predicting sheeting joints

FRACOD[2D] analyses of large rock blocks (> 500 m) were carried out for the simulation of rebound fractures and stresses due to the removal of the overburden (PAPER7) analyses were made possible by the newly introduced gravity function in the numerical code that allows considering the gravity field and linear stress gradients at the boundaries (Shen et al., 2007). The

analyses considered a variety of factors affecting the results such as: boundary conditions, symmetry, surface topography, initial ratio between the horizontal and vertical in-situ stresses, Poisson's ratio, presence of pre-existing faults.

The numerical models were able to recreate fracture patterns in the upper 100-200 m of brittle rocks that can be compared with the more intensive sub-horizontal fracturing observed on the field in the Upper Highly Fractured Domain (UHFD) at the Shobasama and MIU Construction Site. The models could actually predict the depth of the transition between the UHFD and the LSFD. This result seemed to be possible thanks to the account for the gravity forces that by counterbalancing the rebound deformations and stresses due to vertical unloading cause the sheeting joints to cease with depth. In this extend, the method seems to be more successful than others (e.g. ref. 16),17)) in capturing the removal of the overburden as the main mechanism of formation of the sheeting joints.

The presence of sheeting joints also controls the stress distribution in the bedrock at shallow depth. The removal of the overburden induces greatly varying vertical stresses when approaching the surface. Large tensile stresses may frequently occur leading to failure of the rock and formation of gently dipping sheeting joints. The presence of sheeting joints also affects the distribution of the horizontal stress that tends to increase when approaching the surface. These model results ate confirmed by a multitude of filed observations and stress measurements close to the surface in hard rocks.

The models also show that the effect of the boundary conditions and the presence of pre-existent faults govern the extension of the jointing. Pre-existent faults behave as limit of the sheeting joints that often cannot trespass them leading to different patterns and depth of the joints on the two sides of the faults. Vertical faults do not markedly affect the distribution of the stresses while gently dipping faults reduce the horizontal stresses and might even induce an abrupt inversion of the gradient of the vertical stresses above their trace.

The high vertical tensile stresses in relation to an enhancement of the horizontal stresses causing sheeting joints close to the bedrock surface can also cause other damage of the intact rock in the form of cracks and microcracks. Due to the resolution of the models presented in PAPER7, this small size cracking could not be recreated numerically. However, the values of the uniaxial compressive strength and Brazilian tensile strength of the samples taken from the UHFD show a very consistent linear increase with depth from the surface to the interface with the LSFD where they finally reach values as high as for the deeper rock (Figure 11). This phenomenon should not be interpreted as core damage during drilling but should be explained with the high stresses occurring before and during the formation of the sheeting joints. After fracturing has occurred, the stresses tend to reduce to levels compatible with the strength of the rock. It was also inferred that small variation of the water pressure after the formation of the sheeting joints could also contribute to their propagation and evolution, although no analyses were carried out on this topic.

Stress relaxation and creep phenomena (e.g. ref. 18),19)) would have the effect of reducing the stresses acting on the rock by ensuring the stability of the sheeting joint pattern if the overburden or the water pressure are not drastically changed[20].
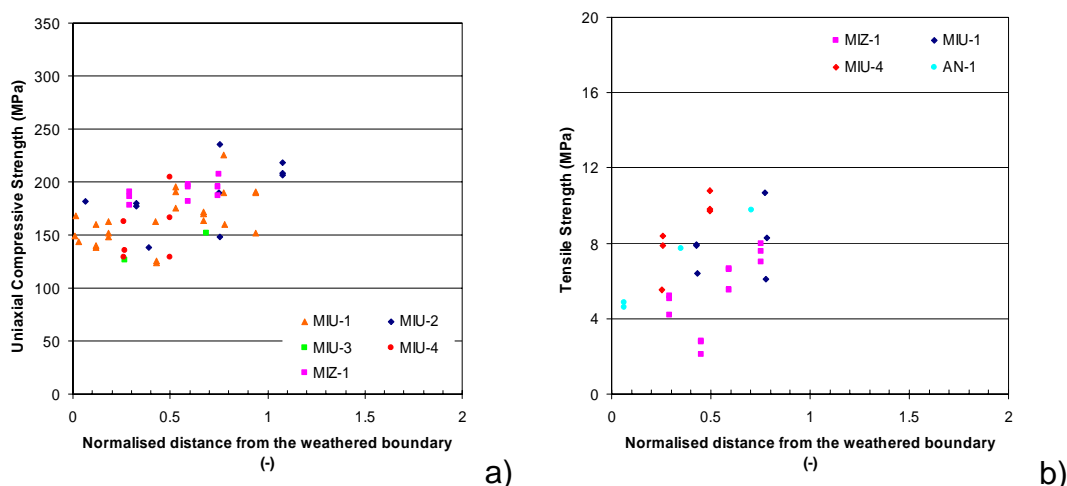
Figure 11. Variation of the uniaxial compressive strength (a) and Brazilian tensile strength (b) within the Upper Highly Fractured Domain at the Shobasama and MIU Construction Site. The distance from the superficial weathered surface is normalised so that is zero at the top and one at the bottom of UHFD.

3   Crack patterns in the core samples

Crack patterns can be directly or indirectly determined. This section presents examples from this study and from the literature that enhance the understanding of the damage processes.

3.1   Crack patterns and P-wave velocity

There seems to be a disagreement between the general opinion of the adepts of the Differential Strain Curve analysis (DSCA) and some published numerical results concerning the orientation of the micro-cracks opened or initiated by the stress release of the core during drilling. The Differential Strain Curve analysis affirms that the core released from the in-situ stresses relaxes just as the stresses would be simply set to zero (e.g. ref. 21), 22) ,23)). In this way, pre-existing cracks perpendicular to the direction of the maximum principal stress would preferentially be opened or initiated. For this reason, the P-wave velocity measured across a core would be minimum in the direction of the maximum stress[24]. This assumption, however, completely disregards the complicated stress-path the core undergoes during drilling in a real in-situ stress field.

Although using tri-dimensional finite element analyses which cannot take into account the presence and initiation of micro-cracks, some authors (e.g. ref. 25), 26)) have demonstrated that, depending on the orientation of the in-situ principal stresses with respect to the core axis, tensile stresses are generated in the core that can induce cracking at different angles with respect to the direction of the maximum principal stress. In the models, a large resultant of the tensile stresses is observed approximately parallel to the direction of the minimum principal stress. Such resultant of the tensile stresses is largest when the minimum principal stress is parallel to the core axis. Since they models always predict opened or induced cracks at a large angle with the direction of the maximum principal stress, these results only apparently contradict the assumption of the DSCA method.

Figure 13 shows a summary of the modelling result obtained by Sakaguchi et al. [26] for a simplified configuration where the principal stresses are parallel and perpendicular to the core axis. The analyses showed that rotation of the principal directions with respect to the core axis would marginally affect the orientation of the resultant of the tensile stresses inside the core which always tends to align itself with the core axis or perpendicularly to it. Assuming that initiated or opened cracks are perpendicular to the direction of the resultant of the tensile stresses in the core,

it results that the cracks are, with only slight deviations, parallel to the plane containing the maximum and intermediate principal stress.

A consequence of this fact is that the P-wave velocity across the core should in general be minimum in the direction of the minimum principal stress, which means perpendicularly to the core axis (Figure 13 a and b) or parallel to it (Figure 13 c).

However, if the directions of the principal stresses are not restricted to the core axis and to the plane perpendicular to it, small rotation of the cracks (at maximum about 30°) with respect to the core axes are expected. These rotations might change the relation between the orientation of the minimum P-wave velocity transversally to the core axis and the maximum horizontal stress (assuming a vertical borehole). In fact, results of in-situ stresses obtained by hydro-fracturing method and measurements of the P-wave velocity determined from cores from the same boreholes (Figure 12) show that the angle between the minimum P-wave velocity across the core and the maximum horizontal stress tend to be either a small angle (0 to 30°) or a large angle (60 to 90°). Stress configurations similar to Figure 13 a and b would result into large angles. On the other hand, according to the numerical models, a slight rotation of the principal stresses in Figure 13 c causes the cracks to dip approximately in the same direction as for the maximum horizontal stress. This could actually cause the minimum P-wave velocity across the core in that direction to approximately align itself with the maximum horizontal stress as it was observed by Kato[24] in borehole MIU-3 at the Shobasama Site. This is, however, a special stress case where the minimum principal stress is nearly vertical that is quite frequent at depth where the minimum horizontal stress overthrown the magnitude of the overburden vertical stress.

For the samples from borehole MIZ-1, this hypothesis is confirmed by the fact that the estimated vertical stress seems to be the minimum stress component, and the angle between the maximum horizontal stress and the direction of the minimum P-wave velocity is about 20 to 40°. Moreover, the P-wave velocity in the axial direction is rather close to the minimum P-wave velocity across the core, as the cracks in Figure 13 c would also suggest.
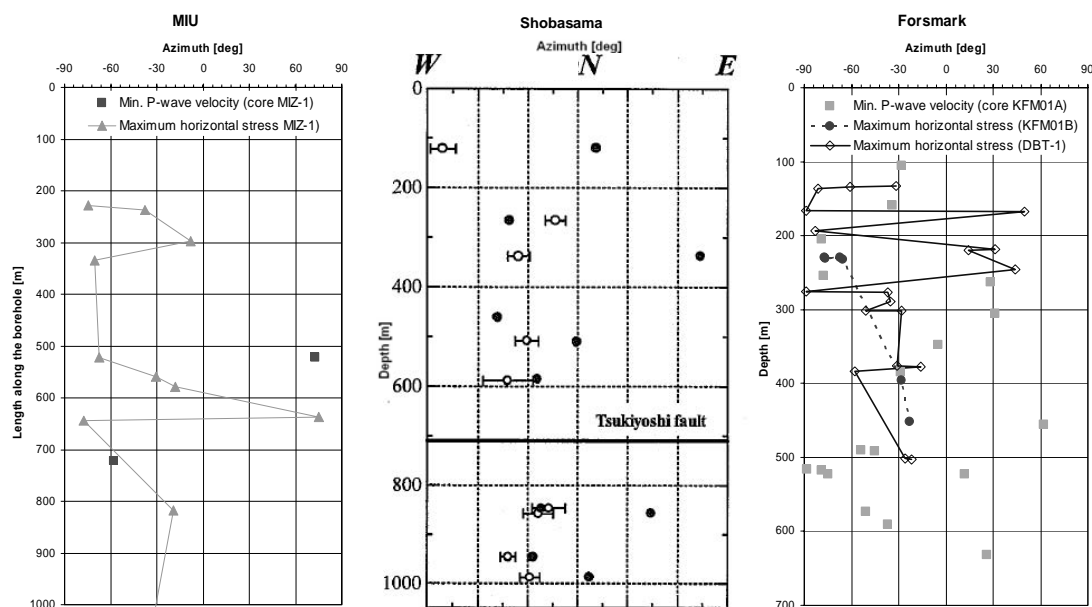

Figure 12. Plot of the orientation of the in-situ maximum horizontal stress versus the orientation of the minimum P-wave velocity: for the samples from borehole MIZ-1 at the MIU Construction Site (left); for the samples from borehole MIU-3 at Shobasama[24] (centre) and; for comparison, the same kind of data are shown for adjacent boreholes KFM01A, KFM01B and DBT-1 at Forsmark, Sweden (right).
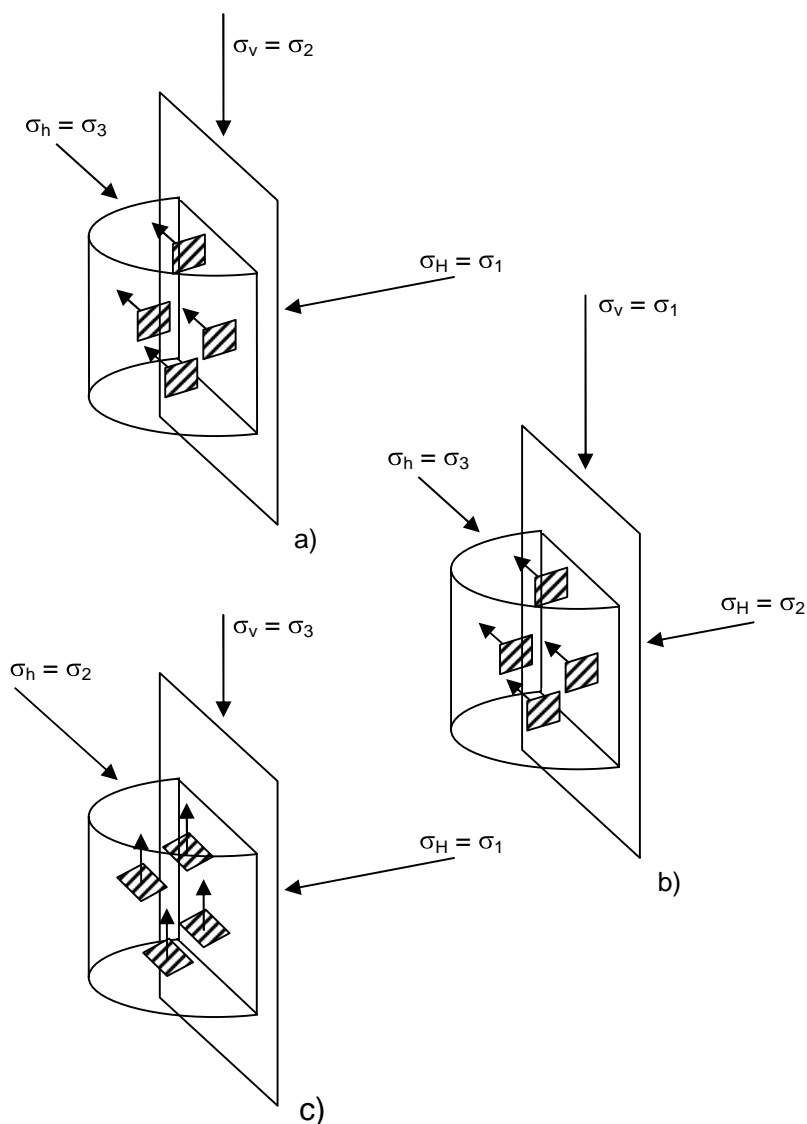
Figure 13. Sketches summarizing the 3D FEM models by Sakaguchi et al. [26] : the magnitude of the principal stresses is changed keeping constant the direction of the maximum horizontal stress.

3.2 Crack patterns in samples for uniaxial compressive testing

In relation to the research work by Bäckström et al. [27] and Bäckström & Hudson [28], core samples of diorite from the TASQ Tunnel, Äspö Hard Rock Laboratory, Sweden, were tested in uniaxial conditions. Some samples were not tested but impregnated with fluorescent epoxy resin and cut along the axis for the sake of comparison with the samples mechanically tested. The non-tested core samples present very clearly defined micro-cracks of millimetric length which traces on the longitudinal saw-cut section almost form a right angle with the core axis. The core sample in Figure 14 was taken from the horizontal borehole KF0066A01 at 454 m, 28 m from the tunnel wall. The bearing angle of the borehole is 15.7°. At the depth the samples were taken, the in-situ stresses were evaluated by back-calculation of the convergence measurements performed in the TASQ Tunnel (Table 2) [29]. I was found that the minimum principal stress is horizontal and has a trend of 220°. These data show that the borehole axis is nearly parallel to the direction of the minimum principal stress. Thus, the orientation of the cracks can be predicted by the mechanism in Figure 13 c where the borehole axis is turned to horizontal. The slight deviation between the

orientation of the borehole and the trend of the minor principal stress justifies the fact that the cracks are not perfectly perpendicular to the core axis. Sketches of the plausible crack pattern are presented in Figure 15 where: a) the cracks are predicted as in Figure 13 c; b) two perpendicular saw-cut sections parallel to the core axis are shown and; c) the crack traces on the section perpendicular to the axis are presented.

Rinne et al.[20] conducted extensive simulations of uniaxial and triaxial compression tests by means of FRACOD[2D]. They also numerically investigated long term strength and time related aspects related to brittle rocks (i.e. Äspö diorite, Sweden). In these simulations, the length of the initiated cracks in the models that gave the best match with the experimental results was also found to be around 10 mm (see Sec. 5.2).

The influence of different stress-paths was investigated by Lavrov et al.[30] by pre-loading samples in Brazilian testing and reloading in uniaxial compression. They found that the stress-path affects, not only the onset of the Kaiser effect in the Acoustic Emissions, but also the crack patterns that become more rugged for the samples that previously experienced tensile stresses with magnitude between 44% and 88% the uniaxial compressive strength.

Table 2. In-situ stresses obtained by back-calculation of convergence measurements at the TASQ Tunnel, Äspö Hard Rock Laboratory, Sweden[29] .

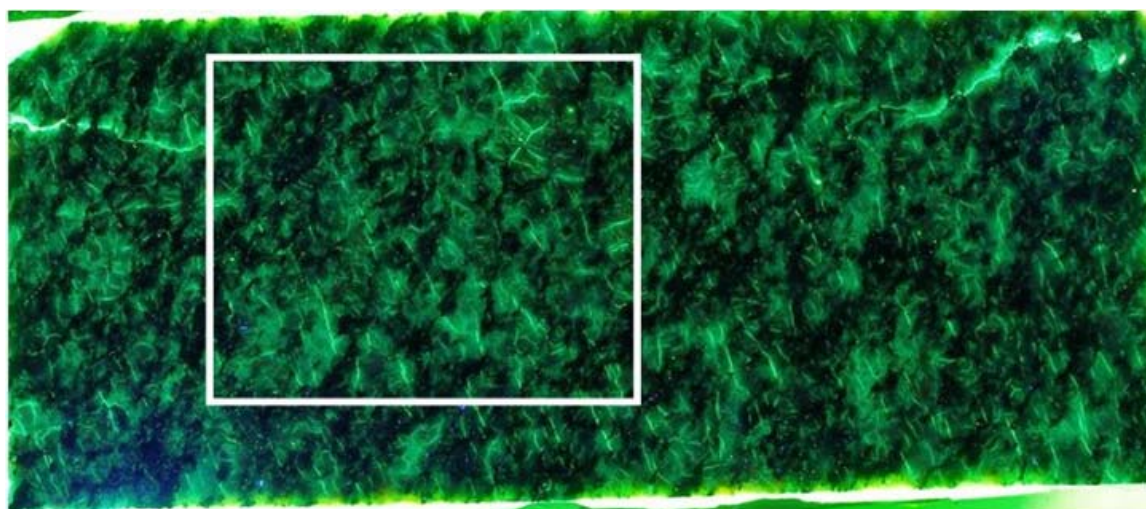| Principal Stresses	Magnitude [MPa]	Trend [deg]	Plunge [deg]
σ_1	30	310	0
σ_2	15	-	90
σ_3	10	220	0

Figure 14. Axial saw-cut section o a diorite core from the TASQ Tunnel, Äspö Hard Rock Laboratory, Sweden (borehole KF0066A01)[28] . Before cutting, the sample was impregnated with fluorescent epoxy resin. In the picture, the axis of the core is horizontal, the diameter is 51 mm and the window marked in white has size 33×44 mm, respectively.
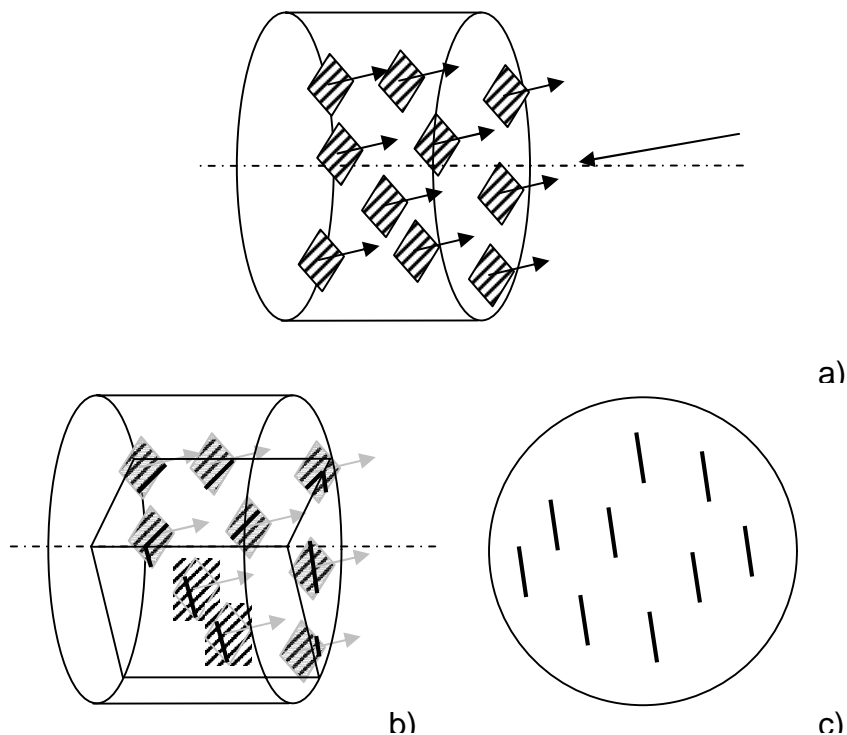
Figure 15. Conceptual model for explaining verisimilar crack patterns inside core samples for a stress configuration similar to Figure 13 c: a) minor principal stress slightly inclined to the core axis and related cracks; b) crack traces on the core sections parallel to the core axis and; c) crack traces on the transversal section of the core.

Ganne et al.[7] also studied pre-loaded samples of limestone in compression and tension by means of thin-slices and Acoustic Emission. They show that already at levels of compressive stress of about 30% of the strength, intra-granular cracks start to grow while no inter-granular crack can be observed. Subsequently, the cracks start to interact (50% of the strength) to finally coalesce when the AE experience a sharp increase in slope. A similar behavior was observed in tension, where, however, the start of the AE and of the growth of intra-granular cracks is delayed to about 60% of the tensile strength. These observations, which apply also to Sec. 3.3, show that fracture propagation in rock can occur for stress levels far from failure.

3.3   Crack patterns in samples for Brazilian testing

Figure 15 shows a possible explanation of the crack pattern observed on the core samples from the TASQ Tunnel at Äspö HRL. The same figure also provide a plausible explanation for the crack patterns used for numerical modelling of the Brazilian tests on Toki granite presented in PAPER6.

In PAPER4, two-dimensional simulations of the drilling process were performed by FRACOD[2D] that implements linear elastic fracture propagation in a continuum medium (Figure 16). The numerical models agree with the results from Sakaguchi et al.[26] when the difference between the magnitudes of the principal stresses is large (a). This model predicts cracks perpendicular to the direction of the minimum principal stress. When the difference between the magnitudes of the principal stresses decreases (b and c), however, it seems that the initiated cracks occur peripherally, leaving the centre of the core more intact. Furthermore, cracks sub-parallel to the core axis also appear as the principal stresses become similar in magnitude. The numerical models, in plane strain and symmetrical with respect to the trace of the core axis, could not consider any inclination of the principal stresses.

Based the results presented by Li & Schmitt [25], Sakaguchi et al. [26] and in PAPER4, the pre-existent crack patterns in the FRACOD^{2D} models designed for simulating Brazilian testing on Toki granite in PAPER6 can be justified (Figure 17).

Analyses of the thin-sections transversal to the core axis of samples taken at 522.4 and 765.3 m along borehole MIZ-1 the MIU Construction Site (Figure 19; see also PAPER8) were conducted. The microphotographs show that a sample taken from a section of borehole with relatively high stresses shows more extensive microcracking than for a sample taken form a section with lower stresses. In the former, the microcracks are probably open while, in the latter, they appear to be filled by sericite (fine-grained potassium mica).
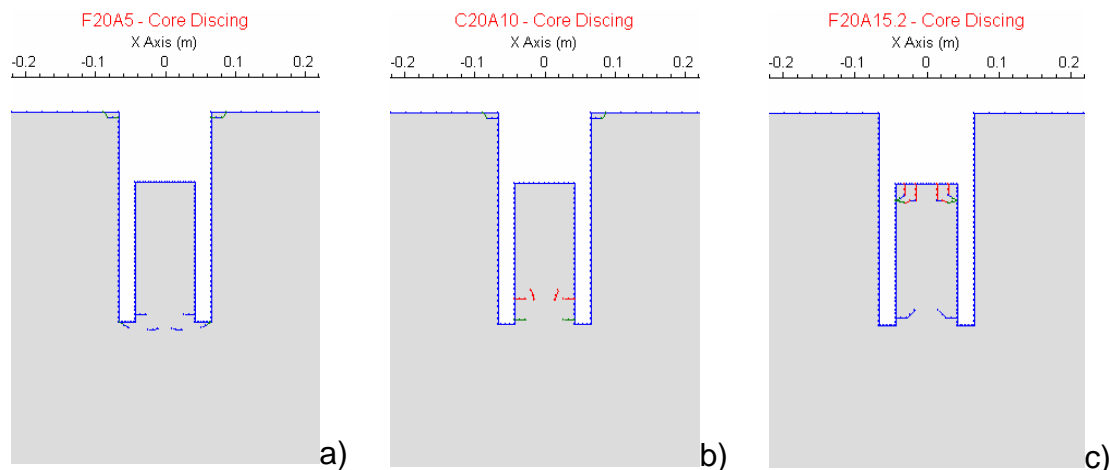
Figure 16. Numerical modelling of the core drilling process by FRACOD^{2D} for: a) vertical stress of 5 MPa and horizontal stress of 20 MPa; b) vertical stress of 10 MPa and horizontal stress of 20 MPa and; c) vertical stress of 15 MPa and horizontal stress of 20 MPa.
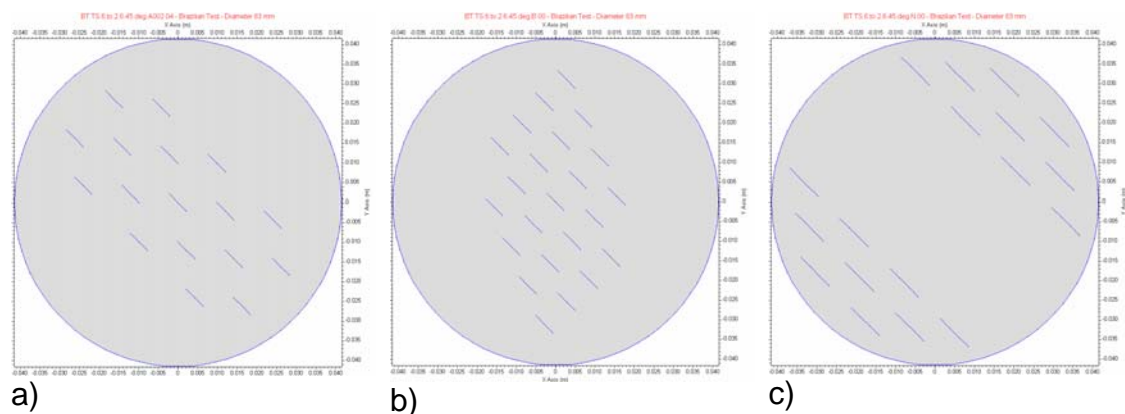

Figure 17. Crack patterns modelled with FRACOD^{2D} to simulate Brazilian testing on samples of Toki granite presented in PAPER6.
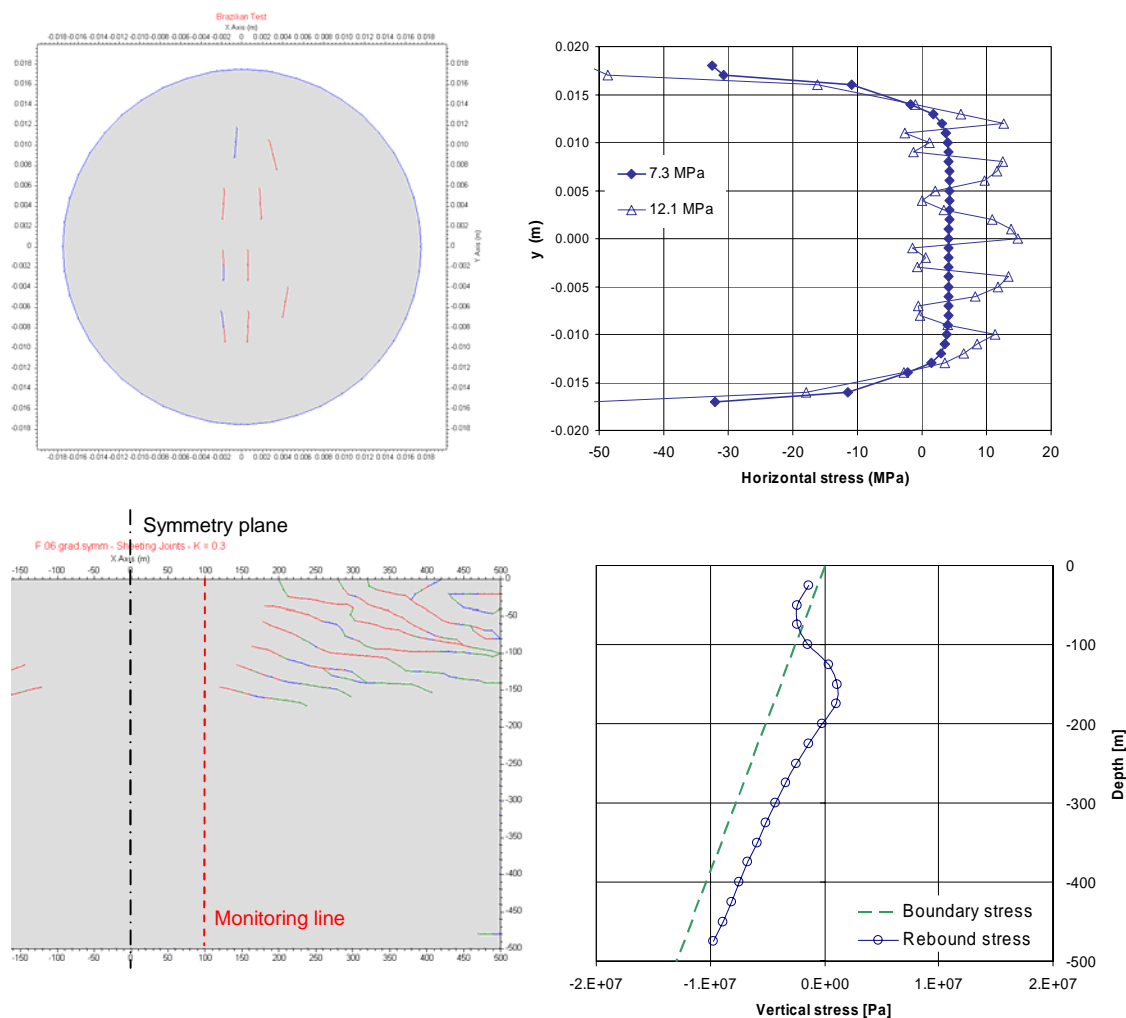
Figure 18. Influence of the crack initiation and propagation on the stress distributions of the models of Brazilian testing (PAPER3, model K2, size = 3 mm) and sheeting joint formation (PAPER7, symmetrical model, K = 0.3). On the left, crack patterns in the models; on the right, stresses in the models before and after crack initiation.
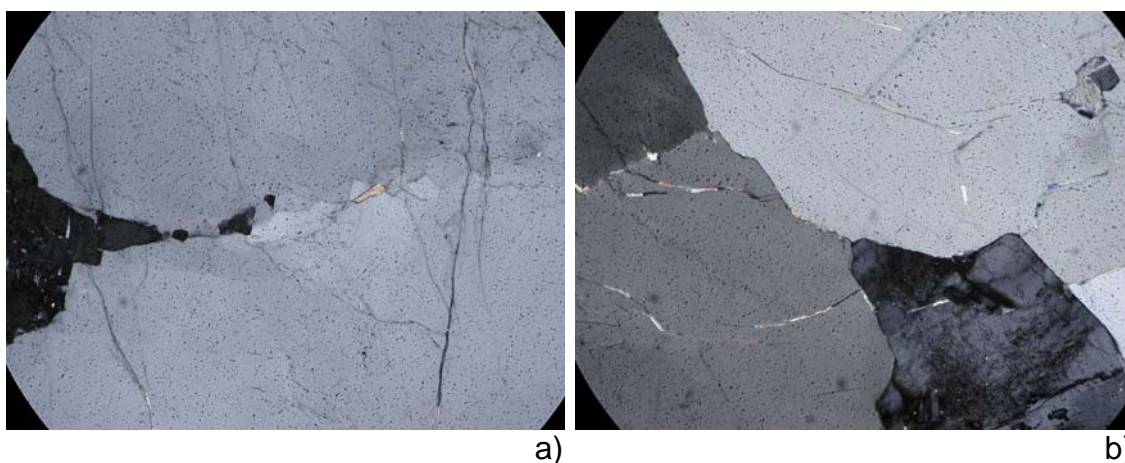

a)   b)

Figure 19. Examples of microphotographs taken on the thin-sections of samples from borehole MIZ-1 (PAPER8): a) sample 1-4 from a section with relatively high in-situ stresses; b) sample 2-4 from a section with relatively low in-situ stresses. The width of the portion of sample represented in the pictures is 1.75 mm.

4 Crack patterns and stress distribution

The numerical simulation of Brazilian tests (PAPER3 and PAPER6) and the simulation of the occurrence of sheeting joints (PAPER6) show that the stress distributions inside the models before and after the crack initiation and propagation are deeply different (Figure 18). The formation of the cracks greatly affects the stresses around the crack tips and also induces stress concentrations in the locations where several interact during their propagation. This imply that making predictions of strength by assuming continuous models might be far from reality as proposed in PAPER3 for the Brazilian test strength (indirect tensile strength). Even analyses that only consider cracks terminating against each other might be far from reality because they completely ignore the stress concentration at the tip of the fractures. This is also true for models that, although explicitly including cracks, cannot consider the stress redistributions occurring due to crack initiation and propagation.

5 Linear elastic fracture mechanics and scale effects

The simplest configuration considered in linear elastic fracture mechanics is the case of a "penny-shaped" crack of length c in an infinite body loaded with a uniform tensile stress perpendicular to the crack. In plane stress, when the far-field stress σ_A reaches a certain critical value σ_g (i.e. the Griffith's tensile strength) the crack will start to propagate. This value is given as:

$$\sigma_g = \sqrt{\frac{2E\gamma}{\pi c}} = \frac{K_{IC}}{\sqrt{\pi c}} \qquad (1)$$

where E is the Young's modulus of the material, γ the specific surface energy of the crack and K_{IC} is the toughness of the crack in Mode I propagation. For a crack characterized by a fracture toughness of 2 MPa m$^{1/2}$, the relation between the critical far-field stress and the length of the crack is shown in Figure 20. Thus, the tensile strength of the body depends on the initial length of the crack. This is because the energy stored in the system is proportional to the volume of the solid affected by the crack whereas the energy absorbed by the system due to the crack propagation depends on the area of the crack [31]. It can be concluded that linear fracture mechanics implicitly considers scale effects as Eq. (1) can also be generalized into:

$$\sigma_g = \frac{Const}{\sqrt{c}} \qquad (2)$$

where Const is a proportionality constant depending on the material properties of the continuum body and of the crack, and on the geometry of the problem.
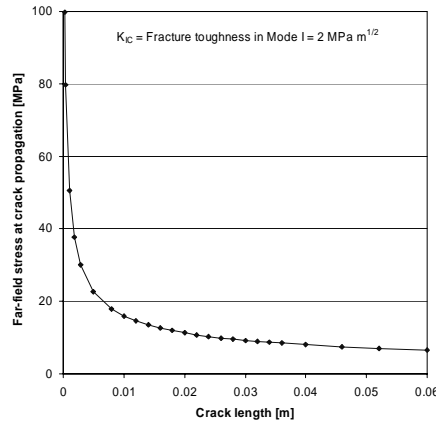

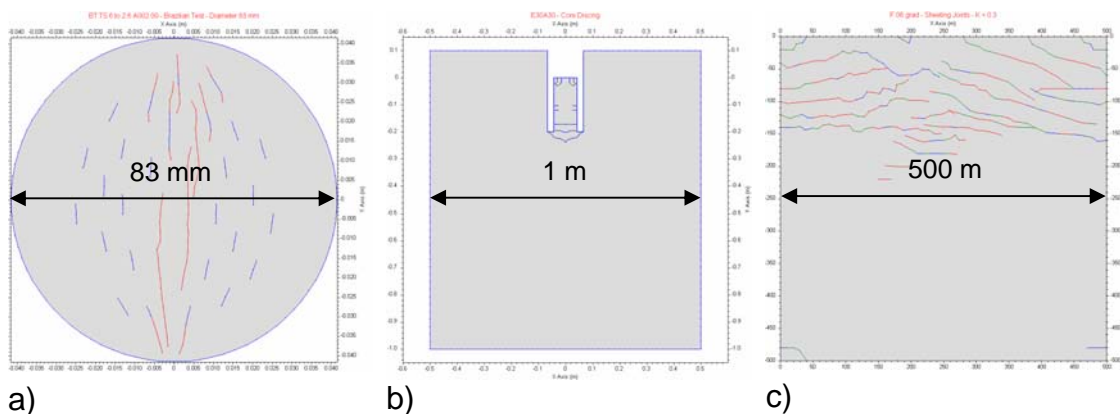**Figure 20. Relation between the far-field stress and the length of the crack as in Eq. (1).**

a)   b)   c)

Figure 21. Examples of different scales analysed in this report by means of FRACOD²ᴰ: a) core size (PAPER3 and 6); b) borehole size (PAPER4) and; c) whole-site size (PAPER7).

As consequence, choosing the size of the volume of interest (e.g. grain size, sample size, tunnel size and whole-site size; Figure 21) implies to limit the length of the maximum crack that can be considered and thus set an upper boundary for the strength. On the other hand, assigning the length of the propagating crack element set the boundary for the level of detail that can be analysed (i.e. resolution of the model). In fracture mechanics applications, for example by means of FRACOD²ᴰ, the resulting strength of the model will depend on its size even if all the input parameters characterizing the continuum material and the crack are exactly the same.

5.1 Meso- and macro-scale

To demonstrate the dependency of the strength upon the size of the critical crack in a FRACOD²ᴰ model, analyses in plane strain conditions were carried out with perfectly similar model geometry. The models represent a block of square cross section with a crack in the centre (Figure 22, left). The length of the crack in the models is always one tens of the section edge (e.g. 10 mm for the model of edge 10 cm, 50 m for the model of edge 500 m). Also the length of the elementary propagating crack is always one twenty fifth of the section edge. The model is subjected to a uniform tensile stress on the edges parallel to the crack. The same set of parameters used in PAPER6 is used. The only exception is the fracture toughness K_{IIC} in Mode II that here is assumed to be 6 MPa m$^{1/2}$ (i.e. for confinement stresses around 5 MPa; cfg. Backers [9]) instead of 11.6 MPa m$^{1/2}$ since small confinement stresses are expected in the models.

Figure 22 (b) shows a curve very similar to Figure 20 although the former applies for a body of limited dimension in plane strain conditions whether the latter for an infinite body in plane stress conditions. It is interesting to notice that the crack patterns developing in the FRACOD²ᴰ models are very different depending on the size of the models (i.e. length of the pre-existent crack and of the crack propagation elements), although the ratio between the length of the pre-existent central crack and that of the edge of the model is the same for all models. The tensile stress able to cause failure drops from about 2 MPa to about 0.2 MPa when the size of the considered block is changed from 0.1 m to 500 m because the block can contain larger and larger cracks.

This has major implications on the strength of the rock mass when blocks of different sizes are chosen. It also provides an explanation to the scale dependency of strength in fractured rock masses. In PAPER7, it was shown that for a model of 500 m size the removal of the weight of the overburden alone can cause extensive failure of the rock mass.

When Eq. (2) is fitted to the data in Figure 22 (b; blue line) it returns a value of the constant of about 1.35 MPa m$^{1/2}$. However, the fit is excellent for crack sizes of 1 m or larger but provides critical far-field stresses much higher than those calculated by FRACOD²ᴰ for crack sizes smaller than 1 m. This is due to the fact that Eq. (2) applies to a single propagating crack, while the models with pre-existent cracks shorter than 1 m exhibit non-planar crack propagation and multiple crack initiation during failure, thus have different critical stress intensities. The stresses in

the models cannot reach unlimited values because the tensile strength of the continuum body, although it varies from point to point, it is bounded between 3 and 6 MPa, over which newly initiated cracks will appear.
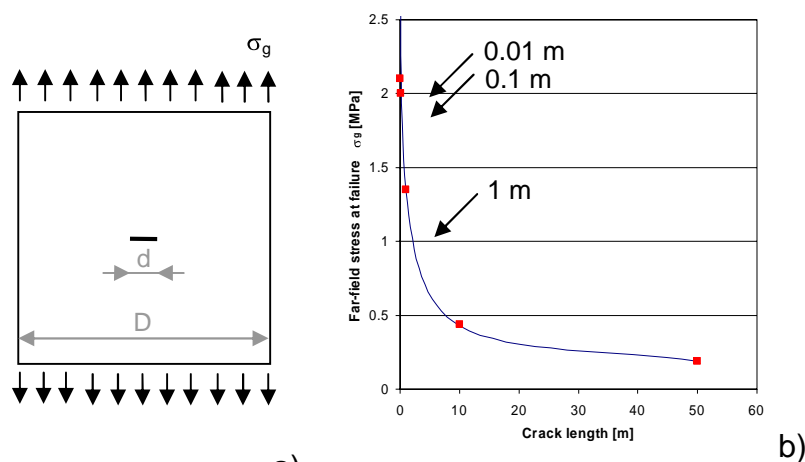
Figure 22. Sketch of the FRACOD^{2D} model geometry with a crack in the centre and its boundary conditions (a); far-field stress at failure versus the crack length (b) for the analyses presented in Figure 23 and Figure 24.

Figure 23 and Figure 24 show that the size of the models also has a major effect on the crack pattern at failure. As the models size increase from centimetric to metric scale, the shape of the propagating crack becomes smoother. Furthermore, for an increasing size of the model, less and less independent new cracks are initiated besides the propagating central crack. For a model size of 10 and 100 m, the pre-existing crack propagates perfectly within its own plane. For the model of 500 m size, the central crack propagates within its plane to a length of about 100 m. However, following further the propagation, it can be seen that the propagating central crack will depart rather linearly from its own plane with an angle of approximately 24°.
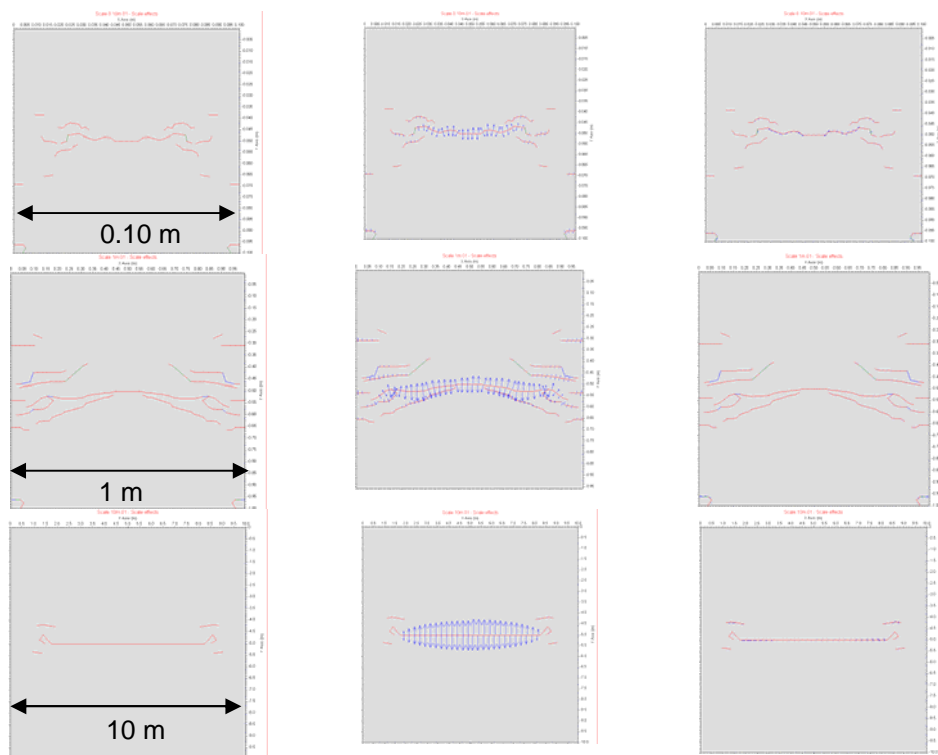
Figure 23. Crack patterns at failure for FRACOD^{2D} models with edge size 0.1, 1 and 10 m. The central crack before propagation was respectively 0.01, 0.1 and 1 m long. On the left, the crack patterns; in the centre, the normal displacements of the cracks; on the right, the shear displacements of the cracks. The scale for the displacements is not the same in all plots, thus they are for qualitative assessments only. Gravity forces are not considered.
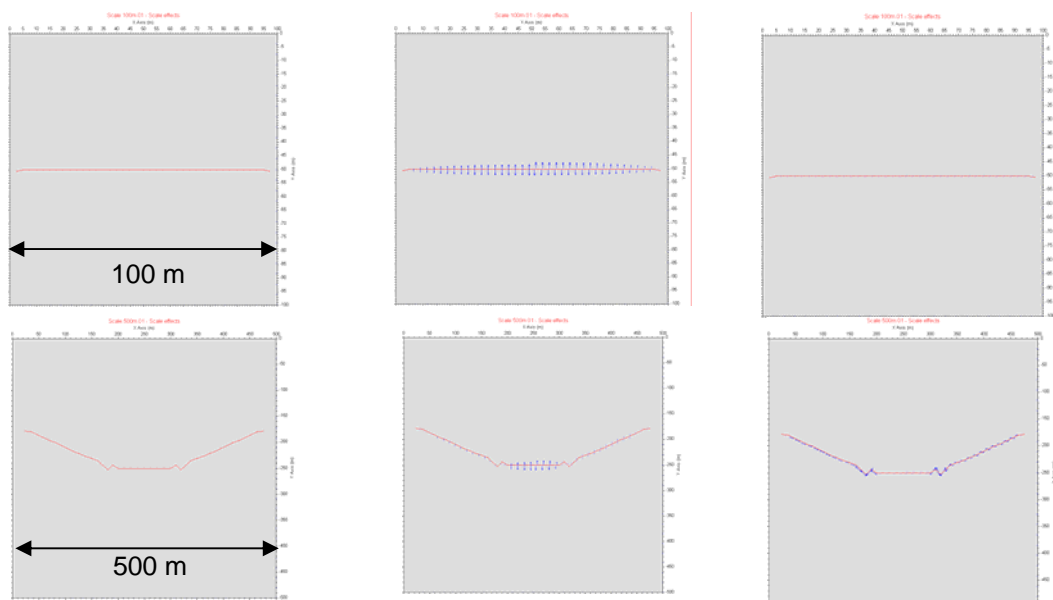

Figure 24. Crack patterns at failure for the FRACOD^{2D} models with edge size 100 and 500 m. The central crack before propagation was respectively 10 and 50 m long. On the left, the crack patterns; in the centre, the normal displacements of the cracks; on the right, the shear displacements of the cracks. The scale for the displacements is not the same in all plots, thus they are for qualitative assessments only. Gravity forces are not considered.

The FRACOD^{2D} modeling results would also focus the attention on two aspects of crack/fracture geometry also observed in nature:

- When looking at the tip of a propagating crack in more detail, what it would look rather smooth and linear from distance might actually contain a large degree of complexity and irregularity at a close-up distance. Looking at a rock fracture in detail, this won't probably appear as a single, thought rough, surface but as a volume of rock in which the propagating crack and a number of secondary cracks are confined. This would lead to the concept of crack/fracture "thickness" or the volume of rock where one or several continuous failure surfaces and their secondary cracks can be contained. The "thickness" of a fracture would depend on the scale of observation until the volume that includes the whole fracture is achieved. This approach would generalize the concept of "thickness" of lineament/deformation/fault zones applied in structural geology [32), 33), 34)];

- The models also inspire a consideration about crack/fracture "roughness": the models shows that if a crack/fracture surface is approximated with its average plane, the distance between the points on the surface and the average plane (i.e. out-of-plane distance or roughness) diminishes as the length of the fracture/fault increases in a "self-affine" fashion (e.g. ref. 35), 36), 37)). Thus, depending on the scale of the observation, the crack/fracture might look rougher or smoother. A rather surprisingly exception to this is the result of the 500 m model, where the propagating crack appears to be, at least locally, much rougher than its counterpart in smaller models. This can be explained with the fact that a very small far-field stress is required for the propagation of such a large fracture. Thus, even very small heterogeneities of the stress field would greatly affect the direction in which the crack is to propagate, resulting in the bend of the crack when the length exceeds 100 m.

These considerations also raise the following question: should the fracture mechanics parameters change with scale or should all scale effects be imputed to the proportionality of the strength to the inverse of the square root of the critical crack length as in Eq. (2)? The fact that the strength decreases of one order of magnitude when the crack length increases by three orders of magnitude alone could explain the variability of rock mass strength with the size of the rock volume considered. This feature, intrinsic to linear elastic fracture mechanics and thus to FRACOD^{2D}, seems to be one a unique feature for a computer code that models rock mass behavior. On the other hand, since the FRACOD^{2D} models meso- and macro-cracks/fractures, the extrapolation cannot be done to very small numerical models (e.g. millimetric scale), where considerations about the grain size, inter-granular and intra-granular cracks, cleavage planes, porosity and other flaws should be explicitly considered (e.g. ref. 7)).

Spatial and scale analyses of the pattern of lineaments, fractures and microcracks were carried out by Koike & Ichikawa[38)] based on satellite images, borehole survey and microscope picture mapping. The analyzed area was centered on the Kamaishi Mine (Eastern Tohoku, North Japan). Although the Authors did not recognize that the presence of the sills in the variogram of the observed lineament/fracture/microcrack density were potentially due to the finite size of the analyzed pictures, they observed that the correlation length evinced by the sills of the variograms varied with scale according to a power law of the median trace length. In other words, the correlation length was increasing for larger analyzed areas. This is typical of fractal patterns that have variograms γ of the lag distance a of the following kind [39), 40)]:

$$\gamma(a) = \gamma_0 \cdot a^{2H} \qquad\qquad (3)$$

where γ_0 is a proportionality constant and H the Hurst exponent of the fractal object with dimension D included in the interval N-1 $\leq$ D $\leq$ N (e.g. for a fractal density, D varies between 0 and 1):

$$D = N - H \qquad\qquad (4)$$

More interestingly, they found that spatial correlation also involved the orientation of the lineaments/fractures/microcracks. By recognizing typical fracture sets, they could assign binary vectors to express to which set each fracture belonged (e.g. *(0,1,0,0)* implies that a fracture belongs to the second set out of four). This technique could be used to evaluate the variograms of the orientation and the correlation distance between all combinations of fracture sets (e.g. six if the sets were four). Using principal values could reduce the amount of independent combinations needed to be analyzed. However, they also found that the correlation distances shown by the variograms were also varying according to a power law of the median trace length, thus showing fractal characteristics. By using the power laws of the density and orientation and by applying a sequential Gaussian simulation, they could generate very realistic fracture patterns at borehole scale that agreed well with those observed at the Kamaishi Mine. This achievement shows that spatial correlation of position and orientation can actually be mathematically described to model fracture clustering and hierarchical structures. Since the dominant direction of the lineament/fracture/ microcrack patterns should be correlated to the regional stress field, this correlation should be the same over different scales (for a reasonably constant regional stress field) (e.g. ref. 41)).

5.2 Micro-scale

Three studies are chosen here to illustrate the process of crack initiation and propagation at a sub-granular and granular scale:

- Short-term uniaxial compressive tests on marble samples (grain size 0.05-0.35 mm; sample size 20×5×2 mm) [42];

- Stress relaxation in tri-axial compressive tests on fine- and coarse-grained granite (grain size 1-4 mm and 3-8 mm, respectively; sample size 40×20×5 mm) [43];

- Stress corrosion in Double Torsion (i.e. tensile) tests on fine-grained granite (grain size about 1 mm; sample size 170×45×2 mm) [44].

Although some of these studies involve time-related aspect and the presence of water, they also show and comment on the distribution of pre-existing cracks that is the key aspect in this section. In all three studies, the area interested by microcracking is rather small.

In the study about the initiation, coalescence and propagation of microcracks in marble [42], pictures of the side of the sample were taken by a Scanning Electron Microscope (SEM). Assuming that the edge is also representative of the inside of the sample, the initial and test induced crack patterns were analysed by means of statistical and fractal tools. It was found that the number N of "boxes" of edge juxtaposed to cover each visible crack on the side of the specimen varied according to a power low of a:

$$N(a) = Fconst \cdot a^{-D} \qquad\qquad (5)$$

where Fconst is a proportionality constant and D is the fractal dimension of the crack distribution detected by the box method. The length of a crack is therefore comparable with the length of the edge of the box that can contain it. The length of a crack is also assumed to have an isotropic spatial distribution since it was investigated by means of square boxes. The power law function in Eq. (5) indicates the self-similarity of the microcrack distribution that was proved to hold until the failure of the specimens in uniaxial compression. It was also observed that the average crack length through the tests was almost perfectly constant (Figure 25b). This would indicate that the growth and coalescence of some microcracks did not inhibit the initiation of new smaller cracks. On the other hand, the total length of the microcracks increased linearly with the applied stress until failure (Figure 26a). This suggested the Author that the microcrack formation occurs at various places simultaneously and the box fractal dimension of the crack distribution would

increase approaching failure (for the marble from 1.5 to 1.75; Figure 25c). It was also observed that the power laws broke for a lower limit of the box size of 0.03 mm that was interpreted either as the scale of loss of self-similarity of the crack population or as the limit of resolution of the analyzed pictures.

What we find remarkable about Eq. (5) is that, for the specific sample size used for the compressive tests, the length of the largest possibly observable crack can be calculated and corresponds to the box size that contains only one crack. Such maximum observable "length" can be calculated from Figure 25a for the sample in from unloaded conditions to failure. For unloaded conditions, the calculated maximum length is 0.32 mm while at failure is 0.63 mm, respectively. In the tests, however, the average length of the cracks was observed to be constant an equal to about 0.05 m (Figure 25b). As we know from fracture mechanics, the critical crack length is not the average length of the cracks but the length of the longest crack, which has the lowest Griffith's tensile strength according to Eq. (1). This is the "weakest link model" introduced by Weibull [45], [46]. In our prediction, the average length is increasing during uniaxial compression because the slope (i.e. fractal dimension) and the intercept of the lines in Figure 25a increase.
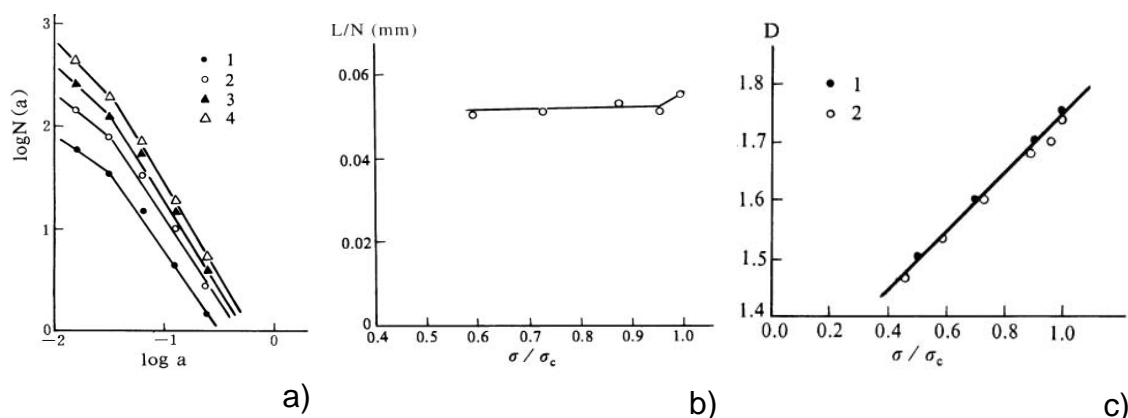

a) b) c)

Figure 25. Analysis of the initiation and propagation of microcracks in uniaxial compression [42]**: a) number of boxes versus box size for sample No. 1 for ratios between the applied σ and the failure stress σ_c of 0, 0.7, 0.91 and 1 (respectively 1, 2, 3 and 4); average crack length for different ratios σ/σ_c and; c) fractal dimension of the crack population for different ratios σ/σ_c for sample No. 1 and 2.**

Liu et al. [43] made observation of subcritical crack growth in tri-axial and saturated conditions by means of stereoscopic microscopy. They also produced a plot similar to that presented by Zhao [42] concerning the initial total microcrack length during a tri-axial stress relaxation test (Figure 26). Both graphs show that the total microcrack length linearly increases with the level of stress. Liu et al. [43] made also some observations about the influence of the grain size of the Inada granite (Ibaraghi Pref., Japan) on the on the crack initiation and propagation in subcritical conditions. They found that coarse-grained granite preferably experienced propagation of the pre-existing cracks while fine-grained granite undergoes initiation of new cracks. We also add that, based on the pictures presented by the Authors, the coarse-grained granite had fewer and longer pre-existent cracks than the fine-grained granite, thus, according to Eq. (1) should preferably experience a propagation of those cracks rather than new initiation. Furthermore, the fine-grained granite had a much larger initial total crack length than for the coarse-grained granite. This can explain why the two granites had the same compressive strength although usually fine-grained granites are more resistant than coarse-grained ones.

This was also suggested by Nara et al. [44] in their study of the influence of cleavage on the subcritical crack growth during stress corrosion. They found that the crack activation energy increases if the pre-existent crack density decreases because propagation usually occurs via connecting pre-existent microcracks. The fewer the pre-existing microcracks, the higher the energy required for the cracks to propagate and the rougher the crack profiles. Also the number of

branching cracks seems to increase. The Authors also interpreted the profiles of the propagating cracks during subcritical growth as rough fractal profiles and could determine the fractal dimension that ranged between 1.05 and 1.57 depending on the orientation of loading with respect to the cleavage planes in the Oshima granite (Ehime Pref., Japan).

Liu et al.[43] and Nara et al.[44] observed that many pre-existent cracks in granite were located in quartz grains. This was explained by the higher thermal expansion coefficient for quartz compared to biotite and feldspar that would enhance the formation of microcracks during cooling of the rock after crystallisation. Quartz grains, however, often act as obstacles during crack propagation to their strength. More pre-existing cracks were also observed in biotite than in feldspar. While cracks in quartz and biotite tend to propagate parallel to the major principal stress, cracks in feldspar seem to need higher stresses that can be reached, for example, at the sharp edges of the biotite grains that thanks to its laminar shape induce stress concentrations. For this reason, crack propagation often change direction crossing feldspar grains following cleavage planes. Thus, the direction of crack initiation and propagation might have an isotropic component, due for example to the presence of pre-existing cracks, flaws, cleavage, voids and intrusions, but also an anisotropic component due to the preferential propagation of pre-existing cracks oriented perpendicularly to the direction of the tensile stress.

Based on this section, it seems that the key features governing the crack initiation and propagation are the maximum length of the pre-existent cracks and their density. The grain size might play a major role in governing the mechanical properties of the cracks.
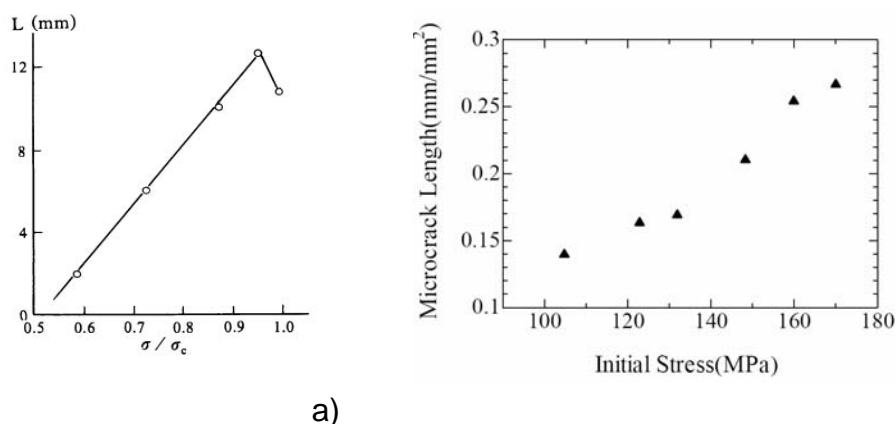

a)   b)

Figure 26. Variation of the measured total length of the microcracks during testing: a) in uniaxial compression (short-term test) [42] **; b) tri-axial compression with confinement 5 MPa (at the start of a stress relaxation test)** [43]**.**

5.3 The concept of weakest crack in a volume

The complexity and heterogeneities of the crack initiation and propagation at the grain size level suggests that this probably cannot be described by linear elastic fracture mechanics, due to the hypothesis of homogeneity and elasticity of the material where the crack is to propagate. At grain and sub-grain scale, the stress field is also very irregular due to concentration at the grain boundaries, microcracks tips and locked-in stresses. In some extent, these aspects can be handled by fine-meshed finite element programs for meso-mechanical crystal plasticity and brittle failure [47, 48] or by discrete element analyses such as bound-particle models [49].

In Sec. 4 it was observed that Eq. (2) does not seem to fit well the results of the FRACOD**2D** models with small pre-existent central cracks (i.e. shorter than 1 m). The same data as in Figure 22 (b) is presented on a double logarithmic plot in Figure 27. This was explained with the non-planar fracture propagation and the stress limit imposed to the tensile strength of the continuum material in the numerical models. Similar material properties would predict a crack propagation stress of

16 MPa for a crack length of 0.01 m (cfg. Figure 20) when planar propagation and unlimited material tensile strength are concerned.

The fact that there is not a univocal crack length corresponding to a certain level of stress but the relation depends on the geometry, damage and loading conditions, suggests that the size of the pre-existent cracks introduced in the models in PAPER6 has to be considered as the "weakest crack" for a volume of rock that quantifies the sample damage. In PAPER6, Brazilian tests performed on core samples of 83 mm diameter were modeled by FRACOD[2D]. To consider sample damage, pre-existing cracks of length 6, 10 and 12 mm were introduced. Some of the fracture length and patterns provided numerical results in such a good agreement with the experimental results that can be considered realistic approximation of the real core samples even if such large cracks were not observed. In the same way, the "weakest crack" length could be defined for the samples presented by Zhao [42].

The concept of length of the "weakest crack" can be formalised in mathematical terms similarly to what was presented by Unosson et al.[50] for non-fractal defects. The presence of pre-existing defects (i.e. cracks) in a material can be quantified by the number of defects N of a certain size a (i.e. box size) occurring in a certain volume V (i.e. sample volume). For a rock material, this number distribution can assume the power law shown in Eq. (5). The total number N_e of defects of size larger than a_e in the volume V can be written as:

$$N_e = \int_{a_e}^{a_{max}} Fconst \cdot a^D \qquad (6)$$

where a_{max} is the size maximum defect observed in the volume V. The probability of finding a defect of size larger than a_e in a volume V_e (i.e. sample size) smaller than V can be written as:

$$P(a_e, V_e) = 1 - \left(1 - \frac{V_e}{V}\right)^{N_e} \qquad (7)$$

when assuming that every defect is occurring independently from the others. Eq. (7) provides the spatial density of defect in a certain volume.
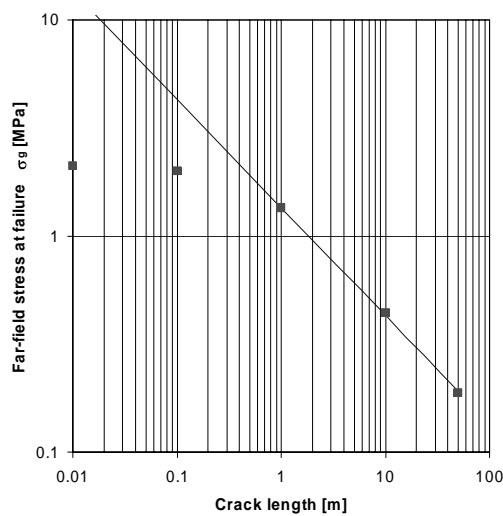

Figure 27. Log-log plot of the relation between the far-field stress at failure and the initial crack length obtained for the FRACOD[2D] models in Figure 23 and Figure 24. The blue line shows the fitting with Eq. (2) for a value of the constant of 1.35 MPa m[1/2].

Equations (5) and (7) provide the statistical base for the stochastic generation of realistic pre-existing crack patterns for numerical modeling. The parameters characterizing the distributions are related to the scale of the model (i.e. the volume of the sample V_e) and to the level of pre-existing damage of the material (i.e. through the fractal dimension D). The provided equations assume a statistically homogeneous crack pattern concerning to orientation and spatial position.

Besides the pre-existing cracks in the models, also the length of the propagating crack element used by FRACOD^{2D} affects the results and the level of tensile stress at which further crack propagation occurs. This is particularly important in models with no pre-existing fractures where the appearance of newly initiated cracks depends on the tensile strength of the continuum body. If the length of such newly initiated cracks is too small, they can probably lead to unrealistic model behaviors due to the fact that the applied stress can be too low to be able to induce their propagation. Intuitively, such models should return higher strength than the experimental analogous.

A way of estimating the optimal length of a propagating element can be to follow the evolution of the maximum crack length as described by Eq. (5) when different level of stress are considered.

The concept of the "weakest crack" also offers a way of estimating the size of the rock volume on which the determination of the "equivalent tensile strength" of the rock to be used to describe the material properties of the medium between the "weakest cracks". In a numerical code as FRACOD^{2D}, such "equivalent tensile strength" would determine the upper boundary of the tensile stress occurring at the grid points of the model where no cracks or crack tips are present. When the "equivalent tensile" strength is reached, an initiated crack element of length equal to the "weakest crack" should be introduced in the model. This explains why the plot Figure 27 does not follows Eq. (2) for arbitrarily smaller modeled crack lengths. This discussion has two implications:

- The tensile strength in the numerical models depends on the size of the maximum pre-existent crack considered. This strength will decrease for larger rock volumes because larger and larger defects are contained in them according to Eq. (5) (Figure 28). Thus, the "equivalent tensile strength" depends on the scale of the model. This also implies that the effect of the "equivalent tensile strength" on the strength of the models diminishes when the model contains large cracks because they alone will determine the level of stress involved and the failure mechanism (Figure 27);

- The "equivalent tensile strength" to be input in the models should be treated as a statistical variable as suggested in Sec. 1.3. This means that the tensile strength is a local feature of the models.
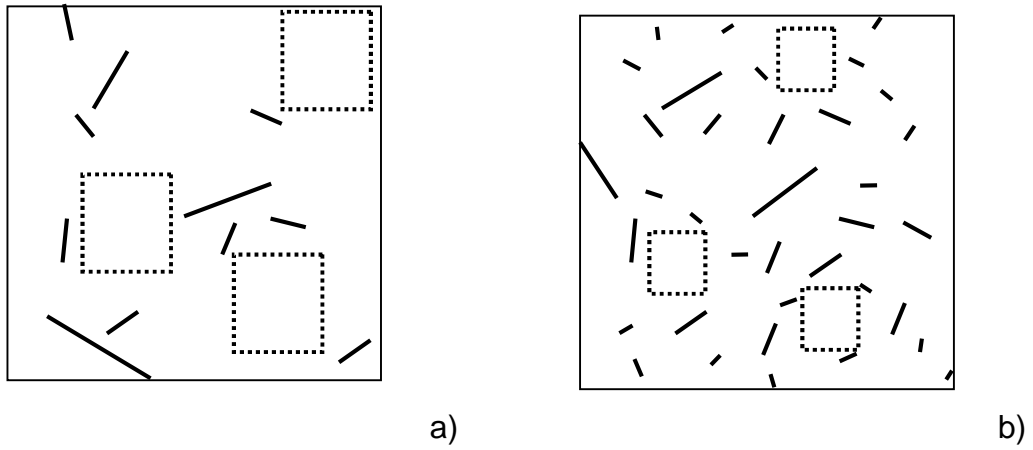
a)

b)

Figure 28. Qualitative examples of generation of "weakest crack" patterns and size of the volumes where the "equivalent tensile strength" should be determined for a case with long (a) and short (b) "weakest cracks".

6 Conclusions

The conclusions of this study can be summarized as follows:

- Core damage permeates the determination of the rock strength from core samples. Depending on the level of in-situ stress, the mismatch between the laboratory and in-situ strength of the rock cannot be neglected. This has consequences, other than for the classification of the rock mass quality from core geomechanical data, on the design of underground facilities when all the phenomena involved are understood;

- The evaluation of the level of damage might offer the opportunity of estimating the level of in-situ stress when the phenomena of damage is completely understood (e.g. drilling and overcoring);

- Linear elastic fracture mechanics incorporates intrinsic scaling properties that could explain the variation of the in-situ strength of the rock when increasing volumes are considered;

- The concept of the "weakest crack" together with the statistical description of the cracks by means of density and frequency distribution of random crack lengths as a function of the scale of observation provides a robust model for the analysis of real crack/fracture patterns and for designing realistic numerical models. The framework for the statistical analysis is Fractal geometry. It was also observed that spatial correlations of the orientation of the cracks due to a certain homogeneous regional stress field can also be simulated at different scales;

- The length of the "weakest crack" considered should also affect the level of "equivalent tensile strength" beyond which new fracture initiation would occur implying that even the strength should be scale dependent. This is also pointed out by the BEM-DDM models of Brazilian testing reported in this study;

- Gravity seems to be the main field force driving the phenomenon of "sheeting joints". Moreover, the pattern of the sheeting joints seems to deeply affect the distribution of in-situ stresses, not only at the depth of their occurrence, but also considerably below that.

7 Further research

Based on the discussion presented in this chapter, some research topics appear to be relevant for the understanding of deep geological environment and for improving the reliability of deep geological disposal technology:

- For more realistic simulation of the *overcoring process*, *sample damage and core discing*, a "bench-cut" function should be implemented in FRACOD[2D] to allow for simulation of drilling in several steps (e.g. deepening of the borehole or drilling of a hollow core after pilot hole drilling). This function would also allow for more realistic simulations of crown-and-bench kind of *tunnelling* ;

- Due to the fact that real stress fields are often anisotropic, modelling of the core damage and tunnel processes should be dealt with in *tri-dimensions* rather than two-dimensions as with FRACOD[2D]. As shown by Lim et al.[51] BEM-DDM, there are good chances to describe fracture propagation in 3D. For this reason, the existent 3D version of the program FRACOD[3D] [52] should be further developed and validated;

- Before carrying out validations of the BEM-DDM program, more investigations on the *pre-existent crack and fracture patterns* should be carried out to properly define the length of the "weakest crack" and the associated "equivalent tensile strength" of the intact rock at that scale. Material-specific relations between the statistical parameters that describe the crack density and frequency distribution of lengths and how these parameters vary with the level of initial stress should also be investigated;

- Since the concept of "weakest crack" is sensitive to scale, the simulation of *sheeting joints* should be revisited in the light of more detailed in-situ fracture pattern observations in boreholes, tunnels and shafts, more carefully chosen boundary conditions and larger numerical models. Mapping the walls of an excavation while it is deepening through a rock mass hosting sheeting joints can also offer opportunity of validation of the conceptual model;

- *Validation of FRACOD[2D]* for uniaxial and tri-axial conditions, considering short and long terms, has been successfully carried out by Rinne et al. [20] and Rinne & Shen [53]. This report contributed to the validation of FRACOD[2D] against Brazilian testing results. A further step would be to validate the program against Punch Through Shear (PTS) tests, since this test provides the fracture toughness in Model II (shearing in direction perpendicular to the crack tip) which is determinant for realistic fracture propagation processes when high confinement is involved;

- *Validation of FRACOD[3D]* for the same testing conditions examined for the 2D version, thus implementing and solving the programming obstacle due to the treatment of Mode II crack behaviour (shearing in direction parallel to the crack tip).

8   References

1)   Tsuruta T., Ota K., Amano K., Matsuoka T., Sasaki K. : Geological investigations during the Surface-Based investigation phase of the Mizunami Underground Research Laboratory (MIU) Project. ICGM'04, JNC Report TN7400 2004-010, p. 83-95, 2004.

2)   Kikuchi K., Fujieda M., Oka N., Kobayashi T.: Geotechnically integrated   evaluation on the stability of dam foundation rocks, Journal of the Japan Society of Engineering Geology, Special Edition, Japan Society of Engineering Geology, p. 103-118 (in Japanese), 1984.

3)   Yamada A., Sato T., Nakama S. : Rock mechanical investigations, 18th NAGRA/JNC Technical Meeting "MIZ-1 Workshop", 11-12 January 2005, MGA, Mizunami, Japan, 2005.

4)   Fairhurst C. : Stress estimation in rock: a brief history and review, Int. J. Rock Mech. Min. Sci., Vol. 40, p. 957-973, 2003.

5)   Holt R.M., Brignoli M., Kenter C. J. : Core quality: quantification of coring-induced rock alteration, Int. J. Rock Mech. Min. Sci., Vol. 37, p 889-907, 2000.

6)   Guo R., Thompson P. : Influences of changes in mechanical properties of an overcored sample on the far-field stress calculation, Int. J. Rock Mech. Min. Sci., Vol. 41, p. 1153-1166, 2004.

7)   Ganne P., Vervoort A., Wevers M. : Quantification of pre-peak brittle damage: Correlation between acoustic emission and observed micro-fracturing, Int. J. Rock Mech. Min. Sci., Vol. 44, p. 720-729, 2007.

8)   Cornet F.H., Berard Th., Bourouis S. : How close is a granite rock at 5 km depth? Int. J. Rock Mech. Min. Sci Vol. 44, p. 47-66, 2007.

9)   Shen B., Rinne M., Stephansson O. : FRACOD[2D] - Two dimensional fracture propagation code (Version 2.3.1), FRACOM Ltd., Finland (www.fracom.fi), 2007.

10) Backers T. : Mode I and Mode II fracture toughness testing and fracture normal stiffness estimation of Tono-Granite, GeoForschungZentrum (Potsdam, Germany), p. 18, 2002.

11) Glamheden R., Fredriksson A., Persson L., Röshoff K., Karlsson J., Bohlin A., Lindberg U., Hakami H., Hakami E., Johansson M., : Rock mechanics Site descriptive modelling – Forsmark stage 2.2, the Swedish Nuclear Fuel and Waste Management Co., Tech. Rep. SKB R-07-31 (in preparation), 2007.

12) Proveti J.R.C., Michot G. : The Brazilian test: a tool for measuring the toughness of a material and its brittle to ductile transition, Int. J. Fract., Vol. 139, p. 455-460, 2006.

13) Hakala M. : Numerical study on core damage and interpretation of in situ state of stress, Report POSIVA 99-25, Posiva Oy, Helsinki, Finland, p. 234, 1999.

14) Kaga N., Matsuki K., Sakaguchi K. : The in situ stress states associated with core discing estimated by analysis of principal tensile stress, I. J. Rock Mech. Min. Sci., Vol. 40, p. 653-665, 2003.

15) Chang C., Haimson B. : Effect of fluid pressure on rock compressive failure in a nearly impermeable crystalline rock: Implications on mechanism of borehole breakouts, Eng. Geo., Vol. 89, p. 230-242, 2007.

16) Hakami H. : Numerical studies on spatial variation of the in situ stress field at Forsmark - a further step. Site descriptive modelling Forsmark - stage 2.1, Swedish Nuclear Fuel and Waste Management Co, Tech. Rep. SKB R-06-124, 2006.

17) Martel S.J. : Effect of topographic curvature on near-surface stress and application to sheeting joints, Geoph. Res. Lett., Vol. 33, Paper L01308, 2006.

18) Backers T., Antikainen J., Rinne M. : Time dependent fracture growth in intact crystalline rock: Laboratory procedures and results, Proc. 2nd Int. Conf. on Coupled T-H-M-C Processes in Geo-Systems: Fundamentals, Modeling, Experiments and Applications, GeoProc2006, Nanjing, P.R. of China, 2006.

19) Rinne M., Shen B., Stephansson O. : Numerical analysis of microstructural breakdown of compressed rock samples, Proc. EUROCK 2006 – Multiphysics Coupling and Long Term Behaviour in Rock Mechanics, Liege, Belgium, (Cottum A. V. ed.), Taylor & Francis Ltd: London, p. 701-705, 2006.

20) Yoshida H., Takeuchi M., Metcalfe R. : Long-term stability of flow-path structure in crystalline rocks distributed in an orogenic belt, Japan, Engineering Geology, Vol. 78, p. 275-284, 2005.

21) Strickland F.D., Ren N.-K. : Use of differential strain curve analysis in predicting the in-situ stress state for deep wells, Proc. 21st US Symp. Rock Mech., Rolla, USA, p. 523-532, 1980.

22) Matsuki K., Takeuchi K. : Three-dimensional in situ stress determination by anelastic strain recovery of a rock core, Int. J. Rock Mech. Min. Sci., Vol. 30(7), p. 1019-1022, 1993.

23) Teufel L.W. : Determination of in situ stress from partial anelastic strain recovery measurements of oriented cores from deep boreholes, Short Course in Modern In Situ Stress Measurement Methods, 34th US Symp. Rock Mech., Madison, USA, p. 19, 1993.

24) Kato H. : In situ stress measurements in MIU-3 borehole using hydraulic fracturing, the Japan Nuclear Cycle Development Institute, Report JNC TN7400 2000-005 (in Japanese with English abstract), 2000.

25) Li Y., Schmitt D.R. : Well-bore bottom stress concentration and induced core fractures, Am. Ass. Petrol. Geol. AAPG Bulletin, Vol. 81(11), p. 1909-1925, 1997.

26) Sakaguchi K., Iino W., Matsuki K. : Damage in a rock core caused by induced tensile stress and its relation to differential strain curve analysis, Int. J. Rock Mech. Min. Sci., Vol. 39, p. 367-380, 2002.

27) Bäckström A., Lanaro F., Christiansson R. : Coupled chemical-mechanical behaviour: the influence of salinity on the uniaxial compressive strength of the Småland granite, Sweden, Proc. 2nd Int. Conf. on Coupled T-H-M-C Processes in Geo-Systems: Fundamentals, Modeling, Experiments and Applications, GeoProc2006, Nanjing, P.R. of China, p. 437-443, 2006.

28) Bäckström A., Hudson J.A. : Consistency and Validity of Numerical Modelling in Rock Mechanics: A Case Study for Uniaxial Compressive Failure with and without Saline Porewater, submitted to Int. J. Rock Mech. Min. Sci., 2007.

29) Andersson C., Eng, A. : Äspö Pillar Stability Experiment. Final experiment design, monitoring results and observations, the Swedish Nuclear Fuel and Waste Management Co, Tech. Rep. SKB R-05-02, 2005.

30) Lavrov A., Vervoort A., Wevers M. : Anisotropic damage formation in brittle rock: Experimental study by means of acoustic emission and Kaiser effect, J. Phys. IV France, Vol. 105, p. 321-328, 2003.

31) Fairhurst C. : Fundamental considerations relating to the strength of rock, Colloquium on Rock Fracture, Veröff. Inst. Bodeenmechanik und Felsmechanik, Karlsuhe, Germany, Vol. 55, p. 1-56, 1971.

32) Vermilye J.M., Scholz C.H. : The Process zone. A microstructural view of fault growth, J. Geophys. Res., Vol. 103(B6), p. 12223–12237, 1998.

33) Vermilye J.M. : The growth of natural fracture systems: A fracture mechanics approach, Ph. D thesis, Colombia University, New York, USA, 1996.

34) Cowie P.A., Shipton Z.K. : Fault tip displacement gradients and process zone dimensions, J. Structural Geology, Vol. 20(8), p. 983–997, 1998.

35) Sagy A., Axen G.J., Brodsky E.E. : LIDAR Measurements of Fault Roughness, Proc. American Geophysical Union, Fall Meeting 2005, Abstract No. #T14B-02, 2005.

36) Wang W.-H., Huang S.-M. : Seismicity and stress evolution in heterogeneous faults with various degrees of roughness, Tectonophysics, Volume 424(3-4), p. 307-318, 2006.

37) Sagy A., Brodsky E.E., Axen G.J. : Evolution of fault-surface roughness with slip, Geology, Vol. 35(3), p.283, 2007.

38) Koike K., Ichikawa Y. : Spatial correlation structures of fracture systems for deriving a scaling law and modelling fracture distributions, Computers & Geociences, Vol. 32, p. 1079-1095, 2006

39) Voss R.F. : Random fractals: characterisation and measurements, in Scaling phenomena in disordered systems, Plenum Press: New York, USA, p. 1-11, 1985.

40) Schmittbuhl J., Schmitt F., Scholz C. : Scaling invariance of crack surfaces, J. Geophys. Res., Vol. 100(B4), p. 5953-5973, 1995.

41) Engelder, T. : Is there a generic relationship between selected regional joints and contemporary stress within the lithosphere of North America? Tectonics, Vol. 1, p. 161-177, 1982.

42) Zhao Y. : Crack pattern evolution and a fractal damage constitutive model for rock, Int. J. Rock Mech. Min. Sci., Vol. 35(3), p. 349-366, 1998.

43) Liu S., Anwar F., Seiki T., Ichikawa Y. : Microcrack generation and propagation in granite during stress relaxation under water saturated tri-axial condition, Journal of the Japan Society of Engineering Geology, Special Edition, Japan Society of Engineering Geology, p. 623-630, 2006.

44) Nara Y., Koike K., Yoneda T., Kaneko K. : Relation between subcritical crack growth behavior and crack paths in granite, Tech. Note, Int. J. Rock Mech. Min. Sci., Vol. 43, p. 1256-1261, 2006.

45) Weibull W. : A statistical theory of the strength of materials, Bull. Accademy of Engineering Sciences, Stockholm, Sweden, Vol. 151, 1939.

46) Weibull W. : A statistical distribution function of wide applicability, J. Appl. Mech., Vol. 18, p. 293-297, 1951.

47) Olovsson L. : KRYP, a finite element tool for crystal plasticity analysis, FOI – the Swedish Defense Research Agency, Method. Report FOI-R--0374--SE, p. 30, 2002.

48) Olovsson L., Unosson M. : Fracture modeling of hard metal in KRYP, FOI – the Swedish Defense Research Agency, Tech. Report FOI-R--1306--SE, p. 12 (in Swedish), 2004.

49) Potyondy D.O., Cundall P.A. : A bounded-particle model for rock, Int. J. Rock Mech. Min. Sci. & Geomech. Abstr., Vol. 41, p. 1329-1364, 2004.

50) Unosson M., Olovsson L., Simonsson K. : Failure modeling in finite element analyses: Random material imperfections, Mech. Mat., Vol. 37(12), p. 1175-1179, 2005.

51) Lim S.S., Martin C.D., Christiansson R : Estimating in-situ stress magnitudes from core discing, Proc. Conf. In-situ Rock Stress – Measurements, Interpretation and Application, Trondheim, Norway, (Lu, Li, Kjørholt and Dahle eds.), p. 159-166, 2006.

52) Shi J., Shen B., Rinne M. : FRACOD[3D] – Developing 3-Dimensional Displacement Discontinuity Code with Cracks Growth, FRACOM Ltd, Report in preparation, 2007.

53) Rinne M., Shen B. : Numerical simulation of core tests using FRACOD, in DECOVALEX-THMC TASK B – Understanding and characterizing the excavation disturbed zone (EDZ), Phase 2 (Hudson J.A. & Jing L. eds.), the Swedish Nuclear Power Inspectorate, SKI Report 2007:08, 2007.

This is a blank page.

-235-

Acknowledgment

This is a blank page.

This is a blank page.

国際単位系（SI）

表1．SI 基本単位

基本量	SI 基本単位 名称	記号
長　　　さ	メートル	m
質　　　量	キログラム	kg
時　　　間	秒	s
電　　　流	アンペア	A
熱力学温度	ケルビン	K
物　質　量	モル	mol
光　　　度	カンデラ	cd

表2．基本単位を用いて表されるSI組立単位の例

組立量	SI 基本単位 名称	記号
面　　　　　積	平方メートル	m^2
体　　　　　積	立法メートル	m^3
速　さ，速度	メートル毎秒	m/s
加　　速　　度	メートル毎秒毎秒	m/s^2
波　　　　　数	毎メートル	m-1
密度（質量密度）	キログラム毎立法メートル	kg/m^3
質量体積（比体積）	立法メートル毎キログラム	m^3/kg
電　流　密　度	アンペア毎平方メートル	A/m^2
磁　界　の　強　さ	アンペア毎メートル	A/m
（物質量の）濃度	モル毎立方メートル	mol/m^3
輝　　　　　度	カンデラ毎平方メートル	cd/m^2
屈　　折　　率	（数　の）　1	1

表5．SI 接頭語

乗数	接頭語	記号	乗数	接頭語	記号
10^{24}	ヨタ	Y	10^{-1}	デシ	d
10^{21}	ゼタ	Z	10^{-2}	センチ	c
10^{18}	エクサ	E	10^{-3}	ミリ	m
10^{15}	ペタ	P	10^{-6}	マイクロ	μ
10^{12}	テラ	T	10^{-9}	ナノ	n
10^{9}	ギガ	G	10^{-12}	ピコ	p
10^{6}	メガ	M	10^{-15}	フェムト	f
10^{3}	キロ	k	10^{-18}	アト	a
10^{2}	ヘクト	h	10^{-21}	ゼプト	z
10^{1}	デカ	da	10^{-24}	ヨクト	y

表3．固有の名称とその独自の記号で表されるSI組立単位

組立量	SI 組立単位 名称	記号	他のSI単位による表し方	SI基本単位による表し方
平　面　角	ラジアン [(a)]	rad		$m・m^{-1}=1$ [(b)]
立　体　角	ステラジアン [(a)]	sr [(c)]		$m^2・m^{-2}=1$ [(b)]
周　波　数	ヘルツ	Hz		s^{-1}
力	ニュートン	N		$m・kg・s^{-2}$
圧　力，応　力	パスカル	Pa	N/m^2	$m^{-1}・kg・s^{-2}$
エネルギー，仕事，熱量	ジュール	J	N・m	$m^2・kg・s^{-2}$
工　率，放射束	ワット	W	J/s	$m^2・kg・s^{-3}$
電　荷，電気量	クーロン	C		s・A
電位差（電圧），起電力	ボルト	V	W/A	$m^2・kg・s^{-3}・A^{-1}$
静　電　容　量	ファラド	F	C/V	$m^{-2}・kg^{-1}・s^4・A^2$
電　気　抵　抗	オーム	Ω	V/A	$m^2・kg・s^{-3}・A^2$
コンダクタンス	ジーメンス	S	A/V	$m^{-2}・kg^{-1}・s^3・A^2$
磁　　　　束	ウェーバ	Wb	V・s	$m^2・kg・s^{-2}・A^{-1}$
磁　束　密　度	テスラ	T	Wb/m^2	$kg・s^{-2}・A^{-1}$
インダクタンス	ヘンリー	H	Wb/A	$m^2・kg・s^{-2}・A^{-2}$
セルシウス温度	セルシウス度 [(d)]	℃		K
光　　　　束	ルーメン	lm	cd・sr [(c)]	$m^2・m^{-2}・cd=cd$
照　　　　度	ルクス	lx	lm/m^2	$m^2・m^{-4}・cd=m^{-2}・cd$
（放射性核種の）放射能	ベクレル	Bq		s^{-1}
吸収線量，質量エネルギー分与，カーマ	グレイ	Gy	J/kg	$m^2・s^{-2}$
線量当量，周辺線量当量，方向性線量当量，個人線量当量，組織線量当	シーベルト	Sv	J/kg	$m^2・s^{-2}$

(a)ラジアン及びステラジアンの使用は、同じ次元であっても異なった性質をもった量を区別するときの組立単位の表し方として利点がある。組立単位を形作るときのいくつかの用例は表4に示されている。
(b)実際には、使用する時には記号rad及びsrが用いられるが、習慣として組立単位としての記号"1"は明示されない。
(c)測光学では、ステラジアンの名称と記号srを単位の表し方の中にそのまま維持している。
(d)この単位は、例としてミリセルシウス度m℃のようにSI接頭語を伴って用いても良い。

表6．国際単位系と併用されるが国際単位系に属さない単位

名称	記号	SI 単位による値
分	min	1 min=60s
時	h	1h＝60 min=3600 s
日	d	1 d=24 h=86400 s
度	°	$1°=(\pi/180)$ rad
分	′	$1'=(1/60)°=(\pi/10800)$ rad
秒	″	$1''=(1/60)'=(\pi/648000)$ rad
リットル	l，L	$1l=1 dm^3=10^{-3}m^3$
トン	t	$1t=10^3$ kg
ネーパ	Np	1Np=1
ベル	B	1B=(1/2)ln10(Np)

表7．国際単位系と併用されこれに属さない単位でSI単位で表される数値が実験的に得られるもの

名称	記号	SI 単位であらわされる数値
電子ボルト	eV	$1eV=1.60217733(49)\times10^{-19}$J
統一原子質量単位	u	$1u=1.6605402(10)\times10^{-27}$kg
天文単位	ua	$1ua=1.49597870691(30)\times10^{11}$m

表4．単位の中に固有の名称とその独自の記号を含むSI組立単位の例

組立量	SI 組立単位 名称	記号	SI 基本単位による表し方
粘　　　　　度	パスカル秒	Pa・s	$m^{-1}・kg・s^{-1}$
力のモーメント	ニュートンメートル	N・m	$m^2・kg・s^{-2}$
表　面　張　力	ニュートン毎メートル	N/m	$kg・s^{-2}$
角　　速　　度	ラジアン毎秒	rad/s	$m・m^{-1}・s^{-1}=s^{-1}$
角　加　速　度	ラジアン毎平方秒	rad/s^2	$m・m^{-1}・s^{-2}=s^{-2}$
熱流密度，放射照度	ワット毎平方メートル	W/m^2	$kg・s^{-3}$
熱容量，エントロピー	ジュール毎ケルビン	J/K	$m^2・kg・s^{-2}・K^{-1}$
質量熱容量（比熱容量），質量エントロピー	ジュール毎キログラム毎ケルビン	J/(kg・K)	$m^2・s^{-2}・K^{-1}$
質量エネルギー（比エネルギー）	ジュール毎キログラム	J/kg	$m^2・s^{-2}・K^{-1}$
熱　伝　導　率	ワット毎メートル毎ケルビン	W/(m・K)	$m・kg・s^{-3}・K^{-1}$
体積エネルギー	ジュール毎立方メートル	J/m^3	$m^{-1}・kg・s^{-2}$
電　界　の　強　さ	ボルト毎メートル	V/m	$m・kg・s^{-3}・A^{-1}$
体　積　電　荷	クーロン毎立方メートル	C/m^3	$m^{-3}・s・A$
電　気　変　位	クーロン毎平方メートル	C/m^2	$m^{-2}・s・A$
誘　　電　　率	ファラド毎メートル	F/m	$m^{-3}・kg^{-1}・s^4・A^2$
透　　磁　　率	ヘンリー毎メートル	H/m	$m・kg・s^{-2}・A^{-2}$
モルエネルギー	ジュール毎モル	J/mol	$m^2・kg・s^{-2}・mol^{-1}$
モルエントロピー，モル熱容量	ジュール毎モル毎ケルビン	J/(mol・K)	$m^2・kg・s^{-2}・K^{-1}・mol^{-1}$
照射線量（X線及びγ線）	クーロン毎キログラム	C/kg	$kg^{-1}・s・A$
吸　収　線　量　率	グレイ毎秒	Gy/s	$m^2・s^{-3}$
放　射　強　度	ワット毎ステラジアン	W/sr	$m^4・m^{-2}・kg・s^{-3}=m^2・kg・s^{-3}$
放　射　輝　度	ワット毎平方メートル毎ステラジアン	W/(m²・sr)	$m^2・m^{-2}・kg・s^{-3}=kg・s^{-3}$

表8．国際単位系に属さないが国際単位系と併用されるその他の単位

名称	記号	SI 単位であらわされる数値
海　里		1海里=1852m
ノット		1ノット=1海里毎時=(1852/3600)m/s
アール	a	$1a=1 dam^2=10^2m^2$
ヘクタール	ha	$1ha=1 hm^2=10^4m^2$
バール	bar	$1bar=0.1MPa=100kPa=1000hPa=10^5Pa$
オングストローム	Å	$1 Å=0.1nm=10^{-10}m$
バーン	b	$1b=100fm^2=10^{-28}m^2$

表9．固有の名称を含むCGS組立単位

名称	記号	SI 単位であらわされる数値
エルグ	erg	$1 erg=10^{-7}$ J
ダイン	dyn	$1 dyn=10^5$N
ポアズ	P	$1 P=1 dyn・s/cm^2=0.1Pa・s$
ストークス	St	$1 St =1cm^2/s=10^{-4}m^2/s$
ガウス	G	$1 G ^10^{-4}$T
エルステッド	Oe	$1 Oe ^(1000/4\pi)A/m$
マクスウェル	Mx	$1 Mx ^10^{-8}$Wb
スチルブ	sb	$1 sb =1cd/cm^2=10^4cd/m^2$
ホト	ph	$1 ph=10^4lx$
ガル	Gal	$1 Gal =1cm/s^2=10^{-2}m/s^2$

表10．国際単位に属さないその他の単位の例

名称	記号	SI 単位であらわされる数値
キュリー	Ci	$1 Ci=3.7\times10^{10}Bq$
レントゲン	R	$1 R = 2.58\times10^{-4}C/kg$
ラド	rad	$1 rad=1cGy=10^{-2}Gy$
レム	rem	$1 rem=1 cSv=10^{-2}Sv$
X 線 単 位		$1X unit=1.002\times10^{-4}nm$
ガンマ	γ	$1 γ=1 nT=10^{-9}T$
ジャンスキー	Jy	$1 Jy=10^{-26}W・m^{-2}・Hz^{-1}$
フェルミ		$1 fermi=1 fm=10^{-15}m$
メートル系カラット		$1 metric carat = 200 mg = 2\times10^{-4}kg$
トル	Torr	$1 Torr = (101 325/760) Pa$
標準大気圧	atm	1 atm = 101 325 Pa
カロリー	cal	
ミクロン	μ	$1 μ =1μm=10^{-6}m$